

# **Physics and Astrophysics of Compact Objects**



# Contents

<b>1</b>	<b>Topics</b>	<b>1107</b>
<b>2</b>	<b>Participants</b>	<b>1111</b>
2.1	ICRANet . . . . .	1111
2.2	External collaborations: professors and senior researchers . . .	1111
2.3	Postdocs . . . . .	1113
2.4	Graduate Students . . . . .	1113
<b>3</b>	<b>Publications 2022</b>	<b>1115</b>
3.1	Refereed Journals . . . . .	1115
3.1.1	Printed . . . . .	1115
3.1.2	Accepted for publication or in press . . . . .	1121
3.1.3	Submitted for publication . . . . .	1123
3.2	Conference Proceedings . . . . .	1124



# 1 Topics

The study of compact objects such as white dwarfs, neutron stars, and black holes requires the interplay between nuclear and atomic physics together with relativistic field theories, e.g., general relativity, quantum electrodynamics, quantum chromodynamics, as well as particle physics. In addition to the theoretical physics aspects, the study of astrophysical scenarios characterized by the presence of at least one of the above compact objects is the focus of extensive research within our group, e.g. physics of pulsars. This research can be divided into the following topics:

- **Nuclear and Atomic Astrophysics.** We study the properties and processes occurring in compact stars in which nuclear and atomic physics have to be necessarily applied. We focus on the properties of nuclear matter under extreme conditions of density, pressure, and temperature in compact star interiors. The matter equation of state is studied in detail taking into account all the interactions between the constituents within a fully relativistic framework.
- **White Dwarfs Physics and Structure.** The aim of this part of our research is the construction of the white dwarf structure within a self-consistent description of the equation of state of the interior together with the solution of the hydrostatic equilibrium equations in general relativity. Non-magnetized, magnetized, non-rotating, and rotating white dwarfs are studied. The interaction and evolution of a central white dwarf with a surrounding disk, as occurred in the aftermath of white dwarf binary mergers, is also a subject of study.
- **White Dwarfs Astrophysics.** We are interested in the astrophysics of white dwarfs both isolated and in binaries. Magnetized white dwarfs, soft gamma repeaters, anomalous X-ray pulsars, white dwarf pulsars, cataclysmic variables, binary white dwarf mergers, and type Ia supernovae are studied. The role of a realistic white dwarf interior structure is particularly emphasized.

- **Neutron Stars Physics and Structure.** We calculate the properties of the interior structure of neutron stars using realistic models of the nuclear matter equation of state within the general relativistic equations of equilibrium. Strong, weak, electromagnetic, and gravitational interactions have to be jointly taken into due account within a self-consistent fully relativistic framework. Non-magnetized, magnetized, non-rotating, and rotating neutron stars are studied.
- **Neutron Stars Astrophysics.** We study astrophysical systems harboring neutron stars such as isolated and binary pulsars, low and intermediate X-ray binaries, and merging double neutron stars and neutron star-white dwarf binaries. Most extreme cataclysmic events involving neutron stars and their role in the explanation of extraordinarily energetic astrophysical events such as gamma-ray bursts are analyzed in detail.
- **Black Hole Physics and Astrophysics.** We study the role of black holes in relativistic astrophysical systems such as gamma-ray bursts, active galactic nuclei, and galactic cores. Special attention is given to the application of the theory of test particle motion both in the neutral and charged case, as well as to general relativity tests.
- **Radiation Mechanisms of Compact Objects.** We here study possible emission mechanisms of compact objects such as white dwarfs, neutron stars, and black holes. We are interested in the electromagnetic, neutrino, and gravitational-wave emission in compact object magnetospheres, and accretion disks surrounding them, as well as inspiraling and merging relativistic binaries (double neutron stars, neutron star-white dwarfs, white dwarf-white dwarf, and neutron star-black holes). We also study the radiation from particle acceleration in the vicinity of stellar-mass and supermassive black holes by surrounding electromagnetic fields.
- **Exact and Numerical Solutions of the Einstein and Einstein-Maxwell Equations in Astrophysics.** We analyze the ability of analytic exact solutions of the Einstein and Einstein-Maxwell equations to describe the exterior spacetime of compact stars such as white dwarfs and neutron stars. For this, we compare and contrast exact (analytic) solutions with numerical solutions of the stationary axisymmetric Einstein equations.

---

The problem of matching between interior and exterior spacetime is addressed in detail. The effect of the quadrupole moment on the properties of the spacetime is also investigated. Particular attention is given to the application of exact solutions in astrophysics, e.g. the dynamics of particles around compact stars and their relevance in astrophysical systems such as X-ray binaries and gamma-ray bursts.

- **Critical Fields and Non-linear Electrodynamics Effects in Astrophysics.** We study the conditions under which ultrastrong electromagnetic fields can develop in astrophysical systems such as neutron stars and in the process of gravitational collapse to a black hole. The effects of non-linear electrodynamics minimally coupled to gravity are investigated. New analytic and numeric solutions to the Einstein-Maxwell equations representing black holes or the exterior field of a compact star are obtained and analyzed. The consequences on extreme astrophysical systems, for instance, gamma-ray bursts, are studied.





## 2 Participants

### 2.1 ICRANet

- C. L. Bianco (ICRANet, Italy)
- J. A. Rueda (ICRANet, Italy)
- L. Li (ICRANet, Italy)
- R. Moradi (ICRANet, Italy)
- R. Ruffini (ICRANet, Italy)
- N. Sahakyan (ICRANet, Armenia)
- G. Vereschagin (ICRANet, Italy)
- S.-S. Xue (ICRANet, Italy)
- Y. Wang (ICRANet, Italy)

### 2.2 External collaborations: professors and senior researchers

- C. Arguelles (Universidad de La Plata, Argentina)
- K. Boshkayev (Al-Farabi Kazakh National University, Kazakhstan)
- R. Camargo (Universidade do Estado de Santa Catarina, Florianópolis, Brazil)
- G. A. Carvalho (Universidade Tecnológica Federal do Paraná, Brazil; Universidade do Vale do Paraíba, Brazil; Instituto Tecnológico de Aeronáutica, Brazil)

## 2 Participants

---

- C. Cherubini (Università Campus Biomedico, Rome, Italy)
- J. G. Coelho (Universidade Federal do Espírito Santo, Brazil)
- J. C. N. de Araujo (Instituto Nacional de Pesquisas Espaciais, Brazil)
- R. C. dos Anjos (Universidade Federal do Paraná, Brazil; Universidade Federal da Fronteira Latino-Americana, Brazil; Universidade Tecnológica Federal do Paraná, Brazil)
- A. Drago (INFN, Università degli Studi di Ferrara, Italy)
- S. Filippi (Università Campus Biomedico, Rome, Italy)
- C. L. Fryer (Los Alamos National Laboratory, USA; University of Arizona, USA)
- G. A. González (Universidad Industrial de Santander, Colombia)
- C. Guidorzi (Università degli Studi di Ferrara, Italy)
- F. D. Lora-Clavijo (Universidad Industrial de Santander, Colombia)
- S. O. Kepler (Universidade Federal do Rio Grande do Sul, Brazil)
- M. Malheiro (Instituto Tecnológico de Aeronáutica, Brazil)
- R. M. Jr. Marinho (Instituto Tecnológico de Aeronáutica, Brazil)
- M. F. Mestre (Universidad de La Plata, Argentina; Instituto de Astrofísica de La Plata, Argentina)
- L. A. Nuñez (Universidad Industrial de Santander, Colombia)
- J. F. Rodriguez (Universidad Industrial de Santander, Colombia)
- J. D. Uribe-Suarez (Universidad Santiago de Cali, Colombia)
- J. I. Zuluaga (Universidad de Antioquia, Colombia)

## 2.3 Postdocs

- L. Becerra (Universidad Industrial de Santander, Colombia)
- E. A. Becerra (Universidad Industrial de Santander, Colombia)
- S. Campion (INFN, Sapienza University of Rome, Italy)
- R. V. Lobato (Universidad de los Andes, Bogotá, Colombia; Texas A&M University-Commerce, Commerce, USA)
- J. P. Pereira (Nicolaus Copernicus Astronomical Center, Polish Academy of Sciences, Poland)
- F. Rastegarnia (ICRANet-Pescara, Italy)

## 2.4 Graduate Students

- V. Crespi (Universidad de La Plata, Argentina)
- G. Nurbakyt (Al-Farabi Kazakh National University, Kazakhstan)
- M. F. Sousa (Instituto Nacional de Pesquisas Espaciais, Brazil)
- G. Zhumakhanova (Al-Farabi Kazakh National University, Kazakhstan)



# 3 Publications 2022

## 3.1 Refereed Journals

### 3.1.1 Printed

1. Sousa, M. F.; Coelho, J. G.; de Araujo, J. C. N.; Kepler, S. O.; Rueda, J. A., *The double white dwarf merger progenitors of SDSS J2211+1136 and ZTF J1901+1458*, *The Astrophysical Journal*, 941, 28, 2022.

Double white dwarf (DWD) mergers are possibly the leading formation channel of massive, rapidly rotating, high-field magnetic white dwarfs (HFMWDs). However, the direct link connecting a DWD merger to any observed HFMWD is still missing. We here show that the HFMWDs SDSS J2211+1136 and ZTF J1901+1458, might be DWD merger products. J2211+1136 is a  $1.27 M_{\odot}$  WD with a rotation period of 70.32 s and a surface magnetic field of 15 MG. J1901+1458 is a  $1.327\text{--}1.365 M_{\odot}$  WD with a rotation period of 416.20 s, and a surface magnetic field in the range 600–900 MG. With the assumption of single-star evolution, the currently measured WD masses and surface temperatures, the cooling ages of J2211+1136 and J1901+1458 are, respectively, 2.61–2.85 Gyr and 10–100 Myr. We hypothesize that these WDs are DWD merger products and compute the evolution of the post-merged configuration formed by a central WD surrounded by a disk. We show that the post-merger system evolves through three phases depending on whether accretion, mass ejection (propeller), or magnetic braking dominates the torque onto the central WD. We calculate the time the WD spends in each of these phases and obtain the accretion rate and disk mass for which the WD rotational age, i.e., the total time elapsed since the merger to the instant where the WD central remnant reaches the current measured rotation period, agrees with the estimated WD cooling age. We infer the mass values of the primary and secondary WD components of the DWD merger that lead to a post-merger evolution consistent with the

observations.

2. Carvalho, G. A.; Anjos, R. C. dos; Coelho, J. G.; Lobato, R. V.; Malheiro, M.; Marinho, R. M.; Rodriguez, J. F.; Rueda, J. A.; Ruffini, R., *Orbital decay of double white dwarfs: beyond gravitational-wave radiation effects*, The Astrophysical Journal, 940, 90, 2022.

The traditional description of the orbital evolution of compact-object binaries, like double white dwarfs (DWDs), assumes that the system is driven only by gravitational wave (GW) radiation. However, the high magnetic fields with intensities of up to gigagauss measured in WDs alert a potential role of electromagnetic (EM) emission in the evolution of DWDs. We evaluate the orbital dynamics of DWDs under the effects of GW radiation, tidal synchronization, and EM emission by a unipolar inductor generated by the magnetic primary and the relative motion of the non-magnetic secondary. We show that the EM emission can affect the orbital dynamics for magnetic fields larger than megagauss. We applied the model to two known DWDs, SDSS J0651+2844 and ZTF J1539+5027, for which the GW radiation alone does not fully account for the measured orbital decay rate. We obtain upper limits to the primary's magnetic field strength, over which the EM emission causes an orbital decay faster than observed. The contribution of tidal locking and the EM emission is comparable, and together they can contribute up to 20% to the measured orbital decay rate. We show that the gravitational waveform for a DWD modeled as purely driven by GWs and including tidal interactions and EM emission can have large relative dephasing detectable in the mHz regime of frequencies relevant for space-based detectors like LISA. Therefore, including physics besides GW radiation in the waveform templates is essential to calibrate the GW detectors using known sources, e.g., ZTF J1539+5027, and to infer binary parameters.

3. Rueda, J. A.; Li, Liang; Moradi, R.; Ruffini, R.; Sahakyan, N.; Wang, Y., *On the X-Ray, Optical, and Radio Afterglows of the BdHN I GRB 180720B Generated by Synchrotron Emission*, The Astrophysical Journal, 939, 62, 2022.

Gamma-ray bursts (GRBs) are systems of unprecedented complexity across the electromagnetic spectrum, including the radio, optical, X-rays, gamma-rays in the megaelectronvolt (MeV) and gigaelectronvolt

(GeV) regime, as well as ultrahigh-energy cosmic rays (UHECRs), each manifested in seven specific physical processes with widely different characteristic evolution timescales ranging from  $10^{-14}$  s to  $10^7$  s or longer. We here study the long GRB 180720B originating from a binary system composed of a massive carbon-oxygen (CO) star of about  $10M_{\odot}$  and a companion neutron star (NS). The gravitational collapse of the CO star gives rise to a spinning newborn NS ( $\nu$ NS), with an initial period of  $P_0 = 1$  ms that powers the synchrotron radiation in the radio, optical, and X-ray wavelengths. We here investigate solely the GRB 180720B afterglows and present a detailed treatment of its origin based on the synchrotron radiation released by the interaction of the  $\nu$ NS and the SN ejecta. We show that in parallel to the X-ray afterglow, the spinning  $\nu$ NS also powers the optical and radio afterglows and allows to infer the  $\nu$ NS and ejecta parameters that fit the observational data.

4. Rueda, J. A; Ruffini, R.; Li, L.; Moradi, R.; Rodriguez, J. F.; Wang, Y., *Evidence for the transition of a Jacobi ellipsoid into a Maclaurin spheroid in gamma-ray bursts*, Physical Review D, 106, 083004, 2022.

In the binary-driven hypernova (BdHN) scenario, long gamma-ray bursts (GRBs) originate in a cataclysmic event that occurs in a binary system composed of a carbon-oxygen (CO) star and a neutron star (NS) companion in close orbit. The collapse of the CO star generates at its center a newborn NS ( $\nu$ NS), and a supernova (SN) explosion. Matter from the ejecta is accreted both onto the  $\nu$ NS because of fallback and onto the NS companion, leading to the collapse of the latter into a black hole (BH). Each of the ingredients of the above system leads to observable emission episodes in a GRB. In particular, the  $\nu$ NS is expected to show up (hereafter  $\nu$ NS-rise) in the early GRB emission, nearly contemporary or superimposed to the ultrarelativistic prompt emission (UPE) phase, but with a different spectral signature. Following the  $\nu$ NS-rise, the  $\nu$ NS powers the afterglow emission by injecting energy into the expanding ejecta leading to synchrotron radiation. We here show that the  $\nu$ NS-rise and the subsequent afterglow emission in both systems, GRB 180720B and GRB 190114C, are powered by the release of rotational energy of a Maclaurin spheroid, starting from the bifurcation point to the Jacobi ellipsoid sequence. This implies that the  $\nu$ NS evolves from a triaxial Jacobi configuration, prior to the  $\nu$ NS-rise, into the axially symmetric Maclaurin configuration observed in the GRB. The triaxial  $\nu$ NS config-

uration is short-lived (less than a second) due to a copious emission of gravitational waves, before the GRB emission, and it could be in principle detected for sources located at distances closer than 100 Mpc. This appears to be a specific process of emission of gravitational waves in the BdHN I powering long GRBs.

5. Becerra, L. M.; Moradi, R.; Rueda, J. A.; Ruffini, R.; Wang, Y., *First minutes of a binary-driven hypernova*, Physical Review D, 106, 083002, 2022.

We simulate the first minutes of the evolution of a binary-driven hypernova (BdHN) event, with a special focus on the associated accretion processes of supernova (SN) ejecta onto the newborn neutron star ( $\nu$ NS) and the NS companion. We calculate the rotational evolution of the  $\nu$ NS and the NS under the torques exerted by the accreted matter and the magnetic field. We take into account general relativistic effects through effective models for the NSs binding energy and the specific angular momentum transferred by the accreted matter. We use realistic hypercritical accretion rates obtained from three-dimensional smoothed-particle-hydrodynamics (SPH) numerical simulations of the BdHN for a variety of orbital periods. We show that the rotation power of the  $\nu$ NS has a unique double-peak structure while that of the NS has a single peak. These peaks are of comparable intensity and can occur very close in time or even simultaneously depending on the orbital period and the initial angular momentum of the stars. We outline the consequences of the above features in the early emission and their consequent observation in long gamma-ray bursts.

6. Rastegarnia, F.; Moradi, R.; Rueda, J. A.; Ruffini, R.; Li, Liang; Es-lamzadeh, S.; Wang, Y.; Xue, S. S., *The structure of the ultrarelativistic prompt emission phase and the properties of the black hole in GRB 180720B*, The European Physical Journal C, 82, 778, 2022.

In analogy with GRB 190114C, we here analyze the ultra-relativistic prompt emission (UPE) of GRB 180720B observed in the rest-frame time interval  $t_{\text{rf}} = 4.84\text{--}10.89$  s by Fermi-GBM. We reveal the UPE hierarchical structure from the time-resolved spectral analysis performed in time sub-intervals: the spectrum in each shorter time interval is always fitted by a composite blackbody plus cutoff power-law model. We explain this structure with the *inner engine* of the binary-driven hypernova (BdHN) model operating in a quantum electrodynamics (QED)



regime. In this regime, the electric field induced by the gravitomagnetic interaction of the newborn Kerr BH with the surrounding magnetic field is overcritical, i.e.,  $E \geq E_c$ , where  $E_c = m_e^2 c^3 / (e\hbar)$ . The overcritical field polarizes the vacuum leading to an  $e^+ e^-$  pair plasma that loads baryons from the surroundings during its expansion. We calculate the dynamics of the self-acceleration of the pair-electromagnetic-baryon (PEMB) pulses to their point of transparency. We characterize the quantum vacuum polarization process in the sequences of decreasing time bins of the UPE by determining the radiation timescale, Lorentz factors, and transparency radius of the PEMB pulses. We also estimate the strength of the surrounding magnetic field  $\sim 10^{14}$  G and obtain a lower limit to the BH mass,  $M = 2.4 M_\odot$ , and correspondingly an upper limit to the spin,  $\alpha = 0.6$ , from the conditions that the UPE is powered by the Kerr BH extractable energy and its mass is bound from below by the NS critical mass.

7. Wang, Yu; Rueda, J. A.; Ruffini, R.; Moradi, R.; Li, Liang; Aimuratov, Y.; Rastegarnia, F.; Eslamzadeh, S.; Sahakyan, N.; Zheng, Yunlong, *GRB 190829A-A showcase of binary late evolution*, The Astrophysical Journal, 936, 190, 2022.

GRB 190829A is the fourth closest gamma-ray burst (GRB) to date ( $z = 0.0785$ ). Owing to its wide range of radio, optical, X-ray, and very-high-energy (VHE) observations by H.E.S.S., it has become an essential new source examined by various models with complementary approaches. We here show in GRB 190829A the double-prompt pulses and the three-multiwavelength afterglows are consistent with the type II binary-driven hypernova (BdHN II) model. The progenitor is a binary composed of a carbon-oxygen (CO) star and a neutron star (NS) companion. The gravitational collapse of the iron core of the CO star produces a supernova (SN) explosion and leaves behind a new neutron star ( $\nu$ NS) at its center. The accretion of the SN ejecta onto the NS companion and onto the  $\nu$ NS via matter fallback spins up the NSs and produces the double-peak prompt emission. The synchrotron emission from the expanding SN ejecta with the energy injection from the rapidly spinning  $\nu$ NS and its subsequent spin-down leads to the afterglow in the radio, optical, and X-ray. We model the sequence of physical and related radiation processes in BdHNe and focus on individuating the binary properties that play the relevant roles.

8. Rueda, J. A.; Ruffini, R.; Kerr, R. P., *Gravitomagnetic interaction of a Kerr black hole with a magnetic field as the source of the jetted GeV radiation of gamma-ray bursts*, *The Astrophysical Journal*, 929, 56, 2022.

We show that the gravitomagnetic interaction of a Kerr black hole (BH) with a surrounding magnetic field induces an electric field that accelerates charged particles to ultra-relativistic energies in the vicinity of the BH. Along the BH rotation axis, these electrons/protons can reach energies of even thousands of petaelectronvolts, so stellar-mass BHs in long gamma-ray bursts (GRBs) and supermassive BHs in active galactic nuclei can contribute to the ultrahigh-energy cosmic rays through this mechanism. At off-axis latitudes, the particles accelerate to energies of hundreds of gigaelectronvolts and emit synchrotron radiation at gigaelectronvolt energies. This process occurs within  $60^\circ$  around the BH rotation axis, and due to the equatorial symmetry, it forms a double-cone emission. We outline the theoretical framework describing these acceleration and radiation processes, how they extract the rotational energy of the Kerr BH, and the consequences for the astrophysics of GRBs.

9. Arguelles, C. R.; Mestre, M. F.; Becerra-Vergara, E. A.; Crespi, V.; Krut, A.; Rueda, J. A.; Ruffini, R., *What does lie at the Milky Way centre? Insights from the S2-star orbit precession*, *Monthly Notices of the Royal Astronomical Society: Letters*, 511, L35, 2022.

it has been recently demonstrated that both, a classical Schwarzschild black hole (BH), and a dense concentration of self-gravitating fermionic dark matter (DM) placed at the Galaxy center, can explain the precise astrometric data (positions and radial velocities) of the S-stars orbiting Sgr A\*. This result encompasses the 17 best-resolved S-stars and includes the test of general relativistic effects such as the gravitational redshift in the S2-star. In addition, the DM model features another remarkable result: The dense core of fermions is the central region of a continuous density distribution of DM whose diluted halo explains the Galactic rotation curve. In this Letter, we complement the above findings by analyzing in both models the relativistic periapsis precession of the S2-star orbit. While the Schwarzschild BH scenario predicts a unique prograde precession for S2, in the DM scenario, it can be either retrograde or prograde, depending on the amount of DM mass enclosed within the S2 orbit, which, in turn, is a function of the DM fermion mass. We show

that all the current and publicly available data of S2 cannot discriminate between the two models, but upcoming S2 astrometry close to the next apocentre passage could potentially establish if Sgr A\* is governed by a classical BH or by a quantum DM system.

10. Rueda, J. A.; Ruffini, R.; Li, Liang; Moradi, R.; Sahakyan, N.; Wang, Y., *The white dwarf binary merger model of GRB 170817A*, International Journal of Modern Physics D, 31, 2230013, 2022.

Following the GRB 170817A prompt emission lasting a fraction of a second,  $10^8$  s of data in the X-rays, optical, and radio wavelengths have been acquired. We here present a model that fits the spectra, flux, and time variability of all these emissions, based on the thermal and synchrotron cooling of the expanding matter ejected in a binary white dwarf merger. The  $10^{-3}M_{\odot}$  of ejecta, expanding at velocities of  $10^9$  cm s $^{-1}$ , are powered by the newborn massive, fast rotating, magnetized white dwarf with a mass of  $1.3M_{\odot}$ , a rotation period of  $\gtrsim 12$  s, and a dipole magnetic field  $\sim 10^{10}$  G, born in the merger of a  $1.0+0.8M_{\odot}$  white dwarf binary. Therefore, the long-lasting mystery of the GRB 170817A nature is solved by the merger of a white dwarf binary that also explains the prompt emission energetics.

### 3.1.2 Accepted for publication or in press

1. Uribe, J. D.; Rueda, J. A., *Neutrino Flavour Oscillations in Gamma-Ray Bursts*, to be published as a chapter in the book "New phenomena and new states of matter in the Universe: from quarks to Cosmos", Eds. Peter Hess, Thomas Boller, and Cesar Zen Vasconcellos, World Scientific 2021.

In the binary-driven hypernova model of long gamma-ray bursts, a carbon-oxygen star explodes as a supernova in the presence of a neutron star binary companion in close orbit. Hypercritical (i.e. highly super-Eddington) accretion of the ejecta matter onto the neutron star sets in, making it reach the critical mass with the consequent formation of a Kerr black hole. We have recently shown that, during the accretion process onto the neutron star, fast neutrino flavor oscillations occur. Numerical simulations of the above system show that a part of the ejecta keeps bound to the newborn Kerr black hole, leading to a new hyper-

critical accretion process. We address here the occurrence of neutrino flavor oscillations given the extreme conditions of high density (up to  $10^{12} \text{ g cm}^{-3}$ ) and temperatures (up to tens of MeV) inside this disk. We estimate the evolution of the electronic and non-electronic neutrino content within the two-flavor formalism ( $\nu_e \nu_x$ ) under the action of neutrino collective effects by neutrino self-interactions. We find that neutrino oscillations inside the disk have frequencies between  $\sim (10^5\text{--}10^9) \text{ s}^{-1}$ , leading the disk to achieve flavor equipartition. This implies that the energy deposition rate by neutrino annihilation ( $\nu + \bar{\nu} \rightarrow e^- + e^+$ ) in the vicinity of the Kerr black hole, is smaller than previous estimates in the literature not accounting by flavor oscillations inside the disk. The exact value of the reduction factor depends on the  $\nu_e$  and  $\nu_x$  optical depths but can be as high as  $\sim 5$ .

2. Rueda, J. A.; Ruffini, R., *An Inner Engine Based on Binary-Driven Hypernovae for the High-Energy Emission of Long Gamma-Ray Bursts*, to be published as a chapter in the book "New phenomena and new states of matter in the Universe: from quarks to Cosmos", Eds. Peter Hess, Thomas Boller, and Cesar Zen Vasconcellos, World Scientific 2021.

A multi-decade theoretical effort has been devoted to finding an efficient mechanism to use the rotational and electromagnetic extractable energy of a Kerr-Newman black hole (BH) to power the most energetic astrophysical sources, gamma-ray bursts (GRBs) and active galactic nuclei (AGN). We show an efficient general relativistic electro-dynamical process that occurs in the "inner engine" of a binary-driven hypernova (BdHN). The *inner engine* is composed of a rotating Kerr BH, surrounded by a magnetic field of strength  $B_0$ , aligned and parallel to the rotation axis, and a very low-density ionized plasma. The gravitomagnetic interaction between the Kerr BH and the magnetic field induces an electric field that accelerates charged particles from the environment. Along the BH rotation axis, the particles reach energies above  $10^{18} \text{ eV}$  hence contributing to ultrahigh-energy cosmic rays, and at other latitudes emit synchrotron radiation at GeV energies which explains the high-energy emission of long GRBs observed by Fermi-LAT.

### 3.1.3 Submitted for publication

1. Wang, Yu; Becerra, L. M.; Fryer, C. L.; Rueda, J. A.; Ruffini, R., *GRB 171205A: Hypernova and Newborn Neutron Star*, submitted to The Astrophysical Journal. E-print: <https://arxiv.org/abs/2208.02725>

GRB 171205A is a low-luminosity, long-duration gamma-ray burst (GRB) associated with SN 2017iuk, a broad-line type Ic supernova (SN). It is consistent with being formed in the core-collapse of a widely separated binary, which we have called the binary-driven hypernova (BdHN) of type III. The core-collapse of the CO star forms a newborn NS ( $\nu$ NS) and the SN explosion. Fallback accretion transfers mass and angular momentum to the  $\nu$ NS here assumed to be born non-rotating. The accretion energy injected into the expanding stellar layers powers the prompt emission. The multiwavelength power-law afterglow is explained by the synchrotron radiation of electrons in the SN ejecta, powered by energy injected by the spinning  $\nu$ NS. We calculate the amount of mass and angular momentum gained by the  $\nu$ NS, as well as the  $\nu$ NS rotational evolution. The  $\nu$ NS spins up to a period of 47 ms, then releases its rotational energy powering the synchrotron emission of the afterglow. The paucity of the  $\nu$ NS spin explains the low-luminosity characteristic and that the optical emission of the SN from the nickel radioactive decay outshines the optical emission from the synchrotron radiation. From the  $\nu$ NS evolution, we infer that the SN explosion had to occur at most 7.36 h before the GRB trigger. Therefore, for the first time, the analysis of the GRB data leads to the time of occurrence of the CO core-collapse leading to the SN explosion and the electromagnetic emission of the GRB event.

2. S. Campion, J. D. Uribe-Suárez, J. D. Melon Fuksman, J. A. Rueda, *MeV, GeV and TeV neutrinos from binary-driven hypernovae*, submitted to Symmetry, Special Issue *Neutrino physics and astrophysics: theory and experiments*.

We analyze neutrino emission channels in energetic ( $\gtrsim 10^{52}$  erg) long gamma-ray bursts within the binary-driven hypernova model (BdHN). The BdHN progenitor is a binary system composed of a carbon-oxygen star and a neutron star companion. The gravitational collapse leads to a type Ic supernova explosion and triggers an accretion process onto the NS. For orbital periods of a few minutes, the NS reaches the criti-

cal mass and forms a black hole. Two physical situations produce MeV neutrinos. First, during the accretion, the NS surface emits neutrino-antineutrino pairs by thermal production. We calculate the properties of such a neutrino emission, including flavor evolution. Second, if the angular momentum of the SN ejecta is high enough, an accretion disk might form around the black hole. The disk's high density and temperature are ideal for MeV-neutrino production. We estimate the flavor evolution of electronic and non-electronic neutrinos and find that neutrino oscillation inside the disk leads to flavor equipartition. This effect reduces (compared to assuming frozen flavor content) the energy deposition rate of neutrino-antineutrino annihilation into electron-positron ( $e^+e^-$ ) pairs in the black hole vicinity. We then analyze the production of GeV-TeV neutrinos around the newborn black hole. The interaction of the magnetic field surrounding the black hole with the gravitomagnetic field induces an overcritical electric field leading to a spontaneous  $e^+e^-$  pair creation by vacuum breakdown. The  $e^+e^-$  plasma self-accelerates due to its internal pressure, and during the expansion, engulfs protons. The hadronic interaction of the protons in the expanding plasma with the ambient protons leads to neutrino emission via the decay chain of  $\pi$ -meson and  $\mu$ -lepton, around and far from the black hole, along different directions. These neutrinos have energies in the GeV-TeV regime, and we calculate their spectrum and luminosity. We also outline the detection probability by some current and future neutrino detectors.

## 3.2 Conference Proceedings

1. Rueda, Jorge A.; Ruffini, Remo; Moradi, Rahim; Wang, Yu, *A brief review of binary driven hypernova*, The Fifteenth Marcel Grossmann Meeting on General Relativity. Edited by E. S. Battistelli, R. T. Jantzen, and R. Ruffini. Published by World Scientific Publishing Co. Pte. Ltd., 2022.

The binary-driven hypernova (BdHN) model of long gamma-ray bursts (GRBs) involves a binary system composed of a carbon-oxygen core and a companion neutron star (NS) or a black hole (BH). This model, first proposed in 2012, succeeds and improves upon the fireshell model and the induced gravitational collapse (IGC) paradigm. After nearly a decade of development, the BdHN model has reached a nearly com-

plete structure, giving an explanation of all the observables of long bursts into its theoretical framework, and has given a refined classification of long GRBs according to the original properties of the progenitors. In this article, we present a summary of the BdHN model and the physical processes at work in each of the envisaged Episodes during its occurrence and lifetime, duly contextualized in the framework of GRB observations.

2. Rueda, Jorge A., *On the origin of the long gamma-ray burst afterglow as synchrotron radiation from binary-driven hypernovae*, to appear in AIP Conf. Proc. as a contribution to the Proceedings of the 17th Italian-Korean Symposium on Relativistic Astrophysics, held on August 2-6, 2021.

Long gamma-ray bursts show an afterglow emission in the X-rays, optical, and radio wavelengths with luminosities that fade with time with a nearly identical power-law behavior. In this talk, I present an analytic treatment that shows that this afterglow is produced by synchrotron radiation from the supernova ejecta associated with binary-driven hypernovae.







# The Double White Dwarf Merger Progenitors of SDSS J2211+1136 and ZTF J1901+1458

M. F. Sousa<sup>1,2</sup> , J. G. Coelho<sup>1,3</sup> , J. C. N. de Araujo<sup>1</sup> , S. O. Kepler<sup>4</sup> , and J. A. Rueda<sup>2,5,6,7</sup>

<sup>1</sup> Divisão de Astrofísica, Instituto Nacional de Pesquisas Espaciais, Avenida dos Astronautas 1758, 12227-010, São José dos Campos, SP, Brazil; [manoelfelipesousa@gmail.com](mailto:manoelfelipesousa@gmail.com)

<sup>2</sup> ICRArNet-Ferrara, Dip. di Fisica e Scienze della Terra, Università degli Studi di Ferrara, Via Saragat 1, I-44122 Ferrara, Italy

<sup>3</sup> Núcleo de Astrofísica e Cosmologia (Cosmo-Ufes) & Departamento de Física, Universidade Federal do Espírito Santo, 29075-910, Vitória, ES, Brazil

<sup>4</sup> Instituto de Física, Universidade Federal do Rio Grande do Sul, 91501-970 Porto Alegre, RS, Brazil

<sup>5</sup> ICRArNet, Piazza della Repubblica 10, I-65122 Pescara, Italy

<sup>6</sup> Dip. di Fisica e Scienze della Terra, Università degli Studi di Ferrara, Via Saragat 1, I-44122 Ferrara, Italy

<sup>7</sup> INAF, Istituto di Astrofisica e Planetologia Spaziali, Via Fosso del Cavaliere 100, I-00133 Rome, Italy

Received 2022 August 19; revised 2022 November 2; accepted 2022 November 2; published 2022 December 9

## Abstract

Double white dwarf (DWD) mergers are possibly the leading formation channel of massive, rapidly rotating, high-field magnetic white dwarfs (HFMWDs). However, a direct link connecting a DWD merger to any observed HFMWD is still missing. We here show that the HFMWDs SDSS J221141.80+113604.4 (hereafter J2211+1136) and ZTF J190132.9+145808.7 (hereafter J1901+1458) might be DWD merger products. J2211+1136 is a  $1.27 M_{\odot}$  white dwarf (WD) with a rotation period of 70.32 s and a surface magnetic field of 15 MG. J1901+1458 is a  $1.327\text{--}1.365 M_{\odot}$  WD with a rotation period of 416.20 s, and a surface magnetic field in the range 600–900 MG. With the assumption of single-star evolution and the currently measured WD masses and surface temperatures, the cooling ages of J2211+1136 and J1901+1458 are, respectively, 2.61–2.85 Gyr and 10–100 Myr. We hypothesize that these WDs are DWD merger products and compute the evolution of the postmerged configuration formed by a central WD surrounded by a disk. We show that the postmerger system evolves through three phases depending on whether accretion, mass ejection (propeller), or magnetic braking dominates the torque onto the central WD. We calculate the time the WD spends in each of these phases and obtain the accretion rate and disk mass for which the WD rotational age, i.e., the total time elapsed since the merger to the instant where the WD central remnant reaches the current measured rotation period, agrees with the estimated WD cooling age. We infer the mass values of the primary and secondary WD components of the DWD merger that lead to a postmerger evolution consistent with the observations.

*Unified Astronomy Thesaurus concepts:* [Stellar remnants \(1627\)](#); [White dwarf stars \(1799\)](#); [Stellar mergers \(2157\)](#); [Compact binary stars \(283\)](#); [Compact objects \(288\)](#); [Stellar rotation \(1629\)](#)

## 1. Introduction

It has long been proposed that double white dwarf (DWD) mergers can produce high-field magnetic white dwarfs (HFMWDs; see, e.g., Wickramasinghe & Ferrario 2000). There are increasing observational results pointing to this scenario (see below), but still a direct link is missing connecting a DWD merger to any observed HFMWD. Here, we aim to provide such a link.

In general, the central remnant of a DWD merger can be (i) a stable newborn white dwarf (WD), (ii) a type-Ia supernova (SN Ia), or (iii) a newborn neutron star (NS). Sub-Chandrasekhar remnants might end either as (i) or (ii) (Benz et al. 1990; Raskin et al. 2012; Zhu et al. 2013; Becerra et al. 2018, 2019; Schwab 2021a), super-Chandrasekhar remnants as (ii) or (iii) (Saio & Nomoto 1985; Schwab et al. 2016; Becerra et al. 2018, 2019; Schwab 2021a). We are here interested in those DWD mergers whose remnant is a stable, ultramassive ( $\gtrsim 1 M_{\odot}$  but sub-Chandrasekhar) HFMWD. Those central remnants might avoid unstable burning, leading to an SN Ia if their central density remains under some critical value of a few

$10^9 \text{ g cm}^{-3}$  (see Becerra et al. 2018, for further details). Numerical simulations show that HFMWDs might indeed originate in DWD mergers (see, e.g., García-Berro et al. 2012; and Section 2 for further details). The general merged configuration is a central remnant that contains the mass of the (undisrupted) primary, surrounded by a hot corona with about half of the (disrupted) secondary mass, and a rapidly rotating Keplerian disk with roughly the other half of the secondary mass. Little mass ( $\sim 10^{-3} M_{\odot}$ ) is ejected from the system (see Section 4 for further details). The hot and convective corona works as an efficient  $\alpha\omega$ -type dynamo that might lead to magnetic fields of  $\lesssim 10^{10}$  G (García-Berro et al. 2012). For a recent discussion of the emergence of high magnetic fields in observed WDs, we refer the reader to Bagnulo & Landstreet (2022).

Therefore, theory tells us that stable WD remnants of DWD mergers can exist (see, e.g., Schwab 2021a). It remains to have observational support. Observations confirm the existence of HFMWDs with magnetic field strengths in the range  $10^8\text{--}10^9$  G (Külebi et al. 2009; Ferrario et al. 2015; Kepler et al. 2016), and that most of them are massive (see, e.g., Kepler et al. 2016). The latest measurements of the transverse velocities of massive WDs also suggest that a fraction of them are DWD merger products (see Cheng et al. 2020, and references therein). There is an additional observational argument supporting this conclusion. The rate of DWD mergers is

expected to be  $(5\text{--}9) \times 10^{-13} \text{ yr}^{-1} M_{\odot}^{-1}$  (Maoz & Hallakoun 2017; Maoz et al. 2018). Using a Milky Way–like stellar mass  $6.4 \times 10^{10} M_{\odot}$  and the extrapolating factor of Milky Way equivalent galaxies,  $0.016 \text{ Mpc}^{-3}$  (Kalogera et al. 2001), the above rate translates into a local cosmic merger rate of  $(3.7\text{--}6.7) \times 10^5 \text{ Gpc}^{-3} \text{ yr}^{-1}$ . This merger rate is 5–8 times larger than the population of SN Ia (see, e.g., Ruiter et al. 2009). Therefore, even if we were to explain the entire SN Ia population with the double-degenerate channel, i.e., with DWD mergers, we can safely conclude that many DWD mergers do not produce SNe Ia (see also Cheng et al. 2020).

All the above leads to a rather obvious question (but with no obvious answer), where and which are the WDs produced by (some of) those mergers? To answer this question, we here reconstruct the DWD progenitor of two recently detected HFMWDs, SDSS J221141.80+113604.4 (hereafter J2211+1136; Kilic et al. 2021b) and ZTF J190132.9+145808.7 (hereafter J1901+1458; Caiazzo et al. 2021). J2211+1136 has a mass of  $1.27 M_{\odot}$ , rotation period of 70.32 s, surface magnetic field strength of 15 MG, effective temperature  $T_{\text{eff}} \approx 9020 \text{ K}$ , and cooling age 2.61–2.85 Gyr (Kilic et al. 2021a, 2021b). The corresponding parameters of J1901+1458 are a mass in the range of 1.327–1.365  $M_{\odot}$ , rotation period of 416.20 s, surface magnetic field in the range 600–900 MG, effective temperature  $T_{\text{eff}} = 46,000^{+19000}_{-8000} \text{ K}$ , and cooling age 10–100 Myr (Caiazzo et al. 2021). The cooling age is estimated assuming single-star evolution and the currently measured WD masses and effective temperatures.

Following numerical simulations of DWD mergers, we model the postmerger configuration as a central HFMWD remnant surrounded by a Keplerian disk (see Section 2 for details). We compute the postmerger rotational evolution of the system and infer the model parameters for which the WD rotational age, i.e., the time at which it reaches the current value of the rotation period, agrees with the estimated cooling age. We show that the postmerger configuration evolves through three phases dominated by accretion, mass ejection (propeller), and magnetic braking (see Section 3 for details). The latter phase dominates the duration of the rotational age. We derive the accretion rate, the disk mass, and the mass of the premerger DWD primary and secondary binary components for which the postmerger system agrees with observations.

We organize the article as follows. In Section 2, we summarize the properties of the merged configuration derived from numerical simulations that serve as the starting point of our calculations. Section 3 describes the theoretical treatment to compute the rotational evolution of the postmerger configuration. Section 4 explains the different types of rotational evolution. We apply in Section 5 the theoretical model to the HFMWDs J2211+1136 and J1901+1458. In Section 6, we infer the parameters of the premerger DWD progenitors for the two sources. Finally, Section 7 outlines the conclusions of this article.

## 2. Merger and Postmerger Properties

According to numerical simulations of DWD mergers (see, e.g., Benz et al. 1990; Guerrero et al. 2004; Lorén-Aguilar et al. 2009; Longland et al. 2012; Raskin et al. 2012; Zhu et al. 2013; Dan et al. 2014; Becerra et al. 2018), the merged configuration is the central, rigidly rotating, isothermal WD core of mass  $M_{\text{core}}$ , surrounded by a hot envelope of mass  $M_{\text{env}}$  with differential rotation and a rapidly rotating Keplerian disk

of mass  $M_d$ . The mass of the disrupted secondary star distributes between the envelope and the disk. Some material of mass  $M_{\text{fb}}$  falls back onto the WD remnant, and only a tiny amount of mass  $M_{\text{ej}}$  escapes from the system. Dan et al. (2014) obtained the following fitting polynomials of the properties of the merged configurations from numerical simulations of DWD mergers for a variety of initial conditions:

$$M_{\text{core}} = M_{\text{tot}}(0.7786 - 0.5114 q), \quad (1a)$$

$$M_{\text{env}} = M_{\text{tot}}(0.2779 - 0.464 q + 0.7161 q^2), \quad (1b)$$

$$M_d = M_{\text{tot}}(-0.1185 + 0.9763 q - 0.6559 q^2), \quad (1c)$$

$$M_{\text{fb}} = M_{\text{tot}}(0.07064 - 0.0648 q), \quad (1d)$$

$$M_{\text{ej}} = \frac{0.0001807 M_{\text{tot}}}{-0.01672 + 0.2463 q - 0.6982 q^2 + q^3}, \quad (1e)$$

where  $M_{\text{tot}} = M_1 + M_2$  is the total binary mass, with  $M_1$  and  $M_2$  the masses of the primary and secondary, and  $q \equiv M_2/M_1 \leq 1$  is the binary mass ratio. The goodness of the polynomial fitting was reported in Dan et al. (2014) with  $R^2$  statistic values of 0.97, 0.88, 0.78, and 0.8, respectively, for the first four fitting functions (1a)–(1d), which means they fit the 97%, 88%, 78%, and 80% of the corresponding variance.

We model the postmerger evolution after the short-lived phase in which the WD core incorporates the envelope. The postmerger system is thus composed of the WD remnant of mass  $M$ , radius  $R$ , surrounded by the accretion disk of mass  $M_d$ . As for the magnetic field configuration, we adopt a dipole +quadrupole model with a dipole strength  $B$  and a quadrupole strength  $B_{\text{quad}}$ . Hence, the magnetic dipole moment is  $\mu = BR^3$ .

For fixed  $M_{\text{tot}}$ , Equation (1e) shows that the unbound mass decreases for increasing  $q$ , so the lowest value is obtained for the largest possible binary mass ratio ( $q = 1$ ), i.e.,  $M_{\text{ej}} \approx 3.4 \times 10^{-4} M_{\text{tot}}$ . Given the approximate mass conservation, we estimate the mass of the final WD by

$$M = M_{\text{core}} + M_{\text{env}} + M_{\text{fb}} + M_{\text{acc}}, \quad (2)$$

where  $M_{\text{acc}} \leq M_d$  is the accreted mass. As we shall show,  $M < M_{\text{tot}}$  because some mass is ejected from the system during the propeller phase (see more details in Section 4). With the aid of Equations (1a)–(1e), Equation (2), and the estimate of the accreted mass, in Section 6 we estimate the parameters of the merging binary.

In the following calculations, we assume a constant value of  $M$  given by the current value of the mass of the WD, i.e., the final value given by Equation (2), neglecting the effect of the increase in mass,  $M_{\text{acc}}$ . We also assume a constant accretion rate onto the central WD,  $\dot{M}$ . These assumptions have a negligible effect on the results because mass accretion and ejection consume the disk mass in a timescale much shorter than the WD lifetime, and so magnetic braking dominates the rotational evolution.

## 3. Postmerger Rotational Evolution

### 3.1. Accretion and Propeller Torque

When the magnetosphere radius,  $R_m$ , is smaller than the WD radius,  $R$ , the disk extends up to the WD surface, i.e.,  $r_i = R$ . When  $R_m > R$ , the disk extends up to  $r_i = R_m$ . Therefore, we have

$$r_i = \max(R, R_m), \quad (3)$$

where  $R_m$  is the Alfvén radius<sup>8</sup> (see, e.g., Pringle & Rees 1972):

$$R_m = \left( \frac{\mu^2}{\dot{M} \sqrt{2GM}} \right)^{2/7}. \quad (4)$$

From Equation (4), we obtain that the condition  $R_m > R$  is satisfied for accretion rates

$$\frac{\dot{M}}{M_\odot \text{ yr}^{-1}} < 9.74 \times 10^{-4} \frac{B_8^2 R_8^{5/2}}{(M/M_\odot)^{1/2}}, \quad (5)$$

where  $B_8 = B/(10^8 \text{ G})$  and  $R_8 = R/(10^8 \text{ cm})$ .

As we shall see, the accretion rate onto the remnant WD is much lower than the above value, so the WD evolves always in the regime  $R_m > R$ . In this case, the magnetic field lines thread the disk at  $r_i = R_m$  and the matter flows from the disk to the WD through the magnetic field lines. Whether this mass flow spins up or down the central WD depends on the value of the so-called *fastness* parameter:

$$\omega \equiv \frac{\Omega}{\Omega_K}, \quad (6)$$

where  $\Omega_K$  is the Keplerian angular velocity at  $r_i = R_m$ :

$$\Omega_K = \sqrt{\frac{GM}{R_m^3}}. \quad (7)$$

The specific (i.e., per unit mass) angular momentum of the matter leaving the disk is  $l_i = \Omega_K r_i^2 = \Omega_K R_m^2 = \sqrt{GMR_m}$ , while the specific angular momentum of the corotating magnetosphere at  $r = R_m$  is  $l_m = \Omega R_m^2$ . Therefore, the WD will change its angular momentum at a rate given by (Menou et al. 1999)

$$\dot{J}_{\text{acc}} = T_{\text{acc}} = (l_i - l_m)\dot{M} = \delta(1 - \omega), \quad (8)$$

where

$$\delta \equiv \dot{M} R_m^2 \Omega_K = \dot{M} \sqrt{GMR_m}, \quad (9)$$

$\dot{M}$  being the accretion rate, i.e., the rate at which mass flows from the disk to the WD at the inner disk radius,  $r = r_i = R_m$ . When  $\omega < 1$ , the inflowing material accretes onto the WD and transfers angular momentum to it (exerts a positive torque). When  $\omega > 1$ , the system enters into a so-called *propeller* regime, in which the WD centrifugal barrier expels the inflowing mass from the disk. Such mass leaves the system removing angular momentum from the central WD, i.e., it exerts a negative torque onto it. For additional discussions about the propeller mechanism, we refer the reader to, for example, Illarionov & Sunyaev (1975) and Wang (1995).

### 3.2. Magnetic Dipole Torque

The central remnant is also subjected to the torque by the magnetic field. Since the ratio between the stellar radius,  $R$ , and the light-cylinder radius,  $R_{\text{lc}} = c/\Omega$ , is small, i.e.,  $R/R_{\text{lc}} = \Omega R/c \lesssim 10^{-3}$ , finite-size effects in the determination of the radiation field can be safely neglected. Therefore, we use the torque exerted by a point-like dipole+quadrupole magnetic field configuration (Pétri 2015):

$$T_{\text{mag}} = T_{\text{dip}} + T_{\text{quad}}, \quad (10)$$

<sup>8</sup> This magnetosphere radius assumes spherical accretion and a pure dipole magnetic field configuration.

$$T_{\text{dip}} = -k_{\text{dip}} \Omega^3, \quad (11)$$

$$T_{\text{quad}} = -k_{\text{quad}} \Omega^5, \quad (12)$$

where

$$k_{\text{dip}} = \frac{2}{3} \frac{B^2 R^6}{c^3} \sin^2 \theta, \quad (13)$$

$$k_{\text{quad}} = \frac{32}{135} \frac{B_{\text{quad}}^2 R^8}{c^5} \sin^2 \theta_1 (\cos^2 \theta_2 + 10 \sin^2 \theta_2), \quad (14)$$

$\theta$  being the inclination angle of the magnetic dipole moment with respect to the WD rotation axis, and the angles  $\theta_1$  and  $\theta_2$  specifying the geometry of the quadrupole field. We can write the total magnetic torque as

$$T_{\text{mag}} = -\frac{2}{3} \frac{B^2 R^6 \Omega^3}{c^3} \left( \sin^2 \theta + \eta^2 \frac{16}{45} \frac{R^2 \Omega^2}{c^2} \right), \quad (15)$$

where  $\eta$  is a parameter that measures the quadrupole-to-dipole magnetic field strength ratio as

$$\eta = \frac{B_{\text{quad}}}{B} \sqrt{\sin^2 \theta_1 (\cos^2 \theta_2 + 10 \sin^2 \theta_2)}. \quad (16)$$

Having defined the torques acting on the central WD, we can write the equation of angular momentum conservation as

$$T_{\text{tot}} = T_{\text{acc}} + T_{\text{mag}} = \dot{J} \approx I \dot{\Omega}, \quad (17)$$

whose integration gives the evolution of the WD rotational properties (e.g., angular momentum and angular velocity). The last equality neglects the change in time of the WD moment of inertia,  $I$ , as required by self-consistency with the approximation of constant mass. The above differential equation can be integrated given initial condition to the angular velocity,  $\Omega_0 = \Omega(t_0 = 0)$ , and setting all the model parameters, i.e.,  $\{M, R, I, \dot{M}, M_d, B, B_{\text{quad}}, \theta, \theta_1, \theta_2, \}$ . The qualitative and quantitative features of the result are not sensitive to the initial condition of the angular velocity,  $\Omega_0$ . We shall explore a variety of initial rotation periods ranging from a few seconds to hundreds of seconds.

The magnetic field and the mass of the WD are set by observations (and so its radius and moment of inertia from its structure properties, e.g., mass–radius relation), so it remains to set  $\dot{M}$ ,  $M_d$ , and  $\theta$ . Without loss of generality, we shall assume an orthogonal dipole,  $\theta = 90^\circ$ , and an  $m = 1$  mode for the quadrupole, i.e.,  $(\theta_1, \theta_2) = (\pi/2, 0)$ . For the disk mass, we shall set values around  $M_d \approx 0.30 M_\odot$  according to numerical simulations (see, e.g., Dan et al. 2014, Becerra et al. 2018, and Sections 5 and 6 for details on the effect of different disk masses). Therefore, it remains only to set the value of  $\dot{M}$ . We shall do so by requesting that the value of  $\Omega$  equals the current observed value at the evolution time consistent with estimated WD cooling age.

## 4. Types of Rotational Evolution

The WD might follow different types of rotational evolution depending on the model parameters and initial conditions. In the most general case, the system evolves through three stages until it reaches the current rotation period: a *phase I* of accretion (the WD spins up) or ejection of matter (the WD spins down) by propeller, a *phase II* in which accretion and matter ejection episodes balance each other so the WD spin

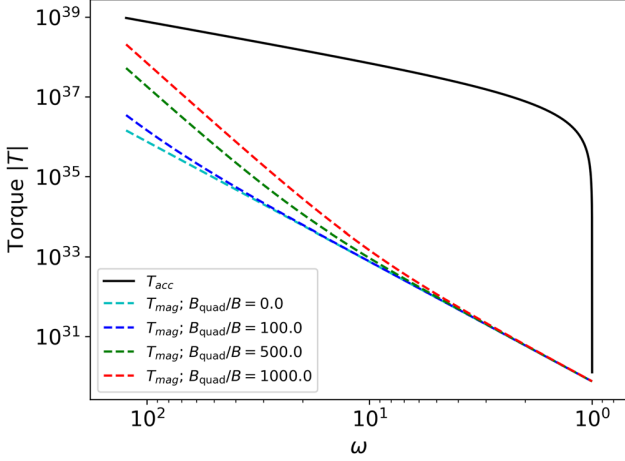


**Figure 1.**  $|T_{\text{acc}}|$  and  $|T_{\text{mag}}|$  as a function of  $\omega > 1$  where we considered a WD with  $B = 100$  MG,  $\dot{M} = 10^{-7} M_{\odot} \text{ yr}^{-1}$ , and a quadrupole-to-dipole magnetic field strength ratio  $B_{\text{quad}}/B$ . The ratio  $B_{\text{quad}}/B = 0.0$  corresponds to the case of a pure dipole magnetic field.

remains at an equilibrium value, and a *phase III* which the system enters once the disk mass ends, so the WD spins down because of magnetic braking.

Because DWD mergers always form a debris disk around the newborn central remnant (see, e.g., Lorén-Aguilar et al. 2009; Dan et al. 2014), we rule out an evolution with only phase III, i.e., without either accretion or matter ejection and only evolving due to magnetic braking. Therefore, the postmerger WD necessarily starts its evolution either at the phase I or II.

We now focus on the most general case, i.e., when the system evolves through the above three stages until it reaches the current rotation period. The division of the evolution into three phases depends on the value of the fastness parameter, that is,  $\omega > 1$ ,  $\omega \approx 1$ , and  $\omega < 1$ . Depending on the initial angular velocity,  $\Omega_0$ , the initial value of the fastness parameter can either be  $\omega_0 > 1$  ( $\Omega_0 > \Omega_K$ ) or  $\omega_0 < 1$  ( $\Omega_0 < \Omega_K$ ). The torque,  $T_{\text{acc}}$ , is either negative when the propeller mechanism is active ( $\omega > 1$ ) or positive when the accretion process is active ( $\omega < 1$ ). On the other hand, the magnetic torque,  $T_{\text{mag}}$ , always removes angular momentum. When there is mass flowing from the inner radius of the disk, the propeller or the accretion dominates the changes in the rotational period given that  $T_{\text{acc}}$  dominates over  $T_{\text{mag}}$ . Figure 1 shows  $T_{\text{acc}}$  and  $T_{\text{mag}}$  as a function of  $\omega > 1$  up to the value of  $\omega \approx 1$ , for fiducial values of the dipole magnetic field and the accretion rate, respectively,  $B = 100$  MG, and  $\dot{M} = 10^{-7} M_{\odot} \text{ yr}^{-1}$ . We consider  $T_{\text{mag}}$  with different values of  $B_{\text{quad}}/B$  in order to assess the effect of  $B_{\text{quad}}$  on the spin evolution. Figure 2 is analogous to Figure 1 but for  $\omega < 1$ . Here, we only consider the pure magnetic dipole case,  $B_{\text{quad}}/B = 0$ , because for low values of the angular velocity the torque by the quadrupole magnetic field is very small compared to that produced by the magnetic dipole (see Equation (15)). These figures show that  $|T_{\text{acc}}| \gg |T_{\text{dip}}|$  for the entire present phase, with the only exception being when  $\omega \approx 1$ , where they become comparable as  $T_{\text{acc}}$  drops significantly.

It is worth mentioning that for  $B_{\text{quad}}/B = 1000$ , the intensity of  $T_{\text{mag}}$  approaches the intensity of  $T_{\text{acc}}$  for values of the angular velocity around a few seconds. However, when the angular velocity decreases,  $T_{\text{mag}}$  drops rapidly while  $T_{\text{acc}}$  remains high for nearly the entire phase of  $\omega > 1$ . Thus,  $T_{\text{acc}}$

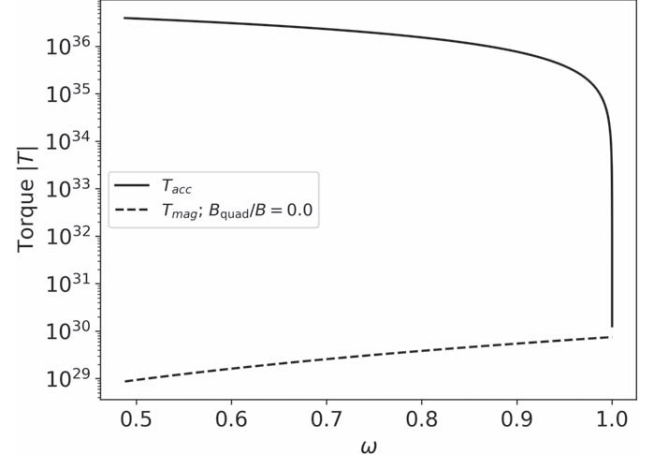


**Figure 2.**  $|T_{\text{acc}}|$  and  $|T_{\text{mag}}|$  as a function of  $\omega < 1$  where we considered a WD with  $B = 100$  MG,  $\dot{M} = 10^{-7} M_{\odot} \text{ yr}^{-1}$ , and a quadrupole-to-dipole magnetic field strength ratio  $B_{\text{quad}}/B = 0.0$ , since the effect of the quadrupole magnetic field is very small when we take into account the values of  $\omega < 1$  presented here (See Equation (15)).

still dominates the torque and  $T_{\text{mag}}$  (even with  $B_{\text{quad}}/B = 1000$ ) contributes very little to this first evolution stage.

Taking the above into account in this first regime, we can approximate with sufficient accuracy the total torque by  $T_{\text{tot}} \approx T_{\text{acc}}$ . Within this approximation, Equation (17) has the analytic solution

$$\omega = 1 + (\omega_0 - 1)e^{-t/\tau_{\text{acc}}}, \quad (18)$$

where  $\omega_0 = \Omega_0/\Omega_K$  is initial fastness parameter and  $\tau_{\text{acc}}$  is the timescale (e-folding time) of the propeller/accretion phase:

$$\tau_{\text{acc}} = \frac{I \Omega_K}{\delta} = \frac{I}{\dot{M} R_m^2} = 50.27 \frac{I_{49}}{\dot{M}_{-7} R_{m,9}^2} \text{ kyr}, \quad (19)$$

where  $I_{49}$  is the moment of inertia in units of  $10^{49} \text{ g cm}^2$ ,  $\dot{M}_{-7}$  is the accretion rate in units of  $10^{-7} M_{\odot} \text{ yr}^{-1}$  and  $R_{m,9}$  is the Alfvén radius in units of  $10^9 \text{ cm}$ .

When  $\omega \approx 1$ , the WD enters phase II of evolution, characterized by  $T_{\text{acc}} \approx T_{\text{mag}}$ . When this occurs,  $T_{\text{mag}}$  decelerates the star to an angular velocity slightly smaller than  $\Omega_K$ , so to a fastness parameter  $\omega \lesssim 1$ . Then,  $T_{\text{acc}}$  turns positive and the WD accretes matter, spinning it up. This happens until the WD returns once more to the regime of  $\omega \gtrsim 1$ . Upon reaching this regime, due to the torques  $T_{\text{acc}}$  and  $T_{\text{mag}}$ , the WD rotation decelerates once more until  $\omega \lesssim 1$ . The accretion acts, and the propeller process ceases again. In summary, in this stage the WD goes through successive spin-up and spin-down stages in which the fastness parameter oscillates around unity, so the angular velocity oscillates around an *equilibrium* value,  $\Omega \approx \Omega_{\text{eq}} = \Omega_K$ . Therefore, we can assume that in this phase  $\Omega$  remains constant at

$$\begin{aligned} \Omega_{\text{eq}} = \Omega_K &= \left[ \frac{\sqrt{2} (GM)^{5/3} \dot{M}}{B^2 R^6} \right]^{3/7} \\ &= 0.225 \left[ \frac{(M/M_{\odot})^{5/3} \dot{M}_{-7}}{B_8^2 R_8^6} \right]^{3/7} \text{ rad s}^{-1}. \end{aligned} \quad (20)$$

This phase lasts until the disk can feed the accretion and propeller. Thus, the duration timescale of this phase is of the

order  $\tau_{\text{disk}} \approx M_d/\dot{M} \sim 10^6$  yr, that is, the time required to consume the disk mass.

After the disk is exhausted, the system evolves to the regime  $\omega < 1$ . Without mass flowing from the disk, only the magnetic dipole exerts torque. Equation (15) and Figure 1 show that the effect of the quadrupole magnetic field on the magnetic torque is negligible in the range of angular velocities of the regime  $\omega \lesssim 1$ . In this case, the torque due to dipole radiation dominates and we can accurately approximate the total torque by  $T_{\text{tot}} = T_{\text{mag}} \approx T_{\text{dip}}$ . Thus, we can solve Equation (17) analytically:

$$\omega = \left(1 + \frac{\Delta t}{\tau_{\text{dip}}}\right)^{-1/2}, \quad (21)$$

where  $\delta t = t - t_i$ , with  $t_i$  being the initial time of the pure magnetic dipole torque phase, and here we have assumed that this phase starts with an initial value of the fastness parameter equal to unity, i.e.,  $\omega(t = t_i) = 1$ . The characteristic spin-down timescale,  $\tau_{\text{dip}}$ , is given by

$$\begin{aligned} \tau_{\text{dip}} &= \frac{I}{2 k_{\text{dip}} \Omega_K^2} = \frac{c^3 I R_m^3}{2 G M B^2 R^3 (1 + \sin^2 \theta)} \\ &= 3.22 \frac{I_{49} R_{m,9}^3}{(M/M_\odot) B_8^2 R_8^3 (1 + \sin^2 \theta)} \text{ Gyr}, \end{aligned} \quad (22)$$

which is much longer than the timescale of the previous phases. The above implies that we can approximate the total postmerger age of the WD to the time it spends in this final phase.

We can invert Equation (21) and find the elapsed time,  $\Delta t_{\text{obs}}$ , for the WD to reach an observed angular velocity,  $\Omega_{\text{obs}}$ , i.e.,

$$\Delta t_{\text{obs}} = \tau_{\text{dip}} \left[ \left( \frac{\Omega_K}{\Omega_{\text{obs}}} \right)^2 - 1 \right]. \quad (23)$$

Since  $\tau_{\text{dip}}$  depends on  $\Omega_K$  and the latter depends on  $R_m$ , and so on  $\dot{M}$ , we can use Equation (23) to express  $\dot{M}$  in terms of  $\Omega_{\text{obs}}$  and  $\Delta t_{\text{obs}}$ :

$$\dot{M} = \frac{B^2 R^6 \Omega_{\text{obs}}^{7/3}}{\sqrt{2} (GM)^{5/3}} \left( 1 - \frac{2 k_{\text{dip}} \Omega_{\text{obs}}^2 \Delta t_{\text{obs}}}{I} \right)^{-7/6}. \quad (24)$$

Therefore, Equation (24) allows one to obtain, from observational parameters such as mass, angular velocity, magnetic field, and the estimated age of the WD (e.g., the cooling age), the accretion rate for which the rotational evolution agrees with observations.

## 5. Analysis of Specific Sources

Having described all the generalities of the postmerger evolution, we turn to describe the rotational evolution of two observed HFMWDs, namely, J2211+1136 and J1901+1458. We infer the time the WD spends in each phase, and calculate the accretion rate that leads to the rotational evolution to agree with the estimated WD cooling age. This assumption agrees with the fact that the cooling tracks of these sources are estimated considering the current mass of the WD, so the cooling age is the evolution time of the postmerger central remnant after the envelope has been fully incorporated into the isothermal core and the WD composition has settled down (see, e.g., Schwab 2021b, for more details). The above is also

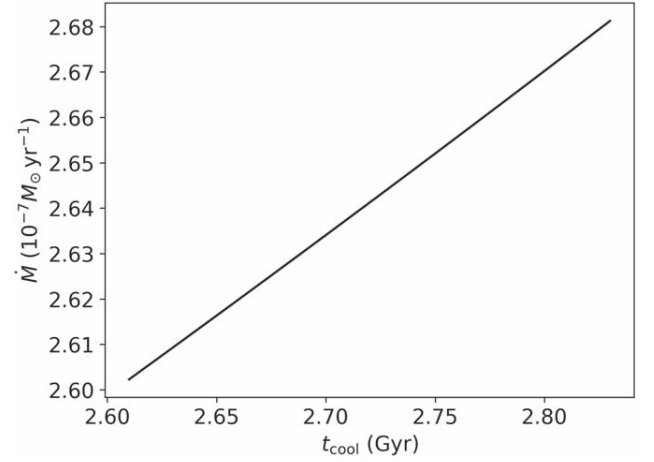


**Figure 3.** Accretion rate as a function of cooling age, calculated from Equation (24), for J2211+1136. The WD parameters are  $M = 1.27 M_\odot$ ,  $R = 3.21 \times 10^8$  cm, and  $P_{\text{obs}} = 70.3$  s. The dipole magnetic field is  $B = 15$  MG and  $\theta = 90^\circ$ .

supported by the fact that the initial phase of fusion containing the envelope is short lived ( $\sim 10^4$ – $10^5$  yr; see, e.g., García-Berro et al. 2012; Schwab 2021a) compared to the estimated age of the WD and, as we show in this article, also the duration of the accreting phase is negligible.

We do not take into account any delay due to crystallization, phase separation due to sinking or dilution of heavier elements, or nuclear energy that can possibly occur as proposed, for example, by Cheng (2020) and Blouin & Daligault (2021).

### 5.1. Rotational Evolution of J2211+1136

J2211+1136 is a recently observed isolated WD with a rotation period  $P_{\text{obs}} = 70.32$  s (Kilic et al. 2021b). It has a mass  $M = 1.27 M_\odot$ , a stellar radius  $R = 3210$  km,<sup>9</sup> and a surface (dipole) magnetic field  $B = 15$  MG. The cooling age is in the range  $t_{\text{cool}} = 2.61$ – $2.85$  Gyr depending on the WD interior composition (Kilic et al. 2021a, 2021b).

First, to explore the evolutionary path of the WD rotation, we need to know the accretion rate values for which the rotational evolution time agrees with the cooling age. For this task, we use Equation (24), assuming  $\Delta t_{\text{obs}} = t_{\text{cool}}$ . Figure 3 shows that this condition implies that  $\dot{M}$  must be in the range  $\approx (2.60$ – $2.68) \times 10^{-7} M_\odot \text{ yr}^{-1}$ . For an aligned rotator ( $\theta = 0$ ), the corresponding accretion rate range is  $(2.21$ – $2.24) \times 10^{-7} M_\odot \text{ yr}^{-1}$ .

To analyze in detail the phases of spin evolution, we consider a value of  $\dot{M}$  within the above range, e.g.,  $\dot{M} = 2.62 \times 10^{-7} M_\odot \text{ yr}^{-1}$ . Furthermore, we consider six values for the initial rotation period to verify that the solution is not sensitive to this initial condition. For this task, we choose three values below and three values above the equilibrium period,  $P_{\text{eq}} = 2\pi/\Omega_{\text{eq}} \approx 61.5$  s, i.e.,  $P_0 = (3.14, 21.5, 41.5, 81.5, 101.5, 119.8)$  s. Figure 4 shows the evolution of the WD rotation period for these initial conditions. We observe that, irrespective of  $P_0$ , the WD accelerates or decelerates toward  $P_{\text{eq}}$  on a comparable timescale. Therefore, the duration of the rotational evolution in phase I is not sensitive to the specific value of  $P_0$ .

<sup>9</sup> We estimate the radius from the measured mass and surface gravity,  $\log(g) = 9.214$  (Kilic et al. 2021b), i.e.,  $R = \sqrt{GM/g}$ .

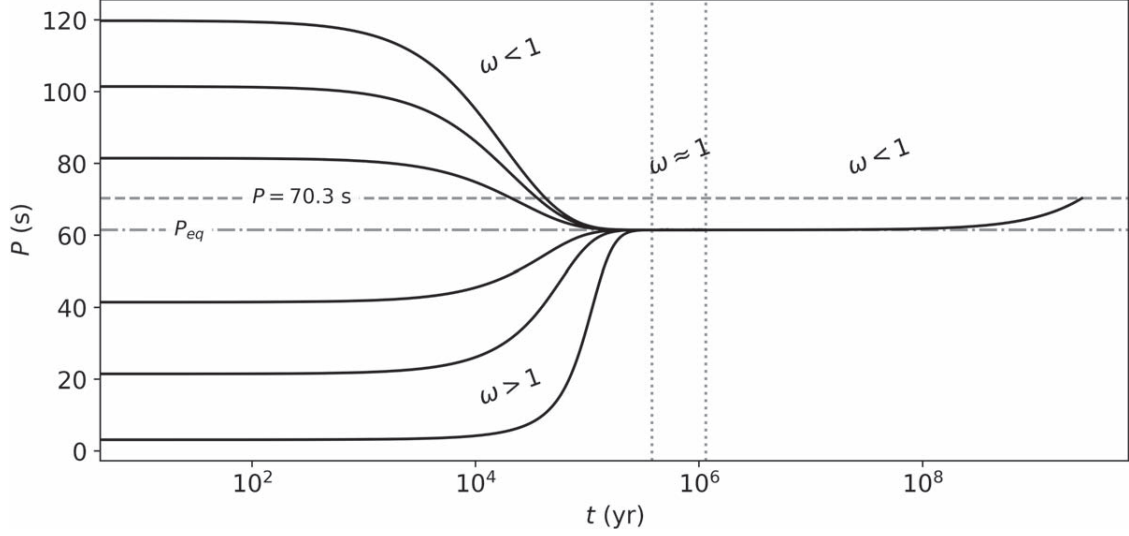


**Figure 4.** Evolution of the rotation period of the J2211+1136 for an accretion rate of  $\dot{M} = 2.62 \times 10^{-7} M_{\odot} \text{ yr}^{-1}$  and for different values of initial rotational periods,  $P_0 = (3.14, 21.5, 41.5, 81.5, 101.5, 119.8) \text{ s}$ . The dotted lines divide the evolution into three stages according to the value of  $\omega$ . In the first stage, the WD can start with  $\omega > 1$  or  $\omega < 1$  depending whether the initial period is below or above the equilibrium period,  $P_{\text{eq}} = 61.5 \text{ s}$  (Equation (20)), respectively. For both values, the involved torques are magnetic torque,  $T_{\text{mag}}$ , and accretion torque,  $T_{\text{acc}}$ . However,  $T_{\text{acc}}$  is the dominant torque in this phase. For  $\omega \approx 1$ ,  $T_{\text{mag}} \approx T_{\text{acc}}$  and the system goes through the  $P_{\text{eq}}$ . For  $\omega < 1$ , the involved torque is  $T_{\text{mag}}$ .  $T_{\text{acc}}$  no longer acts on the star, as in the third stage the disk has already been exhausted. The upper dashed line indicates the current rotation period of the WD.

Because of the above result, we examine in detail the evolution curve for a single case, e.g.,  $P_0 = 3.14 \text{ s}$ . For the parameters of this WD, and a  $M_d = 0.30 M_{\odot}$ , which lies within the range of consistent values obtained for the disk mass and numerical simulations (see Section 6 for more details), the evolution of the rotation period of J2211+1136 crosses the three stages until it reaches the current value of the rotation period. First, it passes through the regime of  $\omega > 1$ , such that the torques  $T_{\text{acc}}$  and  $T_{\text{dip}}$  spin-down the WD to a period of 61.5 s in  $\Delta t_1 \approx 0.37 \text{ Myr}$ . This time is marked by the first dotted line in Figure 4. The amount of disk mass ejected by the propeller effect during this time is  $M_{\text{loss},1} = \dot{M} \Delta t_1 \approx 0.096 M_{\odot}$ .

From this period value, the parameter  $\omega \approx 1$  and the system enters the equilibrium period regime, where the WD rotation period is oscillating around  $P_{\text{eq}}$  (see Equation (20)). The system remains at this stage until the disk mass ends. The phase lasts  $\Delta t_2 \approx 0.78 \text{ Myr}$ . Therewith, adding the duration of the first and second stages, we have up to this point an evolution time of  $\Delta t_1 + \Delta t_2 \approx 1.15 \text{ Myr}$ . This time is marked by the second dotted line in Figure 4. In this phase II, the disk mass loss is divided in equal parts in accretion and ejection, so  $M_{\text{acc},2} = M_{\text{loss},2} = (1/2) \dot{M} \Delta t_2 \approx 0.102 M_{\odot}$ . Therefore, by the end of phase II, the total disk mass has indeed been consumed, i.e.,  $0.096 M_{\odot} + 0.204 M_{\odot} = M_d$ . The disk mass has been distributed in a total ejected mass  $M_{\text{loss}} = M_{\text{loss},1} + M_{\text{loss},2} \approx 0.2 M_{\odot}$  and a total accreted mass  $M_{\text{acc}} = M_{\text{acc},2} \approx 0.1 M_{\odot}$ .

After this point, the system enters the regime of  $\omega < 1$ , where the only active torque is  $T_{\text{mag}}$ . Thus,  $T_{\text{mag}}$  spins the WD down from a period of 61.5 s to the observed period  $P_{\text{obs}} = 70.3 \text{ s}$ , reached at a time of 2.66 Gyr (see Figure 4). Phase III is by far the longest, so the WD spends most of its evolution in this regime.

In addition to the agreement of the rotational and cooling ages, the full proof of the present scenario would arise from the further agreement of the model spin-down rate with corresponding observational measurement (see, e.g., the case of 4U

0142+61 in Rueda et al. 2013). For the magnetic dipole braking mechanism (see Equation (15)), the spin-down rate is given by

$$\dot{P} = \frac{8\pi^2 R^6 B^2}{3c^3 I P_{\text{obs}}} \sin^2 \theta. \quad (25)$$

For J2211+1136, adopting  $R = 3210 \text{ km}$ ,  $I = (2/5)MR^2 = 1.04 \times 10^{50} \text{ g cm}^2$ , and  $B = 15 \text{ MG}$ , we obtain  $\dot{P} \approx 3.3 \times 10^{-17} \sin^2 \theta \text{ s s}^{-1}$  (see also Williams et al. 2022). This spin-down rate is too low to be detected, e.g., two orders of magnitude lower than the one of the pulsating WD G 117-B15A,  $\dot{P} \approx 5.12 \times 10^{-15} \text{ s s}^{-1}$  (Kepler et al. 2021).

## 5.2. Rotational Evolution of J1901+1458

J1901+1458 has a period of rotation  $P_{\text{obs}} = 416.2 \text{ s}$ , a mass  $M = 1.327\text{--}1.365 M_{\odot}$ , a stellar radius  $R = 2140_{-230}^{+160} \text{ km}$ , and a surface (dipole) magnetic field in the range  $B = 600\text{--}900 \text{ MG}$ . The cooling age is  $t_{\text{cool}} = 10\text{--}100 \text{ Myr}$  (Caiazzo et al. 2021). For simplicity, we consider  $M = 1.35 M_{\odot}$  with  $R = 2140 \text{ km}$  in the analysis of this source. Furthermore, we follow the analogous procedure described above for J2211+1136. We analyze the evolution of the WD rotation period for different values of the initial rotation period, a disk mass of  $M_d = 0.34 M_{\odot}$  consistent with the range of values obtained in Section 6, and a value of  $\dot{M}$  consistent with Equation (24). We use a dipole magnetic field strength of  $B = 800 \text{ MG}$ , inferred in Caiazzo et al. (2021) from the analysis of the position of the H $\alpha$ , H $\beta$ , and H $\gamma$  spectral lines.

Using Equation (24), we obtain the accretion rate as a function of  $t_{\text{cool}}$ . Considering  $\theta = 90^\circ$ , we obtain  $\dot{M} \approx (6.92\text{--}8.05) \times 10^{-7} M_{\odot} \text{ yr}^{-1}$  (See Figure 5). For an aligned rotator,  $\dot{M} \approx (6.87\text{--}7.39) \times 10^{-7} M_{\odot} \text{ yr}^{-1}$ . Figure 6 shows the rotation-period evolution for  $\dot{M} = 8.0 \times 10^{-7} M_{\odot} \text{ yr}^{-1}$ , and initial values of the rotation period  $P_0 = (3.14, 108.7, 258.7, 558.7, 708.7, 814.2) \text{ s}$ . The curves approach the equilibrium period,  $P_{\text{eq}}$ , in a timescale of the same order of magnitude.

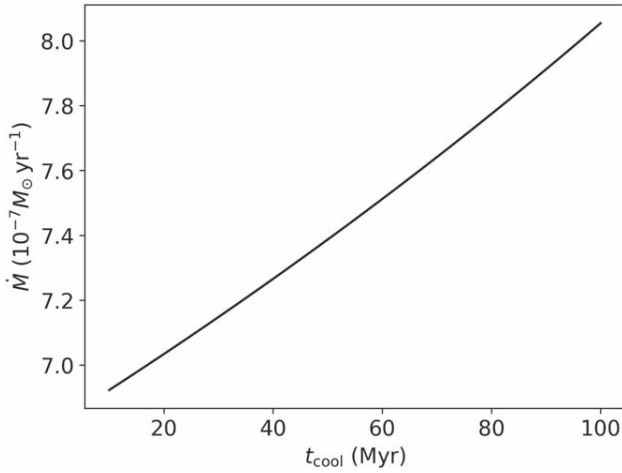


**Figure 5.** Accretion rate as a function of cooling age calculated from Equation (24) for J1901+1458. The WD parameters are  $M = 1.35 M_{\odot}$ ,  $R = 2.14 \times 10^8$  cm,  $P_0 = 3.14$  s, and  $P_{\text{obs}} = 416.2$  s. The magnetic field strength is  $B = 800$  MG and  $\theta = 90^{\circ}$ .

Thus, also for this source, we see that the final evolution time is not affected by the choice of the initial period.

Without loss of generality, we now describe the phases of the spin evolution in the case  $P_0 = 3.14$  s. The system first evolves through the propeller regime  $\omega > 1$ , in which the WD spins down to a period of 388.6 s in  $\Delta t_1 \approx 5.98$  kyr (marked by the first dotted line in Figure 6). During this time, the amount of the disk mass ejected was  $M_{\text{loss},1} = M \Delta t_1 \approx 4.8 \times 10^{-3} M_{\odot}$ .

After the rotation period reaches  $\omega \approx 1$ , the second stage starts. Thus, J1901+1458 evolves through spin-down and spin-up stages around the equilibrium period value, until the disk mass ends. We estimate that this phase lasts  $\Delta t_2 \approx 0.42$  Myr. Up to this point, the postmerger evolution time adding the two stages is  $\Delta t_1 + \Delta t_2 \approx 0.425$  Myr, which is marked by the second dotted line in Figure 6. In this phase II, we have  $M_{\text{acc},2} = M_{\text{loss},2} = (1/2) \dot{M} \Delta t_2 \approx 0.168 M_{\odot}$ . Thus, in this source, nearly the entire disk mass is consumed in phase II, so we have a total ejected mass  $M_{\text{loss}} = M_{\text{loss},1} + M_{\text{loss},2} \approx 0.17 M_{\odot}$  and a total accreted mass  $M_{\text{acc}} = M_{\text{acc},2} \approx 0.17 M_{\odot}$ .

In the subsequent evolution, the only torque acting on the WD is  $T_{\text{dip}}$ , so the WD enters the phase characterized by  $\omega < 1$ . The WD spins down from a period of 388.6 s to the observed period  $P_{\text{obs}} = 416.2$  s. This occurs in  $\approx 96.2$  Myr. Figure 6 shows this last stage for the spin evolution.

The spin-down rate in the current phase for J1901+1458 can be estimated from Equation (25). Adopting  $R = 2140$  km,  $I = (2/5)MR^2 = 5.0 \times 10^{49}$  g cm<sup>2</sup>, and  $B = 800$  MG, we obtain  $\dot{P} \approx 2.9 \times 10^{-15} \sin^2 \theta$  s s<sup>-1</sup>, which is consistent with the upper limit value of  $\dot{P} < 10^{-11}$  s s<sup>-1</sup> presented in Caiazzo et al. (2021). In this case, the resulting spin-down rate is similar to the spin-down rate of G 117-B15A. Therefore, although experimentally challenging, timing analyses, as in the one done by Kepler et al. (2021) for G 117-B15A, could lead in the future to the final proof of the DWD merger scenario for J1901+1458 presented in this work.

## 6. The DWD Merger Progenitors

We now turn to estimate the masses of the components ( $M_1$  and  $M_2$ ) of the DWD progenitor of the above two systems. For

this task, we have to estimate the binary total mass,  $M_{\text{tot}}$ , and mass ratio,  $q$ , so that

$$M_1 = \frac{1}{1+q} M_{\text{tot}}, \quad M_2 = \frac{q}{1+q} M_{\text{tot}}. \quad (26)$$

First, we use the fact that DWDs eject a tiny amount of mass during merger (Lorén-Aguilar et al. 2009; Dan et al. 2014), which allows us to assume baryon mass conservation with an error of at most one part in a thousand. Then, for a given disk mass,  $M_d$ , and accretion rate,  $\dot{M}$ , we have here obtained in the postmerger evolution the total accreted mass by the central WD remnant,  $M_{\text{acc}}$ , and the total mass loss due to action of the propeller,  $M_{\text{loss}}$ . Clearly,  $M_d = M_{\text{acc}} + M_{\text{loss}}$ . Therefore, we can write the total binary mass as

$$M_{\text{tot}} = M + M_{\text{loss}} + M_{\text{ej}} \approx M + M_{\text{loss}}, \quad (27)$$

where we recall that  $M$  is the current measured mass of the WD, and  $M_{\text{loss}}$  can be written as

$$M_{\text{loss}} = \frac{M_d \pm M_{\text{cons}}}{2}, \quad (28)$$

where the  $\pm$  sign is used when phase I starts with propeller ( $\omega_0 > 1$ ) or accretion ( $\omega_0 < 1$ ). The quantity  $M_{\text{cons}}$  is the disk mass consumed in phase I. We now can find an equation for  $M_d$  as a function of the mass ratio,  $q$ . To do this, we substitute Equation (27) into Equation (1c) and solve it for  $M_d$ , which leads to

$$M_d = \frac{Q}{2-Q} (2M \pm M_{\text{cons}}), \quad (29)$$

where  $Q = -0.1185 + 0.9763q - 0.6559q^2$ . Furthermore, we can use Equation (29) together with Equation (28) to express  $M_{\text{loss}}$  in terms of  $q$ :

$$M_{\text{loss}} = \frac{Q}{2-Q} \left( M \pm \frac{M_{\text{cons}}}{Q} \right). \quad (30)$$

Therefore, with the equations obtained above, we can calculate  $M_{\text{tot}}$  and the masses of the components of the DWD progenitor with the following general procedure. Having chosen the initial rotation period and the accretion rate, we calculate the disk mass consumed in phase I,  $M_{\text{cons}}$ . Thus, the disk mass function  $M_d = M_d(M_{\text{cons}}, q)$ , given by Equation (29), and the mass loss function  $M_{\text{loss}} = M_{\text{loss}}(M_{\text{cons}}, q)$ , given by Equation (30), become a function of  $q$ . These functions are concave-down parabolas with maximums at  $q^*$ , so the disk mass and mass loss increase with  $q$  up to the maximum value  $M_d^{\text{max}} = M_d(q^*)$  and  $M_{\text{loss}}^{\text{max}} = M_{\text{loss}}(q^*)$ , to then decrease up to the values  $M_d(q=1)$  and  $M_{\text{loss}}(q=1)$ , respectively. Therefore, if  $M_d \leq M_d(q=1)$  or  $M_{\text{loss}} \leq M_{\text{loss}}(q=1)$ , there is a unique solution for  $q$ . If  $M_d > M_d(q=1)$  or  $M_{\text{loss}} > M_{\text{loss}}(q=1)$ , there are two solutions for  $q$ .

We shall seek for solutions with a disk mass that satisfies  $M_d \gtrsim M_d^{\text{min}}$ , where  $M_d^{\text{min}} = 0.1 M_{\odot}$  is approximately the minimum disk mass obtained in the numerical simulations of Dan et al. (2014), taking into account that  $M \approx 1.3 M_{\odot}$  in the two analyzed systems.

We recall that in view of the nonzero disk mass left by DWD mergers, we have already discarded solutions in which the system evolves only through phase III, i.e., only under the action of the magnetic dipole torque. Therefore, we are left with three possible cases: (i) evolution with phases I+III, (ii)

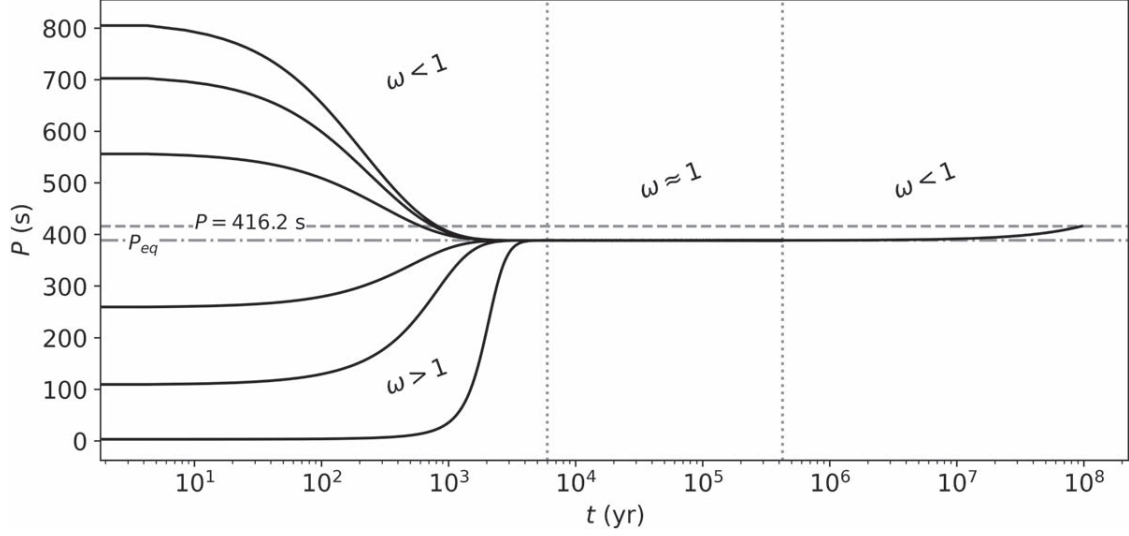


**Figure 6.** Evolution of spin period of the J1901+1458 for  $\dot{M} = 8.0 \times 10^{-7} M_{\odot} \text{ yr}^{-1}$  (with  $B = 800 \text{ MG}$ ) and for different values of initial rotational periods,  $P_0 = (3.14, 108.7, 258.7, 558.7, 708.7, 814.2) \text{ s}$ . The dotted lines divide the evolution into three stages according to the value of  $\omega$ . In the first stage, the WD can start with  $\omega > 1$  or  $\omega < 1$  depending whether the initial period is below or above the equilibrium period,  $P_{\text{eq}} = 388.6 \text{ s}$  (Equation (20)), respectively. For both values, the involved torques are dipole radiation torque,  $T_{\text{mag}}$ , and accretion torque,  $T_{\text{acc}}$ , in the propeller phase. However,  $T_{\text{acc}}$  is the dominant torque in this phase. For  $\omega \approx 1$ ,  $T_{\text{mag}} \approx T_{\text{acc}}$  and the system goes through the equilibrium period,  $P_{\text{eq}}$ . For  $\omega < 1$ , the involved torque is  $T_{\text{dip}}$ .  $T_{\text{acc}}$  no longer acts on the star, as in the third stage the disk has already been exhausted. The upper dashed line indicates the current rotation period of the WD.

with phases II+III, and, the most general case, (iii) with phases I+II+III. We now analyze each case.

#### 6.1. Case (i): Evolution with Phases I+III

In this case, the system does not evolve through phase II, so the entire disk mass is consumed in phase I, i.e.,  $M_{\text{cons}} = M_d$ . From Equation (28), we have that when phase I is a propeller ( $\omega_0 > 1$ ),  $M_{\text{loss}} = M_d$ , while if it is an accretor ( $\omega_0 < 1$ ),  $M_{\text{loss}} = 0$ . It can be shown that under these conditions, to satisfy the boundary condition of approximate equality of the rotational and the cooling age, either the disk mass must be  $M_d \ll M_d^{\text{min}} = 0.1 M_{\odot}$  or the accretion rate must have very large values  $\gtrsim 10^{-5} M_{\odot} \text{ yr}^{-1}$ . Therefore, we do not consider this case as astrophysically viable.

#### 6.2. Case (ii): Evolution with Phases II+III

In this case, the initial angular velocity satisfies  $\Omega_0 = \Omega_{\text{eq}}$ , so there is no phase I and the disk mass is divided in equal parts into accretion and propeller. We have  $M_{\text{cons}} = 0$ , so Equation (28) leads to  $M_{\text{loss}} = M_d/2$ .

#### 6.3. Case (iii): Evolution with Phases I+II+III

In this general case, the system evolves through the three phases as described in Section 4. The angular velocity at the beginning of phase III, say  $\Omega_{\text{dip}}$ , is approximately given by the equilibrium value, i.e.,  $\Omega_{\text{dip}} \approx \Omega_{\text{eq}}$ . With this constraint, we can estimate  $M_{\text{cons}}$  by

$$M_{\text{cons}} \approx I \left( \frac{\Omega_{\text{eq}}^2}{GM} \right)^{2/3} \ln \left( \frac{\Omega_0 - \Omega_{\text{eq}}}{\Omega_{\text{dip}} - \Omega_{\text{eq}}} \right), \quad (31)$$

which is obtained from Equation (18), solving it for  $t$ , making  $t = \Delta t_1 = M_{\text{cons}}/\dot{M}$  and  $\Omega = \Omega_{\text{dip}}$ . Therefore,  $M_{\text{cons}}$  lies in the range  $0 < M_{\text{cons}} < M_d$ .

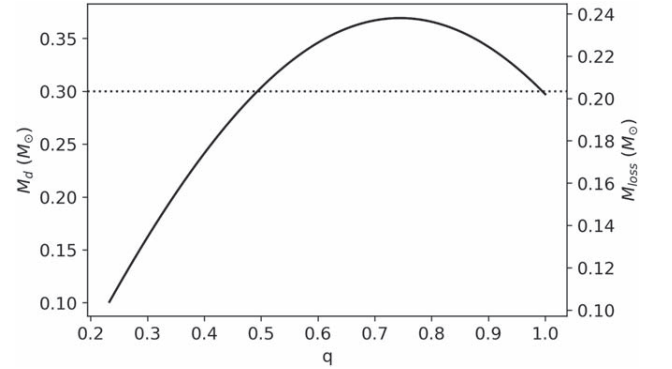


**Figure 7.** Disk mass,  $M_d$ , and mass loss,  $M_{\text{loss}}$ , as a function of the binary mass ratio,  $q$ . The solid curve represents the solutions for J2211+1136 ( $M = 1.27 M_{\odot}$ ,  $P_0 = 3.14 \text{ s}$ ,  $\dot{M} = 2.62 \times 10^{-7} M_{\odot} \text{ yr}^{-1}$ ), while the dashed horizontal line shows the corresponding value used in the simulation.

#### 6.4. Specific Examples

To exemplify the approach above, we consider the cases of J2211+1136 and J1901+1458 in Section 5, i.e., in the general evolution (iii) in which the system evolves through phases I+II+III. Figure 7 shows the functions  $M_d(M_{\text{cons}}, q)$  and  $M_{\text{loss}}(M_{\text{cons}}, q)$  for J2211+1136, given  $M_{\text{cons}} \approx 0.1 M_{\odot}$  ( $P_0 = 3.14 \text{ s}$  and  $\dot{M} = 2.62 \times 10^{-7} M_{\odot} \text{ yr}^{-1}$ ). Figure 8 is analogous to Figure 7 but for J1901+1458, with  $M_{\text{cons}} \approx 4.8 \times 10^{-3} M_{\odot}$  ( $P_0 = 3.14 \text{ s}$  and  $\dot{M} = 8.0 \times 10^{-7} M_{\odot} \text{ yr}^{-1}$ ). Thus, for J2211+1136 and J1901+1458, we obtain  $M_d^{\text{max}} \approx 0.36 M_{\odot}$ ,  $M_d(q=1) \approx 0.297 M_{\odot}$ , and  $M_d^{\text{min}} \approx 0.37 M_{\odot}$ ,  $M_d(q=1) \approx 0.304 M_{\odot}$ , respectively. From the  $M_d^{\text{min}}$  and  $M_d^{\text{max}}$  values obtained above, we note that our choice for the disk mass of J2211+1136,  $M_d = 0.30 M_{\odot}$ , and of J1901+1458,  $M_d = 0.34 M_{\odot}$ , are within the range of physically plausible values. The horizontal dashed lines in Figures 7 and 8 represent these values and their intersection with the curve of the source gives the mass ratio  $q$  to these cases.



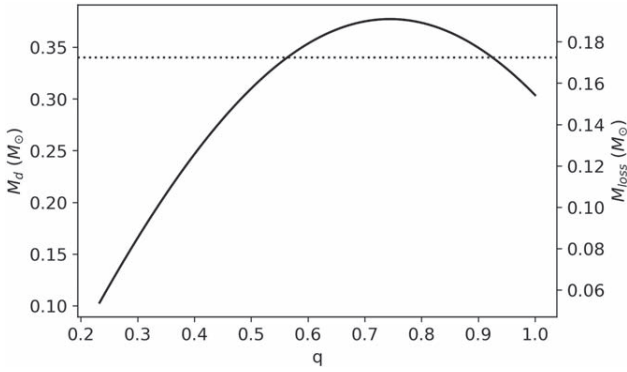


**Figure 8.** Disk mass,  $M_d$ , and mass loss,  $M_{\text{loss}}$ , as a function of the binary mass ratio,  $q$ . The solid curve represents the solutions for J1901+1458 ( $M = 1.35 M_{\odot}$ ,  $P_0 = 3.14$  s,  $\dot{M} = 8.0 \times 10^{-7} M_{\odot} \text{ yr}^{-1}$ ), while the dashed horizontal line shows the corresponding value used in the simulation.

Moreover, Figures 7 and 8 show that, given a value of  $q$ , we can estimate the  $M_d$  and  $M_{\text{loss}}$ , so we can calculate  $M_{\text{tot}}$  from Equation (27). With these values, we can obtain the primary and secondary mass via Equation (26). In Figure 9, we show the  $M_1$ – $M_2$  plane of possible solutions of the DWD progenitor. Each pair ( $M_2$ ,  $M_1$ ) in this figure corresponds to a value of  $q$  and, consequently, to a value of  $M_d$ . Therefore, we can infer the values  $M_1$  and  $M_2$  for the simulated cases in Section 5 taking into account the assumed value of  $M_d$ .

Therefore, since for the two systems we have chosen a disk mass value  $M_d > M_d(q = 1)$ , there are two possible values of mass ratio,  $q_a$  and  $q_b$  (see Figures 7 and 8). For J2211+1136, we obtain  $q_a = 0.495$  and  $q_b = 0.993$ , while for J1901+1458,  $q_a = 0.565$  and  $q_b = 0.924$ . For J2211+1136, the mass ratio  $q_a$  gives  $M_1 = 0.983 M_{\odot}$ ,  $M_2 = 0.487 M_{\odot}$ , while the solution  $q_b$  gives  $M_1 = 0.737 M_{\odot}$ ,  $M_2 = 0.732 M_{\odot}$ . For J1901+1458, the mass ratio  $q_a$  gives  $M_1 = 0.971 M_{\odot}$ ,  $M_2 = 0.549 M_{\odot}$ , and  $q_b$  gives  $M_1 = 0.790 M_{\odot}$ ,  $M_2 = 0.729 M_{\odot}$ . Table 1 summarizes the results of the above analysis. In particular, it lists the parameters of the premerger DWD and the parameters of the postmerger system for the disk mass and accretion rate in the simulations of Section 5.

Interestingly, the inferred parameters of the DWD progenitor of J1901+1458 and J2211+1136 (see Table 1) are consistent with the parameters of known systems, e.g., NLTT 12758, a  $0.83 + 0.69 M_{\odot}$  DWD (Kawka et al. 2017). This result further supports the link that we have here provided between DWD mergers and the formation of HFMWDs.

## 7. Discussion and Conclusions

In this article, we have investigated the possibility that the HFMWDs J2211+1136, and J1901+1458 are DWD merger products. Based on numerical simulations of DWD mergers, we have modeled the postmerger system as a central WD surrounded by a disk from which there is a mass inflow toward the WD remnant. We have calculated the postmerger rotational evolution of the WD and inferred the system parameters for which the rotational age agrees with the WD cooling age.

We have shown that the postmerger configuration evolves through three different phases depending on whether accretion, mass ejection (propeller), or magnetic braking dominate the torque on the WD. We have shown that the WD spends most of its lifetime in the third phase, in which only magnetic braking torques the WD (see Figures 4 and 6). We have used the

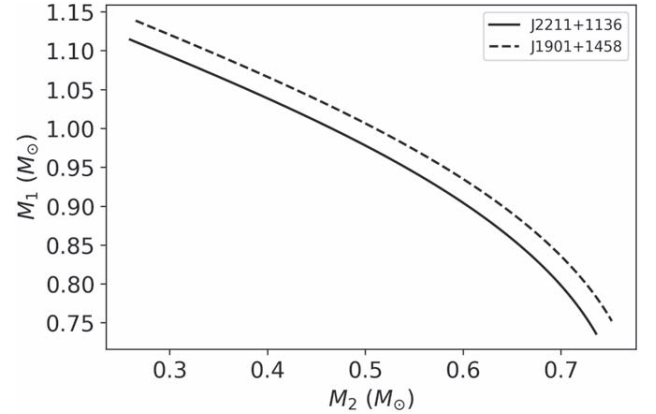


**Figure 9.** Predicted range of the primary and secondary mass. The solid curve represents the solutions for J2211+1136 (postmerger WD mass of  $M = 1.27 M_{\odot}$ ,  $P_0 = 3.14$  s, and  $\dot{M} = 2.62 \times 10^{-7} M_{\odot} \text{ yr}^{-1}$ ) and the dashed curve for J1901+1458 (postmerger WD mass of  $M = 1.35 M_{\odot}$ ,  $P_0 = 3.14$  s, and  $\dot{M} = 8.0 \times 10^{-7} M_{\odot} \text{ yr}^{-1}$ ).

**Table 1**

Parameters of the Premerger (DWD) and Postmerger (Central Remnant WD +Disk) Systems Leading to the Current Observed Parameters of J2211+1136 and J1901+1458

Parameter	J2211+1136	J1901+1458
Premerger system		
$q_a, q_b$	0.49, 0.99	0.56, 0.92
$M_{\text{tot}} (M_{\odot})$	1.47	1.52
$M_1 (M_{\odot})$	0.98, 0.74	0.97, 0.79
$M_2 (M_{\odot})$	0.49, 0.73	0.55, 0.73
$M_{\text{ej}} (10^{-3} M_{\odot})$	4.96, 0.51	3.61, 0.68
Postmerger system		
$M (M_{\odot})$	1.27 <sup>a,b</sup>	1.35 <sup>c</sup>
$R$ (km)	3210	2140 <sup>c</sup>
$P$ (s)	70.32 <sup>a</sup>	416.20 <sup>c</sup>
$B (10^6 \text{ G})$	15 <sup>a</sup>	800 <sup>c</sup>
$B_{\text{quad}} \text{ (G)}$	Unconstrained	Unconstrained
$M_d (M_{\odot})$	0.30	0.34
$\dot{M} (10^{-7} M_{\odot} \text{ s}^{-1})$	2.62	8.0
$M_{\text{loss}} (M_{\odot})$	0.20	0.17
$\Delta t_{\text{obs}} \text{ (Gyr)}$	2.66	0.096

**Notes.** There are two possible solutions for the mass of the DWD components,  $M_1$  and  $M_2$ , corresponding to the two values of the binary mass ratio,  $q_a$  and  $q_b$ , that solve the system constraints (see Figures 7 and 8).  $\Delta t_{\text{obs}}$  is the rotational age, i.e., the total time elapsed since the merger to the instant when the WD reaches the current measured rotation period. We recall that we constrain the system to have  $\Delta t_{\text{obs}}$  equal to the estimated WD cooling age. See the text for further details.

### References.

- <sup>a</sup> Kilic et al. (2021b).  
<sup>b</sup> Kilic et al. (2021a).  
<sup>c</sup> Caiazzo et al. (2021).

measured mass, magnetic field strength, and cooling age to infer the mass accretion rate and the disk mass.

The results of this article are the first attempt to establish a direct link between observed HFMWDs and their DWD merger progenitors. We conclude that the observed parameters of J2211+1136 and J1901+1458 are consistent with a DWD merger origin, and we have obtained the mass of the premerger

DWD primary and secondary binary components (see Table 1). Interestingly, the derived parameters of the merging DWDs are in line with those of known DWDs (like NLTT 12758; see Kawka et al. 2017), which further supports the connection between HFMWDs and DWD mergers.

If HFMWDs like J2211+1136 and J1901+1458 are DWD merger products, the newborn merged remnant, besides being massive and highly magnetic, might be fast rotating in its early postmerger life (e.g., in its first 1–100 kyr; see Figures 4 and 6). WDs with such extreme properties might power a variety of transient and persistent electromagnetic phenomena in astrophysical sources. For instance, Schwab (2021a) discusses evolutionary models of DWD merger remnants and how they might experience a  $\sim 10$  kyr luminous giant phase during their final approach to the single massive WD or a NS fate.

The DWD merger and its early activity can also lead to low-energy gamma-ray bursts. Phenomena in the merged magnetosphere can power the prompt gamma-ray emission, the cooling of the expanding ( $\sim 10^{-3} M_{\odot}$ ) ejecta can power an infrared/optical transient days to week postmerger, and synchrotron emission of the ejecta and the WD pulsar-like emission can lead to extended (years) X-ray, optical, and radio emission (Rueda et al. 2019, 2022).

Massive, fast-rotating HFMWDs with pulsar-like activity might show up as magnetars (see, e.g., Malheiro et al. 2012; Rueda et al. 2013; Coelho & Malheiro 2014; Mukhopadhyay & Rao 2016; Coelho et al. 2017; Cáceres et al. 2017; Becerra et al. 2018; Borges et al. 2020, and references therein). Other high-energy phenomena involving DWD mergers and HFMWD products are the emission of high-energy neutrinos (see, e.g., Xiao et al. 2016) and particle acceleration leading to very-high-energy ( $\gtrsim 10^{15}$  eV) and ultra-high-energy ( $\gtrsim 10^{18}$  eV) cosmic rays. In addition, space-based detectors of gravitational waves (GWs) like the Laser Interferometer Space Antenna expect to detect the GW radiation driving the dynamics of compact, detached DWDs (see, e.g., Stroer & Vecchio 2006; Korol et al. 2022). Electromagnetic radiation phenomena might affect the evolution of merging DWDs detectable through the deviations from the case when pure GW radiation drives the orbital dynamics (see Carvalho et al. 2022, and references therein), and the fast rotation and high magnetic fields might also lead to GW radiation from HFMWD pulsars (see, e.g., Sousa et al. 2020a, 2020b).

We thank the referee for their thoughtful comments and suggestions that helped us to improve the presentation of our results. M.F.S. thanks CAPES-PrInt (88887.351889/2019-00) for the financial support. J.G.C. is likewise grateful for the support of CNPq (311758/2021-5) and FAPESP (2021/01089-1), and financial support by “Fenômenos Extremos do Universo” of Fundação Araucária. J.C.N.A. thanks CNPq (308367/2019-7) for partial financial support.

#### ORCID iDs

M. F. Sousa <https://orcid.org/0000-0002-5438-3460>  
 J. G. Coelho <https://orcid.org/0000-0001-9386-1042>  
 J. C. N. de Araujo <https://orcid.org/0000-0003-4418-4289>  
 S. O. Kepler <https://orcid.org/0000-0002-7470-5703>

J. A. Rueda <https://orcid.org/0000-0003-4904-0014>

#### References

- Bagnulo, S., & Landstreet, J. D. 2022, *ApJL*, **935**, L12  
 Becerra, L., Boshkayev, K., Rueda, J. A., & Ruffini, R. 2019, *MNRAS*, **487**, 812  
 Becerra, L., Rueda, J. A., Lorén-Aguilar, P., & García-Berro, E. 2018, *ApJ*, **857**, 134  
 Benz, W., Cameron, A. G. W., Press, W. H., & Bowers, R. L. 1990, *ApJ*, **348**, 647  
 Blouin, S., & Daligault, J. 2021, *ApJ*, **919**, 87  
 Borges, S. V., Rodrigues, C. V., Coelho, J. G., Malheiro, M., & Castro, M. 2020, *ApJ*, **895**, 26  
 Cáceres, D. L., de Carvalho, S. M., Coelho, J. G., de Lima, R. C. R., & Rueda, J. A. 2017, *MNRAS*, **465**, 4434  
 Caiazzo, I., Burdge, K. B., Fuller, J., et al. 2021, *Natur*, **595**, 39  
 Carvalho, G. A., dos Anjos, R. C., Coelho, J. G., et al. 2022, *ApJ*, **940**, 90  
 Cheng, S. 2020, in IAU Symp. 357, White Dwarfs as Probes of Fundamental Physics: Tracers of Planetary, Stellar and Galactic Evolution, ed. M. A. Barstow et al. (Cambridge: Cambridge Univ. Press), 175  
 Cheng, S., Cummings, J. D., Menard, B., & Toonen, S. 2020, *ApJ*, **891**, 160  
 Coelho, J. G., Cáceres, D. L., de Lima, R. C. R., et al. 2017, *A&A*, **599**, A87  
 Coelho, J. G., & Malheiro, M. 2014, *PASJ*, **66**, 14  
 Dan, M., Rosswog, S., Bruggen, M., & Podsiadlowski, P. 2014, *MNRAS*, **438**, 14  
 Ferrario, L., de Martino, D., & Gänsicke, B. T. 2015, *SSRv*, **191**, 111  
 García-Berro, E., Lorén-Aguilar, P., Aznar-Siguán, G., et al. 2012, *ApJ*, **749**, 25  
 Guerrero, J., García-Berro, E., & Isern, J. 2004, *A&A*, **413**, 257  
 Illarionov, A. F., & Sunyaev, R. A. 1975, *A&A*, **39**, 185  
 Kalogera, V., Narayan, R., Spergel, D. N., & Taylor, J. H. 2001, *ApJ*, **556**, 340  
 Kawka, A., Briggs, G. P., Vennes, S., et al. 2017, *MNRAS*, **466**, 1127  
 Kepler, S. O., Pelisoli, I., Koester, D., et al. 2016, *MNRAS*, **455**, 3413  
 Kepler, S. O., Winget, D. E., Vanderbosch, Z. P., et al. 2021, *ApJ*, **906**, 7  
 Kilic, M., Bergeron, P., Blouin, S., & Bédard, A. 2021a, *MNRAS*, **503**, 5397  
 Kilic, M., Kosakowski, A., Moss, A. G., Bergeron, P., & Conly, A. A. 2021b, *ApJL*, **923**, L6  
 Korol, V., Hallakoun, N., Toonen, S., & Karnesis, N. 2022, *MNRAS*, **511**, 5936  
 Külebi, B., Jordan, S., Euchner, F., Gänsicke, B. T., & Hirsch, H. 2009, *A&A*, **506**, 1341  
 Longland, R., Lorén-Aguilar, P., José, J., García-Berro, E., & Althaus, L. G. 2012, *A&A*, **542**, A117  
 Lorén-Aguilar, P., Isern, J., & García-Berro, E. 2009, *A&A*, **500**, 1193  
 Malheiro, M., Rueda, J. A., & Ruffini, R. 2012, *PASJ*, **64**, 56  
 Maoz, D., & Hallakoun, N. 2017, *MNRAS*, **467**, 1414  
 Maoz, D., Hallakoun, N., & Badenes, C. 2018, *MNRAS*, **476**, 2584  
 Menou, K., Esin, A. A., Narayan, R., et al. 1999, *ApJ*, **520**, 276  
 Mukhopadhyay, B., & Rao, A. R. 2016, *JCAP*, **2016**, 007  
 Pétri, J. 2015, *MNRAS*, **450**, 714  
 Pringle, J. E., & Rees, M. J. 1972, *A&A*, **21**, 1  
 Raskin, C., Scannapieco, E., Fryer, C., Rockefeller, G., & Timmes, F. X. 2012, *ApJ*, **746**, 62  
 Rueda, J. A., Boshkayev, K., Izzo, L., et al. 2013, *ApJL*, **772**, L24  
 Rueda, J. A., Ruffini, R., Li, L., et al. 2022, *IJMPD*, **31**, 2230013  
 Rueda, J. A., Ruffini, R., Wang, Y., et al. 2019, *JCAP*, **2019**, 044  
 Ruiter, A. J., Belczynski, K., & Fryer, C. 2009, *ApJ*, **699**, 2026  
 Saio, H., & Nomoto, K. 1985, *A&A*, **150**, L21  
 Schwab, J. 2021a, *ApJ*, **906**, 53  
 Schwab, J. 2021b, *ApJ*, **916**, 119  
 Schwab, J., Quataert, E., & Kasen, D. 2016, *MNRAS*, **463**, 3461  
 Sousa, M. F., Coelho, J. G., & Araujo, J. C. N. 2020b, *MNRAS*, **498**, 4426  
 Sousa, M. F., Coelho, J. G., & de Araujo, J. C. N. 2020a, *MNRAS*, **492**, 5949  
 Stroer, A., & Vecchio, A. 2006, *CQGra*, **23**, S809  
 Wang, Y.-M. 1995, *ApJL*, **449**, L153  
 Wickramasinghe, D. T., & Ferrario, L. 2000, *PASP*, **112**, 873  
 Williams, K. A., Hermes, J. J., & Vanderbosch, Z. P. 2022, *AJ*, **164**, 131  
 Xiao, D., Mészáros, P., Murase, K., & Dai, Z. -G. 2016, *ApJ*, **832**, 20  
 Zhu, C., Chang, P., van Kerkwijk, M. H., & Wadsley, J. 2013, *ApJ*, **767**, 164



# Orbital Decay of Double White Dwarfs: Beyond Gravitational-wave Radiation Effects

G. A. Carvalho<sup>1,2,3</sup> , R. C. dos Anjos<sup>4,5,6</sup>, J. G. Coelho<sup>7,8</sup> , R. V. Lobato<sup>9,10</sup> , M. Malheiro<sup>3</sup> , R. M. Marinho<sup>3</sup>,  
J. F. Rodriguez<sup>11,12</sup>, J. A. Rueda<sup>12,13,14,15,16</sup>, and R. Ruffini<sup>12,13,17</sup>

<sup>1</sup> Departamento de Física, Universidade Tecnológica Federal do Paraná, Medianeira, PR, Brazil; [gacarvalho@utfpr.edu.br](mailto:gacarvalho@utfpr.edu.br)

<sup>2</sup> Instituto de Pesquisa e Desenvolvimento (IP&D), Universidade do Vale do Paraíba, 12244-000, São José dos Campos, SP, Brazil

<sup>3</sup> Instituto Tecnológico de Aeronáutica, 12228-900, São José dos Campos, SP, Brazil

<sup>4</sup> Departamento de Engenharias e Exatas, Universidade Federal do Paraná (UFPR), Pioneiro, 2153, 85950-000 Palotina, Brazil

<sup>5</sup> PPGFISA, Universidade Federal da Fronteira Latino-Americana, PR, Brazil

<sup>6</sup> PPGFA, Universidade Tecnológica Federal do Paraná, PR, Brazil

<sup>7</sup> Núcleo de Astrofísica e Cosmologia (Cosmo-Ufes) & Departamento de Física, Universidade Federal do Espírito Santo, 29075-910, Vitória, ES, Brazil

<sup>8</sup> Divisão de Astrofísica, Instituto Nacional de Pesquisas Espaciais, Avenida dos Astronautas 1758, 12227-010, São José dos Campos, SP, Brazil

<sup>9</sup> Departamento de Física, Universidad de los Andes, Bogotá, Colombia

<sup>10</sup> Department of Physics and Astronomy, Texas A&M University-Commerce, Commerce, TX 75429, USA

<sup>11</sup> Escuela de Física, Universidad Industrial de Santander, Ciudad Universitaria, Bucaramanga, Colombia

<sup>12</sup> ICRAInet, Piazza della Repubblica 10, I-65122 Pescara, Italy

<sup>13</sup> ICRA, Dipartimento di Fisica, Sapienza Università di Roma, Piazzale Aldo Moro 5, I-00185 Rome, Italy

<sup>14</sup> ICRAInet-Ferrara, Dipartimento di Fisica e Scienze della Terra, Università degli Studi di Ferrara, Via Saragat 1, I-44122 Ferrara, Italy

<sup>15</sup> Dip. di Fisica e Scienze della Terra, Università degli Studi di Ferrara, Via Saragat 1, I-44122 Ferrara, Italy

<sup>16</sup> INAF, Istituto di Astrofisica e Planetologia Spaziali, Via Fosso del Cavaliere 100, I-00133 Rome, Italy

<sup>17</sup> INAF, Viale del Parco Mellini 84, I-00136 Rome, Italy

Received 2022 July 19; revised 2022 October 3; accepted 2022 October 4; published 2022 November 23

## Abstract

The traditional description of the orbital evolution of compact-object binaries, like double white dwarfs (DWDs), assumes that the system is driven only by gravitational-wave (GW) radiation. However, the high magnetic fields with intensities of up to gigagausses measured in WDs alert a potential role of the electromagnetic (EM) emission in the evolution of DWDs. We evaluate the orbital dynamics of DWDs under the effects of GW radiation, tidal synchronization, and EM emission by a unipolar inductor generated by the magnetic primary and the relative motion of the nonmagnetic secondary. We show that the EM emission can affect the orbital dynamics for magnetic fields larger than megagausses. We applied the model to two known DWDs, SDSS J0651+2844 and ZTF J1539+5027, for which the GW radiation alone does not fully account for the measured orbital decay rate. We obtain upper limits to the primary's magnetic field strength, over which the EM emission causes an orbital decay faster than observed. The contribution of tidal locking and the EM emission is comparable, and together they can contribute up to 20% to the measured orbital decay rate. We show that the gravitational waveform for a DWD modeled as purely driven by GWs and including tidal interactions and EM emission can have large relative dephasing detectable in the mHz regime of frequencies relevant for space-based detectors like LISA. Therefore, including physics besides GW radiation in the waveform templates is essential to calibrate the GW detectors using known sources, e.g., ZTF J1539+5027, and to infer binary parameters.

*Unified Astronomy Thesaurus concepts:* White dwarf stars (1799); Close binary stars (254); Compact binary stars (283); Stellar magnetic fields (1610); Gravitational waves (678)

## 1. Introduction

Our Galaxy hosts a predicted number of  $(1-3) \times 10^8$  double white dwarfs (hereafter DWDs; Nelemans et al. 2001, 2005; Maoz et al. 2012), of which observational facilities have detected only about 100. This situation can improve thanks to forthcoming space-based detectors of gravitational waves (GWs) like the Laser Interferometer Space Antenna (LISA), which expects to detect the GW radiation driving the dynamics of compact, detached DWDs (see, e.g., Stroeer & Vecchio 2006; Korol et al. 2022). The detection and analysis of GW signals need the development of gravitational waveform templates that accurately encode the physics driving the binary dynamics. The traditional description of the orbital evolution of compact-object binaries, like DWDs, assumes that the GW

radiation of two point-like masses orbiting the common center of mass is an accurate description of the binary dynamics, neglecting any other interactions. However, the orbital evolution is affected by additional effects like the dark matter background (see, e.g., Pani 2015; Gómez & Rueda 2017) and the electromagnetic (EM) emission (see, e.g., Marsh & Nelemans 2005; Wang et al. 2018). We focus in this article on the effects of the latter.

There is mounting observational evidence that the components of DWDs can be highly magnetized. Depending on the binary component masses, the merger of a DWD may not lead to a prompt type Ia supernova (SN) but a newborn, massive, fast-rotating, highly magnetic WD (see, e.g., Becerra et al. 2018). Mergers of DWDs have been proposed as progenitors of ZTF J190132.9+145808.7 Caiazzo et al. (2021) and the recently discovered isolated, highly magnetic, rapidly rotating WD (rotation period of 70.32 s), SDSS J221141.80+113604.4 (see Kilic et al. 2021 for details). These rotation rates are consistent with the theoretical predictions for DWD merger remnants, in agreement with the many works published in the

last decade about the theory of highly magnetic, massive, and fast WDs from DWD mergers (Malheiro et al. 2012; Coelho & Malheiro 2012; Rueda et al. 2013; Coelho & Malheiro 2014; Coelho et al. 2014; Lobato et al. 2016; Mukhopadhyay & Rao 2016; Cáceres et al. 2017; Coelho et al. 2017; Becerra et al. 2018; Otoniel et al. 2019; Sousa et al. 2020a, 2020b; and Borges et al. 2020).

The above extreme properties of some WDs have led to the proposal that DWD mergers can power low-energy gamma-ray bursts (GRBs). The prompt gamma-ray emission arises from the transient activity of the magnetosphere during the merger, the infrared/optical transient from the merger ejecta, and an extended X-ray and radio emission powered by the WD central merger remnant (Rueda et al. 2019). In addition, high-energy neutrinos may be the product of cosmic-ray acceleration in DWD mergers and newborn pulsars (Xiao et al. 2016). The rapid rotation and strong magnetic fields can accelerate particles to energies higher than petaelectronvolts (PeV; i.e.,  $10^{15}$  eV), and the surrounding material can naturally generate ultrahigh-energy cosmic rays (UHECR) with energies larger than exaelectronvolts (EeV; i.e.,  $10^{18}$  eV), in particular, with a heavy composition (Piro & Kollmeier 2016; dos Anjos et al. 2021). The rotational magnetic instability surrounding the source can lead to the formation of hot, magnetized corona and high-velocity outflows. Additionally, the low volume of the surrounding material facilitates the escape of UHECRs from the environment (Piro & Kollmeier 2016; Ji et al. 2013; Beloborodov 2014; Venters et al. 2020). The operation of the near generation of multimessenger observatories like the Cherenkov Telescope Array (CTA; Actis et al. 2011), POEMMA (Olinto et al. 2017), and IceCube (The IceCube Collaboration 2011) will shed more light on several high-energy scenarios and interpretations for understanding particle acceleration in a DWD merger.

Given all the above, in this article, we analyze the dynamics of DWDs in the premerger stage under the action of GW emission, tidal interactions, and EM emission. The inclusion of a large variety of possible emissions besides the GW radiation could complicate the analysis of the results and hide the essential physics we would like to spot here. Therefore, we emphasize here only the effects of the EM emission on the binary dynamics using the unipolar inductor model (UIM; Goldreich & Lynden-Bell 1969) applied to DWDs (see, e.g., Wu et al. 2002; Dall’Osso et al. 2006; Lai 2012). The EM emission in the UIM originates from the energy dissipation of the closed circuit formed by the magnetized primary star, the nonmagnetic secondary, and the magnetic field lines. The motion of the secondary relative to the magnetic field lines of the primary generates the electromotive force (EMF) that drives the current through the magnetic field lines (see, e.g., Wu et al. 2002; Lai 2012). We refer the reader to Lai (2012; and references therein) for estimates of the EM emission from the UIM in a variety of compact-object binaries.

We show with specific examples that the EM emission by the UI overcomes the emission from a hot WD and magnetic-dipole braking. Such an EM emission is comparable to the quadrupolar GW radiation by two orbiting point-like masses. Therefore, we include the EM emission in the binary dynamics and quantify its contribution to the rate of orbital decay. We show that the EM emission can significantly affect the binary dynamics, accounting for a sizable part of the orbital decay measured in some compact DWDs and the GW properties (e.g.,

phase, intensity). Therefore, it is of paramount relevance to understand and model the physical phenomena that drive the binary dynamics to develop astrophysical waveform templates useful to detect and infer binary parameters from GW signals (see, e.g., Bourgoin et al. 2022).

We organize the article as follows. In Section 2, we recall the aspects of the UIM that are relevant for the modeling of the DWD dynamics, estimate the EM dissipation for fiducial values of the masses and magnetic field, solve (numerically) the equations of motion, and compare with the orbital decay of a pure GW-radiation-driven dynamics. Section 3 analyzes within the UIM two known DWDs, SDSS J0651+2844 and ZTF J1539+5027. We analyze the constraints on the system given by the measured orbital decay, obtain upper limits to the primary’s magnetic field, and estimate the contribution of tidal synchronization and EM emission to the orbital decay. We quantify in Section 4 the effect of the EM emission in the phase evolution of the GWs. Finally, we present in Section 5 the conclusions of this article.

## 2. Unipolar Inductor and Orbital Dynamics

We follow the general framework of the UIM presented in Wu et al. (2002) and use the associated EM dissipation estimated in Lai (2012). The binary system is composed of a magnetic primary with mass  $M_1$ , radius  $R_1$ , and magnetic moment  $\mu_1$ , and a nonmagnetic secondary with mass  $M_2$  and radius  $R_2$ . Unless otherwise stated, we estimate the WD radius from the mass–radius relation presented in Carvalho et al. (2018) and Carvalho (2019). The secondary is synchronous, so it has angular velocity  $\omega_s = \omega_0$ , where

$$\omega_0 = \sqrt{\frac{GM}{r^3}} \quad (1)$$

is the orbital angular velocity according to Kepler’s third law. The primary is asynchronous with angular velocity  $\Omega$  measured by the parameter  $\alpha = \Omega/\omega_0$ . Hereafter, we denote with  $M = M_1 + M_2$  and  $r$  the binary’s total mass and orbital separation.

The evolution of the binary system under the combined (nonlinearly coupled) GW radiation, tides, and EM emission losses in the UIM is obtained from energy and angular momentum conservation, which lead to the system of equations Wu et al. (2002)

$$\frac{\dot{\omega}_0}{\omega_0} = -\frac{\dot{P}}{P} = \frac{1}{g(\omega_0)} \left[ \dot{E}_{\text{GW}} - \frac{L}{1-\alpha} \right], \quad (2)$$

$$\frac{\dot{\alpha}}{\alpha} = -\frac{1}{g(\omega_0)} \left\{ \dot{E}_{\text{GW}} - \frac{L}{1-\alpha} \left[ 1 + \frac{g(\omega_0)}{\alpha I_1 \omega_0^2} \right] \right\}, \quad (3)$$

where  $P = 2\pi/\omega_0$  is the orbital period,  $L$  is the EM power released by the circuit, and  $\dot{E}_{\text{GW}}$  is the rate of energy loss via GW radiation for a system of two point-like masses in circular orbit

$$\begin{aligned} \dot{E}_{\text{GW}} &= -\frac{32}{5} \frac{G}{c^5} \left( \frac{q}{1+q} \right)^2 M_1^2 r^4 \omega_0^6 \\ &= -\frac{32}{5} \frac{G}{c} \left( \frac{q}{1+q} \right)^2 M_1^2 \left( \frac{GM\omega_0}{c^3} \right)^{4/3}, \end{aligned} \quad (4)$$

where we have used Equation (1) in the second equality, and

$$g(\omega_0) = -\frac{1}{3} \left( \frac{q^3}{1+q} G^2 M_1^5 \omega_0^2 \right)^{1/3} \left[ 1 - \frac{6}{5} (1+q) \left( \frac{R_2}{r} \right)^2 \right], \quad (5)$$

with  $q = M_2/M_1$  the binary's mass ratio.

The above model of the binary dynamics remains valid to the point when either Roche lobe overflow of the secondary or a merger takes place. Therefore, the maximum orbital angular velocity of the system is

$$\omega_0^{\max} = \sqrt{\frac{GM}{r_{\min}^3}}, \quad (6)$$

being  $r_{\min} = \text{Max}(r_L, r_{\text{mrg}})$ , where according to Eggleton's formula for the Roche lobe Eggleton (1983)

$$r_L = \frac{0.6q^{2/3} + \ln(1+q^{1/3})}{0.49q^{2/3}} R_2, \quad (7)$$

and  $r_{\text{mrg}} = R_1 + R_2$ . For instance, for a  $0.6 + 0.6 M_\odot$  binary, with  $R_1 = R_2 \approx 7.8 \times 10^8$  cm,  $r_L \approx 2.06 \times 10^9$  cm, and  $r_{\text{mrg}} \approx 1.56 \times 10^9$  cm. For these figures, Equation (6) leads to  $\omega_0^{\max} \approx 0.13$  rad s<sup>-1</sup>, corresponding to a minimum orbital period of 46.43 s. In all the examples presented in this article, the orbital dynamics is analyzed far from any of the above two physical situations.

The equations of motion, Equations (2)–(3), account for the torques due to the EM emission and from tides (see Wu et al. 2002 for details). We now recall the EM power of the UIM. The motion of the conductive secondary into the primary's rotating magnetosphere induces an electromotive force  $\mathcal{E} = 2R_2|\vec{E}|$ , where the electric field and associated electric potential  $U$  through the secondary star are

$$\vec{E} = \frac{\vec{v} \times \vec{B}}{c}, \quad U = 2R_2|E|, \quad (8)$$

being

$$\vec{v} = r(\omega_0 - \Omega)\hat{\phi} = (GM\omega_0)^{1/3}(1-\alpha)\hat{\phi}, \quad (9)$$

and we have used Equation (1) in the second equality. The total energy dissipation is Wu et al. (2002)

$$L = 2I^2\mathcal{R}, \quad (10)$$

where the factor 2 accounts for the upper and lower parts of the circuit,  $\mathcal{R}$  is the total resistance of the system, and  $I = U/\mathcal{R}$  is the electric current.

Lai (2012) has shown that a high twist of the magnetic field causes the disruption of the magnetic flux tubes, hence short-circuiting the system. The azimuthal twist is given by  $\xi_\phi = -B_{\phi+}/B_z = 16v/(c^2\mathcal{R})$ , where  $B_{\phi+}$  is the toroidal magnetic field generated by the current in the circuit on the upper side of the primary. Therefore, we limit the twist parameter to  $\xi_\phi \lesssim 1$  (i.e.,  $\mathcal{R} \gtrsim 16v/c^2$ ), so that the circuit remains active. Bearing the above in mind, we parameterize the resistance in terms of the value given by the impedance of free space, i.e.,

$$\mathcal{R} = \frac{4\pi}{c} \frac{1}{\eta}, \quad (11)$$

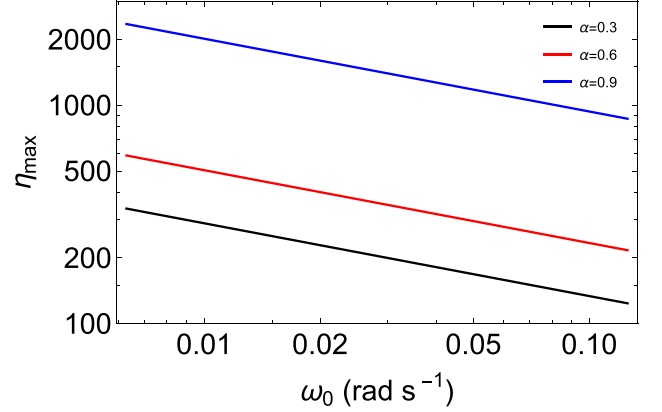


**Figure 1.** Value of  $\eta_{\max}$  as a function of  $\omega_0$ , given by Equation (13), for selected values of  $\alpha$ .

which leads to

$$\xi_\phi = \eta \frac{4v}{\pi c} = \frac{4}{\pi} \left( \frac{GM\omega_0}{c^3} \right)^{1/3} (1-\alpha)\eta, \quad (12)$$

where we have used Equation (9) to obtain the second equality. We limit the value of  $\eta$  so to have  $\xi \leq 1$  during the entire evolution. Therefore,  $\eta_{\max}$  is

$$\eta_{\max} = \frac{\pi}{4} \left( \frac{c^3}{GM\omega_0} \right)^{1/3} \frac{1}{1-\alpha}. \quad (13)$$

Figure 1 shows the value of  $\eta_{\max}$  as a function of the  $\omega_0$ , for selected values of  $\alpha$ .

Having set all the above, the EM power, Equation (10), derived in Lai (2012) can be written as

$$\frac{L}{1-\alpha} = \frac{2}{\pi c} (1-\alpha)\eta \omega_0^2 \frac{\mu_1^2 R_2^2}{r^4}. \quad (14)$$

Normalizing the physical quantities in Equation (14) to fiducial parameters for DWDs, the EM power reads

$$\frac{L}{1-\alpha} = 7.72 \times 10^{32} \left( \frac{\tilde{B}}{10^6 \text{ G}} \right)^2 \left( \frac{R_1}{10^9 \text{ cm}} \right)^6 \times \left( \frac{R_2}{10^9 \text{ cm}} \right)^2 \left( \frac{M_\odot}{M} \right)^{4/3} \left( \frac{100 \text{ s}}{P} \right)^{14/3} \text{ erg s}^{-1}, \quad (15)$$

where we have used the primary's magnetic moment  $\mu_1 = BR_1^3$ , with  $B$  the magnetic field, and have introduced

$$\tilde{B} \equiv \sqrt{(1-\alpha)\eta} B, \quad (16)$$

a quantity that encloses the degeneracy among  $\alpha$ ,  $\eta$ , and  $B$  in Equations (2) and (3).

Figure 2 shows the EM power, Equation (15), as a function of the orbital angular velocity, in the case of  $\alpha = 0.9$ , and  $M_1 = M_2 = 0.6 M_\odot$  ( $R_1 = R_2 = 7.79 \times 10^8$  cm), for selected values of the magnetic field strength ranging from  $10^6$  G to  $10^9$  G. For instance, for a magnetic field  $B = 10^9$  G,  $\eta = 100$ , and orbital period of 50 and 300 s, Equation (15) leads, respectively, to an EM power of  $2.66 \times 10^{39}$  erg s<sup>-1</sup> and  $6.23 \times 10^{35}$  erg s<sup>-1</sup>. This luminosity is much larger than the blackbody luminosity of a hot WD with surface temperature of  $10^4$  K,  $L_{\text{BB}} = 4\pi R_1^2 \sigma T^4 \approx 4.33 \times 10^{30}$  erg s<sup>-1</sup>, or the EM emission owing to magnetic-dipole braking, respectively,

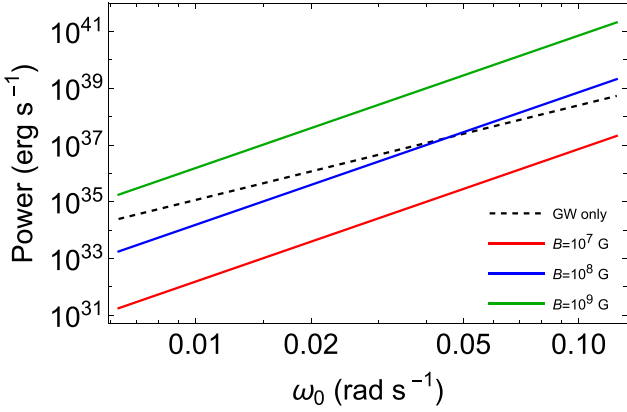


**Figure 2.** EM power as a function of orbital angular frequency given by Equation (15), for selected values of the primary’s magnetic field. In this example, we set  $\eta=100$ , and the binary is mass-symmetric with  $M_1=M_2=0.6 M_\odot$ . The mass–radius relation is taken from Carvalho et al. (2018). For comparison, we also show the GW power (black dashed curve) given by Equation (4).

$$L_{\text{dip}} \sim (1/c^3) B^2 R_1^6 \Omega^4 \approx 1.36 \times 10^{36} \text{ erg s}^{-1} \quad \text{and} \quad 1.05 \times 10^{33} \text{ erg s}^{-1}.$$

Figure 2 also indicates that for magnetic fields of the order of  $10^9$  G, the EM emission of the UIM can even overcome the GW emission before merger, so it largely affects the orbital dynamics at those evolution stages. For lower magnetic fields, the EM emission lowers but remains comparable to the GW emission at high frequencies, i.e., for compact binaries. Under these conditions, the orbital evolution is not driven only by GW radiation, but rather by a coupling between GW and EM emission. Figure 3 shows the evolution of  $\omega_0$  with time, for an initial orbital period of 10 minutes. We compare the results of the orbital dynamics given by Equation (2), which accounts for GWs, tides, and EM emission, with the case when the dynamics is purely driven by GW radiation. In the latter case, the rate of orbital decay is given by

$$\dot{P}_{\text{obs}} = \dot{P}_{\text{GW}} = -\frac{96}{5} (2\pi)^{8/3} \frac{G^{5/3} M_1 M_2}{c^5 M^{1/3}} P^{-5/3}. \quad (17)$$

In this specific example, for magnetic fields  $\gtrsim 10^6$  G, the tidal locking and the EM emission starts to affect the orbital dynamics, and for fields  $\gtrsim 10^8$  G the effects become noticeably large.

### 3. Constraining the Magnetic Field in Observed Double White Dwarfs

Since the orbital evolution of the binary is affected by the EM emission and tides, it is theoretically possible to infer the magnetic field or at least to put constraints on it from measurements of the orbital decay rate. Therefore, given measurements of the orbital period,  $P$ , the spin-down rate of the orbital period,  $\dot{P}_{\text{obs}}$ , and the binary component masses,  $M_1$  and  $M_2$  (the corresponding WD radii are assumed to be known from the mass–radius relation), we can constrain the magnetic field. For this task, we request that the spin-down rate predicted by the UIM, which includes the effect of the GWs, the EM emission, and tides, does not exceed the measured orbital decay,  $\dot{P}_{\text{obs}}$ , i.e.,

$$\dot{P}_{\text{obs}} = \dot{P}, \quad (18)$$

where  $\dot{P}$  is the period decay given by the model, which is obtained from the solution of the system of Equations (2)–(3). In this light, we analyze two known compact DWDs, ZTF J1539+5027 (Burdge et al. 2019) and SDSS J0651+2844 (Brown et al. 2011; Hermes et al. 2012).

#### 3.1. SDSS J0651+2844

Table 1 lists the parameters  $M_1$ ,  $M_2$ ,  $P$ , and  $\dot{P}_{\text{obs}}$  of SDSS J0651+2844, reported in Brown et al. (2011) and Hermes et al. (2012). Given values of  $\dot{P}$  and  $P$ , Equation (18), with  $\dot{P}$  given by Equation (2), gives a relation between  $M_1$  and  $M_2$  for every given value of  $\bar{B}$ . Figure 4 shows examples of the constraints on the masses obtained from the orbital period and decay rate of SDSS J0651+2844. We compare the results of the UIM with the case of pure GW radiation, i.e., when using Equation (17), the case with 90% of GW radiation and the case with GW radiation plus tides, i.e., Equations (2) and (3) with  $L=0$ . The agreement with the observational data requires that the  $M_2$ – $M_1$  relations cross the measurements of  $M_1$  and  $M_2$  represented within  $1\sigma$  error by the blue rectangle. The pure GW-driven evolution is consistent with the data, but the current statistical uncertainties in the measured masses and  $\dot{P}$  allow alternative explanations of the binary dynamics including additional physics to the GW emission, like UI and tides, for a relatively wide parameter space. Therefore, tighter constraints on  $\dot{P}$  are needed to conclude more on the sole basis of timing. The absence of Zeeman splitting in the spectra of J0651+2844 rules out magnetic fields  $B > 10^6$  G.

In Hermes et al. (2012) and Burdge et al. (2019), it has been pointed out that, indeed, a sizable portion of the observed orbital decay might arise in these DWDs from tidal interactions. Besides GWs and tides, the model studied in this work takes also into account the effect of EM emission from an active UI in the binary. Figure 4 shows three curves of the UIM, and the case of including GWs and a full tidal locking but without EM emission ( $\bar{B}=0$ ). We recall that as the synchronization parameter  $\alpha$  changes with time (see, e.g., Figure 3), the value of  $\bar{B}$  must be considered as a constraint at the observational period. For  $\bar{B}=10^7$  G (red curve), the effect of the EM emission is relatively small, so the dynamics is dominated by GW radiation and tidal synchronization. This model nearly follows the curve of the model  $\dot{P}_{\text{GW}} = 0.9\dot{P}_{\text{obs}}$ , which suggests that roughly 90% of the orbital decay is due to GW radiation, and the remaining 10% to tidal locking. For  $\bar{B}=5.8 \times 10^7$  G (green curve), the EM emission has considerable effects in the dynamics, as shown by the difference of this curve in comparison with the examples with lower magnetic field values. In fact, the data do not favor models with high values of  $\bar{B}$  as shown by the upper limit on  $\bar{B}$  set by the  $3\sigma$  upper limit on  $\dot{P}$ . For  $\bar{B} \gtrsim 9.7 \times 10^7$  G, the  $M_1$ – $M_2$  curve for those cases lie outside the rectangle of  $1\sigma$  uncertainties in the masses. Although due to the nonlinearity of the model is not possible to separate the individual contributions to the  $\dot{P}$ , we have checked that a curve in which 77% of the orbital decay is due to GW radiation approaches the green curve in the lower right part of the rectangle (middle panel), suggesting that the contribution of GW radiation in the green-curve model could be around that value, and the remaining  $\approx 23\%$  is shared in comparable amounts by the tidal interactions and EM emission.

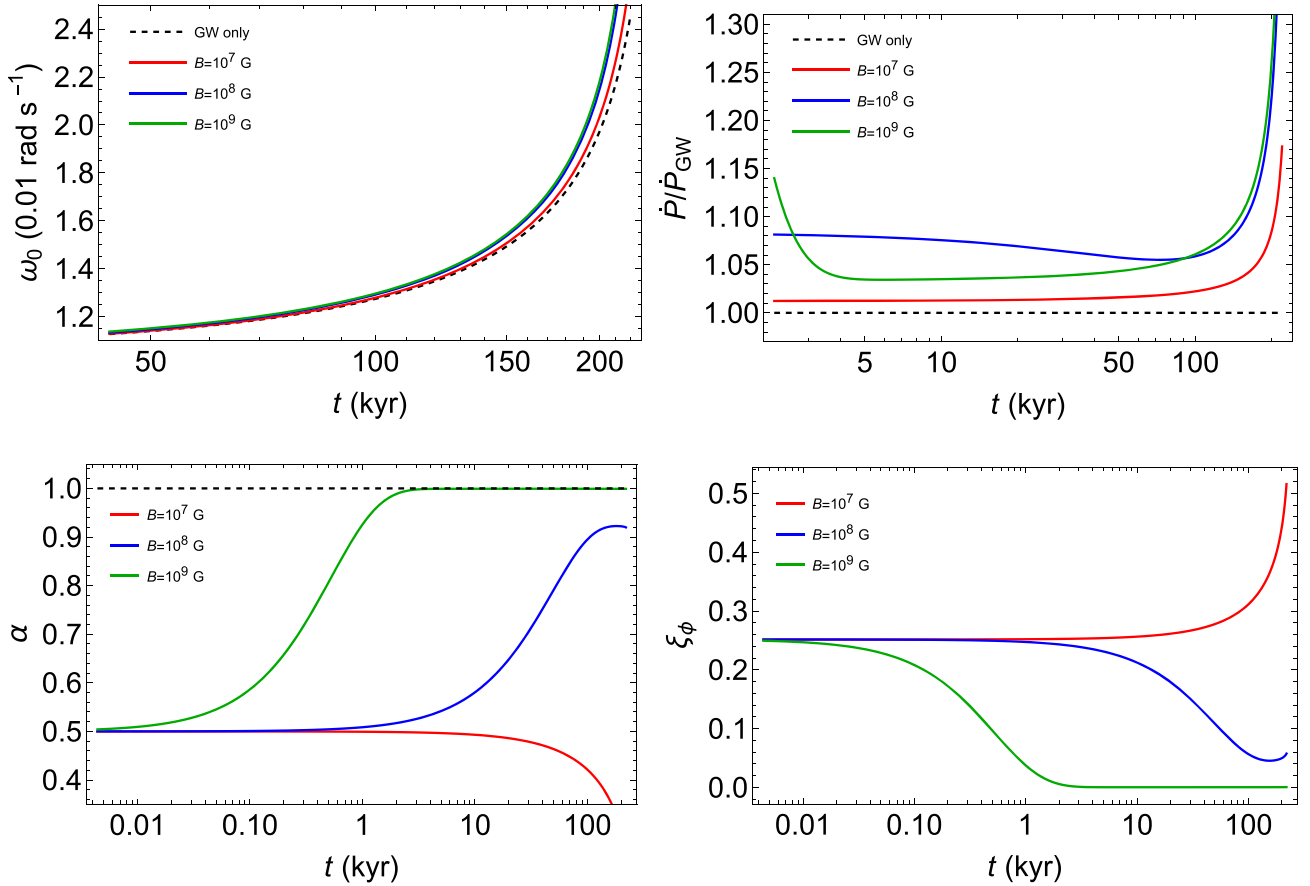


**Figure 3.** Examples of numerical solution of the equations of motion, Equations (2)–(3), for selected values of the primary’s magnetic field. In these examples, we set  $\eta = 100$ , the binary is mass-symmetric with  $M_1 = M_2 = 0.6 M_\odot$ , and we assign an initial ( $t = 0$ ) values for the orbital period and the degree of synchronization of the primary, respectively,  $P(0) = 10$  min (i.e.,  $\omega_0(0) = 0.0105$ ) and  $\alpha(0) = 0.5$ . The mass–radius relation is taken from Carvalho et al. (2018). For comparison, we also show the solution of the equations of motion when only GW radiation is considered, i.e., the solution to Equation (17). Upper left: orbital evolution,  $\omega_0$ . Upper right: orbital decay rate,  $\dot{P}$ , normalized to the value for the case of only GW radiation,  $\dot{P}_{\text{GW}}$ . Lower left: evolution of the primary’s synchronization,  $\alpha$ . Lower right: evolution of the twist parameter,  $\xi_\phi$ .

**Table 1**  
Example of DWDs with Short Orbital Periods That Are Targets for LISA-like Missions

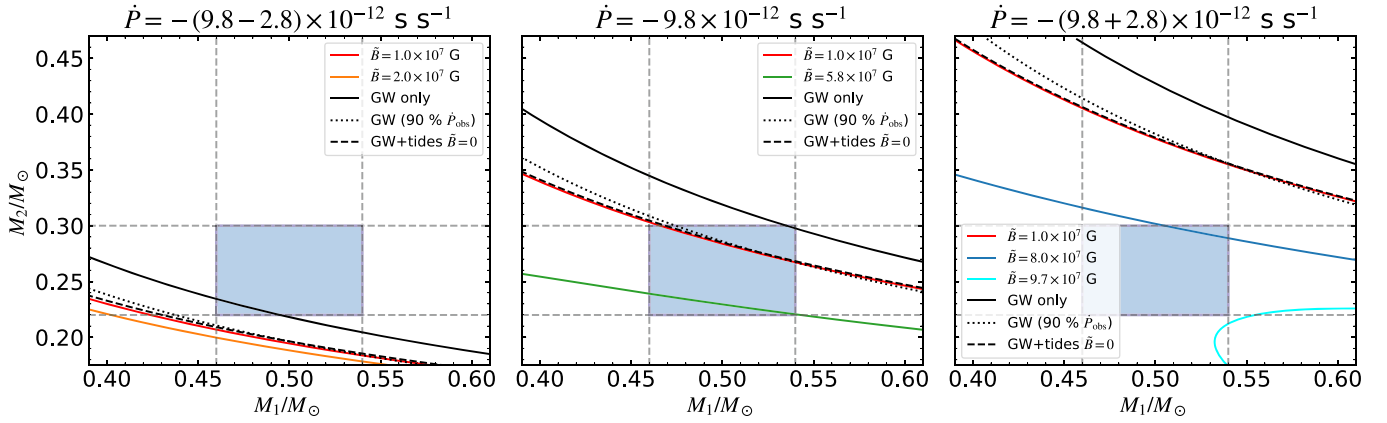
Binary	$M_1/M_\odot$	$M_2/M_\odot$	$P$ (s)	$\dot{P}_{\text{obs}}$ ( $\text{s s}^{-1}$ )	References
ZTF J1539+5027	$0.610_{-0.022}^{+0.017}$	$0.210_{-0.015}^{+0.014}$	$414.79 \pm 2.9 \times 10^{-6}$	$(-2.373 \pm 0.005) \times 10^{-11}$	Burdge et al. (2019)
SDSS J0651+2844	$0.50 \pm 0.04$	$0.26 \pm 0.04$	$765.2 \pm 5.5 \times 10^{-5}$	$(-9.8 \pm 2.8) \times 10^{-12}$	Brown et al. (2011); Hermes et al. (2012)

**Note.** An upper limit for the magnetic field of the UIM can be set if the DWD has measured  $P$ ,  $\dot{P}$ ,  $M_1$ , and  $M_2$ . See main text for details.

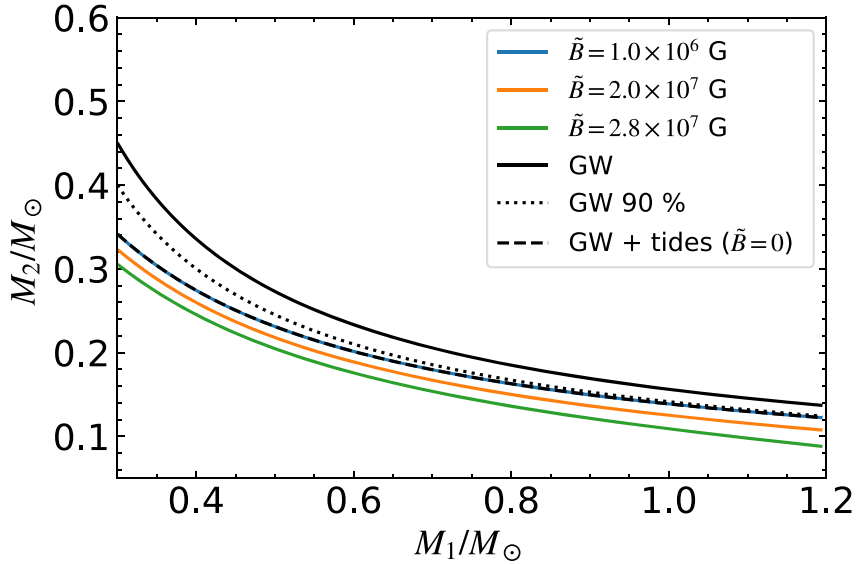
### 3.2. ZTF J1539+5027

Table 1 lists the parameters  $M_1$ ,  $M_2$ ,  $P$ , and  $\dot{P}_{\text{obs}}$  of ZTF J1539+5027, reported in Burdge et al. (2019). In this case, the masses of the DWD components are not known from photometric and/or spectroscopic measurements. The reported values of the masses have been obtained in Burdge et al. (2019) from crossed information by the measured spectroscopic radial-velocity semi-amplitudes, the constraint to the mass–radius relation of the primary combined with the ratio of the primary’s radius to the semimajor axis,  $R_1/r$  inferred from lightcurve modeling, and constraints imposed by the binary chirp mass assuming that the orbital decay is 100% driven by GW radiation (solid black curve), or 90% (dotted black curve), assuming a 10% from tidal interaction considering full synchronization of both the primary and the secondary.

Since in this case the mass values depend on the adopted model, we apply the present model considering GW radiation, tides, and the EM emission by the UI, and cross-check it with the other independent constraints. We plot in Figure 5 the results for  $\tilde{B} = 1.0 \times 10^6$  G (blue curve),  $2.0 \times 10^7$  G (orange curve), and  $2.8 \times 10^7$  G (green curve). In doing this, we adopted in the function  $g(\omega_0)$  given by Equation (5), the observational constraint on the secondary’s radius,  $R_2/r = 0.28$ , as reported in Burdge et al. (2019). For  $\tilde{B} \lesssim 10^7$  G, the EM emission effect is relatively small. In fact, the blue curve partly overlaps with the black dotted curve  $\dot{P}_{\text{GW}} = 0.9\dot{P}$ , with the remaining  $\approx 10\%$  dominated by the partial tidal synchronization. For larger values of  $\tilde{B}$ , the EM emission has appreciable effects. Indeed, models with  $\tilde{B} \gtrsim 2.8 \times 10^7$  G are not favored by the observational data, since the resulting  $M_1$ – $M_2$  relation falls below the lower limit imposed by the 50%



**Figure 4.** Constraints on the binary masses and magnetic field for SDSS J0651+2844. We have used the values inferred from photometric and spectroscopic measurements of the orbital period, decay rate, and masses reported in Hermes et al. (2012) (see also Table 1). The blue rectangle represents the  $1\sigma$  uncertainties on the masses. Left: constraints considering the lower limit for the decay rate,  $\dot{P} = -(9.8 - 2.8) \times 10^{-12} \text{ s s}^{-1}$ , which gives the lower limit to the contribution of  $\tilde{B}$  and tides. Pure GW radiation is consistent with  $1\sigma$  errors in the masses. Center: constraints considering the central value of the decay rate,  $\dot{P} = -9.8 \times 10^{-12} \text{ s s}^{-1}$ . Right: constraints considering the upper limit for the decay rate,  $\dot{P} = -(9.8 + 2.8) \times 10^{-12} \text{ s s}^{-1}$ , which we use to estimate the upper limit on  $\tilde{B}$ . Summarizing, the current decay rate is consistent with a pure GW-driven dynamics, but the uncertainties on the mass measurements and  $\dot{P}$  are broad enough to allow solutions of GW emission admixed with a UI and tides, although the absence of Zeeman splitting in the spectra rule out magnetic field strengths  $B > 10^6 \text{ G}$ .



**Figure 5.** Constraint on the binary masses and magnetic field of the primary in ZTF J1539+5027. We have used the orbital period and decay rate reported in Burdge et al. (2019) and listed in Table 1.

contour level of the mass–radius constraint shown in Burdge et al. (2019). Figure 5 shows that within the above range of allowed values of  $\tilde{B}$ , some solutions allow slightly lower values for the masses with respect to the solution considered in Burdge et al. (2019) of nearly 90% of  $\dot{P}$  arising from GWs and 10% from tidal synchronization.

#### 4. Intrinsic Time-domain Phase Evolution of Gravitational Waves

Having shown that physics besides GW radiation, e.g., tidal and EM emission, can have appreciable effects on the orbital dynamics, we analyze in this section the effect that this could have on the gravitational waveform.

The evolution of the orbital angular frequency is quite slow for a considerable part of the lifetime of the binary. Consequently, these systems can be considered as quasi-

monochromatic GW emitters. It is worth mentioning that if the source is exactly monochromatic (given the sensitivity of the detector) the nature of the system cannot be determined by observing its gravitational radiation. We will consider only the evolution stages when the system is not monochromatic, that is, only those orbital frequency regimes of the system in which an interferometer is capable of detecting changes in frequency.

For a quasi-monochromatic source, the intrinsic parameters of the gravitational waveform template are the frequency,  $f$ , its time derivative,  $\dot{f}$ , and the wave amplitude,  $h_0$  (Takahashi & Seto 2002). The amplitude depends both on intrinsic parameters (e.g., the binary mass) and also on external parameters like the distance to the source. The first two parameters ( $f$  and  $\dot{f}$ ) define the intrinsic time-domain phase



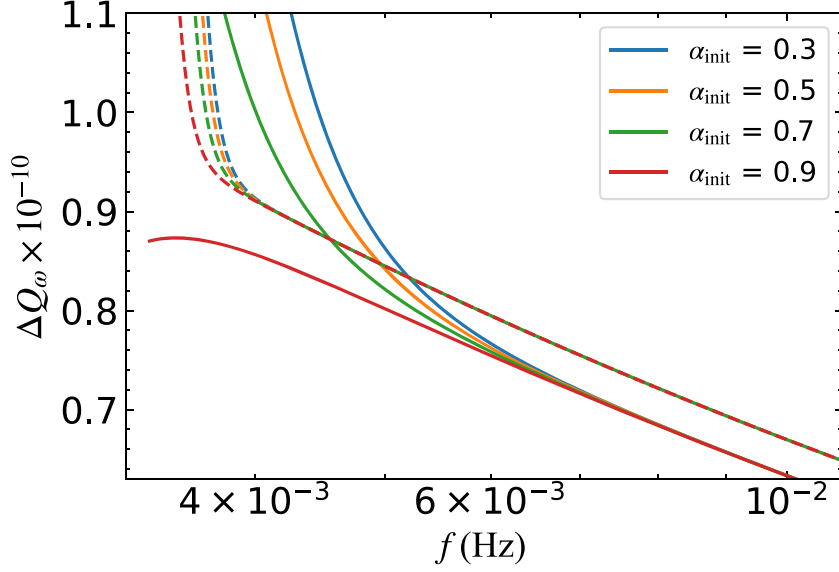


**Figure 6.** Difference in the intrinsic time-domain phase evolution between the two models  $\Delta Q_\omega \equiv Q_\omega^{\text{GW}} - Q_\omega^{\text{UIM}}$ , for a binary with  $M = 1.2 M_\odot$ ,  $q = 1$ ,  $\eta = 100$ , and two selected values of the magnetic field  $B = 8 \times 10^7$  G (solid curves),  $B = 2 \times 10^8$  G (dashed curves). The different colors correspond to different initial values of  $\alpha$  used in the numerical integration. The intrinsic time-domain phase parameter encapsulates two of the intrinsic observable obtained from GW data. Since  $\Delta Q_\omega \gg 1$ , the UIM waveform gets out of phase with respect to the waveform in the case of only GW radiation. A sufficiently large dephasing can be detected by LISA for appropriate conditions (see main text for details).

evolution of the GWs as (Damour et al. 2013)

$$Q_\omega = \frac{\omega^2}{\dot{\omega}} = -\frac{2\pi}{\dot{P}} = 2\pi \frac{dN}{d \ln \omega}, \quad (19)$$

which provides information on the rate change of the GW phase per logarithmic change in frequency. Here,  $\omega = 2\omega_0$  is the GW angular frequency. The quantity  $Q_\omega$  is useful to compare the phase evolution of two waveforms given it is invariant under phase and time shifts. The integral of the difference between the value of  $Q_\omega$  of two waveforms gives their relative *dephasing*. For a binary emitting only GW in the pure point-like quadrupole approximation, the phase evolution  $Q_\omega^{\text{GW}}$  is

$$Q_\omega^{\text{GW}} = \frac{5}{3\nu} 2^{-\frac{7}{3}} \left( \frac{GM\omega}{c^3} \right)^{-\frac{5}{3}} = \frac{5}{48\nu} \left( \frac{GM\omega_0}{c^3} \right)^{-\frac{5}{3}}, \quad (20)$$

where  $\nu = M_1 M_2 / M^2 = q / (q + 1)^2$  is the so-called symmetric mass ratio. For example, a binary with  $M = 1.2 M_\odot$ ,  $q = 1$  ( $\nu = 1/4$ ), driven only by GW emission, has  $Q_\omega^{\text{GW}} = 3.2 \times 10^{12}$  at  $f = \omega / (2\pi) = 1$  mHz.

As already mentioned, the frequency evolution of a binary under GW, tidal interaction, and EM emission is different from a pure GW-radiation-driven dynamics. Therefore, the GW phase evolution is also different. The slower a system changes its frequency, the more cycles it achieves before changing its frequency, i.e.,  $Q_\omega$  is larger. Since the evolution of the binary under pure GW emission is slower (see Figure 3), we can infer that  $Q_\omega^{\text{UIM}} < Q_\omega^{\text{GW}}$ .

Figure 6 shows the difference in the parameter  $Q_\omega$  between the UIM and the pure GW emission model,  $\Delta Q_\omega \equiv Q_\omega^{\text{GW}} - Q_\omega^{\text{UIM}}$ , as a function of the GW frequency, for  $M = 1.2 M_\odot$ ,  $q = 1$ ,  $\eta = 100$ , two selected values of the magnetic field,  $B = 8 \times 10^7$  G (continuous curves) and  $B = 2 \times 10^8$  G (dashed curves), and for different initial values of synchronization parameter  $\alpha$ . For each magnetic field case,

the different curves corresponding to different  $\alpha_{\text{init}}$  converge rapidly. This is a consequence of the existence of a *quasi-attractor* different from unity in the dynamics of synchronization parameter,  $\alpha$  (see, e.g., Figure 3). Furthermore, the intrinsic time-domain evolution is affected for increasing values of the magnetic field.

The considerable difference between the models implies a relative dephasing of the gravitational waveforms, even when the changes in frequency are small. Suppose that we observe the above system at a GW frequency of 6 mHz, i.e., at an orbital period of  $P = 5.6$  minutes, and the synchronization is  $\alpha = 0.8$ . After 2 yr of evolution, the GW frequency has changed  $1.57 \times 10^{-3} \%$ , in the case of the UIM model with magnetic field  $B = 8 \times 10^7$  G, and  $1.47 \times 10^{-3} \%$ , in the case of GW emission. For the former frequency change, the difference in phase of the waveforms is  $\Delta\Phi \approx \Delta Q_\omega d \ln \omega = 1.48 \times 10^5$  rad. For a magnetic field of  $2 \times 10^8$  G, the system changes its frequency  $1.88 \times 10^{-3} \%$  in the same time interval and the dephasing between the two waveforms increases to  $\approx 5.19 \times 10^5$  rad.

From the observational viewpoint, we can distinguish the two systems by the fact that the observable  $\dot{f}$  is different at the same frequency. This difference can be measured by GW detectors like LISA (Amaro-Seoane et al. 2017). The error in estimating  $\dot{f}$  by using the matched-filtering method is (Takahashi & Seto 2002)

$$\Delta \dot{f}_{\text{error}} \approx 0.43 \left( \frac{10}{\langle \rho \rangle} \right) \frac{1}{T_{\text{obs}}^2}, \quad (21)$$

where  $\langle \rho \rangle$  is the signal-to-noise ratio (S/N) accumulated in the observing time,  $T_{\text{obs}}$ . The S/N for quasi-monochromatic sources can be estimated as (Maggiore 2008)

$$\langle \rho^2 \rangle = \frac{6}{25} \frac{\hat{h}_c^2(f_{\text{obs}})}{f_{\text{obs}} S_n(f_{\text{obs}})}, \quad (22)$$

where the factor  $6/25$  comes from averaging over the angles and considering two Michelson interferometers,  $f_{\text{obs}}$  is the observed GW frequency,  $S_n(f)$  is the power spectrum density of the detector noise, and  $\hat{h}_c$  is the *reduced* characteristic amplitude (Flanagan & Hughes 1998)

$$\hat{h}_c(f) = h_0(f)\sqrt{N} = h_0(f)\sqrt{fT_{\text{obs}}}, \quad (23)$$

with  $h_0 = 4\nu(GM/dc^2)(\pi GMf/c^3)^{2/3}$  the GW amplitude and  $d$  is the distance to source.

Using the same system at a GW frequency  $f = 6$  mHz, the differences between the UIM and the pure GW emission model for  $B = 8 \times 10^7$  G and  $B = 2 \times 10^8$  G are, respectively,  $\Delta\dot{f} = 9.26 \times 10^{-17}$  Hz s $^{-1}$  and  $\Delta\dot{f} = 3.91 \times 10^{-16}$  Hz s $^{-1}$ . Suppose that the binary is located at a distance of 1 kpc, so after 2 yr of observations by LISA, it could reach an S/N  $\langle\rho\rangle \approx 246$ , and Equation (21) gives  $\Delta\dot{f}_{\text{error}} \approx 4.38 \times 10^{-18}$  Hz s $^{-1}$ . These figures imply that LISA could discriminate between the two waveforms.

This effect can be used to calibrate the detectors observing known astrophysical sources and pinpoint additional effects besides GW radiation in the orbital dynamics. For instance, we have shown that the gravitational waveform has the imprint of the EM emission, so the detection of GW radiation from these binaries can constrain the magnetic fields present. The above can be accomplished if the additional effects like the EM emission are accounted in the gravitational waveform templates.

## 5. Conclusions

We have shown in this article that both tidal locking and EM emission from the UI mechanism can contribute to binary dynamics of DWDs as much as the GW radiation. Therefore, physics besides GW radiation can cause large effects in the orbital decay rate and, consequently, on the GW waveforms. At the same time, this can modify the outcome of population synthesis models and the DWD merger delay time distribution, relevant for the massive WD population from merging DWDs and the double-degenerate channel of type Ia SN.

Particularly relevant is the effect of the EM emission on the orbital decay for a magnetic field parameter  $\tilde{B} \gtrsim 10^7$  G, leading to the possibility of constraining the magnetic field from measurements of the orbital decay in known DWDs. We applied the present model to two DWDs. For SDSS J0651+2844 (see Section 3.1 and Figure 4), we obtain an upper limit  $\tilde{B} \approx 6 \times 10^7$  G, and for ZTF J1539+5027 (see Section 3.2 and Figure 5), the upper limit is  $\tilde{B} \approx 2.8 \times 10^7$  G. We have estimated that in these systems tidal locking and EM emission can be of the same order and might have a combined contribution of  $\sim 20\%$  to the orbital decay.

The fact that the contribution of physics beyond the GW radiation is already evident in known binaries motivated us to quantify the effect of the different orbital dynamics on the GW time-domain phase evolution, i.e., on the gravitational waveform (see Section 4). We have shown that the waveforms obtained assuming two different dynamics, one driven totally by GW radiation and one driven by GW, tides, and EM emission, have an extremely diverse phase evolution (see Figure 6) that can be measured by LISA. The sensitivity of LISA to distinguish differences in the phase evolution of different waveforms is particularly important for known sources, since the accurate modeling of the templates will

allow an accurate test of the detector itself. For instance, as pointed out in Burdge et al. (2019), a *crucial verification source* for LISA is ZTF J1539+5027, which emits GWs with frequency  $f \approx 5$  Hz and could be detected with an accumulative large S/N of about 143 in 4 yr of LISA observations. For this S/N and observing time, Equation (21) states that the error in estimating  $\dot{f}$  by matched filtering will be  $\Delta\dot{f}_{\text{error}} \approx 2 \times 10^{-18}$  Hz s $^{-1}$ . This value of  $\Delta\dot{f}_{\text{error}}$ , together with our estimates in Section 4, implies that LISA will be sensitive enough to discriminate between different models for this system. The difference in  $\dot{f}$  at the GW frequency of this source between a model accounting for GW radiation, tidal interactions, and EM emission and a model with only GW radiation is in the range  $10^{-17}$ – $10^{-15}$  Hz s $^{-1}$  for magnetic fields  $10^7$ – $10^9$  G. In addition, the well-constrained binary inclination angle constrains the relative amplitude of two GW polarizations, and the measured orbital decay already constrains the chirp mass (Burdge et al. 2019) and, as shown in this article (see Figure 4), physics beyond GW radiation.

There are additional targets of interest for potential studies of this topic, e.g., the eclipsing DWD ZTF J2243+5242, with an orbital period of 8.8 minutes and masses  $M_1 = 0.323 M_\odot$  and  $M_2 = 0.335 M_\odot$  derived from photometric measurements (Burdge et al. 2020). The most relevant feature of ZTF J2243+5242 for the present analysis is that neither WD component is close to fill its Roche lobe, which allows a cleaner a simpler analysis of the binary dynamics.

We have shown that the dynamics of DWDs is largely affected by the UI for  $\tilde{B} = \sqrt{(1-\alpha)\eta}B$  in the range 10–100 MG. For large values of  $\eta = 10^2$ – $10^3$  (see Figure 1), the above implies that the binary dynamics might deviate from the pure GW-driven dynamics even for moderate values of the magnetic field strength  $B \gtrsim 10^6$  G. Those fields are detectable by Zeeman splitting and features of the spectral absorption lines at optical and UV wavelengths (see, e.g., Ferrario et al. 2015, for details). Magnetic fields near  $\sim 1000$  MG shift the spectral lines at wavelengths far off their zero-field locations and show *stationary* transitions (see, e.g., ZTF J1901+1458 in Caiazzo et al. 2021). In the case of SDSS J0651+2844, ZTF J1539+5027, and ZTF J2243+5242, strong magnetic fields in the luminous components are ruled out by the absence of Zeeman splittings in the cores of the Balmer absorption lines. However, as we have shown above, the UI might still be present and affect the orbital dynamics for high values of  $\eta$ , leading to a high effective magnetic field  $\tilde{B}$ . Therefore, the measurement of the magnetic field strength of a high-magnetic WD in a close DWD via measured Zeeman splitting would become a compelling target for follow-up timing to test the theoretical framework presented in this work.

G.A.C. thanks financial support from the Coordenação de Aperfeiçoamento de Pessoal de Nível Superior (CAPES) under the grants PDSE 88881.188302/2018–01 and PNPd 88887.368365/2019–00. J.G.C. is grateful for the support of CNPq (311758/2021–5) and FAPESP (2021/01089–1). The research of R.C.A. is supported by Conselho Nacional de Desenvolvimento Científico e Tecnológico (CNPq), grant number 310448/2021-2, and Serrapilheira Institute grant number Serra-1708–15022. She also thanks the support by L’Oreal Brazil, with the partnership of ABC and UNESCO, Brazil. J.G.C. and R.C.A. acknowledge financial support by “Fenômenos Extremos do Universo” of Fundação Araucária.

R.V.L. thanks financial support by the U.S. Department of Energy (DOE) under the grant DE-FG02-08ER41533, and Universidad de Los Andes, Colombia. M.M is grateful for the support of CAPES, CNPq and project INCT-FNA Proc. No. 464898/2014-5. J.F.R. thanks financial support from the Patrimonio Autónomo—Fondo Nacional de Financiamiento para la Ciencia, la Tecnología y la Innovación Francisco José de Caldas (MINCIENCIAS—COLOMBIA) under the grant No. 110685269447 RC-80740-465-2020, project 6955.

### ORCID iDs

G. A. Carvalho  <https://orcid.org/0000-0001-8718-6925>  
 J. G. Coelho  <https://orcid.org/0000-0001-9386-1042>  
 R. V. Lobato  <https://orcid.org/0000-0001-5755-5363>  
 M. Malheiro  <https://orcid.org/0000-0002-4915-8672>  
 R. Ruffini  <https://orcid.org/0000-0003-0829-8318>

### References

- Actis, M., Agnetta, G., Aharonian, F., et al. 2011, *ExA*, **32**, 193  
 Amaro-Seoane, P., Audley, H., Babak, S., et al. 2017, arXiv:1702.00786  
 Becerra, L., Rueda, J. A., Lorén-Aguilar, P., & García-Berro, E. 2018, *ApJ*, **857**, 134  
 Beloborodov, A. M. 2014, *MNRAS*, **438**, 169  
 Borges, S. V., Rodrigues, C. V., Coelho, J. G., Malheiro, M., & Castro, M. 2020, *ApJ*, **895**, 26  
 Bourgoin, A., Le Poncin-Lafitte, C., Mathis, S., & Angonin, M.-C. 2022, *PhRvD*, **105**, 124042  
 Brown, W. R., Kilic, M., Hermes, J. J., et al. 2011, *ApJL*, **737**, L23  
 Burdge, K. B., Coughlin, M. W., Fuller, J., et al. 2019, *Natur*, **571**, 528  
 Burdge, K. B., Coughlin, M. W., Fuller, J., et al. 2020, *ApJL*, **905**, L7  
 Cáceres, D. L., de Carvalho, S. M., Coelho, J. G., de Lima, R. C. R., & Rueda, J. A. 2017, *MNRAS*, **465**, 4434  
 Caiazzo, I., Burdge, K. B., Fuller, J., et al. 2021, *Natur*, **595**, 39  
 Carvalho, G. A., Marinho, R. M., & Malheiro, M. 2018, *GRGr*, **50**, 38  
 Carvalho, G. A. 2019, PhD thesis, São José dos Campos, Instituto Tecnológico de Aeronáutica  
 Coelho, J. G., Cáceres, D. L., de Lima, R. C. R., et al. 2017, *A&A*, **599**, A87  
 Coelho, J. G., & Malheiro, M. 2012, *IJMPS*, **18**, 96  
 Coelho, J. G., & Malheiro, M. 2014, *PASJ*, **66**, 14  
 Coelho, J. G., Marinho, R. M., Malheiro, M., et al. 2014, *ApJ*, **794**, 86  
 Dall’Osso, S., Israel, G. L., & Stella, L. 2006, *A&A*, **447**, 785  
 Damour, T., Nagar, A., & Bernuzzi, S. 2013, *PhRvD*, **87**, 084035  
 dos Anjos, R. C., Coelho, J. G., Pereira, J. P., & Catalani, F. 2021, *JCAP*, **2021**, 023  
 Eggleton, P. P. 1983, *ApJ*, **268**, 368  
 Ferrario, L., de Martino, D., & Gänsicke, B. T. 2015, *SSRv*, **191**, 111  
 Flanagan, É. É., & Hughes, S. A. 1998, *PhRvD*, **57**, 4535  
 Goldreich, P., & Lynden-Bell, D. 1969, *ApJ*, **156**, 59  
 Gómez, L. G., & Rueda, J. A. 2017, *PhRvD*, **96**, 063001  
 Hermes, J. J., Kilic, M., Brown, W. R., et al. 2012, *ApJL*, **757**, L21  
 Ji, S., Fisher, R. T., Garcia-Berro, E., et al. 2013, *ApJ*, **773**, 136  
 Kilic, M., Kosakowski, A., Moss, A. G., Bergeron, P., & Conly, A. A. 2021, *ApJL*, **923**, L6  
 Korol, V., Hallakoun, N., Toonen, S., & Kamesis, N. 2022, *MNRAS*, **511**, 5936  
 Lai, D. 2012, *ApJL*, **757**, L3  
 Lobato, R. V., Malheiro, M., & Coelho, J. G. 2016, *IJMPS*, **25**, 1641025  
 Maggiore, M. 2008, *Gravitational Waves: Volume 1: Theory and Experiments* (Oxford: Oxford Univ. Press)  
 Malheiro, M., Rueda, J. A., & Ruffini, R. 2012, *PASJ*, **64**, 56  
 Maoz, D., Badenes, C., & Bickerton, S. J. 2012, *ApJ*, **751**, 143  
 Marsh, T. R., & Nelemans, G. 2005, *MNRAS*, **363**, 581  
 Mukhopadhyay, B., & Rao, A. R. 2016, *JCAP*, **2016**, 007  
 Nelemans, G., Yungelson, L. R., Zwart, S. P., & Verbunt, F. 2001, *A&A*, **365**, 491  
 Nelemans, G., Napiwotzki, R., Karl, C., et al. 2005, *A&A*, **440**, 1087  
 Olinto, A. V., Adams, J. H., Aloisio, R., et al. 2017, *ICRC (Bexco, Busan)*, **35**, 542  
 Otoniel, E., Franzon, B., Carvalho, G. A., et al. 2019, *ApJ*, **879**, 46  
 Pani, P. 2015, *PhRvD*, **92**, 123530  
 Piro, A. L., & Kollmeier, J. A. 2016, *ApJ*, **826**, 97  
 Rueda, J. A., Boshkayev, K., Izzo, L., et al. 2013, *ApJL*, **772**, L24  
 Rueda, J. A., Ruffini, R., Wang, Y., et al. 2019, *JCAP*, **2019**, 044  
 Sousa, M. F., Coelho, J. G., & de Araujo, J. C. N. 2020a, *MNRAS*, **492**, 5949  
 Sousa, M. F., Coelho, J. G., & de Araujo, J. C. N. 2020b, *MNRAS*, **498**, 4426  
 Stroer, A., & Vecchio, A. 2006, *CQGra*, **23**, S809  
 Takahashi, R., & Seto, N. 2002, *ApJ*, **575**, 1030  
 The IceCube Collaboration 2011, arXiv:1111.2736  
 Venters, T. M., Reno, M. H., Krizmanic, J. F., et al. 2020, *PhRvD*, **102**, 123013  
 Wang, J.-S., Peng, F.-K., Wu, K., & Dai, Z.-G. 2018, *ApJ*, **868**, 19  
 Wu, K., Cropper, M., Ramsay, G., & Sekiguchi, K. 2002, *MNRAS*, **331**, 221  
 Xiao, D., Mészáros, P., Murase, K., & Dai, Z.-G. 2016, *ApJ*, **832**, 20



# On the X-Ray, Optical, and Radio Afterglows of the BdHN I GRB 180720B Generated by Synchrotron Emission

J. A. Rueda<sup>1,2,3,4,5</sup> , Liang Li<sup>1,2,6</sup> , R. Moradi<sup>1,2,6</sup> , R. Ruffini<sup>1,2,7,8</sup> , N. Sahakyan<sup>1,9</sup> , and Y. Wang<sup>1,2,6</sup>

<sup>1</sup>ICRANet, Piazza della Repubblica 10, I-65122 Pescara, Italy; [jorge.rueda@icra.it](mailto:jorge.rueda@icra.it), [liang.li@icranet.org](mailto:liang.li@icranet.org), [rahim.moradi@icranet.org](mailto:rahim.moradi@icranet.org), [ruffini@icra.it](mailto:ruffini@icra.it), [narek.sahakyan@icranet.org](mailto:narek.sahakyan@icranet.org), [yu.wang@icranet.org](mailto:yu.wang@icranet.org)

<sup>2</sup>ICRA, Dip. di Fisica, Sapienza Università di Roma, Piazzale Aldo Moro 5, I-00185 Roma, Italy

<sup>3</sup>ICRANet-Ferrara, Dip. di Fisica e Scienze della Terra, Università degli Studi di Ferrara, Via Saragat 1, I-44122 Ferrara, Italy

<sup>4</sup>Dip. di Fisica e Scienze della Terra, Università degli Studi di Ferrara, Via Saragat 1, I-44122 Ferrara, Italy

<sup>5</sup>INAF, Istituto di Astrofisica e Planetologia Spaziali, Via Fosso del Cavaliere 100, I-00133 Rome, Italy

<sup>6</sup>INAF, Osservatorio Astronomico d'Abruzzo, Via M. Maggini snc, I-64100, Teramo, Italy

<sup>7</sup>Université de Nice Sophia-Antipolis, Grand Château Parc Valrose, Nice, CEDEX 2, France

<sup>8</sup>INAF, Viale del Parco Mellini 84, I-00136 Rome, Italy

<sup>9</sup>ICRANet-Armenia, Marshall Baghramian Avenue 24a, Yerevan 0019, Republic of Armenia

Received 2022 April 1; revised 2022 September 9; accepted 2022 September 22; published 2022 November 3

## Abstract

Gamma-ray bursts (GRBs) are systems of unprecedented complexity across all the electromagnetic spectrum, including the radio, optical, X-rays, gamma rays in the MeV and GeV regimes, as well as ultrahigh-energy cosmic rays, each manifested in seven specific physical processes with widely different characteristic evolution timescales ranging from  $10^{-14}$  s to  $10^7$  s or longer. We here study the long GRB 180720B originating from a binary system composed of a massive carbon-oxygen (CO) star of about  $10M_{\odot}$  and a companion neutron star (NS). The gravitational collapse of the CO star gives rise to a spinning newborn NS ( $\nu$ NS), with an initial period of  $P_0 = 1$  ms that powers the synchrotron radiation in the radio, optical, and X-ray wavelengths. We here investigate solely the GRB 180720B afterglows and present a detailed treatment of its origin based on the synchrotron radiation released by the interaction of the  $\nu$ NS and the SN ejecta. We show that in parallel to the X-ray afterglow, the spinning  $\nu$ NS also powers the optical and radio afterglows and allows to infer the  $\nu$ NS and ejecta parameters that fit the observational data.

*Unified Astronomy Thesaurus concepts:* [Gamma-ray bursts \(629\)](#)

## 1. Introduction

GRB 180720B was observed in gamma rays by Fermi Gamma-ray Burst Monitor (GBM; Roberts & Meegan 2018), the CALorimetric Electron Telescope (CALET) GMB (Cherry et al. 2018), Swift Burst Alert Telescope (BAT; Siegel et al. 2018), Fermi Large Area Telescope (LAT; Bissaldi & Racusin 2018), and Konus-Wind (Frederiks et al. 2018). The High Energy Stereoscopic System (H.E.S.S.) observed the source in the sub-TeV energy domain (100–440 GeV; Abdalla et al. 2019). In the X-rays, the X-ray telescope (XRT) on board the Neil Gehrels Swift Observatory (for short, Swift) observed the source from 91 s after the Fermi GBM trigger (Siegel et al. 2018), Monitor of All-sky X-ray Image (MAXI) Gas Slit Camera (GSC) started at 296 s (Negoro et al. 2018), and NuStar from 243 to 318 ks (Bellm & Cenko 2018). The 1.5 m Kanata telescope observed the source in the optical and near-infrared as early as 78 s from the gamma-ray burst (GRB) trigger time (Sasada et al. 2018). Additional observations by optical, infrared, and radio telescopes can be found in Martone et al. (2018), Sasada et al. (2018), Itoh et al. (2018), Kann et al. (2018), Crouzet & Malesani (2018), Watson et al. (2018), Schmalz et al. (2018), Covino & Fugazza (2018), Lipunov et al. (2018), Jelinek et al. (2018), Zheng & Filippenko (2018), Sfaradi et al. (2018), Izzo et al. (2018), and Abdalla et al. (2019). The identification of the Fe II and Ni II lines in the optical observations by the Very Large Telescope (VLT) X-shooter

telescope led to the source cosmological redshift of  $z = 0.654$  (Vreeswijk et al. 2018). With the knowledge of the redshift, the GRB 180720B isotropic energy released is  $E_{\text{iso}} = 5.92 \times 10^{53}$  erg (Ruffini et al. 2018b; Fraija et al. 2019; Abdalla et al. 2019). For additional details on the GRB 180720B data, we refer the reader to Section 3.

Therefore, GRB 180720B is specially relevant to test GRB models given the statistical significance of the available multi-wavelength observational data. In this article, we analyze the source X-ray, optical, and radio afterglow emission. The description of the afterglow emission of GRB 180720B within the traditional jetted fireball model driven by the interaction of internal and external shocks with the surrounding and interstellar medium, we refer, e.g., to Abdalla et al. (2019), Fraija et al. (2019), Ronchi et al. (2020), and Rhodes et al. (2020). We here focus on the description of the GRB 180720B afterglow emission within the binary-driven hypernova (BdHN) model.

The BdHN scenario proposes that the GRB progenitor is a binary consisting of a carbon-oxygen (CO) star and a neutron star (NS) companion of  $\sim 2 M_{\odot}$ . The gravitational collapse of the CO star, unlike considerations of the collapsar scenario that purports the formation of a single black hole (BH) of  $\sim 5\text{--}10 M_{\odot}$  (Woosley 1993), creates in the supernova (SN) explosion a newborn NS ( $\nu$ NS) of  $\sim 1.5 M_{\odot}$ . For compact CO–NS binaries with orbital periods of the order of a few minutes, the accretion of the SN ejecta onto the companion NS leads to the formation of a BH (see, e.g., Fryer et al. 2014, 2015). These systems, called BdHN I, explain the long GRBs with energy release  $\gtrsim 10^{52}$  erg. For wider binaries, the accretion is not sufficient for the NS to reach the critical mass for gravitational collapse, so it remains

stable as a massive NS. These systems, called BdHN II, are characterized by energies  $\lesssim 10^{52}$  erg. In agreement with the above arguments, GRB 180720B has been classified as a BdHN I (see Moradi et al. 2021a, hereafter Paper I). We give further observational and theoretical details below and in Section 2.

The interaction of the SN ejecta with the  $\nu$ NS and the companion BH leads to complementary explosive episodes, which have been gradually identified in the last 20 years (Ruffini et al. 2021). In Section 2, we present a detailed description of the physical processes that occur in BdHN I and their related observables, based on the ongoing interplay between theoretical developments and numerical simulations to fit up-to-date observations. In addition to the X-rays, GeV and sub-TeV afterglows, the presence of the six episodes in GRB 180720B, marked by their specific spectra representing different underlying physical processes has been confirmed in Paper I (see Section 2 for additional details):

- I. Episode 1 (UPE I): the BH formation and its consequent ultrarelativistic emission (UPE) phase originated from the vacuum polarization with its characteristic Lorentz factor  $\Gamma \sim 100$  (Ruffini et al. 1999, 2000). This marks the first manifestation of the BH (BH rise). In GRB 180720B, the UPE I extends from  $t_{\text{rf}} = 4.84$  s to  $t_{\text{rf}} = 6.05$  s, its isotropic energy is  $E_{\text{UPE I}}^{\text{MeV}} = (6.37 \pm 0.48) \times 10^{52}$  erg, and its spectrum is best fitted by a CPL+BB model (index  $\alpha = -1.13$ , cutoff energy  $E_c = 2220.569$  keV, and blackbody (BB) temperature  $kT = 50.31$  keV in the observer's frame); see Figure 5(A) in Paper I.
- II. Episode 2 ( $\nu$ NS-rise): the accretion of ejecta onto the  $\nu$ NS leads to the  $\nu$ NS spin-up, which we describe in this article. The first appearance of this interaction in GRB 180720B, referred as the  $\nu$ NS-rise, extends from  $t_{\text{rf}} = 6.05$  s to  $t_{\text{rf}} = 9.07$  s, has an isotropic energy of  $E_{\nu\text{NS}}^{\text{MeV}} = (1.13 \pm 0.04) \times 10^{53}$  erg, and its spectrum is best fitted by a CPL model ( $\alpha = -0.98$ , and  $E_c = 737$  keV, in the observer's frame); see Figure 5(B) in Paper I.
- III. Episode 3 (UPE II): is marked by the observation of the first significant GeV photon at  $t_{\text{rf}} = 7.06$  s and includes as well the continuation of the UPE phase from  $t_{\text{rf}} = 9.07$  s to  $t_{\text{rf}} = 10.89$  s, with an isotropic energy of  $E_{\text{UPE II}}^{\text{MeV}} = (1.6 \pm 0.95) \times 10^{53}$  erg. The spectrum of the UPE II is best fitted by a CPL+BB model with model parameters of  $\alpha = -1.06_{-0.01}^{+0.01}$ ,  $E_c = 1502.5_{-87.5}^{+88.6}$  keV, and  $kT = 39.8_{-1.6}^{+1.6}$  keV; see Figure 5(C) in Paper I.
- IV. Episode 4 (Cavity): this radiation occurs in the cavity formed during the gravitational collapse of the NS and the consequent BH formation, which becomes further depleted by the UPE phase (Ruffini et al. 2019a). For GRB 180720B, it occurs from  $t_{\text{rf}} = 16.94$  s to  $t_{\text{rf}} = 19.96$  s, with an isotropic energy of  $E_{\text{C}}^{\text{MeV}} = (4.32 \pm 0.19) \times 10^{52}$  erg, characterized by a CPL spectrum ( $\alpha = -1.16$ ,  $E_c = 607.96$  keV). Its spectrum is given in Figure 5(D) in Paper I.
- V. Episode 5 (SXF), and VI) Episode 6 (HXF): the interaction of the UPE with the SN ejecta, which has a typical torus-like morphology with a cone of half-opening angle  $\sim 60^\circ$  from the normal to the orbital plane (Ruffini et al. 2021), creates the further emission of hard X-ray flares (HXFs) and soft X-ray flares (SXF; Ruffini et al. 2018c). The HXF of GRB 180720B occurs from  $t_{\text{rf}} = 28.95$  s to  $t_{\text{rf}} = 34.98$  s, with  $L_{\text{HXF,iso}}^{\text{MeV}} = (7.8 \pm 0.07) \times 10^{51}$  erg s $^{-1}$ , and is best fitted by a CPL model

with  $E_c = (5.5_{-0.7}^{+0.8}) \times 10^2$  keV,  $\alpha = -1.198 \pm 0.031$ ; see Figure 5(E) in Paper I. The SXF occurs from  $t_{\text{rf}} = 55$  s to  $t_{\text{rf}} = 75$  s, with  $L_{\text{SXF,iso}}^{\text{X}} = 1.45 \times 10^{50}$  erg, and is best fitted by a PL+BB spectrum with  $\alpha = -1.79 \pm 0.23$ , and  $kT = 0.99 \pm 0.13$  keV; see Figure 5(F) in Paper I.

In GRB 180720B, as indicated in Paper I, the emission processes originate from three independent energy sources, following the evolution of the progenitors composed of a CO $_{\text{core}}$  and a companion NS:

1. The SN. As all SNe, it generates a pulsar, which here is indicated by  $\nu$ NS.
2. The  $\nu$ NS. The first appearance of the  $\nu$ NS ( $\nu$ NS-rise) shows that it has been spun up by fallback accretion of SN ejecta and is then followed by the late X-ray afterglow with a power-law luminosity  $L_X \propto t^{-1.44 \pm 0.01}$ . From the energetics of the  $\nu$ NS-rise and the X-ray afterglow, we infer that the  $\nu$ NS period and magnetic field are  $P_{\nu\text{NS},0} = 1.01$  ms and  $B_{\text{dip}} = 4.2 \times 10^{13}$  G.
3. The BH. The appearance of the BH (BH rise), formed from the NS companion collapse by accretion of SN ejecta, is marked by the UPE phase followed by the observation of GeV, cavity, HXF, and SXF. From the MeV–GeV emission powered by the BH extractable energy, we infer the BH mass  $M = 2.4M_{\odot}$ , and spin parameter,  $\alpha = 0.55$  (see Paper I).

During the UPE phase of GRB 180720B, the *inner engine* of the GRB operates in an overcritical regime. The inner engine consists of a Kerr BH of mass  $M$  and angular momentum  $J$ , surrounded by a very-low-density plasma of ions and electrons with  $\rho \sim 10^{-14}$  g cm $^{-3}$  (Ruffini et al. 2019b) in the presence of a uniform magnetic field around the BH, amplified by the gravitational collapse (Rueda et al. 2020). Following the quantum vacuum polarization process in decreasing time bins, we have determined the timescale of the radiation ( $\tau \sim 10^{-9}$  s), the Lorentz factors ( $\Gamma \sim 30$ ), the radius of transparency ( $R^{\text{tr}} \sim 10^9$  cm), and energy ( $E \sim 10^{44}$  erg) of radiation pulses during the UPE phase. The detailed analysis of the UPE phase of GRB 180720B is presented in Rastegarnia et al. (2022). Figure 1 shows the light curve and spectra of different astrophysical processes underlying different episodes in GRB 180720B; for more details see Paper I.

In this article, we exclusively analyze the radio, optical, and X-ray afterglows of GRB 180720B. We extend the description of the GRB afterglow developed by Ruffini et al. (2018a) within the BdHN scenario. In this approach, the afterglow originates from the synchrotron radiation produced by the expansion of the SN ejecta in the presence of the  $\nu$ NS magnetic field. We here provide the theoretical formulation of the underlying synchrotron radiation and demonstrate that the spinning  $\nu$ NS, in addition to the X-ray afterglow, also originates from the optical and the radio afterglows.

In addition, we present the fundamental result that in GRB 180720B, Episode VI, namely, the luminosity of the optical SN bump is expected to be comparable to the optical synchrotron radiation. Unfortunately, there was no optical follow-up of GRB 180720B  $\sim 15$ – $20$  days after the trigger predicted in Ruffini et al. (2018b); see Figure 2.

The article is organized as follows. Section 2 summarizes the sequence of physical phenomena that occur in a BdHN and their related observables in GRB data. In Section 3, we represent the X-ray, optical, and radio afterglow data of GRB 180720B. In

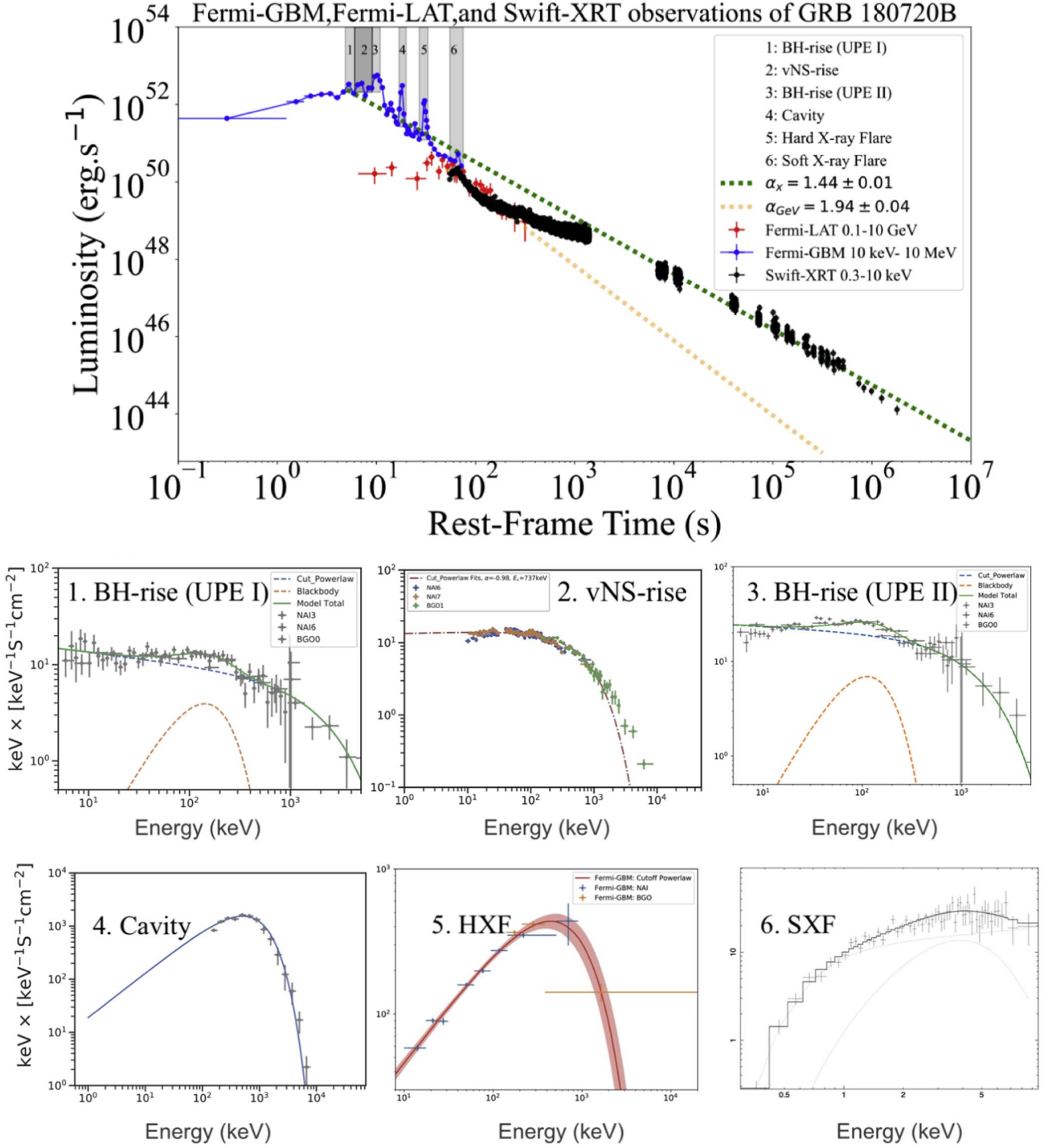


**Figure 1.** Luminosity light curve of GRB 180720B and spectra related to the different Episodes identified in GRB 180720B. The plots and best fits are reproduced from Paper 1 by the author's permission.

Section 4, we represent the formulation related to synchrotron and pulsar radiation of the  $\nu$ NS. In Section 5, we represent the concluding remarks.

## 2. Physical Processes and Observables of BdHNe

We summarize the sequence of physical phenomena in a BdHN, their related electromagnetic emission, and associated observed emission episodes in GRBs data. The BdHN event roots

in the induced gravitational collapse (IGC) scenario proposed in Rueda & Ruffini (2012). It starts with the core collapse of the CO star that leads to the  $\nu$ NS at its center, and the ejection of the outermost layers in form of SN explosion. The latter produces a hypercritical accretion process onto the NS companion (Fryer et al. 2014; Becerra et al. 2016), while fallback of the innermost layers accrete onto the  $\nu$ NS (Becerra et al. 2019).

**Precursors.** The hypercritical accretion onto both NSs can be observed as precursors to the prompt gamma-ray emission

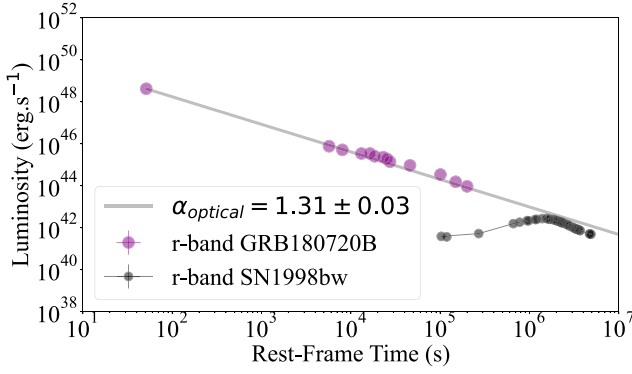


**Figure 2.** Optical luminosity of prototype SN 1998bw (gray) vs. optical (purple) afterglow of GRB 180720B. In this GRB, no optical data were observed  $\sim 16$ –24 days after the trigger as we predicted in Ruffini et al. (2018b). Most likely, the associated SN could have been detected if optical observations had been made at the time. The  $r$ -band optical data are retrieved from Abdalla et al. (2019). The optical luminosity of prototype SN 1998bw is plotted from reference (Iwamoto et al. 1998).

of BdHN I (see, e.g., GRB 090618 in Becerra et al. 2016; GRB 130427A in Wang et al. 2019; and also Becerra et al., submitted, for new numerical simulations), or in the prompt emission itself of BdHN II (see, e.g., GRB 180728A in Wang et al. 2019; and, very recently, GRB 190829A in Wang et al. 2022).

From now on, we specialize the discussion on BdHN I. The newborn Kerr BH is surrounded by the magnetic field inherited from the collapsed NS (see Rueda et al. 2020, for a discussion on the nature of the magnetic field in BdHN I) and by low-density ionized matter (Becerra et al. 2016; Ruffini et al. 2019a; Becerra et al. 2019). These three ingredients conform the so-called inner engine of the high-energy emission of the GRB (Ruffini et al. 2019b; Rueda & Ruffini 2020; Moradi et al. 2021b; Ruffini et al. 2021). The BH extractable energy powers both the ultrarelativistic prompt emission (UPE) phase and the GeV emission (see below).

The gravitomagnetic interaction of the Kerr BH of mass  $M$  and angular momentum  $J$ , with the external magnetic field of strength  $B$ , induce an electric field in the vicinity of the BH horizon,  $E \sim \Omega_H r_H B_0 / c = \alpha B_0 / 2$ , where  $\Omega_H = c \alpha / (2r_H)$  and  $r_H$  are the Kerr BH angular velocity and outer horizon, respectively. Here,  $\alpha = cJ / (GM^2)$  is the BH dimensionless spin parameter. The full mathematical expressions of the electromagnetic field outside the Kerr BH for a parallel, asymptotically uniform exterior magnetic field are given by the Papapetrou–Wald solution (Wald 1974). The above electric field is overcritical, i.e.,  $E > E_c = m_e^2 c^3 / (e\hbar)$ , for magnetic field strengths  $B \gtrsim 2E_c / \alpha$ . These values are attainable if the magnetic field is amplified in the process of gravitational collapse of the NS to a BH (see, e.g., discussion in Rueda et al. 2020).

**The UPE phase.** One of the most exciting recent developments is the explanation of the MeV radiation of the UPE phase of GRBs. The necessity of introducing new physics in the GRB prompt emission has arisen from the revealed hierarchical or self-similar structure observed in the UPE of GRB 190114C (Moradi et al. 2021c) and GRB 180720B (Rastegarnia et al. 2022). The quality of the data of the Fermi satellite and Swift has allowed to perform an in-depth time-resolved analysis of the GRB prompt emission. Such analysis has shown that the spectra of the UPE, on ever decreasing time intervals (of up to a fraction of a second), shows similar BB+CPL spectra. These self-similar BB+CPL

spectra on rebinned time intervals point to a microscopic phenomenon operating on shorter and shorter timescales. We are not aware of any explanation of the above UPE hierarchical structure from traditional models based on an ultrarelativistic jet. We have recently explained this phenomenon in the context of the inner engine of BdHN I, for GRB 190114C in Moradi et al. (2021c) and for GRB 180720B in Rastegarnia et al. (2022). The UPE phase is explained by the overcritical regime of the electric field that leads to the quantum electrodynamics (QED) process of vacuum polarization, i.e., the formation of an electron–positron ( $e^+e^-$ ) pair plasma. The  $e^+e^-$  plasma self-accelerates, loads baryons from the medium, and reaches transparency at large radii  $R_{tr}$  with Lorentz factor  $\Gamma$ . Ruffini et al. (1999) presented the first numerical simulations of the dynamics of the expansion and transparency of such optically thick electromagnetic–baryon plasma, which has been called the PEMB pulse. The dynamics of the plasma depends only on the initial conditions of energy and baryon load, which following the inner engine theory, depend only on the mass, angular momentum, and electric energy stored in the dyadregion, i.e., the region outside the BH where the electric field is overcritical. Therefore, the plasma dynamics is set by the inner engine parameters  $M$ ,  $J$ , and  $B_0$ . As the electric energy is induced by the gravitomagnetic interaction of the BH and the magnetic field, it is the BH extractable energy that ultimately powers the UPE. Therefore, in each process of expansion and transparency of a PEMB pulse, the Kerr BH loses a fraction of  $M$  and  $J$ . After the energy release of a PEMB pulse, the mass and angular momentum of the BH have decreased to  $M = M_0 - \Delta M$  and  $J = J_0 - \Delta J$ . For the UPE of GRB 190114C, we have estimated that the initial PEMB pulse has  $R_{tr} \sim 10^9$  cm,  $\Gamma \sim 10^2$ , and plasma energy  $\sim 10^{43}$  erg, leading to  $\Delta M/M \sim \Delta J/J \sim 10^{-9}$  (Moradi et al. 2021c). Related to the new lower value of  $J$ , it corresponds to a new lower value of the electric field,  $E = E_0(1 - \Delta J/J)$ . Therefore, the system restarts a new process characterized by new lower values of  $M$ ,  $J$ , and  $E$ , which lead to a lower  $e^+e^-$  plasma energy. The extremely short QED timescale of the vacuum polarization process,  $\sim \hbar / (m_e c^2) \approx 10^{-21}$  s, guarantees that the process can repeat over time until the electric field reaches the critical value. For GRB 180720B, the UPE phase driven by the above QED mechanism, ends at  $t_{tr} = 10.89$  s.

**The Cavity.** The SPH simulations of the SN explosion and the NS accretion show the region around the NS that collapses to a BH is characterized by a low density of the order of  $10^{-6}$  g cm $^{-3}$ . Numerical simulations show that the density inside this cavity is further depleted by the BH formation and the expansion of the  $e^+e^-$  plasma to values of the order of  $\sim 10^{-14}$ – $10^{-13}$  g cm $^{-3}$  (Ruffini et al. 2019a). The emission from the cavity walls, characterized by a CPL spectrum, has been there identified in the case of GRB 190114C. The cavity emission has been also identified in GRB 180720B (see Figure 1 and Table 1).

**The soft and hard X-Ray flares (SXF and HXF).** They originate from the breakout of the  $e^+e^-$  plasma from high-density regions of the ejecta around the BH. In those regions, the  $e^+e^-$  plasma loads more baryons than in the case of the low-density regions leading to the UPE phase. This leads the plasma to reach transparency with a lower Lorentz factor  $\lesssim 5$  (Ruffini et al. 2018d). The occurrence of this emission in several GRBs has been analyzed in light of the numerical simulations of the  $e^+e^-$  plasma expansion in the realistic SN ejecta obtained from the three-dimensional simulations, and it has been shown that the emission is viewed within at an intermediate angle, between the binary plane and the rotation axis (see, also, Ruffini et al. 2021).

**Table 1**  
Episodes and Afterglows of GRB 180720B

Event	Astrophysical Process	Duration(s)	Spectrum	$E_{\text{iso}}$ (erg)	References
I) BH rise (UPE I)	Vacuum polarization around BH	1.21	CPL+BB $\alpha = -1.13$ , $E_c = 2220.57$ keV $kT=50.31$ keV	$(6.37 \pm 0.48) \times 10^{52}$	Moradi et al. (2021c)
II) $\nu$ NS-rise	Synchrotron radiation powered by $\nu$ NS	3.01	CPL $\alpha = -0.98$ , $E_c = 737$ keV	$(1.13 \pm 0.04) \times 10^{53}$	Rueda et al. (2020)
III) BH rise (GeV radiation)	Synchrotron radiation powered by BH	600	CPL $\alpha = -2.0 \pm 0.1$	$(2.2 \pm 0.2) \times 10^{52}$	Ruffini et al. (2019b)
BH rise (UPE II)	Vacuum polarization around BH	1.82	CPL+BB $\alpha = -1.06$ , $E_c = 1502.5$ keV $kT=39.8$ keV	$(1.6 \pm 0.95) \times 10^{53}$	Moradi et al. (2021c)
IV) Cavity	Radiation from cavity's wall	3.02	CPL $\alpha = -1.16$ , $E_c = 607.96$ keV	$(4.32 \pm 0.19) \times 10^{52}$	Ruffini et al. (2019a)
V) HXF	Emission from outer SN layers	6.03	CPL $\alpha = -1.198 \pm 0.031$ $E_c = 550$ keV	$(3.93 \pm 0.33) \times 10^{52}$	Ruffini et al. (2018d)
VI) SXF	Emission from outer SN layers	15.12	CPL+BB $\alpha = -1.79 \pm 0.23$ $kT = 0.99 \pm 0.13$ keV	$(2.89 \pm 0.42) \times 10^{52}$	Ruffini et al. (2018c)
VII) Optical SN	Nickel decay	expected to be $\sim 10^6$	PL	expected to be $\sim 10^{49}$	Not observed for GRB 180720B
X-ray Afterglow	Synchrotron radiation powered by $\nu$ NS	$\sim 10^7$	PL	$(2.61 \pm 1.0) \times 10^{52}$	Rueda et al. (2020)
Optical Afterglow	Synchrotron radiation powered by $\nu$ NS	$\sim 3 \times 10^5$	PL	$(6.10 \pm 1.0) \times 10^{50}$	Abdalla et al. (2019) This work
sub-TeV emission	Unknown	$\sim 3 \times 10^3$	PL	$(2.40 \pm 1.8) \times 10^{50}$	Abdalla et al. (2019)
Radio Afterglow	Synchrotron radiation powered by $\nu$ NS	$\sim 2 \times 10^6$	PL	$(2.21 \pm 0.24) \times 10^{46}$	Rhodes et al. (2020) This work

**Note.** This table reports the name, the underlying astrophysical process, the duration (s), the best-fit spectrum, the isotropic energy (erg), and the reference for each event in GRB 180720B.

**The GeV emission.** The induced electric field accelerates to ultrarelativistic energies electrons surrounding the BH. Along the BH rotation axis, the electric and magnetic field are parallel, and the electrons accelerate without energy losses. Under these conditions, the electrons reach energies of up to  $10^{18}$  eV and protons of up to  $10^{21}$  eV (Rueda & Ruffini 2020), leading to ultrahigh-energy cosmic rays (UHECRs). Outside the polar axis, the synchrotron radiation of the accelerated electrons peaks at GeV energies, explaining the observed GeV radiation of GRBs (Ruffini et al. 2019b; Rueda & Ruffini 2020; Moradi et al. 2021b; Rueda et al. 2022a). The theoretical framework of the inner engine based on the above description has been applied to the explanation of the GeV emission of GRBs. The case of GRB 130427A has been analyzed in Ruffini et al. (2019b), and GRB 190114C and the extension of the theoretical framework to active galactic nuclei (AGNs) like M87\* in Rueda & Ruffini (2020) and

Moradi et al. (2021b). A rigorous general relativistic treatment of the inner engine and the emission produced by charged particles accelerated by the induced electric field can be found in Rueda et al. (2022a). The theoretical model predicts that the above emission process occurs within  $60^\circ$  degrees from the BH rotation axis, which agrees with the lack of observed GeV emission in a fraction of BdHN I (see Ruffini et al. 2021, for details).

**The multiwavelength afterglow.** This is the main topic of this article. In the BdHN model, the afterglow originates from synchrotron radiation in the SN ejecta, powered by the  $\nu$ NS and not from ultrarelativistic blastwaves, as shown in Ruffini et al. (2018a), Wang et al. (2019), and Rueda et al. (2020). These works have carried out the numerical integration of the electron kinetic equation taking into account the expansion of the SN from numerical simulations, the radial dependence of the magnetic field expected from pulsar theory, and the power of the  $\nu$ NS as a pulsar.



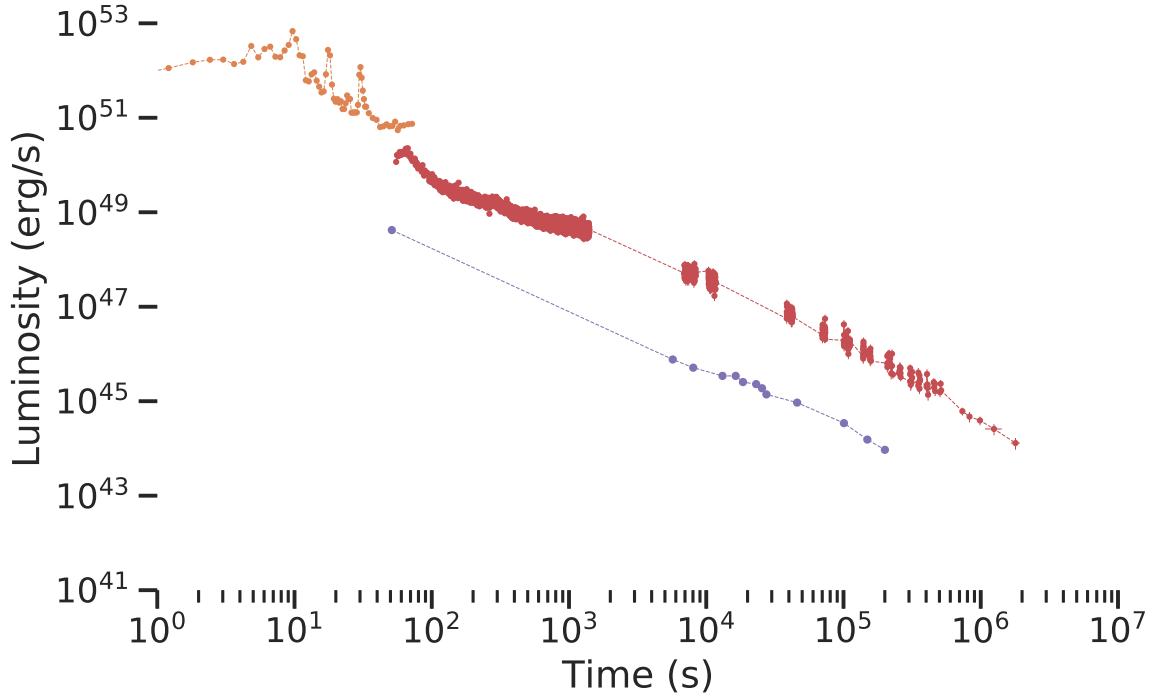


**Figure 3.** Luminosity light curve of GRB 180720B including the observations in gamma rays from Fermi GBM (yellow), soft X-rays from Swift XRT (red), radio data from AMI-LA (brown diamonds; retrieved from Rhodes et al. 2020), and  $r$ -band optical data (purple circles; retrieved from Abdalla et al. 2019).

More recently, we have presented analytic solutions of the above treatment that are consistent with our previous numerical calculations. Wang et al. (2022) has presented the analytic treatment of the X-ray, radio, and optical afterglow emission of GRB 190829A. The consistency of this theoretical treatment with the multi-wavelength afterglow data is here extended to the case of GRB 180720B.

**The optical SN.** We finish the general description of BdHNe with the emission of the SN in the optical wavelengths. This emission is powered by the energy release of nickel decay (into cobalt) in the ejecta. The SN associated with GRBs are similar with each other, roughly independent of the wide GRB energetics (see, e.g., Cano et al. 2017 and Aimuratov et al., to be submitted). This indicates that the pre-SN progenitor (i.e., the CO star) leading to the core-collapse SN event triggering the GRB, is similar in all GRBs. This is a relevant information for the formation channel of the CO–NS binaries leading to GRBs (see, e.g., Fryer et al. 2015).

### 3. Data of GRB 180720B

On 20 July 2018, GRB 180720B triggered Fermi GBM at 14:21:39.65 UT (Roberts & Meegan 2018), Swift BAT at 14:21:44 UT (Siegel et al. 2018), and Fermi LAT at 14:21:44.55 UT (Bissaldi & Racusin 2018). Swift XRT began to observe 91 s after the Fermi GBM trigger (Siegel et al. 2018). These gamma-ray and X-ray data are retrieved and analyzed by Fermi GBM Data Tools (Goldstein et al. 2021) and HEASoft<sup>10</sup>, respectively. The corresponding gamma-ray and X-ray luminosity light curves are shown in Figure 3. This GRB also triggered several optical telescopes. The optical light curve of the  $r$  band in Figure 3 is reproduced from Abdalla et al. (2019), which gathers the observations from Kanata (Sasada et al. 2018), Multicolor Imaging

Telescopes for Survey and Monstrous Explosions (Itoh et al. 2018), Tien Shan Astronomical Observatory (Reva et al. 2018), Mobile Astronomical System of Telescope-Robots (Lipunov et al. 2018), International Scientific Optical Network-Castelgrande (Schmalz et al. 2018), Observatorio de Sierra Nevada (Kann et al. 2018), Las Cumbres Observatory (Martone et al. 2018), and Katzman Automatic Imaging Telescope (KAIT; Zheng & Filippenko 2018).

KAIT provides the latest observation at 3.874 days after the trigger. This time is much before than the time expected for the SN optical bump, based on the previous SNe statistics (Cano et al. 2017). Considering the burst occurs at a distance of  $z = 0.654$ , Ruffini et al. (2018b) predicted that the SN optical flux should have peaked at  $21.8 \pm 4.3$  days after the trigger, i.e., on 2018 August 11, with the uncertainty from 2018 August 7 to 15. In Figure 2, we plot the optical luminosity of SN 1998bw and the observed optical afterglow of GRB 180720B. The peak luminosities of other SNe associated with GRBs vary about 0.5–3 times (Cano et al. 2017). The figure shows that the expected optical flux of the SN is not much lower than the optical flux of the synchrotron radiation. Therefore, the SN signal could have been observed if the source were monitored at the optical wavelengths at  $21.8 \pm 4.3$  days, as suggested in Ruffini et al. (2018b). Regrettably, we have to conclude that the missing of SN optical signal is due to the missed prolonged optical follow-up of GRB 180720B (see Figure 2), which has been a big missing opportunity for a further observational verification of a theoretical prediction of the BdHN model.

The GRB 180720B triggered also radio emission observed by the Arcminute Microkelvin Imager Large Array (AMI-LA; Staley et al. 2012; Anderson et al. 2017). The observed flux, which comprises over 5 logarithmically spaced data points, was retrieved from Rhodes et al. (2020).

The broad-band luminosity light curve of GRB 180720B is presented in Figure 3.

<sup>10</sup> <https://heasarc.gsfc.nasa.gov/lheasoft/>

#### 4. Synchrotron and Pulsar Radiation of the $\nu$ NS

We here follow and extend the treatment of the GRB afterglow by Ruffini et al. (2018a) within the BdHN scenario. In this picture, the afterglow originates from the synchrotron radiation produced by the expansion of the SN ejecta in the presence of the magnetic field of the  $\nu$ NS. We now estimate the emission generated by the synchrotron mechanism in the X-rays, in the optical, and in the radio, together with the pulsar emission of the  $\nu$ NS.

##### 4.1. Synchrotron Emission by the Expanding Ejecta

The evolution of the distribution of radiating electrons per unit energy,  $N(E, t)$ , is determined by the kinetic equation (see, e.g., Kardashev 1962; Rybicki & Lightman 1979)

$$\frac{\partial N(E, t)}{\partial t} = -\frac{\partial}{\partial E}[\dot{E} N(E, t)] + Q(E, t), \quad (1)$$

where  $Q(E, t)$  is the number of injected electrons into the ejecta per unit time  $t$ , per unit energy  $E$ , and  $\dot{E}$  is the electron energy loss rate.

In the present model, the electrons are subjected to adiabatic losses due to the ejecta expansion and synchrotron radiation losses because of the presence of the  $\nu$ NS magnetic field. The electrons lose their energy efficiently by synchrotron radiation, so we can assume a one-zone model adopting that the emission originates from the innermost layer of the ejecta, which we denote as  $r = R_*$ . We assume that the ejecta expand at constant velocity  $v_{*,0}$ , so the radius evolves as

$$R_*(t) = R_{*,0} \hat{t}, \quad (2)$$

where  $\hat{t} \equiv t/t_*$ , and  $t_* \equiv R_{*,0}/v_{*,0}$ .

Having specified the pace at which the ejecta expand, we can write the energy balance equation governing the evolution of the electron's energy (see, e.g., Kardashev 1962)

$$-\dot{E} = \frac{E}{t} + P_{\text{syn}}(E, t), \quad (3)$$

where the first term on the right-hand side accounts for expansion and adiabatic losses, and the second term is given by the bolometric synchrotron radiation power (see, e.g., Longair 2011)

$$P_{\text{syn}}(E, t) = \beta B_*^2(t) E^2, \quad (4)$$

where  $\beta = 2e^4/(3m_e^4 c^7)$ , and  $B_*(t)$  is the magnetic field the electrons are subjected to. From the traditional pulsar theory, we expect that, beyond the light cylinder,  $r = c/\Omega$ , where  $\Omega$  is the rotation angular velocity of the  $\nu$ NS, the magnetic field of the  $\nu$ NS decreases linearly with distance (see, e.g., Ostriker & Gunn 1969; Goldreich & Julian 1969). Therefore, we adopt that the magnetic field strength at the ejecta position varies with time as

$$B_*(t) = B_{*,0} \frac{R_{*,0}}{R_*} = \frac{B_{*,0}}{\hat{t}}, \quad (5)$$

where  $B_i^{(0)}$  is the magnetic field strength at  $r = R_{*,0}$ , and we have used Equation (2).

For completing the specification of Equation (1), we need to introduce the distribution of the injected electrons. We assume a power-law distribution (see, e.g., Kardashev 1962; Pacini & Salvati 1973; Rybicki & Lightman 1979;

Longair 2011)

$$Q(E, t) = Q_0(t) E^{-\gamma}, \quad 0 \leq E \leq E_{\text{max}}, \quad (6)$$

where  $\gamma$  and  $E_{\text{max}}$  are parameters to be determined from the observational data, and  $Q_0(t)$  can be related to the power released by the  $\nu$ NS and injected into the ejecta. We adopt an injected power of the form

$$L_{\text{inj}}(t) = L_0 \left(1 + \frac{t}{t_q}\right)^{-k}, \quad (7)$$

where  $L_0$ ,  $t_q$ , and  $k$  are model parameters to be obtained from the fit of the observational data. Therefore, the function  $Q_0(t)$  can be found from

$$L_{\text{inj}}(t) = \int_0^{E_{\text{max}}} E Q(E, t) dE = Q_0(t) \frac{E_{\text{max}}^{2-\gamma}}{2-\gamma}, \quad (8)$$

which using Equation (7) leads to

$$Q_0(t) = q_0 \left(1 + \frac{t}{t_q}\right)^{-k}, \quad (9)$$

where  $q_0 \equiv (2-\gamma)L_0/E_{\text{max}}^{2-\gamma}$ .

Having specified the evolution of the ejecta by Equation (2) and the magnetic field by Equation (5), as well as the rate of particle injection given by Equations (6) and (9), we can now proceed to the integration of the kinetic Equation (1).

First, we find the evolution of a generic electron injected at time  $t = t_i$  with energy  $E_i$ . Equation (3) can be integrated analytically leading to the energy evolution (Rueda et al. 2022b; Rueda 2022)

$$E = \frac{E_i(t_i/t)}{1 + \mathcal{M} E_i t_i \left(\frac{1}{\hat{t}_i^2} - \frac{1}{\hat{t}^2}\right)}, \quad (10)$$

where  $\mathcal{M} \equiv \beta B_{*,0}^2/2$ .

The solution of Equation (1) can be written as (see, e.g., Pacini & Salvati 1973)

$$N(E, t) = \int_E^\infty Q[E_i, t_i(t, E_i, E)] \frac{\partial t_i}{\partial E} dE_i, \quad (11)$$

where  $t_i(t, E_i, E)$  is obtained from Equation (10).

We can write  $N(E, t)$  as a piecewise function of time depending upon the behavior of the energy injection (9). All the observational data of GRB 190114C is contained in the regime where synchrotron losses are dominant. In this case, the solution of Equation (11) is well approximated by Rueda (2022)

$$N(E, t) \approx \begin{cases} \frac{q_0}{\beta B_{*,0}^2(\gamma-1)} \hat{t}^2 E^{-(\gamma+1)}, & t < t_q \\ \frac{q_0(t_q/t_*)^k}{\beta B_{*,0}^2(\gamma-1)} \hat{t}^{2-k} E^{-(\gamma+1)}, & t_q < t < t_b, \end{cases} \quad (12)$$

where  $E_b < E < E_{\text{max}}$ , being

$$E_b = \frac{\hat{t}}{\mathcal{M} t_*}, \quad t_b = t_*^2 \mathcal{M} E_{\text{max}}. \quad (13)$$

The electrons emit most of the synchrotron radiation at frequencies close to the critical frequency  $\nu_{\text{crit}} = \alpha B_* E^2$ , where  $\alpha = 3e/(4\pi m_e^3 c^5)$ . Therefore, we can assume  $\nu \approx \nu_{\text{crit}}$ , so the bolometric synchrotron power from Equation (4) can be written

approximately in terms of the radiation frequency as

$$P_{\text{syn}}(E, t) \approx P_{\text{syn}}(\nu, t) = \frac{\beta}{\alpha} B_* \nu, \quad (14)$$

and the spectral density, i.e., energy per unit time, per unit frequency, as (see, e.g., Longair 2011)

$$\begin{aligned} J_{\text{syn}}(\nu, t) &\approx P_{\text{syn}}(\nu, t) N(E, t) \frac{dE}{d\nu} \\ &= \frac{\beta}{2} \frac{\eta}{\alpha^{\frac{p-3}{2}}} B_{*,0}^{\frac{p+1}{2}} \hat{t}^{\frac{2l-p-1}{2}} \nu^{\frac{3-p}{2}}. \end{aligned} \quad (15)$$

where we have used  $N(E, t) = \eta \hat{t}^l E^{-p}$ , where  $\eta$ ,  $l$ , and  $p$  are known constants from Equation (12).

The synchrotron luminosity radiated in the frequencies  $[\nu_1, \nu_2]$  can be then obtained as

$$L_{\text{syn}}(\nu_1, \nu_2; t) = \int_{\nu_1}^{\nu_2} J_{\text{syn}}(\nu, t) d\nu \approx \nu J_{\text{syn}}(\nu, t), \quad (16)$$

where  $\nu_1 = \nu$ ,  $\nu_2 = \nu + \Delta\nu$ , with  $\Delta\nu$  denoting the bandwidth. Because  $J_{\text{syn}}$  shows a power-law behavior in frequency (see Equation (15)), we have used in the second equality of Equation (16) the approximation  $\Delta\nu/\nu \ll 1$ . By substituting Equation (15) into Equation (17), we obtain that, at the frequency  $\nu$ , the synchrotron luminosity is given by

$$L_{\text{syn}}(\nu, t) = \frac{\beta}{2} \alpha^{\frac{p-3}{2}} \eta B_{*,0}^{\frac{p+1}{2}} \hat{t}^{\frac{2l-p-1}{2}} \nu^{\frac{3-p}{2}}. \quad (17)$$

Equation (17) implies that the synchrotron radiation follows a power-law behavior both in time and radiation frequency,  $L_{\text{syn}} \propto t^{\frac{2l-p-1}{2}} \nu^{\frac{3-p}{2}}$ , where  $p = \gamma + 1$  and the value of  $l$  depend on whether we are in the phase of constant injection or power-law injection (see Equation (12)). Therefore, the synchrotron radiation leads to a *rainbow* luminosity, characterized by the same power-law index in the X-ray, optical, and radio wavelengths (see Figure 4). This occurs when the system remains over time in the same physical regime, namely, when the observational data are contained within times  $t < t_b$ , and the electron energies are in the range  $E_b < E < E_{\text{max}}$ ; see Equation (13). Otherwise, the power-law behavior changes when the system makes a transition to a regime of dominance of adiabatic over synchrotron losses. In the present case, we did not find evidence in the GRB afterglow data of the occurrence of the transition to such a physical regime. This implies that the ratio of the luminosity at different frequencies depends only on the power-law index of the injection rate as (Rueda 2022)

$$\frac{L_{\text{syn}}(\nu_1)}{L_{\text{syn}}(\nu_2)} = \left( \frac{\nu_1}{\nu_2} \right)^{\frac{3-p}{2}} = \left( \frac{\nu_1}{\nu_2} \right)^{\frac{2-\gamma}{2}}. \quad (18)$$

Therefore, we can set the value of  $\gamma$  by fitting the observed X-rays to optical luminosity ratio. Once we have fixed  $\gamma$ , the optical (or X-rays) to radio luminosity ratio is also set. Figure 4 shows that the obtained synchrotron luminosity at radio wavelengths also agrees with the observational data. This result implies that the model leads to the correct observed spectrum of the afterglow emission in a wide range of energies from the radio to the X-rays, which strongly supports the present scenario.

#### 4.2. Newborn NS Evolution and Pulsar Emission

At some point in the time evolution, when the synchrotron luminosity has fallen sufficiently, the pulsar emission of the  $\nu$ NS becomes observable. We calculate this emission by adopting a dipole+quadrupole magnetic field model following Pétri (2015). In this model, the total pulsar (spin-down) luminosity is given by

$$\begin{aligned} L_{\text{sd}} &= L_{\text{dip}} + L_{\text{quad}} \\ &= \frac{2}{3c^3} \Omega^4 B_{\text{dip}}^2 R^6 \left( 1 + \xi^2 \frac{16}{45} \frac{R^2 \Omega^2}{c^2} \right), \end{aligned} \quad (19)$$

with  $R$  the  $\nu$ NS radius, and  $\xi$  defines the quadrupole to dipole strength ratio

$$\xi \equiv \sqrt{\cos^2 \chi_2 + 10 \sin^2 \chi_2} \frac{B_{\text{quad}}}{B_{\text{dip}}}, \quad (20)$$

where the angles  $\chi_1$  and  $\chi_2$  define the quadrupole field geometry, and we have assumed the dipole field in the  $m = 1$  mode, i.e., inclined  $90^\circ$  with respect to the stellar rotation axis. The quadrupole field span between the  $m = 0$  and  $m = 1$  modes for values of the angles in the range  $0^\circ - 90^\circ$  (see Pétri 2015, for further details).

The evolution of the  $\nu$ NS is calculated from by integrating the energy balance equation

$$-(\dot{W} + \dot{T}) = L_{\text{tot}} = L_{\text{inj}} + L_{\text{sd}}, \quad (21)$$

where  $W$  and  $T$  are the  $\nu$ NS gravitational and rotational energy, respectively.

Table 2 lists the values of the model parameters that fit the afterglow of GRB 180720B in the X-ray, optical, and radio energy bands. Figure 4 shows that the observed afterglow luminosity that fades with time with the same power-law behavior in the X-rays, optical, and radio is explained by the synchrotron emission. The synchrotron luminosity in the X-rays decays exponentially after a few  $10^2$  s, while it keeps its power-law behavior at lower energies. This occurs because around this time the critical synchrotron radiation energy ( $h\nu_{\text{crit}}$ ) falls below the keV range. After this time, the pulsar emission from the  $\nu$ NS dominates the X-ray emission. The pulsar emission is characterized by a plateau followed by a power-law decay (at times longer than the characteristic spin-down timescale). However, in the afterglow there is also the additional power-law contribution from the synchrotron emission. When the plateau phase of the pulsar emission is comparable (but smaller) to the synchrotron power-law luminosity, the sum of the two contributions can lead to a power-law luminosity shallower than the power law of the pure synchrotron radiation. In GRB 180720B, the X-ray afterglow shows two different power laws, the first at times  $10^2 - 10^3$  s and the second at times  $> 10^4$  s (there is a hole in the data at  $10^3 - 10^4$  s). In the time interval  $10^2 - 10^3$  s, the X-ray luminosity shows a shallower power law than the pure synchrotron luminosity, as it can be seen by comparing it with the power law of the optical and radio synchrotron at times  $> 10^4$  s. Such a shallower power-law luminosity indicates the presence of the  $\nu$ NS magnetic-braking radiation, and indeed it is well fitted by the sum of the synchrotron and the plateau of the newborn NS pulsar emission (see Figure 4).

The subsequent dominant role of the pulsar emission in the observed X-ray emission has allowed us to infer the strength of the dipole and the quadrupole components of the magnetic field, as well as the rotation period of the  $\nu$ NS. Therefore, in the BdHN model the afterglow is characterized by a typical

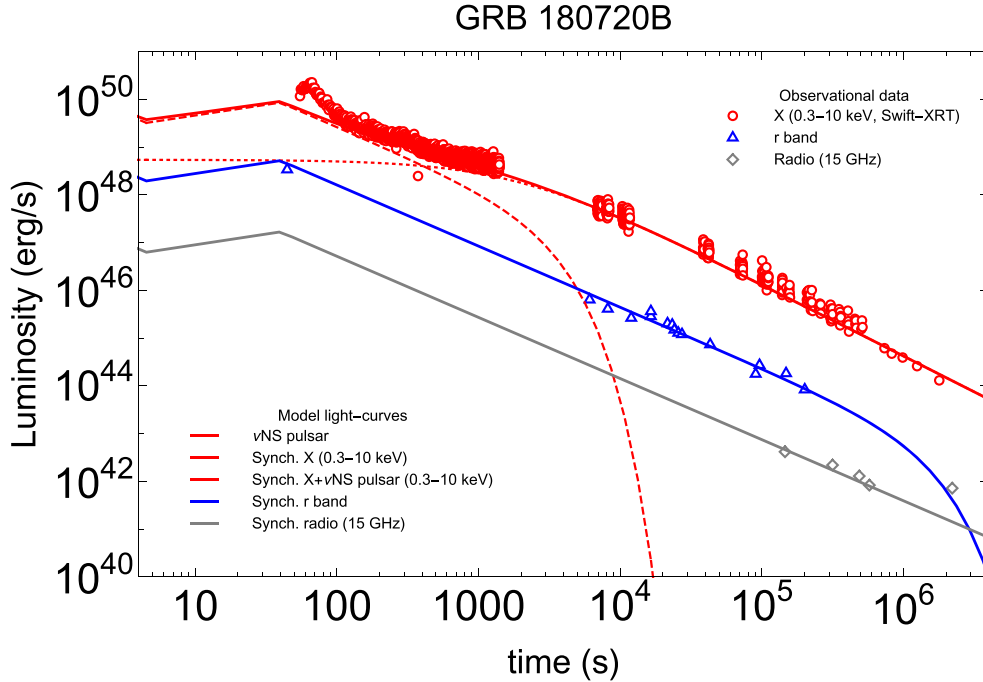


**Figure 4.** Luminosity of GRB 180720B in the X-ray (0.3–10 keV), optical ( $r$  band), and radio (5.0 and 9.0 GHz) energy bands. The X-ray data are produced by the methods developed by the Swift XRT team to produce the light curves (Evans et al. 2009). The radio data from AMI-LA are retrieved from Rhodes et al. (2020), and the  $r$ -band optical data are retrieved from Abdalla et al. (2019).

**Table 2**

Numerical Values of the Theoretical Model of Synchrotron Radiation that Fit the Multiwavelength Observational data of GRB 180720B as Shown in Figure 4

Parameter	Value
$\gamma$	1.34
$k$	1.73
$L_0$ ( $10^{50}$ erg $s^{-1}$ )	5.50
$E_{\max}$ ( $10^4 m_e c^2$ )	1.00
$t_q$ (s)	40.00
$R_{*,0}$ ( $10^{10}$ cm)	1.99
$v_{*,0}$ ( $10^9$ cm $s^{-1}$ )	1.00
$B_{*,0}$ ( $10^6$ G)	2.51
$\xi$	200.00
$B_{\text{dip}}$ ( $10^{13}$ G)	1.50
$P$ (ms)	1.00

power-law luminosity in the X-ray, optical, and radio wavelengths, given by the synchrotron radiation emitted by the expanding SN ejecta in the magnetized medium of the  $\nu$ NS, together with the pulsar-like emission of the latter.

The radio emission shows an excess over the synchrotron emission at a few  $10^6$  s whose nature is unclear. This excess could be a signature of the SN or the emergence of the  $\nu$ NS pulsar in the radio wavelengths, but further observational data at longer times and additional theoretical modeling are needed to confirm or disregard any of these possibilities.

## 5. Conclusions

We have pointed out the essential role of the gravitational collapse of the CO star of about  $10M_{\odot}$  in the presence of a companion NS leading to a variety of independent processes: 1) the SN originated from the CO<sub>core</sub> collapse, 2) the ejecta accreting on the  $\nu$ NS spins it up to milliseconds and generates

the radio, optical, and X-ray afterglows, 3) the ejecta accreting onto the companion NS, leading to the BH formation that generates the UPE phase and GeV emission.

We have here addressed the afterglows driving the three different components of the X-ray, radio, and optical emissions. We have shown that the synchrotron emission generated by accelerated electrons in the expanding SN ejecta, powered by the  $\nu$ NS injected energy, explain the observed power-law emission in the X-ray, optical, and radio wavelengths. In our interpretation, the synchrotron power-law luminosity in the X-rays ends about  $\sim 10^2$  s due to the transition of the synchrotron critical frequency to values below the X-ray range. At  $10^2$ – $10^3$  s, the X-ray luminosity shows a shallower decay that resembles a plateau, which we have interpreted as the emergence of the  $\nu$ NS pulsar emission. The fit of such a behavior of the X-ray luminosity and its subsequent power-law emission with the pulsar emission has allowed us to infer the  $\nu$ NS initial spin (1 ms), and the dipole and quadrupole magnetic field strengths, respectively,  $B_{\text{dip}} = 1.5 \times 10^{13}$  G and  $B_{\text{quad}} = 200B_{\text{dip}}$  (see Table 2 for the values of all the model parameters).

The synchrotron radiation in the optical wavelengths overcomes most of the optical SN except for the SN peak that could have been barely observed. However, no observational data of GRB 180720B were acquired at the needed time of  $\sim 20$  day after the trigger, where we predicted the occurrence of the SN peak time (Ruffini et al. 2018b). The associated SN could have been detected if observations at optical wavelengths had been taken at those times.






From the analysis presented in Paper I, the most general BdHN I, GRB 180720B, comprises seven independent episodes characterized by specific spectral signatures and energetics. They originate from the gravitational collapse of a CO star in the presence of a binary NS companion. Their successful analysis has clarified the occurrence of the most energetic and possibly one of the most

complex systems in the universe. Some episodes have been observed in selected BdHNe I, e.g., in GRB 190114C (Ruffini et al. 2021) and GRB 130427A (Ruffini et al. 2019b). It is the first time that six of these episodes have been observed in a single source. This has been made possible by the statistically significant data available and the special inclination of the viewing angle with respect to the equatorial plane of the binary system in GRB 180720B. The latter made possible the observation of the HXF and the SXF. Only the seventh episode, the final observation of the optical SN due to the nickel decay, with a predicted peak bolometric optical luminosity of  $L_{p,avg} = (8.9 \pm 3.8) \times 10^{42} \text{ erg s}^{-1}$  and rest-frame peak time of  $t_{p,avg} = (1.2 \pm 0.24) \times 10^6 \text{ s}$ , was observationally missed.

In summary, the interaction of the SN ejecta with the  $\nu$ NS originated the emission of  $(1.39 \pm 0.05) \times 10^{53} \text{ erg}$ , revealed in the  $\nu$ NS-rise, and different afterglows in the X-ray, optical, radio, and sub-TeV emission. Likewise, an emission of  $(1.7 \pm 1.0) \times 10^{53} \text{ erg}$  originates from the accretion of the SN ejecta onto the companion fast-spinning magnetized NS, creates the two events of ultrarelativistic jetted emissions (UPE I and UPE II), and the jetted GeV emission; see details in Table 1.

Therefore, BdHNe I are characterized by seven episodes and four long-lasting emissions in the radio, optical, X-ray, and GeV bands. The total energy originating into the gravitational collapse of the  $\text{CO}_{\text{core}}$  in GRB 180720B is therefore  $(8.0 \pm 1.0) \times 10^{53} \text{ erg}$ , which classifies this source as a Giganova.

### ORCID iDs

J. A. Rueda  <https://orcid.org/0000-0003-4904-0014>  
 Liang Li  <https://orcid.org/0000-0002-1343-3089>  
 R. Moradi  <https://orcid.org/0000-0002-2516-5894>  
 R. Ruffini  <https://orcid.org/0000-0003-0829-8318>  
 N. Sahakyan  <https://orcid.org/0000-0003-2011-2731>

### References

Abdalla, H., Adam, R., Aharonian, F., et al. 2019, *Natur*, **575**, 464  
 Anderson, G. E., Staley, T. D., van der Horst, A. J., et al. 2017, *MNRAS*, **473**, 1512  
 Becerra, L., Bianco, C. L., Fryer, C. L., Rueda, J. A., & Ruffini, R. 2016, *ApJ*, **833**, 107  
 Becerra, L., Ellinger, C. L., Fryer, C. L., Rueda, J. A., & Ruffini, R. 2019, *ApJ*, **871**, 14  
 Bellm, E. C., & Cenko, S. B. 2018, GCN, **23041**, 1  
 Bissaldi, E., & Racusin, J. L. 2018, GCN, **22980**, 1  
 Cano, Z., Wang, S.-Q., Dai, Z.-G., & Wu, X.-F. 2017, *AdAst*, **2017**, 8929054  
 Cherry, M. L., Yoshida, A., Sakamoto, T., et al. 2018, GCN, **23042**, 1  
 Covino, S., & Fugazza, D. 2018, GCN, **23021**, 1  
 Crouzet, N., & Malesani, D. B. 2018, GCN, **22988**, 1  
 Evans, P. A., Beardmore, A. P., Page, K. L., et al. 2009, *MNRAS*, **397**, 1177  
 Fraija, N., Dichiara, S., Pedreira, A. C. C. d. E. S., et al. 2019, *ApJ*, **885**, 29

Frederiks, D., Golenetskii, S., Aptekar, R., et al. 2018, GCN, **23011**, 1  
 Fryer, C. L., Oliveira, F. G., Rueda, J. A., & Ruffini, R. 2015, *PhRvL*, **115**, 231102  
 Fryer, C. L., Rueda, J. A., & Ruffini, R. 2014, *ApJL*, **793**, L36  
 Goldreich, P., & Julian, W. H. 1969, *ApJ*, **157**, 869  
 Goldstein, A., Cleveland, W. H., & Kocevski, D. 2021, Fermi GBM Data Tools: v1.1.0, <https://fermi.gsfc.nasa.gov/ssc/data/analysis/gbm>  
 Itoh, R., Murata, K. L., Tachibana, Y., et al. 2018, GCN, **22983**, 1  
 Iwamoto, K., Mazzali, P. A., Nomoto, K., et al. 1998, *Natur*, **395**, 672  
 Izzo, L., Kann, D. A., de Ugarte Postigo, A., et al. 2018, GCN, **23040**, 1  
 Jelinek, M., Strobl, J., Hudec, R., & Polasek, C. 2018, GCN, **23024**, 1  
 Kann, D. A., Izzo, L., & Casanova, V. 2018, GCN, **22985**, 1  
 Kardashev, N. S. 1962, *SvA*, **6**, 317  
 Lipunov, V., Gorbovskoy, E., Tiurina, N., et al. 2018, GCN, **23023**, 1  
 Longair, M. S. 2011, *High Energy Astrophysics* (Cambridge: Cambridge Univ. Press)  
 Martone, R., Guidorzi, C., Kobayashi, S., et al. 2018, GCN, **22976**, 1  
 Moradi, R., Li, L., Rueda, J. A., et al. 2021a, arXiv:2103.09158  
 Moradi, R., Rueda, J. A., Ruffini, R., & Wang, Y. 2021b, *A&A*, **649**, A75  
 Moradi, R., Rueda, J. A., Ruffini, R., et al. 2021c, *PhRvD*, **104**, 063043  
 Negoro, H., Tanimoto, A., Nakajima, M., et al. 2018, GCN, **22993**, 1  
 Ostriker, J. P., & Gunn, J. E. 1969, *ApJ*, **157**, 1395  
 Pacini, F., & Salvati, M. 1973, *ApJ*, **186**, 249  
 Pétri, J. 2015, *MNRAS*, **450**, 714  
 Rastegarnia, F., Moradi, R., Rueda, J. A., et al. 2022, *EPJ C*, **82**, 778  
 Reva, I., Pozanenko, A., Volnova, A., et al. 2018, GCN, **22979**, 1  
 Rhodes, L., van der Horst, A. J., Fender, R., et al. 2020, *MNRAS*, **496**, 3326  
 Roberts, O. J., & Meegan, C. 2018, GCN, **22981**, 1  
 Ronchi, M., Fumagalli, F., Ravasio, M. E., et al. 2020, *A&A*, **636**, A55  
 Rueda, J. A. 2022, arXiv:2202.00316  
 Rueda, J. A., & Ruffini, R. 2012, *ApJL*, **758**, L7  
 Rueda, J. A., & Ruffini, R. 2020, *EPJ C*, **80**, 300  
 Rueda, J. A., Ruffini, R., Karlica, M., Moradi, R., & Wang, Y. 2020, *ApJ*, **893**, 148  
 Rueda, J. A., Ruffini, R., & Kerr, R. P. 2022a, *ApJ*, **929**, 56  
 Rueda, J. A., Ruffini, R., Li, L., et al. 2022b, *IJMPD*, **31**, 2230013  
 Ruffini, R., Aimuratov, Y., Bianco, C. L., et al. 2018b, GCN, **23019**, 1  
 Ruffini, R., Becerra, L., Bianco, C. L., et al. 2018c, *ApJ*, **869**, 151  
 Ruffini, R., Karlica, M., Sahakyan, N., et al. 2018a, *ApJ*, **869**, 101  
 Ruffini, R., Melon Fuksman, J. D., & Vereshchagin, G. V. 2019a, *ApJ*, **883**, 191  
 Ruffini, R., Moradi, R., Rueda, J. A., et al. 2019b, *ApJ*, **886**, 82  
 Ruffini, R., Moradi, R., Rueda, J. A., et al. 2021, *MNRAS*, **504**, 5301  
 Ruffini, R., Salmonson, J. D., Wilson, J. R., & Xue, S. 2000, *A&A*, **359**, 855  
 Ruffini, R., Salmonson, J. D., Wilson, J. R., & Xue, S.-S. 1999, *A&A*, **350**, 334  
 Ruffini, R., Wang, Y., Aimuratov, Y., et al. 2018d, *ApJ*, **852**, 53  
 Rybicki, G. B., & Lightman, A. P. 1979, *Radiative Processes in Astrophysics* (New York: Wiley)  
 Sasada, M., Nakaoka, T., Kawabata, M., et al. 2018, GCN, **22977**, 1  
 Schmalz, S., Graziani, F., Pozanenko, A., et al. 2018, GCN, **23020**, 1  
 Sfaradi, I., Bright, J., Hoeshe, A., et al. 2018, GCN, **23037**, 1  
 Siegel, M. H., Burrows, D. N., Deich, A., et al. 2018, GCN, **22973**, 1  
 Staley, T. D., Titterton, D. J., Fender, R. P., et al. 2012, *MNRAS*, **428**, 3114  
 Vreeswijk, P. M., Kann, D. A., Heintz, K. E., et al. 2018, GCN, **22996**, 1  
 Wald, R. M. 1974, *PhRvD*, **10**, 1680  
 Wang, Y., Rueda, J. A., Ruffini, R., et al. 2019, *ApJ*, **874**, 39  
 Wang, Y., Rueda, J. A., Ruffini, R., et al. 2022, *ApJ*, **936**, 190  
 Watson, A. M., Butler, N., Becerra, R. L., et al. 2018, GCN, **23017**, 1  
 Woosley, S. E. 1993, *ApJ*, **405**, 273  
 Zheng, W., & Filippenko, A. V. 2018, GCN, **23033**, 1

## Evidence for the transition of a Jacobi ellipsoid into a Maclaurin spheroid in gamma-ray bursts

J. A. Rueda<sup>1,2,3,4,5,\*</sup> R. Ruffini<sup>1,2,6,†</sup> L. Li<sup>1,2,7</sup> R. Moradi<sup>1,2,7,‡</sup> J. F. Rodriguez<sup>8,2</sup> and Y. Wang<sup>1,2,7</sup>

<sup>1</sup>ICRA, Dipartimento di Fisica, Sapienza Università di Roma, Piazzale Aldo Moro 5, I-00185 Roma, Italy

<sup>2</sup>ICRANet, Piazza della Repubblica 10, I-65122 Pescara, Italy

<sup>3</sup>ICRANet-Ferrara, Dipartimento di Fisica e Scienze della Terra, Università degli Studi di Ferrara, Via Saragat 1, I-44122 Ferrara, Italy

<sup>4</sup>Dipartimento di Fisica e Scienze della Terra, Università degli Studi di Ferrara, Via Saragat 1, I-44122 Ferrara, Italy

<sup>5</sup>INAF, Istituto di Astrofisica e Planetologia Spaziali, Via Fosso del Cavaliere 100, 00133 Rome, Italy

<sup>6</sup>INAF, Viale del Parco Mellini 84, 00136 Rome, Italy

<sup>7</sup>INAF, Osservatorio Astronomico d'Abruzzo, Via M. Maggini snc, I-64100 Teramo, Italy

<sup>8</sup>Escuela de Física, Universidad Industrial de Santander, Ciudad Universitaria, Bucaramanga 680002, Colombia



(Received 30 March 2022; accepted 20 September 2022; published 7 October 2022)

In the binary-driven hypernova (BdHN) scenario, long gamma-ray bursts (GRBs) originate in a cataclysmic event that occurs in a binary system composed of a carbon-oxygen (CO) star and a neutron star (NS) companion in close orbit. The collapse of the CO star generates at its center a newborn NS ( $\nu$ NS), and a supernova (SN) explosion. Matter from the ejecta is accreted both onto the  $\nu$ NS because of fallback and onto the NS companion, leading to the collapse of the latter into a black hole (BH). Each of the ingredients of the above system leads to observable emission episodes in a GRB. In particular, the  $\nu$ NS is expected to show up (hereafter  $\nu$ NS-rise) in the early GRB emission, nearly contemporary or superimposed to the ultrarelativistic prompt emission (UPE) phase, but with a different spectral signature. Following the  $\nu$ NS-rise, the  $\nu$ NS powers the afterglow emission by injecting energy into the expanding ejecta leading to synchrotron radiation. We here show that the  $\nu$ NS-rise and the subsequent afterglow emission in both systems, GRB 180720B and GRB 190114C, are powered by the release of rotational energy of a Maclaurin spheroid, starting from the bifurcation point to the Jacobi ellipsoid sequence. This implies that the  $\nu$ NS evolves from a triaxial Jacobi configuration, prior to the  $\nu$ NS-rise, into the axially symmetric Maclaurin configuration observed in the GRB. The triaxial  $\nu$ NS configuration is short-lived (less than a second) due to a copious emission of gravitational waves, before the GRB emission, and it could be in principle detected for sources located at distances closer than 100 Mpc. This appears to be a specific process of emission of gravitational waves in the BdHN I powering long GRBs.

DOI: [10.1103/PhysRevD.106.083004](https://doi.org/10.1103/PhysRevD.106.083004)

### I. INTRODUCTION

The progenitor of long gamma-ray bursts (GRBs) in the binary-driven hypernova (BdHN) model is a binary system composed of a carbon-oxygen (CO) star and a neutron star (NS) companion (see, e.g., Refs. [1–7]). The gravitational collapse of the iron core of the CO star leads to the formation of a newborn NS ( $\nu$ NS) at its center and to a supernova (SN) explosion that ejects the outer layers of the star. Some part of the ejecta is accreted by the NS companion and also by the  $\nu$ NS via matter fallback

accretion. Both accretion processes proceed at hypercritical (i.e., highly super-Eddington) rates thanks to a copious neutrino emission [6,8]. In compact binaries with orbital periods of a few minutes, the hypercritical accretion onto the NS companion brings it the critical mass inducing its gravitational collapse and forming a rotating (Kerr) BH. These systems have been called BdHN I. In less compact binaries, the NS companion does not reach the critical mass and holds stable as a more massive, fast rotating NS. These systems have been called BdHN II.

In this article, we focus on BdHN I. The fallback accretion onto the  $\nu$ NS spins it up to a millisecond rotation period (see [7] for numerical simulations). We shall show in this work that in this early phase, the huge  $\nu$ NS rotational energy of up to a few  $10^{53}$  erg can power what we have

\*jorge.rueda@icra.it

†ruffini@icra.it

‡rahim.moradi@inaf.it

called the  $\nu$ NS-rise, i.e., the first observed emission from the  $\nu$ NS. Subsequently, the  $\nu$ NS fuels the synchrotron radiation originated from the expanding SN ejecta leading to the afterglow observed in the x-rays, optical and radio energy bands following a power-law luminosity [9,10]. The accretion onto the companion NS leads to the BH formation that leads to the ultrarelativistic prompt emission (UPE) phase [11] and the GeV emission [12–16].

We aim here to estimate the  $\nu$ NS energy budget and check if it explains the  $\nu$ NS-rise emission. We use as a proxy the case of GRB 180720B and GRB 190114C. For this task, we first individuate in the data of these sources the  $\nu$ NS-rise emission based on the expectation of the BdHN I model. First, if the  $\nu$ NS powers the  $\nu$ NS-rise and the x-ray afterglow, we look for the conjunction of the back-in-time extrapolation of the observed x-ray power-law luminosity of the afterglow with the  $\nu$ NS-rise power. Second, we expect the  $\nu$ NS-rise to show up either as a precursor to the UPE or at most to superpose to it. Having established the connection between the  $\nu$ NS-rise and the afterglow, and with the knowledge of their energetics, we evaluate if the  $\nu$ NS can indeed power these emissions. For self-consistency with the modeling of the afterglow in the BdHN scenario (see, e.g., [9,10]), we seek for the  $\nu$ NS parameters that can explain the emissions demanding rigid rotation and axial symmetry. With the estimate of the  $\nu$ NS parameters, we discuss the previous early life of the  $\nu$ NS and on the possible associated emission of gravitational waves during its evolution toward the axially symmetric stage.

We describe in Sec. II the sequence of physical phenomena that occur in a BdHN I and their associated observables in the GRB data. In Sec. III, we first individuate the  $\nu$ NS-rise emission in GRB 180720B and GRB 190114C. Then, we proceed to the evaluation of the  $\nu$ NS parameters and their evolution modeling it as a stable Maclaurin

spheroid. This assumption, together with the energy conservation equation, allows to infer the time evolution of the  $\nu$ NS structure without additional assumptions. We show that the  $\nu$ NS-rise and the afterglow emission energetics require that the initial parameters of the Maclaurin spheroid are close to the parameters of the bifurcation point to the Jacobi sequence of ellipsoids. This result suggests that the  $\nu$ NS before the GRB emission evolves from a Jacobi ellipsoid into a Maclaurin spheroid by emission of gravitational waves. Therefore, the only mechanism that can generate gravitational radiation in the BdHN scenario of GRBs originates in the transition from the triaxial configuration (ellipsoid) at birth to the axially-symmetric state (spheroid). In Sec. IV, we elaborate on the entity of this emission and discuss its possible detectability.

## II. SEQUENCE OF BDHN PHYSICAL PHENOMENA AND OBSERVABLES

The above sequence of physical phenomena that occur in a BdHN I are related to specific observational episodes in the GRB data that we summarize in Table I and discussed below for GRB 180720B and GRB 190114C.

*The UPE phase.* The BH forms and together with the surrounding magnetic field and ionized matter from the SN ejecta composes the *inner engine* [12]. The gravitomagnetic interaction of the newborn Kerr BH with the magnetic field induces an electric field [13,16]. The electric field is initially overcritical, i.e., larger than the quantum electrodynamics (QED) critical field for vacuum polarization,  $E_c = m_e^2 c^3 / (e\hbar) \approx 1.32 \times 10^{16} \text{ V cm}^{-1}$ , generating an  $e^+e^-$  plasma. The plasma self-accelerates owing to its internal pressure, loads with it some baryons from the environment, and finally reaches transparency in an ultrarelativistic regime with characteristic Lorentz factor  $\Gamma \sim 100$  [11,18]. The UPE is the first manifestation of the BH and the blackbody (BB)

TABLE I. GRB observables associated with the BdHN I component and physical phenomena.

BdHN I component/phenomena	GRB observable				
	$\nu$ NS-rise (soft-hard x-rays)	UPE (MeV)	GeV emission	X-ray flares early afterglow	Afterglow (X/optical/ radio)
Early SN emission [17]	⊗				
Hypercritical accretion onto the $\nu$ NS and NS [3,6]	⊗				
BH formation from NS gravitational collapse [11,12,15]			⊗		
Transparency of ultrarelativistic $e^+e^-$ (from vacuum polarization) in low baryon load region [11,18]		⊗			
Synchrotron emission by the <i>inner engine</i> : newborn BH + B-field + SN ejecta [12,13,15,16]			⊗		
Transparency of ultrarelativistic $e^+e^-$ (from vacuum polarization) in low baryon load region (SN ejecta) [19]				⊗	
Synchrotron emission from SN ejecta with energy injection from $\nu$ NS [9,10,17]					⊗
Pulsarlike emission from the $\nu$ NS [9,10,17]					⊗

component from the plasma transparency at MeV energies is the signature in the spectrum that allows its identification in the GRB data. Another special signature of the UPE is its *hierarchical* structure shown for the first time in GRB 190114C [11], i.e., a refined time-resolved analysis of the UPE shows that its spectrum in rebinned time intervals (up to a fraction of second) shows always a cutoff power-law + blackbody (CPL + BB) model. Numerical simulations of the QED physical process for the UPE of GRB 190114C, which extends from the rest-frame time  $t_{\text{rf}} = 1.99$  s to  $t_{\text{rf}} = 3.99$  s, show that the plasma transparency occurs in pulses in a nanosecond timescale, which explains the similar spectra of the UPE hierarchical structure (see [11] for details). In GRB 180720B, the UPE has been identified in two time intervals [20]. The UPE I extends from  $t_{\text{rf}} = 4.84$  s to  $t_{\text{rf}} = 6.05$  s, has isotropic energy  $E_{\text{UPEI}} = (6.37 \pm 0.48) \times 10^{52}$  erg, and its spectrum is best fitted by a CPL + BB model, index  $\alpha = -1.13$ , cutoff energy  $E_c = 2220.57$  keV, and BB temperature  $kT = 50.31$  keV in the observer's frame. In the UPE II continues the UPE phase from  $t_{\text{rf}} = 9.07$  s to  $t_{\text{rf}} = 10.89$  s, has an isotropic energy of  $E_{\text{UPEII}} = (1.6 \pm 0.95) \times 10^{53}$  erg, and its spectrum is best fitted by a CPL + BB model with  $\alpha = -1.06$ ,  $E_c = 1502.5$  keV, and  $kT = 39.8$  keV. The UPE of GRB 180720B also shows the hierarchical structure in rebinned time intervals first observed in GRB 190114C. The electric energy that powers the plasma is induced by the gravito-magnetic interaction of the BH and the magnetic field, so the BH extractable energy powers the UPE. Each process of expansion and transparency of the plasma takes away a fraction of mass and angular momentum of the BH. The UPE ends when the induced electric field becomes undercritical. For GRB 190114C, it occurs at  $t_{\text{rf}} = 3.99$  s [11], while for GRB 180720B, at  $t_{\text{rf}} = 10.89$  s [20].

The UPE is similar to the emission of the jet in the traditional fireball model in which the a collimated relativistic jet expands with  $\Gamma \sim 10^2 - 10^3$  (see, e.g., Refs. [21–25]). One of the main differences between this model and the UPE in the BdHN scenario is the duration of this emission. The jetted fireball continues to emit while the central engine powers it, so the internal and external shocks keep interacting with the interstellar medium extending the emission from the prompt to the afterglow, including the very-high-energy emission by synchrotron self-Compton radiation (see, e.g., [26–29], and references therein). In the BdHN model, the UPE occurs only while the induced electric field is overcritical and can create the  $e^+e^-$  plasma. These conditions in the BdHN last short (few seconds) and explain only the prompt emission of the GRB. There are no additional mechanisms to produce  $e^+e^-$  pairs, so when the electric field becomes undercritical, the UPE shuts down. The induced undercritical field keeps extracting the BH energy powering the GeV afterglow emission by synchrotron radiation of accelerated electrons (see details in [12,13,15,16]). The synchrotron radiation from the

expanding ejecta of the SN powered by the emission of the  $\nu\text{NS}$  explains the X-optical-radio afterglow (see below for further details). Therefore, the emission of the  $e^+e^-$  ultrarelativistic ( $\Gamma \sim 100$ ) plasma is limited to the UPE and does not contribute to the GRB afterglow emission.

*The  $\nu\text{NS}$ -rise.* The accretion of ejecta onto the  $\nu\text{NS}$  and the NS companion transfer mass and angular momentum to them. One-dimensional simulations of the above process has been presented in [3,4], two-dimensional in [5], and three-dimensional in [6,7]. Since the magnetic field of the  $\nu\text{NS}$  is expected to be larger than the one of the older NS companion, we expect the  $\nu\text{NS}$  to dominate the observed energy release in this phase. In GRB 190114C, the  $\nu\text{NS}$ -rise emission extends from  $t_{\text{rf}} = 0.79$  s to  $t_{\text{rf}} = 1.18$  s [11,14]. In GRB 180720B, it extends from  $t_{\text{rf}} = 6.05$  s to  $t_{\text{rf}} = 9.07$  s, has an isotropic energy of  $E_{\nu\text{NS}} = (1.13 \pm 0.04) \times 10^{53}$  erg, and its spectrum is best fitted by a CPL model ( $\alpha = -0.98$ , and  $E_c = 737$  keV, in the observer's frame). The energy released from the  $\nu\text{NS}$ -rise becomes dominant over the UPE for about 3 s, which explains the observed apparent split UPEs I and II discussed above. After that time, the  $\nu\text{NS}$ -rise emission fades and the UPE becomes again observable. Recent numerical simulations of the early evolution of BdHN I (Becerra *et al.*, submitted; see also [7]) show that the NS companion can reach the critical mass for BH formation before the second peak of fallback accretion experienced by the  $\nu\text{NS}$ . This phenomenon makes indeed possible for the  $\nu\text{NS}$ -rise emission to superpose to the UPE in some cases.

*The cavity.* The massive accretion process onto the NS companion and the BH formation reduce the matter density around the newborn BH [7]. Numerical simulations show that the expanding  $e^+e^-$  plasma causes a further decrease of the density from  $10^{-7}$  g cm $^{-3}$  to a value as low as  $10^{-14}$  g cm $^{-3}$ , and its interaction with the cavity walls generates emission characterized by a spectrum similar to a Comptonized blackbody with a peak energy of a few hundreds of keV [30]. For GRB 190114C, the emission from the cavity extends from  $t_{\text{rf}} = 11$  s to 20 s [11]. For GRB 180720B, it occurs from  $t_{\text{rf}} = 16.94$  s to  $t_{\text{rf}} = 19.96$  s, with an isotropic energy of  $E_{\text{CV}}^{\text{MeV}} = (4.32 \pm 0.19) \times 10^{52}$  erg, characterized by a CPL spectrum ( $\alpha = -1.16$ ,  $E_c = 607.96$  keV).

*Soft x-ray flares (SXF) and hard x-ray flares (HXF).* In the regions of high matter density surrounding the newborn BH site, the expanding  $e^+e^-$  plasma engulfs high amounts of baryons leading to transparencies occurring at distances  $\sim 10^{12}$  cm with Lorentz factors  $\lesssim 5$ , observable as SXFs and/or HXFs (see [31] for numerical simulations and specific examples). The HXF of GRB 180720B occurs from  $t_{\text{rf}} = 28.95$  s to  $t_{\text{rf}} = 34.98$  s, with  $L_{\text{HXF,iso}} = (7.8 \pm 0.07) \times 10^{51}$  erg s $^{-1}$ , and its spectrum is best fitted by a CPL model with  $E_c = (5.5_{-0.7}^{+0.8}) \times 10^2$  keV,  $\alpha = -1.198 \pm 0.031$ . The SXF occurs from  $t_{\text{rf}} = 55$  s to  $t_{\text{rf}} = 75$  s, with  $L_{\text{SXF,iso}} = 1.45 \times 10^{50}$  erg, and its spectrum



is best fitted by a PL + BB model with  $\alpha = -1.79 \pm 0.23$ , and  $kT = 0.99 \pm 0.13$  keV.

*The x-ray afterglow.* In [14], 380 long GRBs have been identified as BdHN I. It has been there shown that their x-ray afterglow, observed by the Neil Gehrels Swift satellite [19,32,33], with a luminosity in the cosmological source rest-frame that decreases with time as a power-law [14], i.e.,

$$L_X = A_X t^{-\alpha_X}, \quad (1)$$

where  $A_X$  and  $\alpha_X$  depend on the source. In this article, we confine our attention to the BdHN I prototypes GRB 180720B, with  $A_X = (2.5 \pm 0.4) \times 10^{53}$  erg s<sup>-1</sup> and  $\alpha_X = 1.44 \pm 0.01$ , and GRB 190114C, with  $A_X = (5.14 \pm 2.03) \times 10^{52}$  erg s<sup>-1</sup> and  $\alpha_X = 1.37 \pm 0.05$ . Figure 1 shows the  $\nu$ NS-rise and the x-ray afterglow of GRB 180720B and GRB 190114C, in the cosmological rest-frame of the sources. In GRB 180720B, the  $\nu$ NS-rise is observed at 6.05–9.06 s, and in GRB 190114C at 1.12–1.68 s from the Fermi-GBM trigger. The afterglow in the optical and radio energy bands also shows a similar power-law but much less luminous, so the x-ray luminosity is an excellent proxy of the total (bolometric) afterglow luminosity, i.e., we assume  $L_\infty \approx L_X$ .

In the BdHN model, the GRB afterglow is explained by the electron synchrotron radiation produced in the SN ejecta while it expands through the  $\nu$ NS magnetic field lines, and the  $\nu$ NS pulsar emission that becomes observable in the late-time afterglow (see, e.g., [9,10]). Numerical simulations of the hypercritical process onto the  $\nu$ NS [7] show that it gains sufficient energy (and angular momentum) during the early fallback accretion to power the energy of the observed afterglow. The fit of the x-ray afterglow data with the above synchrotron radiation model shows that typically the magnetic field at  $\sim 10^{12}$  cm is  $B \sim 10^5$  G and decreases linearly with the radial distance. This behavior is indeed expected from the toroidal component of the  $\nu$ NS magnetic field at large distances from the light cylinder [9,10,17].

Summarizing, the synchrotron emission occurs in the optically thin region of the SN ejecta that expands at mildly relativistic velocity,  $v \approx 0.1c$ , in the  $\nu$ NS magnetic field, at distances above  $10^{12}$  cm. We refer the reader to [10] for the application of the above afterglow model to GRBs 130427A, 160509A, 160625B, 180728A, and 190114C.

### III. $\nu$ NS STRUCTURE EVOLUTION

In Fig. 1, we show the backward extrapolation to early times of the power-law luminosity of the x-ray afterglow. We notice that it joins the  $\nu$ NS-rise emission. We interpret this coincidence as an observational verification of the BdHN picture that the  $\nu$ NS energy powers the  $\nu$ NS-rise and the afterglow emissions. The above is our central working hypothesis in this article. Therefore, we assume the  $\nu$ NS-rise is the first release of the  $\nu$ NS energy gained during the fallback accretion process and continues to release it at the pace given by the power-law luminosity inferred from the x-ray afterglow.

We are not here interested in the precise modeling of the emission mechanisms but in estimating the  $\nu$ NS parameters and their evolution, consistent with the required energetics at every time. In this way, we avoid including *ad hoc* models for the radiation mechanism and the removal of energy and angular momentum. For instance, the traditional model of magnetic-dipole radiation might not be sufficient for an accurate description of the rotational energy loss of pulsars. The measurements of the pulsar braking index deviate from the expected value ( $n = 3$ ) of magnetic dipole radiation (see, e.g., [34]). Deviations from the pure dipole braking in the very early life of pulsars can be due to the occurrence of glitches (see [34–36] and references therein) which could also release high-energy emission observable in GRBs (see, e.g., [37]). In addition, the explanation of the late-time afterglow of GRBs demands at least the presence of a substantial quadrupole component (see, e.g., [9,10]).

Having established all the above, we obtain the evolution of the  $\nu$ NS from the energy conservation equation

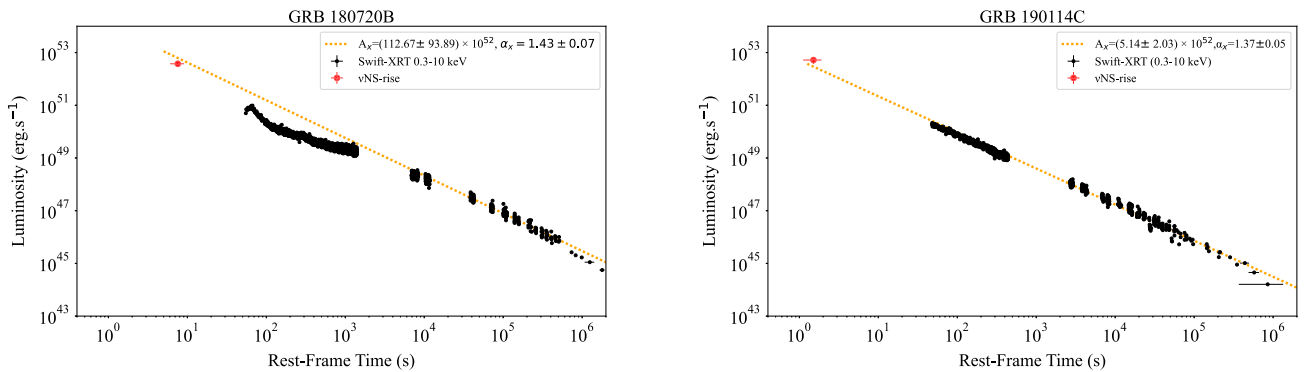


FIG. 1. Luminosity of the  $\nu$ NS-rise (red point) and the x-ray afterglow (black points) of GRB 180720B (left panel) and GRB 190114C (right panel) observed by *Swift*-XRT, measured in the cosmological rest-frame. The dashed yellow line is the power-law fit given by Eq. (1).

$$\dot{E} = -L_\infty \approx -L_X, \quad (2)$$

where  $L_X$  is given by Eq. (1) and we assume it as valid from the  $\nu$ NS-rise time on. In agreement with the afterglow description in the BdHN model, we do not apply a beaming correction to the required  $\nu$ NS energetics, and do not include gravitational-wave radiation losses since the  $\nu$ NS is axially symmetric in this phase. In Eq. (2), we are assuming that the transient proto-NS regime in which the  $\nu$ NS energy loss is dominated by neutrino emission is over. Therefore, we consider the energy loss is dominated by photons and that the  $\nu$ NS is cold, so its energy is dominated by the kinetic rotational energy and the gravitational energy [see Eq. (8) below].

We turn now to evaluate the  $\nu$ NS parameters and their evolution during the  $\nu$ NS-rise and the afterglow emissions. For this task, we model the  $\nu$ NS as a stable Maclaurin spheroid, i.e., a self-gravitating, oblate, homogeneous (i.e., uniform density), rigidly rotating Newtonian configuration of equilibrium. We refer the reader to Ref. [38] for details on these incompressible configurations, and to Ref. [39] for the generalization to compressible polytropes. From the solution of the gravitational Poisson equation, it turns out that given a density  $\rho$ , all the properties of the spheroid are function of the eccentricity,  $e^2 \equiv (a^2 - b^2)/a^2$ , where  $a$  and  $b$  are, respectively, the semimajor (equatorial) and semi-minor (polar) axis. The angular velocity is given by (e.g., [40])

$$\Omega^2 = 2\pi G\rho g(e), \quad (3)$$

$$g(e) = \frac{(3 - 2e^2)(1 - e^2)^{1/2} \arcsin(e)}{e^3} - \frac{3(1 - e^2)}{e^2}. \quad (4)$$

The angular momentum,  $J$ , and moment of inertia,  $I$ , are given by

$$J = I\Omega, \quad I = I_0(1 - e^2)^{-1/3}, \quad I_0 = \frac{2}{5}Ma_0^2, \quad (5)$$

where the mass and equatorial radius are

$$M = \frac{4\pi}{3}\rho a^3(1 - e^2)^{1/2}, \quad a = a_0(1 - e^2)^{-1/6}, \quad (6)$$

being  $a_0$  the radius of the homogeneous, nonrotating (i.e., spherical) star of mass  $M$ , density  $\rho$ , and with the same volume of the spheroid, so it fulfills the equation

$$\rho = \frac{3M}{4\pi a_0^3}. \quad (7)$$

The total energy is the sum of the kinetic rotational ( $T$ ) and gravitational ( $W$ ) energy

$$E = T + W, \quad W = -\frac{3GM^2 \arcsin(e)}{5a}, \quad T = \frac{1}{2}I\Omega^2, \quad (8)$$

Following the BdHN scenario, the  $\nu$ NS must cover the energy released in the  $\nu$ NS-rise and the subsequent afterglow emission. This is confirmed by the backward extrapolation of the X-ray afterglow power-law emission to the time of the  $\nu$ NS-rise, which shows the connection between the two emissions (see Fig. 1).

By integrating analytically Eq. (2), and equating it to Eq. (8), we obtain the following algebraic, nonlinear implicit equation whose solution gives the eccentricity as a function of time

$$\pi G I_0 \rho \mathcal{F}(e) = \frac{A_X}{1 - \alpha_x} t^{1 - \alpha_x}, \quad (9)$$

$$\mathcal{F} \equiv -2 + \frac{3(1 - e^2)^{2/3}}{e^2} + \frac{(4e^2 - 3)(1 - e^2)^{1/6}}{e^3} \arcsin(e), \quad (10)$$

where we have used the asymptotic condition  $e(\infty) = 0$ .

Therefore, Eq. (2) and the equilibrium properties of the Maclaurin spheroid allows us to estimate the evolution of all the relevant physical properties of the  $\nu$ NS. The above framework tells us that given values of  $M$  (or alternatively  $\rho$ ) and  $a_0$ , all stellar parameters (energy, angular momentum, moment of inertia, angular velocity) depend only on the eccentricity,  $e(t)$ . Summarizing, the solution  $e(t)$  is obtained from Eq. (2) which leads to the implicit algebraic equation (9). With the knowledge of  $e(t)$ , the evolution of the rotational energy and the gravitational energy are obtained from Eqs. (8), likewise the evolution of the radius from Eq. (6), the angular momentum and moment of inertia from Eqs. (5), and the angular velocity from Eq. (3).

As for the initial conditions, we must specify a value of  $M$  (or alternatively  $\rho$ ),  $a_0$ , and at the initial time of evolution,  $t_0$ , which is the time of the occurrence of the  $\nu$ NS-rise, a value for the eccentricity,  $e(t_0)$ . We here adopt  $a_0 = 10^6$  cm, and seek for the mass and initial eccentricity of the spheroid that allow to explain the  $\nu$ NS-rise and afterglow emission, which are specified by the values of  $A_X$  and  $\alpha_x$ .

We have found that the high luminosity and energy released at the  $\nu$ NS-rise requires the  $\nu$ NS to have the fast spin and the maximum (or very close to it) eccentricity allowed by the axially symmetric Maclaurin spheroid, namely the values of the bifurcation point to the sequence of Jacobi ellipsoids (triaxial configurations), i.e.,  $e(t_0) = 0.813$  [38]. Table II summarizes the initial conditions of the Maclaurin spheroid modeling the  $\nu$ NS in GRB 180720B and GRB 190114C. The inferred rotation periods correspond to frequencies of 1.72 kHz for GRB 180720B and 1.47 kHz for GRB 190114C. These high rotation rates are indeed close to the maximum allowed values of uniformly

TABLE II. Properties of the  $\nu$ NS modeled as a Maclaurin spheroid that powers the  $\nu$ NS-rise and the x-ray afterglow in GRB 180720B and GRB 190114C. The radius  $a_0$  is assumed to be  $10^6$  cm, and we obtain the mass  $M$  seeking for the solution of Eq. (9) at the initial time  $t_0$  ( $\nu$ NS-rise time) as shown in Fig. 2. The value reported here is the minimum mass, which corresponds to the solution for the maximum eccentricity of stable Maclaurin configurations,  $e_{\max} \approx 0.813$ . The density is given by Eq. (7). The corresponding initial rotation period of the configuration is obtained from the initial rotation angular velocity,  $\Omega_0 = 2\pi/P_0$ , where  $\Omega_0$  is calculated by plunging  $\rho$  and  $e_0$  into Eq. (3).

	GRB 180720B	GRB 190114C
$A_X$	$(2.5 \pm 0.4) \times 10^{53}$	$(5.14 \pm 2.03) \times 10^{52}$
$\alpha_X$	$1.44 \pm 0.01$	$1.37 \pm 0.05$
$t_0$ (s)	6.05	1.12
$e_0$	0.813	0.813
$a_0$ ( $10^6$ cm)	1.0	1.0
$a$ ( $10^6$ cm)	1.2	1.2
$M$ ( $M_\odot$ )	3.19	2.3
$\rho$ ( $10^{15}$ g cm $^{-3}$ )	1.52	1.09
$P_0$ (ms)	0.58	0.68

rotating NSs (see, e.g., [41]), which is consistent with the Maclaurin spheroid be at the bifurcation with the Jacobi sequence. The fallback accretion process in the first minutes of the  $\nu$ NS life can transfer sufficient mass and angular momentum to bring it to these critical values (see [7,42] for recent numerical simulations of this process in BdHNe).

Figure 3 shows the evolution of the eccentricity (upper row) and the contribution of the rotational and gravitational power (lower row) to the total power released during the evolution. The rotational power dominates over the gravitational power during most of the evolution, although the latter contributes significantly at early times. For instance,  $\dot{W}/\dot{E} \gtrsim 0.1$  at eccentricities  $e \gtrsim 0.5$ .

#### IV. CONCLUDING REMARKS

We have calculated the evolution of the  $\nu$ NS in BdHN I assuming that it powers the  $\nu$ NS-rise and the afterglow emission. By modeling the  $\nu$ NS as a Maclaurin spheroid, we have shown that its parameters (rotation period and eccentricity) have to be very close (or equal to) to the ones of the transition point to the Jacobi sequence of ellipsoids (see Table II).

At the bifurcation point with the Jacobi ellipsoids sequence, the ratio of the rotational to gravitational energy of Maclaurin spheroids is  $T/|W| \approx 0.14$ , where the configuration becomes secularly unstable and its evolution driven by gravitational radiation [38]. Since the  $\nu$ NS at the  $\nu$ NS-rise time are at, or close to, the bifurcation point, they have this  $T/W$  ratio. In addition, assuming a spherical radius of  $a_0 = 10^6$  cm, we have found that the mass of the spheroids is  $3.2 M_\odot$  and  $2.3 M_\odot$ , respectively, for GRB 180720B and GRB 190114C (see Table II). Centrally condensed objects (so not of uniform density) at rigid rotation become unstable against mass shedding (Keplerian limit) at lower values of this ratio (see, e.g., [41]). Instead, configurations with differential rotation can have a  $T/|W|$  ratio up to the maximum value of 0.5 set by the virial theorem. Given the mass and  $T/|W|$  ratio, our result suggests that the  $\nu$ NS might have some differential rotation. Therefore, the  $\nu$ NS could evolve from the hypermassive stability region (mass  $>$  maximum mass of rigidly rotating stars; supported by differential rotation) into the supra-massive one (mass  $>$  maximum mass of non-rotating stars; supported by rigid rotation). The above situation is similar to the evolution of a hypermassive NS formed in a NS binary merger (see, e.g., [43,44], for the stability analysis of the merged object modeled as a Riemann-S ellipsoid) and becomes an interesting topic of further investigation in a fully general relativistic framework (see, e.g., [45]).

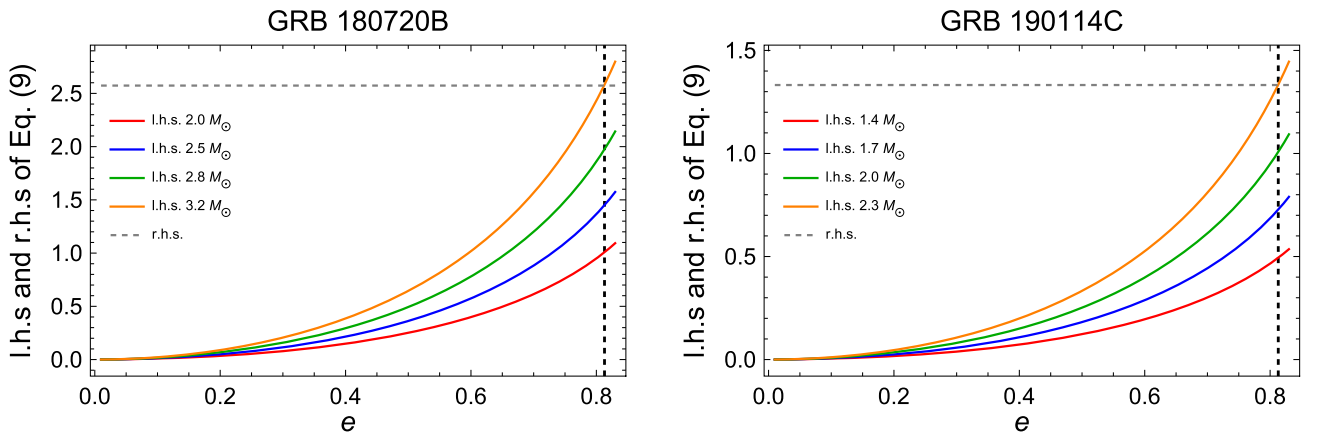


FIG. 2. Left-hand side (lhs, colored curves) and right-hand side (rhs, dashed gray horizontal line) of Eq. (9) at the  $\nu$ NS-rise time, for GRB 180720B (left panel) and GRB 190114C (right panel). The dashed black vertical line marks the maximum eccentricity of stable Maclaurin spheroids,  $e_{\max} \approx 0.813$ . The units of the vertical axis are of  $10^{53}$  erg s $^{-1}$ .

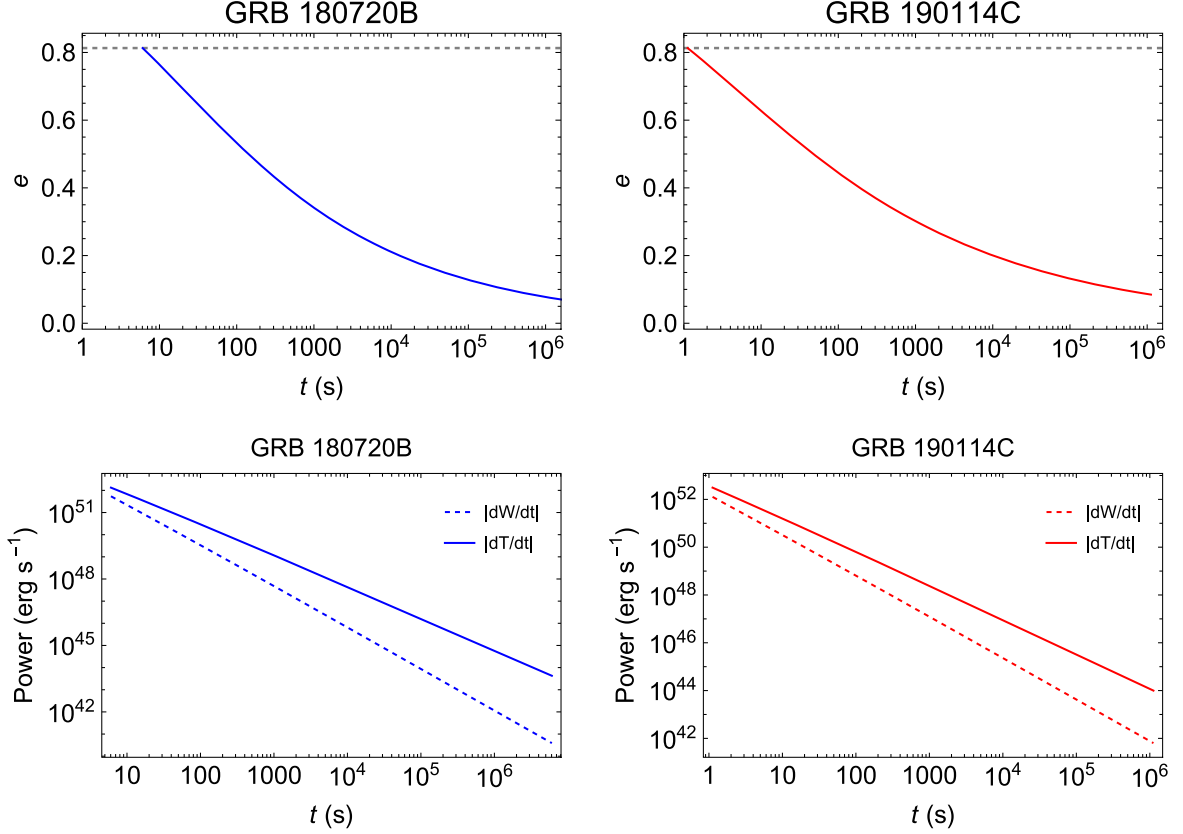


FIG. 3. Evolution of the eccentricity (upper row) and the gravitational and rotational power released (lower row) by the  $\nu$ NS modelled as a Maclaurin spheroid, in the cases of GRB 180720B (blue curves) and GRB 190114C (red curves).

The parameters of the NS inferred from the present model suggest the properties of the  $\nu$ NS even if the exact values can be slightly different depending on factors like the nuclear equations of state, the interior rotation law (i.e., uniform or differential rotation), and the use of general relativity. Our analysis indicates that the NS powering the afterglow emission of these GRBs must be massive (likely  $\sim 2 M_{\odot}$ ), fast rotating (likely  $\sim 1$  kHz), and initially with high eccentricity. Even though, in the present model, the NS is stable since it belongs to the stable branch of Maclaurin spheroids. The high value of the NS mass is comparable to or higher than the critical mass of uniformly rotating NS in general relativity for some nuclear equations of state. It suggests the NS equations of state must be stiff, which is consistent with the observation of stable massive NSs above two solar masses, e.g., PSR J0952-0607, the heaviest NS measured to date with a mass of  $2.35 \pm 0.17 M_{\odot}$  [46].

Therefore, the  $\nu$ NS could have evolved from a triaxial body (Jacobi-like ellipsoid) into an axially symmetric body (Maclaurin spheroid) by emission of gravitational waves, as anticipated in early models of pulsars (e.g., [47–49]) and verified by [50,51]. The gravitational-wave emission drives the evolution of the ellipsoid to the Maclaurin sequence in

relatively short time [49,51]. This emission carries out angular momentum which plays a role in bringing the  $\nu$ NS to the observed short-rotation period: the ellipsoid spins up while it loses angular momentum because the gravitational-wave-driven evolution occurs along the Riemann-S sequence conserving circulation [51]. The gravitational-wave power released by the triaxial configuration with equatorial ellipticity  $\epsilon$  and moment of inertia  $I$  about the rotation axis is  $\dot{E}_{\text{GW}} = (32/5)(G/c^5)I^2\epsilon^2\Omega^6$  [48]. For instance, assuming a rotation frequency of 1 kHz, and the moment of inertia inferred for the  $\nu$ NS in GRB 180720B, we obtain  $\dot{E}_{\text{GW}} \sim 1.5 \times 10^{53}(\epsilon/0.1)^2 \text{ erg s}^{-1}$ , and the characteristic timescale  $\tau_{\text{GW}} \sim E/\dot{E}_{\text{GW}} \lesssim 1$  s, where  $E \sim 10^{53}$  erg is the gravitational energy of the triaxial configuration, and we are assuming that the ellipticity can be as large as 0.1 at early post-birth times. This implies a large amount of energy carried out by this *burst* of gravitational waves,  $\Delta E_{\text{GW}} \sim \dot{E}_{\text{GW}}\tau_{\text{GW}} \sim 10^{53}$  erg. The associated characteristic strain at a detector of gravitational waves is  $h_c \sim 4G/(c^4D)I\epsilon\Omega^2 \sim 1.6 \times 10^{-23}(\epsilon/0.1)(100 \text{ Mpc}/D)$ , where  $D$  is the distance to the source (e.g., [52]). This signal could be detected by upgraded versions of the Nautilus cryogenic detector, which was conceived for this aim (see, e.g., [53]), and working in

coincidence with the Advanced LIGO and Virgo interferometers at these frequencies (e.g., [54]). In view of the above, and the possible enhancement of the strain depending upon the number of cycles of the signal in the detector [52], there is a chance to calibrate gravitational-wave detectors [55] observing this radiation before the GRB prompt emission for sources located at  $D \lesssim 100$  Mpc.

In the present BdHN I scenario, the above is the specific emission of gravitational waves associated with the long GRB. The core-collapse leading to the  $\nu$ NS radiates negligible gravitational waves,  $\Delta E_{\text{GW}} \sim 10^{-7} M_{\odot} c^2 \sim 10^{47}$  erg (see, e.g., [56,57]). Since there is no relativistic jet launch in the BdHN scenario, mechanisms such as the

gravitational-wave emission from an accelerating jet [58] are not expected either to be at work in BdHN [16].

## ACKNOWLEDGMENTS

We thank the referees for insightful comments and suggestions that helped us to improve the presentation of the article. J.F.R. is thankful for financial support from the Patrimonio Autónomo—Fondo Nacional de Financiamiento para la Ciencia, la Tecnología y la Innovación Francisco José de Caldas (MINCIENCIAS—COLOMBIA) under the grant No. 110685269447 RC-80740-465-2020, project 6955.

- 
- [1] J. A. Rueda and R. Ruffini, *Astrophys. J. Lett.* **758**, L7 (2012).
- [2] L. Izzo, J. A. Rueda, and R. Ruffini, *Astron. Astrophys.* **548**, L5 (2012).
- [3] C. L. Fryer, J. A. Rueda, and R. Ruffini, *Astrophys. J. Lett.* **793**, L36 (2014).
- [4] C. L. Fryer, F. G. Oliveira, J. A. Rueda, and R. Ruffini, *Phys. Rev. Lett.* **115**, 231102 (2015).
- [5] L. Becerra, F. Cipolletta, C. L. Fryer, J. A. Rueda, and R. Ruffini, *Astrophys. J.* **812**, 100 (2015).
- [6] L. Becerra, C. L. Bianco, C. L. Fryer, J. A. Rueda, and R. Ruffini, *Astrophys. J.* **833**, 107 (2016).
- [7] L. Becerra, C. L. Ellinger, C. L. Fryer, J. A. Rueda, and R. Ruffini, *Astrophys. J.* **871**, 14 (2019).
- [8] L. Becerra, M. M. Guzzo, F. Rossi-Torres, J. A. Rueda, R. Ruffini, and J. D. Uribe, *Astrophys. J.* **852**, 120 (2018).
- [9] R. Ruffini, M. Karlica, N. Sahakyan, J. A. Rueda, Y. Wang, G. J. Mathews, C. L. Bianco, and M. Muccino, *Astrophys. J.* **869**, 101 (2018).
- [10] J. A. Rueda, R. Ruffini, M. Karlica, R. Moradi, and Y. Wang, *Astrophys. J.* **893**, 148 (2020).
- [11] R. Moradi, J. A. Rueda, R. Ruffini, L. Li, C. L. Bianco, S. Champion, C. Cherubini, S. Filippi, Y. Wang, and S. S. Xue, *Phys. Rev. D* **104**, 063043 (2021).
- [12] R. Ruffini, R. Moradi, J. A. Rueda, L. Becerra, C. L. Bianco, C. Cherubini, S. Filippi, Y. C. Chen, M. Karlica, N. Sahakyan, Y. Wang, and S. S. Xue, *Astrophys. J.* **886**, 82 (2019).
- [13] J. A. Rueda and R. Ruffini, *Eur. Phys. J. C* **80**, 300 (2020).
- [14] R. Ruffini, R. Moradi, J. A. Rueda, L. Li, N. Sahakyan, Y. C. Chen, Y. Wang, Y. Aimuratov, L. Becerra, C. L. Bianco, C. Cherubini, S. Filippi, M. Karlica, G. J. Mathews, M. Muccino, G. B. Pisani, and S. S. Xue, *Mon. Not. R. Astron. Soc.* **504**, 5301 (2021).
- [15] R. Moradi, J. A. Rueda, R. Ruffini, and Y. Wang, *Astron. Astrophys.* **649**, A75 (2021).
- [16] J. A. Rueda, R. Ruffini, and R. P. Kerr, *Astrophys. J.* **929**, 56 (2022).
- [17] Y. Wang, J. A. Rueda, R. Ruffini, L. Becerra, C. Bianco, L. Becerra, L. Li, and M. Karlica, *Astrophys. J.* **874**, 39 (2019).
- [18] C. L. Bianco, R. Ruffini, and S.-S. Xue, *Astron. Astrophys.* **368**, 377 (2001).
- [19] R. Ruffini *et al.*, *Astrophys. J.* **852**, 53 (2018).
- [20] F. Rastegarnia, R. Moradi, J. A. Rueda, R. Ruffini, L. Li, S. Eslamzadeh, Y. Wang, and S. S. Xue, *Eur. Phys. J. C* **82**, 778 (2022).
- [21] A. Shemi and T. Piran, *Astrophys. J. Lett.* **365**, L55 (1990).
- [22] M. J. Rees and P. Meszaros, *Mon. Not. R. Astron. Soc.* **258**, 41P (1992).
- [23] T. Piran, A. Shemi, and R. Narayan, *Mon. Not. R. Astron. Soc.* **263**, 861 (1993).
- [24] P. Meszaros, P. Laguna, and M. J. Rees, *Astrophys. J.* **415**, 181 (1993).
- [25] S. Mao and I. Yi, *Astrophys. J. Lett.* **424**, L131 (1994).
- [26] P. Mészáros, *Annu. Rev. Astron. Astrophys.* **40**, 137 (2002).
- [27] T. Piran, *Rev. Mod. Phys.* **76**, 1143 (2005).
- [28] V. A. Acciari, S. Ansoldi *et al.* (MAGIC Collaboration), *Nature (London)* **575**, 455 (2019).
- [29] B. Zhang, *Nature (London)* **575**, 448 (2019).
- [30] R. Ruffini, J. D. Melon Fuksman, and G. V. Vereshchagin, *Astrophys. J.* **883**, 191 (2019).
- [31] R. Ruffini, L. Becerra, C. L. Bianco, Y. C. Chen, M. Karlica, M. Kovačević, J. D. Melon Fuksman, R. Moradi, M. Muccino, G. B. Pisani, D. Primorac, J. A. Rueda, G. V. Vereshchagin, Y. Wang, and S. S. Xue, *Astrophys. J.* **869**, 151 (2018).
- [32] R. Ruffini, J. A. Rueda, M. Muccino, Y. Aimuratov, L. M. Becerra, C. L. Bianco, M. Kovacevic, R. Moradi, F. G. Oliveira, G. B. Pisani, and Y. Wang, *Astrophys. J.* **832**, 136 (2016).
- [33] G. B. Pisani, R. Ruffini, Y. Aimuratov, C. L. Bianco, M. Kovacevic, R. Moradi, M. Muccino, A. V. Penacchioni, J. A. Rueda, S. Shakeri, and Y. Wang, *Astrophys. J.* **833**, 159 (2016).
- [34] A. G. Lyne, C. A. Jordan, F. Graham-Smith, C. M. Espinoza, B. W. Stappers, and P. Weltevrede, *Mon. Not. R. Astron. Soc.* **446**, 857 (2015).
- [35] M. E. Lower, S. Johnston, L. Dunn, R. M. Shannon, M. Bailes, S. Dai, M. Kerr, R. N. Manchester, A. Melatos,

- L. S. Oswald, A. Parthasarathy, C. Sobey, and P. Weltevrede, *Mon. Not. R. Astron. Soc.* **508**, 3251 (2021).
- [36] M. Millhouse, A. Melatos, G. Howitt, J. B. Carlin, L. Dunn, and G. Ashton, *Mon. Not. R. Astron. Soc.* **511**, 3304 (2022).
- [37] R. Moradi, L. Li, J. A. Rueda, R. Ruffini, N. Sahakyan, and Y. Wang, [arXiv:2103.09158](https://arxiv.org/abs/2103.09158).
- [38] S. Chandrasekhar, *Ellipsoidal figures of equilibrium* (Yale University Press, New Haven, 1969).
- [39] D. Lai, F. A. Rasio, and S. L. Shapiro, *Astrophys. J. Suppl. Ser.* **88**, 205 (1993).
- [40] L. S. Finn and S. L. Shapiro, *Astrophys. J.* **359**, 444 (1990).
- [41] F. Cipolletta, C. Cherubini, S. Filippi, J. A. Rueda, and R. Ruffini, *Phys. Rev. D* **92**, 023007 (2015).
- [42] L. M. Becerra, R. Moradi, J. A. Rueda, R. Ruffini, and Y. Wang, [arXiv:2208.03069](https://arxiv.org/abs/2208.03069).
- [43] P. B. Rau and A. Sedrakian, *Astrophys. J. Lett.* **902**, L41 (2020).
- [44] P. B. Rau and A. Sedrakian, *Mon. Not. R. Astron. Soc.* **509**, 1854 (2021).
- [45] A. Tsokaros, M. Ruiz, V. Paschalidis, S. L. Shapiro, L. Baiotti, and K. Uryō, *Phys. Rev. D* **95**, 124057 (2017).
- [46] R. W. Romani, D. Kandel, A. V. Filippenko, T. G. Brink, and W. Zheng, *Astrophys. J. Lett.* **934**, L18 (2022).
- [47] J. P. Ostriker and J. E. Gunn, *Astrophys. J.* **157**, 1395 (1969).
- [48] A. Ferrari and R. Ruffini, *Astrophys. J. Lett.* **158**, L71 (1969).
- [49] R. Ruffini and J. A. Wheeler, in *Proceeding of the Astrophysical Aspects of Weak Interactions, 1970*, *Problemi Attuali di Scienza e di Cultura* (Accademia Nazionale dei Lincei, Roma, 1971), pp. 165–186.
- [50] S. Chandrasekhar, *Astrophys. J.* **161**, 571 (1970).
- [51] B. D. Miller, *Astrophys. J.* **187**, 609 (1974).
- [52] D. Lai and S. L. Shapiro, *Astrophys. J.* **442**, 259 (1995).
- [53] P. Astone *et al.*, *Phys. Rev. D* **71**, 042001 (2005).
- [54] J. Aasi, B. P. Abbott, R. Abbott *et al.*, *Classical Quantum Gravity* **32**, 074001 (2015).
- [55] D. Ganapathy, L. McCuller, J. G. Rollins, E. D. Hall, L. Barsotti, and M. Evans, *Phys. Rev. D* **103**, 022002 (2021).
- [56] H. Dimmelmeier, J. A. Font, and E. Müller, *Astron. Astrophys.* **393**, 523 (2002).
- [57] C. L. Fryer and K. C. B. New, *Living Rev. Relativity* **14**, 1 (2011).
- [58] E. Leiderschneider and T. Piran, *Phys. Rev. D* **104**, 104002 (2021).

**First minutes of a binary-driven hypernova**L. M. Becerra,<sup>9,1,\*</sup> R. Moradi,<sup>1,3,6,†</sup> J. A. Rueda<sup>Ⓞ,1,2,3,4,5,‡</sup> R. Ruffini,<sup>1,3,7,8,§</sup> and Y. Wang<sup>1,3,6,||</sup><sup>1</sup>ICRANet, Piazza della Repubblica 10, I-65122 Pescara, Italy<sup>2</sup>ICRANet-Ferrara, Dipartimento di Fisica e Scienze della Terra,

Università degli Studi di Ferrara, Via Saragat 1, I-44122 Ferrara, Italy

<sup>3</sup>ICRA, Dipartimento di Fisica, Sapienza Università di Roma, Piazzale Aldo Moro 5, I-00185 Roma, Italy<sup>4</sup>Dipartimento di Fisica e Scienze della Terra, Università degli Studi di Ferrara,

Via Saragat 1, I-44122 Ferrara, Italy

<sup>5</sup>INAF, Istituto di Astrofisica e Planetologia Spaziali, Via Fosso del Cavaliere 100, I-00133 Rome, Italy<sup>6</sup>INAF, Osservatorio Astronomico d'Abruzzo, Via M. Maggini snc, I-64100 Teramo, Italy<sup>7</sup>Université de Nice Sophia-Antipolis, Grand Château Parc Valrose, Nice, CEDEX 2, France<sup>8</sup>INAF, Viale del Parco Mellini 84, I-00136 Rome, Italy<sup>9</sup>Escuela de Física, Universidad Industrial de Santander, A.A.678, Bucaramanga 680002, Colombia

(Received 6 May 2022; accepted 20 September 2022; published 3 October 2022)

We simulate the first minutes of the evolution of a binary-driven hypernova event, with a special focus on the associated accretion processes of supernova ejecta onto the newborn neutron star ( $\nu$ NS) and the NS companion. We calculate the rotational evolution of the  $\nu$ NS and the NS under the torques exerted by the accreted matter and the magnetic field. We take into account general relativistic effects through effective models for the NSs binding energy and the specific angular momentum transferred by the accreted matter. We use realistic hypercritical accretion rates obtained from three-dimensional smoothed-particle-hydrodynamics numerical simulations of the binary-driven hypernova event for a variety of orbital periods. We show that the rotation power of the  $\nu$ NS has a unique double-peak structure while that of the NS has a single peak. These peaks are of comparable intensity and can occur very close in time or even simultaneously depending on the orbital period and the initial angular momentum of the stars. We outline the consequences of the above features in the early emission and their consequent observation in long gamma-ray bursts.

DOI: 10.1103/PhysRevD.106.083002

**I. INTRODUCTION**

The phenomenological classification of gamma-ray bursts (GRBs) is based on the observed time it takes to release 90% of the total isotropic energy ( $E_{\text{iso}}$ ) in the gamma-rays prompt emission,  $T_{90}$ . Long GRBs are those with  $T_{90} > 2$  s and short GRBs are the sources with  $T_{90} < 2$  s [1–5]. The Burst And Transient Source Experiment on board the COMPTON Gamma-Ray Observatory showed the isotropic distribution of GRBs in the sky, which suggests their extragalactic origin [6]. The BeppoSAX satellite launched allowed the follow-up of the GRB emission leading to the discovery of a long-lasting x-ray afterglow with the first case of GRB 970228 [7]. BeppoSAX improved the GRB localization to arcminutes resolution, which allowed the detection of the optical

counterparts and host galaxies by earth-based telescopes. These observations led to measuring the cosmological redshift of GRBs. More afterglows were detected, and the cosmological distances of  $\approx 5$ –10 Gpc confirmed the GRB cosmological origin. These measurements confirmed the (long-time suspected) great energy release of GRBs,  $E_{\text{iso}} \approx 10^{50}$ – $10^{54}$  erg.

It was soon reached the consensus that the huge energetics involved in both short and long GRBs imply they are related to the process of gravitational collapse at the end of massive stars, i.e., processes involving neutron stars (NSs) and/or black holes (BHs). For short bursts, NS-NS and/or NS-BH binary mergers were proposed (see, e.g., the pioneering works [8–11]). For long bursts, the picture of a *collapsar* [12], the core-collapse of a single massive star leading to a BH (or a magnetar) surrounded by a massive accretion disk, has become the traditional GRB model (see, e.g., [13,14], for reviews). The traditional model for the prompt emission of both short and long GRBs follows the dynamics of a *fireball*, an optically thick plasma of electron-positron ( $e^-e^+$ ) pairs and photons in equilibrium with a baryonic plasma [8,9,11,15,16].

\*laura.becerra7@correo.uis.edu.co

†rahim.moradu@icranet.org

‡jorge.rueda@icra.it

§ruffini@icra.it

||yu.wang@icranet.org

The current version of the traditional model of GRB assumes the fireball expands in a collimated relativistic jet expanding with Lorentz factors  $\Gamma \sim 10^2\text{--}10^3$  [17–21]. The internal shock produces the prompt emission, and the external shock generates the afterglow by interacting with the interstellar medium producing synchrotron radiation, and very-high-energy emission by synchrotron self-Compton [13,14,22,23]. There have been additional details, modifications and/or extensions made to the above main picture, and we refer the reader to the recent comprehensive book by [24] for more details on the latest developments of the traditional GRB model.

The optical follow-up of the afterglow guided by the GRB localization by BeppoSAX (then extended by the Neil Gehrels Swift Observatory [25–27]) led to another great discovery: the association of long GRBs with type Ic supernovae (SNe). The first evidence of such an association was the temporal and spatial coincidence of GRB 980425 and SN 1998bw [28]. Many additional associations followed, confirming the GRB-SN connection [29–31]. There have been attempts to overcome the natural drawback of the extreme requirement of the gravitational collapse of a massive star to form a collapsar, the jetted fireball, and an SN explosion. Some models propose that an efficient neutrino emission from the accretion disk might power a successful SN explosion [32] or a beamed outflow/wind that hosts the nucleosynthesis of the nickel required to explain the optical SN (see, e.g., [33–35]).

Having recalled the generalities of the traditional model of GRBs, we turn now to the alternative scenario based on a binary progenitor. First, we recall the seminal work of [36] that, from a binary stellar evolution viewpoint, pointed out a variety of binaries that can lead to GRB events. Second, long GRBs and SNe are characterized by very different energetics, the latter in the range  $10^{49}\text{--}10^{51}$  erg, and the former in the range  $10^{49}\text{--}10^{54}$  erg. The high GRB energetics point to the gravitational collapse to a stellar-mass BH, while a SN originate in the core collapse of a massive star forming a NS. The formation of a BH in core-collapse SN is discarded by the low observed masses of pre-SN progenitors,  $\lesssim 18 M_{\odot}$  [37], which are unable to lead to direct collapse to a BH (see [37,38], although the threshold mass for BH formation is not sharply defined and may depend on several physical pre-SN star properties [39]). From this point of view, it seems unlikely that the GRB and the SN can both originate from the single-star progenitor. One of the most compelling reasons for the quest for a binary GRB progenitor arises from their association with SNe of type Ic, i.e., that lack hydrogen (H) and helium (He) in their spectra. From theory and observations, the most accepted view is that SNe Ic are produced by bare He, carbon-oxygen (CO), or Wolf-Rayet (WR) stars whose hydrogen and helium envelopes have been stripped during their evolution (see, e.g., [40,41]). The stripped envelope He/CO/WR are thought to form tight binaries with a

compact-star companion (e.g., a NS) that helps them to get rid of its H/He layers through multiple mass-transfer and common-envelope phases (see, e.g., [40,42–47], and Sec. II for further details).

The binary-driven hypernova (BDHN) model of long GRBs follows the natural fate of some stripped-envelope binaries. The GRB progenitor is a CO-NS binary at the end of the thermonuclear evolution of the CO star, i.e., at the second core-collapse SN event in the evolution of the binary (the first SN formed the NS companion; see Sec. II for details on the binary evolutionary path). The BDHN is rooted in the concept of induced gravitational collapse that can occur when the CO star undergoes SN in presence of the NS companion [48], and the different emissions observed in the GRB are explained through a sequence of physical processes following the SN explosion (see, e.g., [48–54]). The sequence of physical processes is as follows (see Fig. 1). The gravitational collapse of the iron core of the CO star leads to the formation of a newborn NS ( $\nu$ NS) at its center and ejects the outer layers of the star. The ejecta triggers an accretion process onto the NS companion, while matter fallback also occurs leading to an accretion process onto the  $\nu$ NS. Both accretion processes proceed at hypercritical (i.e., highly super-Eddington) rates thanks to a copious neutrino emission [54,55]. In compact binaries with orbital periods of a few minutes, the hypercritical accretion onto the NS companion brings it the critical mass inducing its gravitational collapse and forming a rotating (Kerr) BH. We have called these systems BDHN of type I (hereafter BDHN I). In less compact binaries, the NS companion does not reach the critical mass and holds stable as a more massive and fast rotating NS. We have called these systems BDHN of type II (hereafter BDHN II). Therefore, if the binary is not disrupted by the explosion, the BDHN scenario contemplates two possible fates, the formation of a NS-NS (in BDHN II), or the formation of a NS-BH (in BDHN I). Only the former fate has been considered in stripped-envelope binaries (see Sec. II).

We recall in Sec. II the sequence of physical processes that occur in BDHN I and II triggered by the SN explosion in the CO-NS progenitor binary. Those processes lead to specific observables (episodes) that can be identified in the data (multiwavelength light-curves and spectra) of high-energetic (BDHN I) and low-energetic (BDHN II) GRBs. In-depth time-resolved analyses have led to the interpretation of the GRB data in terms of the above physical episodes in both BDHN I and II (see, e.g., [57–61] and references therein).

In this article, we focus on the possible observable emission by the  $\nu$ NS and the NS companion during their individual hypercritical accretion processes in the first minutes of evolution following the core collapse of the CO star leading to the SN explosion, and address its possible observables in long GRBs. The relevance of this task is boosted by the recent results obtained in the detailed



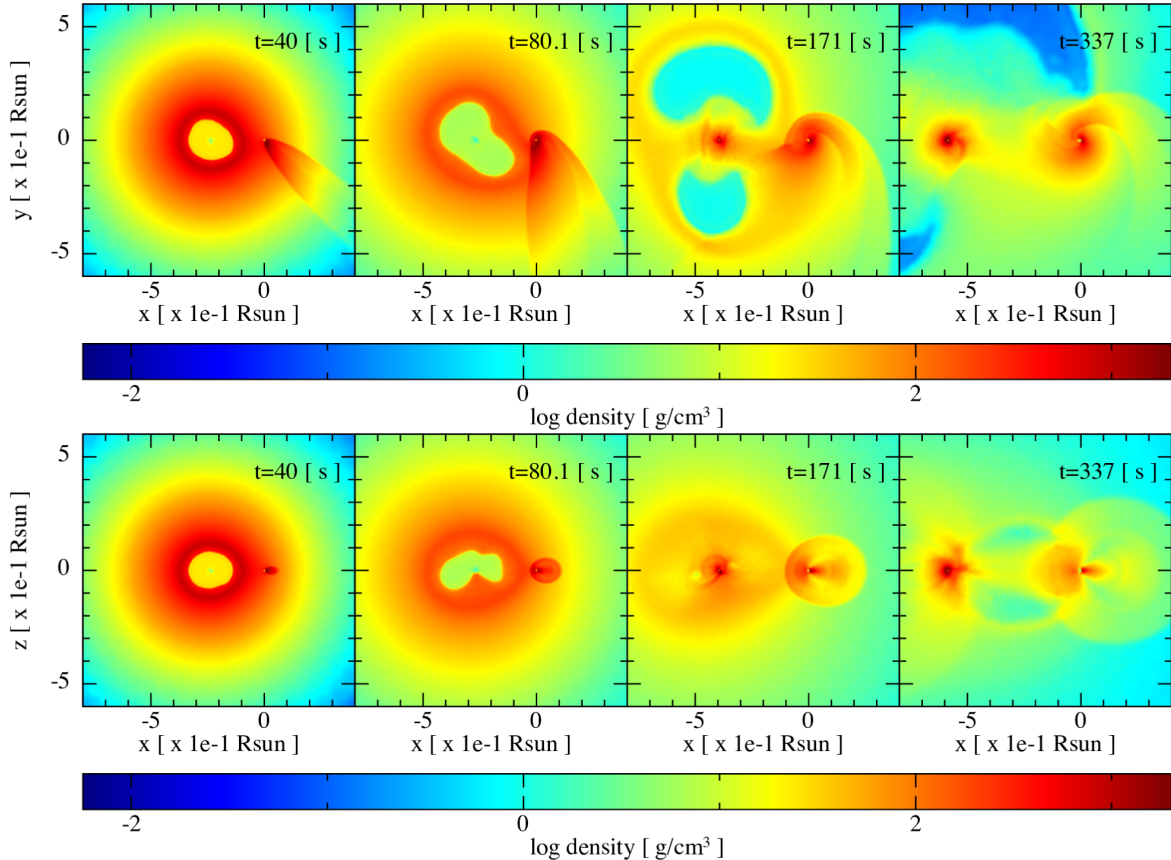


FIG. 1. SPH simulation of a BDHN I: model “30m1p1eb” of Table 2 in [49]. The binary progenitor is composed of a CO star of  $\approx 9 M_{\odot}$ , produced by a ZAMS star of  $30 M_{\odot}$ , and a  $2 M_{\odot}$  NS companion. The orbital period is  $\approx 6$  minutes. Each frame, from left to right, corresponds to selected increasing times with  $t = 0$  s the instant of the SN shock breakout. The upper panel shows the mass density on the equatorial plane and the lower panel the plane orthogonal to the equatorial one. The reference system is rotated and translated to align the  $x$  axis with the line joining the binary components. The origin of the reference system is located at the NS companion position. The first frame corresponds to  $t = 40$  s, and it shows that the particles entering the NS capture region form a tail behind the star. These particles then circularize around the NS, forming a thick disk that is already visible in the second frame at  $t = 80$  s. Part of the SN ejecta is also accreted by the  $\nu$ NS as is appreciable in the third frame at  $t = 171$  s. At  $t = 337$  s (about one orbital period), a disk structure has been formed around the  $\nu$ NS and the NS companion. This figure has been produced with the SNsplash visualization program [56].

time-resolved analysis of GRB 190829A [62]. This source is a low-luminosity GRB, hence interpreted as a BDHNe II. The prompt emission of GRB 190829A shows a double-peak structure as expected from the emissions due to accretion process onto the  $\nu$ NS and the NS companion [49]. The additional properties of the BDHN model, e.g., the multiwavelength afterglow by synchrotron radiation of the SN ejecta powered by the  $\nu$ NS, also fit the observational data of this source.

The above results on the successful qualitative and quantitative interpretation of GRB 190829A encourage us to enlarge our knowledge on the early accretion process in BDHNe by exploring as much as possible the system parameters. In this line, we recall that [49] presented a comprehensive analysis of the accretion process onto both NSs exploring a wide window of values for some system parameters such as the SN explosion energy, orbital period,

initial NS companion mass, CO star mass, asymmetric SN explosions, and three different NS equation of state (EOS). These simulations assume the NSs are initially nonrotating and aim to determine the fate of the NSs. Namely, they evaluate if the NSs reach the critical mass for gravitational collapse and form a BH. We aim here to assess the previously unaccounted effect of an initially rotating NS companion. In particular, we evaluate how an initially nonzero angular momentum of the NS companion affects the rate at which the  $\nu$ NS and the NS gain gravitational mass, angular momentum, and rotational power. The latter is a proxy for the power releasable by the stars in the early BDHN evolution before the BH formation. Based on these results, we discuss the possible observational features of the above process in the data of low-energetic and high-energetic GRBs.

The article is organized as follows. In Sec. II, we summarize the physical processes leading to the GRB

observables and the stellar evolution formation channel of BDHNe. Section III presents the numerical simulations of the SN explosion in the CO-NS binary used in this article, with emphasis on the estimation of the accretion rates onto the  $\nu$ NS and the NS companion. We present in Sec. IV the treatment to calculate the evolution of the NSs structure parameters with focus on the rotational evolution under the action of accretion and magnetic torques. In Sec. V, we calculate the rotational energy gained by the stars during the hypercritical accretion for a variety of initial conditions, and discuss the relevant features for GRB observations. Finally, in Sec. VI we draw the conclusions of this article.

## II. PHYSICAL PROCESSES, OBSERVABLES, AND EVOLUTIONARY PATH OF BDHNE

Before entering into details of the calculation, we recall the emission episodes of a BDHN event and how they are associated with the observed emissions in a long GRB.

### A. Physical processes and related observables

First, as we shall show in this article, the SN explosion and the hypercritical accretion onto the  $\nu$ NS and the NS companion can be observed as precursors to the prompt gamma-ray emission (see, e.g., [54,60]).

In the case of BH formation (BDHN I), the gravito-magnetic interaction of the newborn Kerr BH with the surrounding magnetic field inherited from the collapsed NS induces an electric field. This system is what we have called the *inner engine* of the high-energy emission of long GRBs [58,61,63,64].

The induced electric field is initially overcritical leading to an electron-positron ( $e^+e^-$ ) pair plasma. The plasma self-accelerates to ultrarelativistic velocities and once it becomes transparent its gamma-rays emission is observed as the GRB ultrarelativistic prompt emission (UPE) phase (see [57,65], for details). The  $e^+e^-$  plasma loaded with baryons from the SN ejecta, expand through the ejecta and as it gets transparent lead to the gamma- and x-ray flares observed in the early afterglow [66].

The electric field accelerates to ultrarelativistic velocities the electrons from the matter surrounding the BH. Along the BH rotation axis the electric and magnetic field are parallel, so there are no significant radiation losses, implying that electrons gain a kinetic energy equal to the electric potential energy difference from the acceleration point to infinity. Electrons can reach energies of up to  $10^{18}$  eV and protons of up to  $10^{21}$  eV [63], hence contributing to ultra high-energy cosmic rays. Off-polar axis, synchrotron radiation losses occur leading to the observed GeV emission of long GRBs [61,63,64,67].

Synchrotron radiation by relativistic electrons in the ejecta expanding in the magnetized medium provided by the  $\nu$ NS magnetic field, and powered by the  $\nu$ NS rotational energy, explains the afterglow emission in the x-rays,

optical, and radio wavelengths [59,60,68]. Because this synchrotron afterglow depends only on the  $\nu$ NS, it is present both in BDHN I and II.

Finally, there is the emission observed in the optical band powered by the energy release of nickel decay (into cobalt) in the SN ejecta. We refer to [69–71] for recent reviews on the BDHN scenario of long GRBs and the related physical phenomena.

### B. Evolutionary path

Possible binary evolution paths for the formation of the CO-NS binaries of BDHNe have been discussed in [52]. The natural evolutionary paths are those conceived for the formation of ultrastripped binaries, mainly introduced in the literature for the explanation of the population of binary neutron stars and low-luminosity and/or rapid-decay-rate SNe [72,73]. The evolution starts from two massive stars. The first core-collapse SN of the primary star forms a NS. After that, the system undergoes a series of mass transfer phases, ejecting both the hydrogen and helium shells of the secondary to produce a binary composed of a massive CO star and a NS.

The traditional picture assumes that the second SN explosion in the binary evolution, when the iron core of the CO star undergoes gravitational collapse, forms an NS-NS binary (see, e.g., [73–75]). The BDHN model explores the possibility that for short orbital period binaries, the NS companion of the exploding CO star can accrete enough mass to reach the critical mass and form a Kerr BH. Numerical simulations include most of the relevant physical processes occurring in the cataclysmic event (see Sec. III for details). In those cases, the explosion generates an NS-BH if the binary keeps bound [52]. Our numerical simulations of the BDHN scenario show three possible fates for the binaries: NS-NS, NS-BH, or binary disruption [49].

Simulations of the stellar evolution of massive binaries with detailed physics are still under development. Most stellar evolution simulations have focused on single stars, and most of the existing simulations of binary evolution do not self-consistently account for possible effects of the binary interactions on the thermonuclear and mass loss of the binary components (see discussion in [76,77]). These latter works represent a step toward self-consistent stellar evolution models leading to ultrastripped binaries, and possibly allowing for more compact binaries where the BDHN process occurs. Current simulations have lead to CO/He-NS binaries with orbital periods as short as 50 minutes (e.g., [73]), which is close to the orbital periods we consider here (see, e.g., Fig. 2).

Because of the rareness of the GRB phenomenon, consistent with the short orbital periods required for BH formation in BdHNe, we expect these CO-NS binaries to be a small subset of the ultrastripped binaries. Since 0.1%–1% of the total SN Ibc are expected to be

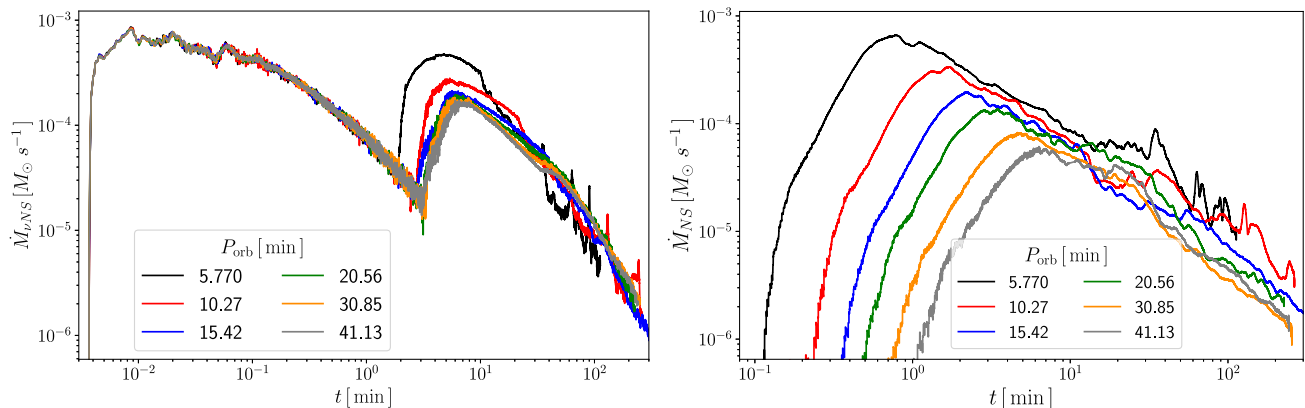


FIG. 2. Accretion rate onto the  $\nu$ NS (left) and onto the NS companion (right) as a function of time, obtained from SPH simulations of BDHNe with different orbital periods.

ultrastripped binaries [73], we estimate that only  $\approx 0.01\%$ – $0.1\%$  of ultrastripped binaries are needed to explain the observed population of BDHNe [52].

### III. SIMULATION OF THE BDHN EARLY EVOLUTION

We first obtain from numerical simulations a realistic time evolution of the accretion rate onto the  $\nu$ NS and the NS companion. We perform smoothed-particle-hydrodynamics (SPH) simulations with the *SNSPH* code adapted to the binary system progenitor of the BDHN presented in [49]. This Newtonian, three-dimensional (3D) Lagrangian code calculates the evolution of the position, momentum (linear and angular), and thermodynamics (pressure, density, temperature) of the particles. The code calculates the accretion rate by counting the particles that become gravitationally captured by either NS. The Newtonian scheme suffices for this task since the size of the gravitational capture region (i.e., the Bondi-Hoyle radius) for the system parameters is hundreds to thousands times bigger than the Schwarzschild radius of the NSs [49]. Having obtained the rate of particles (i.e., baryonic mass) that are gravitationally captured by the NSs, i.e.,  $\dot{M}_{\nu\text{NS}}^{\text{cap}}$  and  $\dot{M}_{\text{NS}}^{\text{cap}}$ , we calculate the NSs gravitational mass and angular momentum evolution including general relativistic effects as described in Sec. III.

Figure 1 shows snapshots of the mass density of the SN ejecta in the  $y$ - $x$  plane, the binary equatorial plane, and the  $z$ - $x$  plane at different times. In this simulation, the mass of the CO star, just before its collapse, is around  $8.89 M_{\odot}$ . This pre-SN configuration is obtained from the thermonuclear evolution of a zero-age-main-sequence (ZAMS) star of  $M_{\text{ZAMS}} = 30 M_{\odot}$ . The NS companion has a mass of  $2 M_{\odot}$ , and the orbital period before the SN explosion is of 5.77 min. The latter is the shortest orbital period that the system can have without triggering Roche-lobe overflow (see, e.g., [51]).

The SPH simulation starts when the SN shock front reaches the CO star surface, i.e., we mapped to a 3D-SPH configuration, the 1D core-collapse supernova simulation of [78]. At this moment, the collapse of the CO star has formed a  $\nu$ NS of  $1.75 M_{\odot}$ , and around  $7.14 M_{\odot}$  is ejected by the SN explosion. In the simulation, the  $\nu$ NS and NS companion are modeled as point masses, and interact only gravitationally with the SN particles and between them. We allow these two point particles to increase their mass by accreting other particles from the SN material following the algorithm described in [49].

Figure 1 shows that the SN ejecta which is gravitationally captured by the NS companion forms first a tail behind the star, and then circularize around it forming a thick disk. At the same time, the particles from the innermost layers of the SN ejecta that were not able to escape from the  $\nu$ NS gravitational field, fallback and are accreted by the  $\nu$ NS. After a few minutes, part of the material in the disk around the NS companion is also attracted by the  $\nu$ NS, producing an enhancement of the accretion process onto the  $\nu$ NS. The hydrodynamics of the matter infalling and accreting onto a NS at hypercritical rates has been extensively studied in different astrophysics contexts taking into account details on the neutrino emission, e.g., fallback accretion in SN [79–82], accreting NS in x-ray binaries [83], and for the case of BDHNe, we refer to [51,54,55] for details. The latter includes a formulation in a general relativistic background, and account for neutrino flavor oscillations. The relevant, not obvious result is that these simulations show that the NS can indeed accrete the matter at the hypercritical rate at which baryonic mass from the SN ejecta falls into the gravitational capture region of the NS. Therefore, we assume in this article that the accretion rate inferred with the SPH code as described in Sec. II as the effective baryonic mass accretion rate onto the NS, i.e., we assume  $\dot{M}_{b,\nu\text{NS}} = \dot{M}_{\nu\text{NS}}^{\text{cap}}$  and  $\dot{M}_{b,\text{NS}} = \dot{M}_{\text{NS}}^{\text{cap}}$ .

Figure 2 shows the accretion rate onto the  $\nu$ NS and the NS companion obtained from SPH simulations for selected

orbital periods that cover a range of BDHN I and II. The accretion rate onto the  $\nu$ NS shows two prominent peaks. The second peak of the fallback accretion rate onto the  $\nu$ NS is a unique feature of BDHNe because, as explained above (see, also, [49], for additional details), it is caused by the influence of NS companion. The accretion rate onto the NS companion shows a single-peak structure, accompanied by additional peaks of smaller intensity and shorter timescales, more evident in binaries with short orbital periods. Such small peaks are produced by episodes of higher and lower accretion that occur as the NS companion orbits across the ejecta and find regions of higher and lower density.

#### IV. NEUTRON STAR ROTATIONAL EVOLUTION

We calculate the evolution of the  $\nu$ NS and the NS companion gravitational mass and angular momentum following the formalism described in [49]. At every time, we describe the NS as a rigidly rotating configuration described by a stationary, axisymmetric metric fulfilling the Einstein field equations. Under these conditions, each equilibrium configuration is characterized by its baryonic mass,  $M_b$ , and its angular momentum,  $J$ . Instead of integrating the Einstein equations at every time step, we adopt the following procedure:

- (1) We neglect any direct effect of the binary companion gravitational field in the self-gravity of the other star. This assumption is based on the relatively large binary separations involved, i.e., about  $10^3$ – $10^4$  Schwarzschild radii of the NS. Therefore, we calculate the evolution of each NS independently on the other. The only effect caused by the presence of the binary companion on the baryonic mass accretion rate as discussed in Sec. II (see Fig. 2).
- (2) We use the NS equilibrium configurations calculated in [84] through the numerical integration of the Einstein equations with the rapidly rotating neutron star numerical code. The main result we use here is that the gravitational (Komar) mass of the NS, fully determined by  $M_b$  and  $J$ , i.e.,  $M = M(M_b, J)$ , can be obtained from the following approximately EOS-independent fitting formula relating the above three quantities [84]:

$$\frac{M_b}{M_\odot} = \frac{M}{M_\odot} + \frac{13}{200} \left( \frac{M}{M_\odot} \right)^2 \left( 1 - \frac{1}{130} j^{1.7} \right), \quad (1)$$

where  $j \equiv cJ/(GM_\odot^2)$  is the dimensionless angular momentum. We notice that this dimensionless parameter is different from the dimensionless Kerr parameter,  $\alpha = cJ/(GM^2)$ , so the two parameters are related by  $j = \alpha(M/M_\odot)^2$ .

- (3) It has been shown in full generality that the evolution of the NS gravitational mass satisfies [85]

$$\dot{M} = \left( \frac{\partial M}{\partial M_b} \right)_J \dot{M}_b + \left( \frac{\partial M}{\partial J} \right)_{M_b} \dot{J}, \quad (2)$$

where  $\dot{M}_b$  is the baryonic mass accretion rate and  $\dot{J}$  is the rate at which angular momentum is transferred to the NS. We recall that  $\dot{M}_b$  is here obtained from the SPH numerical simulations described in Sec. II. For the numerical integration of Eq. (2), we must know the partial derivatives which comes out from the integration of the Einstein equations.

- (4) We can obtain analytic expressions for the two partial derivatives in Eq. (2) readily from Eq. (1):

$$\left( \frac{\partial \mu}{\partial M_b} \right)_j = \frac{1}{1 + \frac{13}{100} \mu \left( 1 - \frac{1}{130} j^{1.7} \right)}, \quad (3)$$

$$\left( \frac{\partial \mu}{\partial j} \right)_{\mu_b} = \frac{\frac{1.7}{2000} \mu^2 j^{0.7}}{1 + \frac{13}{100} \mu \left( 1 - \frac{1}{130} j^{1.7} \right)}, \quad (4)$$

where  $\mu = M/M_\odot$ .

- (5) Finally, we must supply the angular momentum conservation equation by specifying the torques acting onto the stars, i.e., an equation for  $\dot{J}$ . We assume that the NSs are subjected to the positive torque by accretion and the negative torque due to the magnetic braking mechanism, i.e.,

$$\dot{J} = \tau_{\text{acc}} + \tau_{\text{mag}}, \quad (5)$$

where each torque is specified below.

With the above procedure, we obtain the evolution of  $M$  and  $J$  with time. We now proceed to the specification of the torques acting on the NSs. We start with the angular momentum transfer by accretion. Accordingly to the numerical simulations, we assume that the infalling material form a disk around the star before being accreted. Therefore, the accreted matter exerts a (positive) torque

$$\tau_{\text{acc}} = \chi l \dot{M}_b, \quad (6)$$

where  $l$  the specific (i.e., per unit mass) angular momentum of the innermost stable circular orbit around the NS, and  $\chi \leq 1$  is an efficiency parameter of angular momentum transfer. The angular momentum of the last stable circular orbit around rotating NSs was calculated in [86] from numerical integration of the geodesic equations in the exterior stationary axially symmetric spacetime of the NSs. The latter were obtained from numerical integration of the Einstein equations for the same EOS used in [84]. The relevant result that we use here is the following approximate EOS-independent expression of  $l$  in terms of  $M$  and  $J$  that fit the numerical results [86]:

$$l = \frac{GM}{c} \left[ 2\sqrt{3} \mp 0.37 \left( \frac{j}{M/M_\odot} \right)^{0.85} \right], \quad (7)$$

where it can be seen that the first term is the specific angular momentum of the last stable circular orbit for the Schwarzschild metric and the second term is a nonlinear correction due to the rotation.

The stars are also subjected to the (negative) torque by the magnetic field. We adopt the point<sup>1</sup> dipole + quadrupole magnetic field model [87]:

$$\tau_{\text{mag}} = \tau_{\text{dip}} + \tau_{\text{quad}}, \quad (8)$$

$$\tau_{\text{dip}} = -\frac{2 B_{\text{dip}}^2 R^6 \Omega^3}{3 c^3} \sin^2 \xi, \quad (9)$$

$$\tau_{\text{quad}} = -\frac{32 B_{\text{quad}}^2 R^8 \Omega^5}{135 c^5} \sin^2 \theta_1 (\cos^2 \theta_2 + 10 \sin^2 \theta_2), \quad (10)$$

where  $\xi$  is the inclination angle of the magnetic dipole moment with respect to the rotation axis, and the angles  $\theta_1$  and  $\theta_2$  specify the geometry of the quadrupole field. For the dipole magnetic field, with strength  $B_{\text{dip}}$ , the pure axisymmetric mode  $m = 0$  is given by  $\xi = 0$ , and the pure  $m = 1$  mode by  $\xi = \pi/2$ . For the quadrupole, with strength  $B_{\text{quad}}$ , the  $m = 0$  mode is given by  $\theta_1 = 0$  and any value of  $\theta_2$ , the  $m = 1$  mode is given by  $\theta_1 = \pi/2$  and  $\theta_2 = 0$ , and the  $m = 2$  mode is set by  $\theta_1 = \theta_2 = \pi/2$ . For our estimates, we adopt the  $m = 1$  mode for the dipole and leave the quadrupole free to range between the  $m = 1$  and  $m = 2$  modes. Therefore, we can write the total magnetic torque (8) as

$$\tau_{\text{mag}} = -\frac{2 B_{\text{dip}}^2 R^6 \Omega^3}{3 c^3} \left( 1 + \eta^2 \frac{16 R^2 \Omega^2}{45 c^2} \right), \quad (11)$$

where  $\eta$  is the quadrupole to dipole magnetic field strength ratio defined by

$$\eta \equiv \sqrt{\cos^2 \theta_2 + 10 \sin^2 \theta_2} \frac{B_{\text{quad}}}{B_{\text{dip}}}. \quad (12)$$

We compute the stellar angular velocity as  $\Omega = J/I$ , being  $I$  the moment of inertia which we estimate with the EOS-independent approximate expression [88]

$$I \approx \left( \frac{G}{c^2} \right)^2 M^3 \sum_{i=1}^4 \frac{b_i}{(M/M_\odot)^i}, \quad (13)$$

<sup>1</sup>We neglect finite-size effects since the ratio between the stellar radius,  $R$ , and the light-cylinder radius,  $R_L = c/\Omega$ , is small, i.e.,  $R/R_L = \Omega R/c \lesssim 0.1$  (see [87], for further details).

where  $b_1 = 1.0334$ ,  $b_2 = 30.7271$ ,  $b_3 = -12.8839$ , and  $b_4 = 2.8841$ . This expression for the moment of inertia neglects the contribution of rotation. We expect an appreciable contribution near the mass-shedding limit where it can be up to 20% larger than a nonrotating estimate (see, e.g., Fig. 3 and related discussion in [89]). This could change at some level the quantitative estimates but not the qualitative conclusions.

Having specified all the above, the evolution of the stellar angular momentum can be computed from angular momentum conservation equation (5), with the aid of Eqs. (6) and (11).

We can now proceed to the integration of the system of differential equations (2) and (5) for the  $\nu$ NS and the NS companion. For this, we must specify the initial mass and angular momentum, as well as the strength of the magnetic dipole and quadrupole. We plot in Fig. 3 examples of evolution of the rotation period ( $P = 2\pi/\Omega$ ) of the  $\nu$ NS with time. We have set initially a nonrotating configuration, i.e.,  $j(0) = 0$ , an initial mass of  $1.8 M_\odot$ , a magnetic dipole strength  $B_{\text{dip}} = 10^{13}$  G, a stellar radius  $R = 10^6$  cm, selected values of the quadrupole to dipole strength ratio, and the  $m = 1$  mode of the quadrupole, i.e.,  $(\theta_1, \theta_2) = (\pi/2, 0)$ . The figure shows that for shorter orbital periods the  $\nu$ NS becomes a faster rotator. The angular momentum transferred by accretion is proportional to the accretion rate, see Eq. (6), so higher accretion rates imply faster rotation rates. Indeed, the presence of the NS companion creates a second peak of accretion onto the  $\nu$ NS, and that peak of accretion becomes higher for shorter orbital periods (see Fig. 2). Therefore, the shorter the orbital period, the more the accretion rate onto the  $\nu$ NS, and consequently the faster its rotation rate. We can see the phase of spinup of the  $\nu$ NS followed by the phase of spindown due to magnetic braking. The presence of a nonzero quadrupole component enhances the spindown phase, making it start earlier and at a higher rotation period (the minimum of the curve shifts to upper left values). The black curves correspond to the case of a pure dipole magnetic field.

## V. ROTATIONAL POWER EVOLUTION

We turn now to estimate the energy gained during the accretion process and that can be released. We plot in Fig. 4 the time derivative of the energy [90]

$$\dot{E} = \Omega \dot{J}, \quad (14)$$

for the  $\nu$ NS and the NS companion. The energy gain follows the behavior of the accretion rate (see Fig. 2), namely, for the  $\nu$ NS is characterized by two peaks, while the NS companion shows a single peak. The reason for this is that at early times the rotational evolution is dominated by the accretion torque which is proportional to the accretion rate. The relative position and intensity of the peaks depends on the orbital period and on the initial

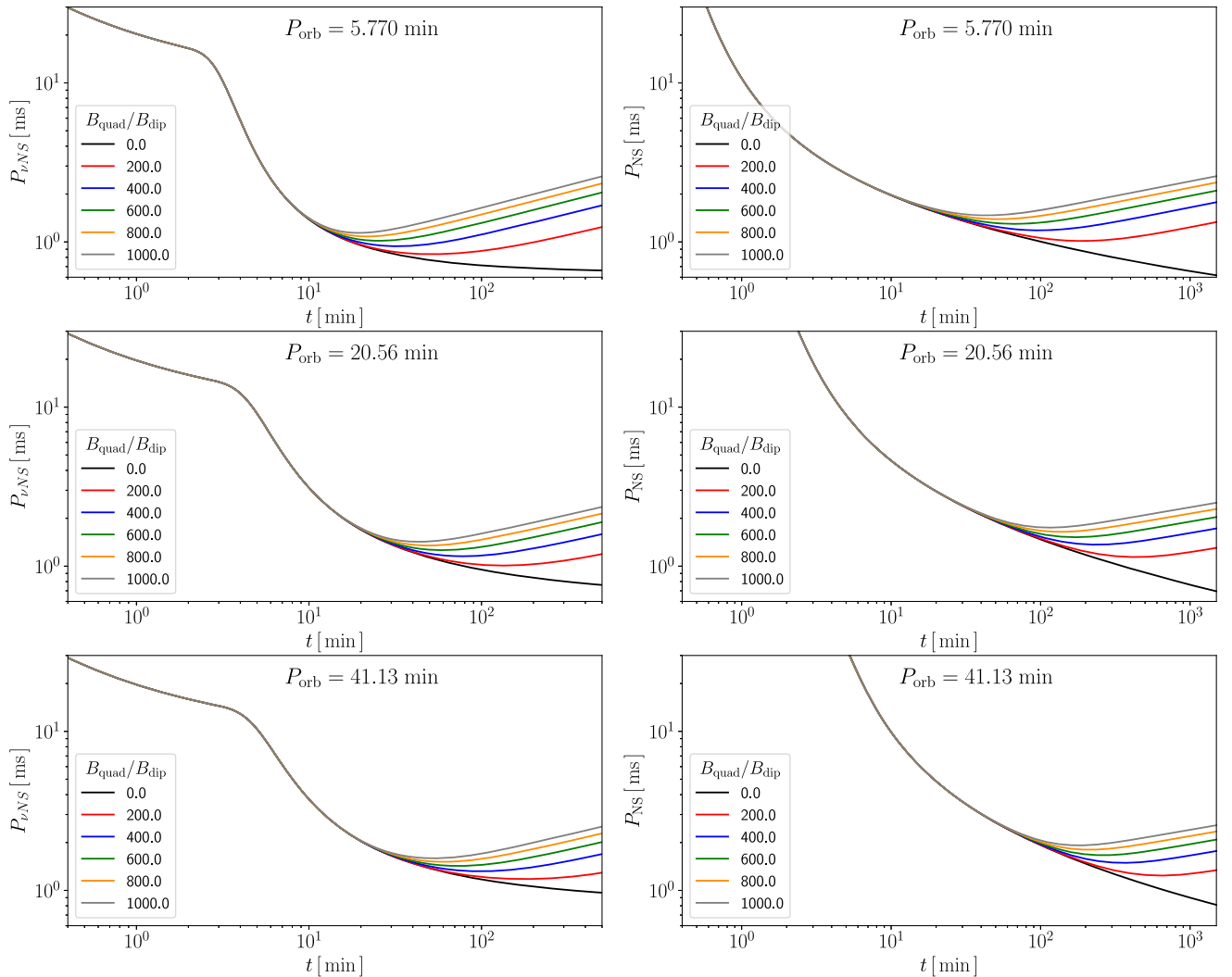


FIG. 3. Evolution of the  $\nu$ NS (left panel) and the NS companion (right panel) rotation period starting from a nonrotating star, i.e.,  $j(0) = 0$ . The  $\nu$ NS and the NS companion initial mass are  $1.8 M_{\odot}$  and  $2 M_{\odot}$ , respectively. For both stars the radius is  $10^6$  cm, the magnetic dipole field strength is  $B_{\text{dip}} = 10^{13}$  G, and the quadrupole to dipole strength ratio is varied from 0 (pure dipole) to 1000. The quadrupole field is set in the  $m = 1$  mode, i.e.,  $(\theta_1, \theta_2) = (\pi/2, 0)$ . The plot shows the phases of spinup and spindown of the  $\nu$ NS. The spindown phase is enhanced by the presence of the quadrupole component. The black curves correspond to the case of a pure dipole magnetic field.

angular momentum of the NSs. In this example, we set an initially nonrotating  $\nu$ NS, and nonzero values for the initial angular momentum of the NS companion (which is more likely to be fast rotator at the time of the BDHN occurrence) in the range  $0 \leq j(0) \leq 1$ . This corresponds to an initial NS angular momentum in the range  $0 \leq J(0) \leq 8.8 \times 10^{48} \text{ g cm}^2 \text{ s}^{-1}$ . Assuming, for instance, an initial mass of  $1.8 M_{\odot}$ , for which Eq. (13) gives a moment of inertia  $I \approx 1.43 \times 10^{45} \text{ g cm}^2$ , this leads to a range of initial rotation frequency  $0 \leq f(0) \leq 685 \text{ Hz}$ , i.e., initial rotation periods  $P(0) \geq 1.46 \text{ ms}$ . This is far from the mass-shedding limit. It has been shown that, at mass shedding, the Kerr parameter reaches an EOS-independent maximum

value  $\alpha \approx 0.7$  (see [91] and also Fig. 7 and Table I in [84]). Instead, the specific value of the angular momentum (or the rotation frequency) depends on the mass of the configuration that reached the mass-shedding limit. The above NS of  $1.8 M_{\odot}$  NS would be at mass shedding if  $j \approx 0.7 \times 1.8^2 \approx 2.27$ . For instance, for the TM1 nuclear EOS, the configuration at the crossing point between the mass-shedding limit and the secular axisymmetric instability has  $\alpha \approx 0.7$  and  $M \approx 2.62 M_{\odot}$ , which leads to  $j \approx 4.8$  and a rotation frequency of 1.34 kHz [84].

The second peak of  $\dot{E}$  of the  $\nu$ NS is a unique feature of BDHNe because this is originated by the second peak of fallback accretion onto the  $\nu$ NS induced by the presence of

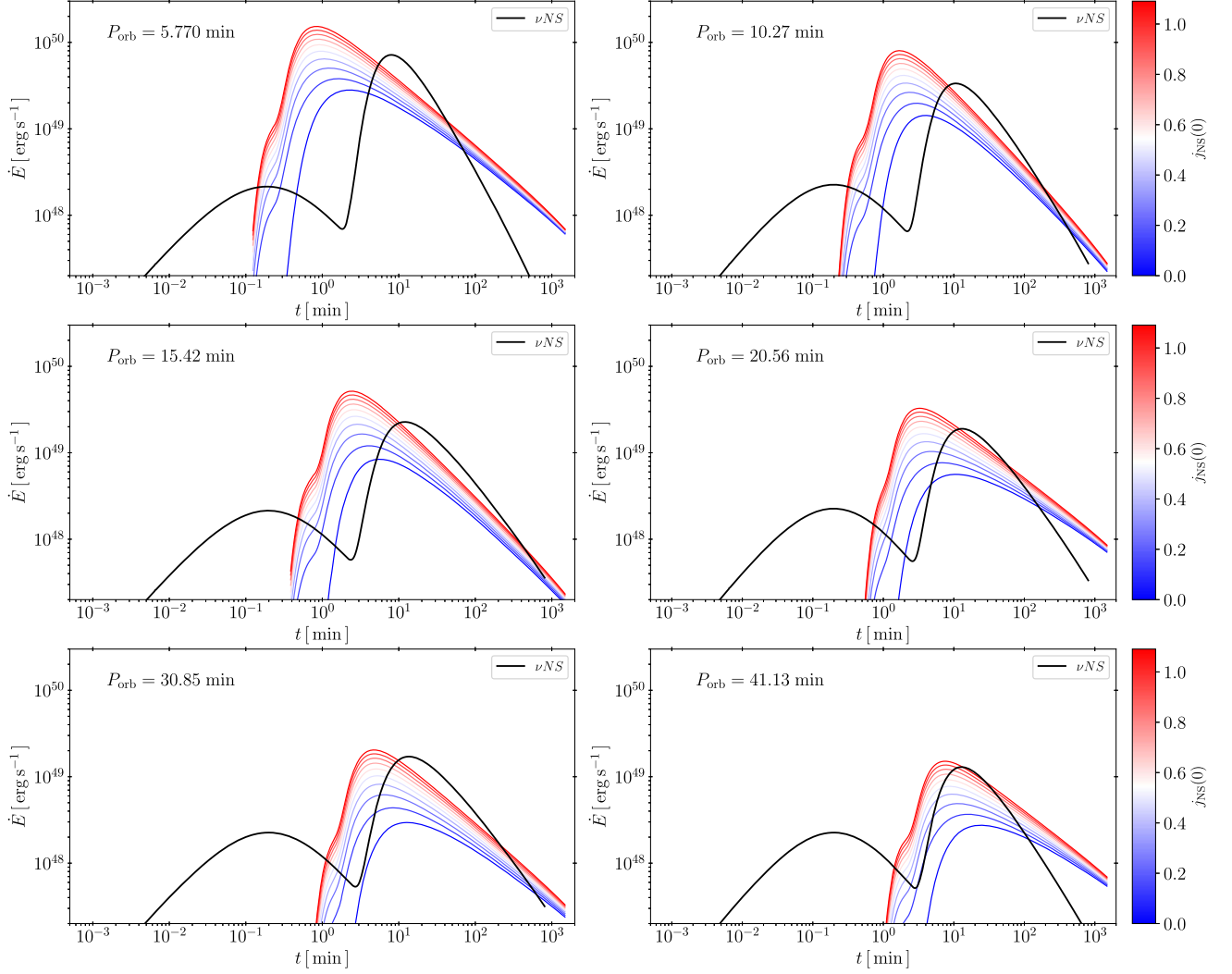


FIG. 4. Evolution with time of  $\dot{E}$ , given by Eq. (14), for the  $\nu$ NS and the NS companion. We set the  $\nu$ NS initially as nonrotating (i.e.,  $J(0) = 0$ ), and explore the effects of a nonzero initial value of the NS companion angular momentum. In this example, we have initial values of the NS dimensionless angular momentum from  $j(0) = 0$  (first curve in blue from bottom to top), to  $j(0) = 1$  (last curve in orange from top to bottom). Each plot corresponds to a binary with a different orbital period (see also Fig. 2). In this example, for simplicity, we set the same initial mass and magnetic dipole moment for both stars, respectively,  $1.8 M_{\odot}$ , radius  $R = 10^6$  cm, and a pure dipole ( $\eta = 0$ ) with magnetic field strength  $B_{\text{dip}} = 10^{13}$  G.

the NS companion (see Fig. 2 and [49] for further details). The intensity of the second peak of the  $\nu$ NS decreases for longer orbital periods. In fact, for a single-star system, the second peak disappears as the second peak of fallback accretion vanishes [49]. The intensity of this peak is comparable to that of the NS companion.

For a faster initial rotation rate, the peak of  $\dot{E}$  for the NS companion increases its intensity and its time of occurrence,  $t_{\text{peak,NS}}$ , shifts to earlier times. Consequently, the time of occurrence of the  $\nu$ NS second peak,  $t_{\text{peak2},\nu\text{NS}}$ , and  $t_{\text{peak,NS}}$  of the NS companion, can be very close to each other (e.g., a few seconds of time separation) or even simultaneous depending on the orbital period and the initial

angular momentum of the stars. For the interpretation of GRB data, it is useful to estimate the time separation of these two peaks, i.e.,

$$\Delta t_{\text{peaks}} = t_{\text{peak,NS}} - t_{\text{peak2},\nu\text{NS}}. \quad (15)$$

We show in Fig. 5  $\Delta t_{\text{peaks}}$  as a function of the initial (dimensionless) angular momentum of the NS companion,  $j(0)$ , and for the selected orbital periods relevant for BDHN I and II studied in this work. We have set the  $\nu$ NS as initially nonrotating. When both stars are initially nonrotating, i.e., for  $j(0) = 0$ , the figure shows that  $\Delta t_{\text{peaks}}$  starts positive for long orbital periods, so the peak of the NS

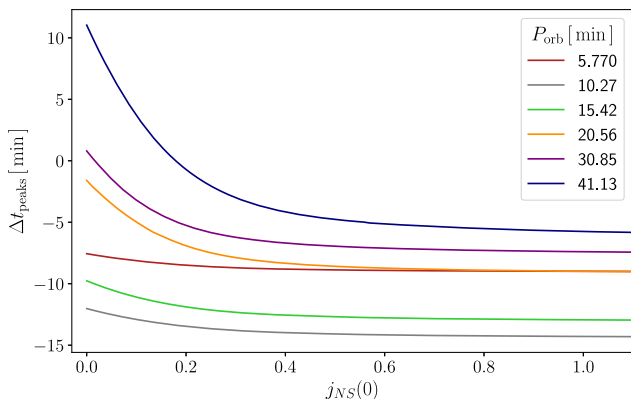


FIG. 5. Time separation between the peak of  $\dot{E}$  of the NS companion and the second peak of  $\dot{E}$  of the  $\nu$ NS (see Fig. 4).

occurs after the second peak of the  $\nu$ NS. For shorter orbital periods, the time separation of the peaks decreases. The peaks become simultaneous for an orbital period close to  $P_{\text{orb}} \approx 31$  min, where  $\Delta t_{\text{peaks}}$  vanishes. For  $P_{\text{orb}} \lesssim 31$  min,  $\Delta t_{\text{peaks}}$  becomes negative, so the peak of the NS occurs before the second peak of the  $\nu$ NS. If we read Fig. 5 at a fixed orbital period, we see that the time separation between peaks decreases for larger initial angular momentum of the NS companion. Therefore, only in binaries with  $P_{\text{orb}} \gtrsim 31$  min the two peaks can occur simultaneously or very close to each other, e.g., with a few seconds of time separation.

## VI. CONCLUSIONS

The increasing amount and quality of the multiwavelength data of GRBs allow us to test theoretical models in great detail. With the aim of providing further tests of the BDHN scenario of GRBs, we calculated in this article the evolution of a BDHN in the first minutes after the SN explosion. Specifically, we calculated the evolution of the  $\nu$ NS formed at the center of the SN, and of the NS companion, as a result of the mass and angular momentum transferred onto them by the hypercritical accretion of SN ejecta. We calculated the accretion rate onto the  $\nu$ NS and the NS companion using three-dimensional SPH numerical simulations performed with the SNSPH code adapted to BDHNe presented in [49].

We followed the evolution of mass and angular momentum calculated from energy and angular momentum conservation accounting for general relativistic effects by using effective models for the NS binding energy and the specific angular momentum transferred by the accreted matter. We have compared and contrasted the features of the accretion rate onto the two stars (see, e.g., Fig. 2). Particularly relevant is the two-peak structure of the accretion rate onto the  $\nu$ NS with respect to the single-peak structure of the one onto the NS companion.

With the knowledge of the accretion rate and having specified the torques due to the accretion process and the magnetic field, we integrated the energy and angular momentum equilibrium equations to determine the rotational evolution of the  $\nu$ NS and the NS companion. We have shown that the NSs evolve first in a spin-up phase dominated by the positive torque due to the accretion process to then start a spin-down phase dominated by the negative torque due to the presence of the magnetic field. We considered both a pure magnetic dipole or a dipole + quadrupole magnetic field configurations (see, e.g., Fig. 3). We show that the shorter the orbital period, the higher the rotation rate acquired by the  $\nu$ NS during the accretion process (see Fig. 3). This result implies that the  $\nu$ NS in BDHN II are slower rotators than the  $\nu$ NS in BDHN I.

We then focused on the evolution of the power gained by the NSs during their corresponding accretion processes. This serves as an estimate of the releasable power by the  $\nu$ NS and the NS companion during this early BDHN evolution. We have shown that the evolution of the power with time reflects the features of the accretion rate, i.e., it has a two-peak structure for the  $\nu$ NS and a single-peak structure for the NS companion (see Fig. 4). We have also studied the dependence of the NS power both on the orbital period and the initial angular momentum of the NS companion. The most relevant feature from the observational point of view is that the second peak of the  $\nu$ NS power is comparable both in intensity as well as in the time of occurrence to the peak of the NS companion power (see Fig. 4). We deepened into this latter feature by studying the time separation between the second peak of the  $\nu$ NS power and the peak of the NS companion power, as a function of the initial angular momentum of the NS companion and for a variety of orbital periods (see Fig. 5).

The rotational energy powered gained by the  $\nu$ NS and the NS companion during their early accretion processes, and the accretion power itself, can lead to early emissions prior to the main prompt emission phase. The results of this work imply the possibility of observing precursors in the x-ray and/or in the gamma rays with a double-peak structure. Therefore, this theoretical prediction of the BDHN evolution and associated emissions during the first minutes after the SN explosion are relevant for the detailed interpretation of GRB multiwavelength data before the prompt emission. In BDHNe II, low-luminosity GRBs in which the NS companion does not collapse to a BH, the  $\nu$ NS and NS emissions presented in this article could be observed as a double-peak prompt emission, as shown in the recent analysis of GRB 190829A [62].

The UPE phase of the GRB (in a BDHN I), the GeV emission, and the following x-optical-radio afterglow are explained by different physical processes occurring in a BDHN after its early evolution analyzed in this work. For details on the UPE phase, see [57], for the GeV emission, see [61,63,64,67], and, for the afterglow, see [59,60,68].



Therefore, the theoretical work presented in this article complements the self-consistent picture developed in the BDHN model for a complete interpretation of the multi-wavelength data of long GRBs, starting from the x and gamma-ray precursors, to the UPE in the MeV, to the GeV emission, to the x-optical-radio afterglow, and finally to the optical emission powered by the radioactive decay of nickel in the SN ejecta.

## ACKNOWLEDGMENTS

We thank the anonymous referees for the insightful comments and suggestions that helped us to improve the presentation of the article. L. M. B. is supported by the Vicerrectoría de Investigación y Extensión—Universidad Industrial de Santander Postdoctoral Fellowship Program No. 2022000293.

- 
- [1] E. P. Mazets, S. V. Golenetskii, V. N. Ilinskii, V. N. Panov, R. L. Aptekar, I. A. Gurian, M. P. Proskura, I. A. Sokolov, Z. I. Sokolova, and T. V. Kharitonova, *Astrophys. Space Sci.* **80**, 3 (1981).
- [2] R. W. Klebesadel, The durations of gamma-ray bursts, in *Gamma-Ray Bursts—Observations, Analyses and Theories*, edited by C. Ho, R. I. Epstein, and E. E. Fenimore (Cambridge University Press, Cambridge, 1992), pp. 161–168.
- [3] J.-P. Dezalay, C. Barat, R. Talon, R. Syunyaev, O. Terekhov, and A. Kuznetsov, in *American Institute of Physics Conference Series*, American Institute of Physics Conference Series Vol. 265, edited by W. S. Paciesas and G. J. Fishman (AIP Publishing, Melville, NY, 1992), pp. 304–309.
- [4] C. Kouveliotou, C. A. Meegan, G. J. Fishman, N. P. Bhat, M. S. Briggs, T. M. Koshut, W. S. Paciesas, and G. N. Pendleton, *Astrophys. J. Lett.* **413**, L101 (1993).
- [5] M. Tavani, *Astrophys. J. Lett.* **497**, L21 (1998).
- [6] C. A. Meegan, G. J. Fishman, R. B. Wilson, W. S. Paciesas, G. N. Pendleton, J. M. Horack, M. N. Brock, and C. Kouveliotou, *Nature (London)* **355**, 143 (1992).
- [7] E. Costa *et al.*, *Nature (London)* **387**, 783 (1997).
- [8] J. Goodman, *Astrophys. J. Lett.* **308**, L47 (1986).
- [9] B. Paczynski, *Astrophys. J. Lett.* **308**, L43 (1986).
- [10] D. Eichler, M. Livio, T. Piran, and D. N. Schramm, *Nature (London)* **340**, 126 (1989).
- [11] R. Narayan, T. Piran, and A. Shemi, *Astrophys. J. Lett.* **379**, L17 (1991).
- [12] S. E. Woosley, *Astrophys. J.* **405**, 273 (1993).
- [13] P. Mészáros, *Annu. Rev. Astron. Astrophys.* **40**, 137 (2002).
- [14] T. Piran, *Rev. Mod. Phys.* **76**, 1143 (2004).
- [15] G. Cavallo and M. J. Rees, *Mon. Not. R. Astron. Soc.* **183**, 359 (1978).
- [16] R. Narayan, B. Paczynski, and T. Piran, *Astrophys. J. Lett.* **395**, L83 (1992).
- [17] A. Shemi and T. Piran, *Astrophys. J. Lett.* **365**, L55 (1990).
- [18] M. J. Rees and P. Meszaros, *Mon. Not. R. Astron. Soc.* **258**, 41P (1992).
- [19] T. Piran, A. Shemi, and R. Narayan, *Mon. Not. R. Astron. Soc.* **263**, 861 (1993).
- [20] P. Meszaros, P. Laguna, and M. J. Rees, *Astrophys. J.* **415**, 181 (1993).
- [21] S. Mao and I. Yi, *Astrophys. J. Lett.* **424**, L131 (1994).
- [22] V. A. Acciari, S. Ansoldi *et al.* (MAGIC Collaboration), *Nature (London)* **575**, 455 (2019).
- [23] B. Zhang, *Nature (London)* **575**, 448 (2019).
- [24] B. Zhang, *The Physics of Gamma-Ray Bursts* (Cambridge University Press, Cambridge, 2018), 10.1017/9781139226530.
- [25] S. D. Barthelmy, L. M. Barbier, J. R. Cummings, E. E. Fenimore, N. Gehrels, D. Hullinger, H. A. Krimm, C. B. Markwardt, D. M. Palmer, A. Parsons, G. Sato, M. Suzuki, T. Takahashi, M. Tashiro, and J. Tueller, *Space Sci. Rev.* **120**, 143 (2005).
- [26] D. N. Burrows *et al.*, *Space Sci. Rev.* **120**, 165 (2005).
- [27] P. W. A. Roming *et al.*, *Space Sci. Rev.* **120**, 95 (2005).
- [28] T. J. Galama, P. M. Vreeswijk, J. van Paradijs, C. Kouveliotou *et al.*, *Nature (London)* **395**, 670 (1998).
- [29] S. E. Woosley and J. S. Bloom, *Annu. Rev. Astron. Astrophys.* **44**, 507 (2006).
- [30] M. Della Valle, *Int. J. Mod. Phys. D* **20**, 1745 (2011).
- [31] J. Hjorth and J. S. Bloom, The Gamma-Ray Burst—Supernova Connection, in *Gamma-Ray Bursts*, Cambridge Astrophysics Series Vol. 51, edited by C. Kouveliotou, R. A. M. J. Wijers, and S. Woosley (Cambridge University Press, Cambridge, 2012), Chap. 9, pp. 169–190.
- [32] A. I. MacFadyen and S. E. Woosley, *Astrophys. J.* **524**, 262 (1999).
- [33] K. Kohri, R. Narayan, and T. Piran, *Astrophys. J.* **629**, 341 (2005).
- [34] M. Milosavljević, C. C. Lindner, R. Shen, and P. Kumar, *Astrophys. J.* **744**, 103 (2012).
- [35] C. C. Lindner, M. Milosavljević, R. Shen, and P. Kumar, *Astrophys. J.* **750**, 163 (2012).
- [36] C. L. Fryer, S. E. Woosley, and D. H. Hartmann, *Astrophys. J.* **526**, 152 (1999).
- [37] S. J. Smartt, *Pub. Astron. Soc. Aust.* **32**, e016 (2015).
- [38] S. J. Smartt, *Annu. Rev. Astron. Astrophys.* **47**, 63 (2009).
- [39] M. Ugliano, H.-T. Janka, A. Marek, and A. Arcones, *Astrophys. J.* **757**, 69 (2012).
- [40] N. Smith, W. Li, J. M. Silverman, M. Ganeshalingam, and A. V. Filippenko, *Mon. Not. R. Astron. Soc.* **415**, 773 (2011).
- [41] J. Teffs, T. Ertl, P. Mazzali, S. Hachinger, and T. Janka, *Mon. Not. R. Astron. Soc.* **492**, 4369 (2020).
- [42] K. Nomoto and M. Hashimoto, *Phys. Rep.* **163**, 13 (1988).
- [43] K. Iwamoto, K. Nomoto, P. Höflich, H. Yamaoka, S. Kumagai, and T. Shigeyama, *Astrophys. J. Lett.* **437**, L115 (1994).
- [44] C. L. Fryer, P. A. Mazzali, J. Prochaska, E. Cappellaro, A. Panaitescu, E. Berger, M. van Putten, E. P. J. van den

- Heuvel, P. Young, A. Hungerford, G. Rockefeller, S.-C. Yoon, P. Podsiadlowski, K. Nomoto, R. Chevalier, B. Schmidt, and S. Kulkarni, *Publ. Astron. Soc. Pac.* **119**, 1211 (2007).
- [45] S.-C. Yoon, S. E. Woosley, and N. Langer, *Astrophys. J.* **725**, 940 (2010).
- [46] S.-C. Yoon, *Pub. Astron. Soc. Aust.* **32**, e015 (2015).
- [47] H.-J. Kim, S.-C. Yoon, and B.-C. Koo, *Astrophys. J.* **809**, 131 (2015).
- [48] J. A. Rueda and R. Ruffini, *Astrophys. J. Lett.* **758**, L7 (2012).
- [49] L. Becerra, C. L. Ellinger, C. L. Fryer, J. A. Rueda, and R. Ruffini, *Astrophys. J.* **871**, 14 (2019).
- [50] L. Izzo, J. A. Rueda, and R. Ruffini, *Astron. Astrophys.* **548**, L5 (2012).
- [51] C. L. Fryer, J. A. Rueda, and R. Ruffini, *Astrophys. J. Lett.* **793**, L36 (2014).
- [52] C. L. Fryer, F. G. Oliveira, J. A. Rueda, and R. Ruffini, *Phys. Rev. Lett.* **115**, 231102 (2015).
- [53] L. Becerra, F. Cipolletta, C. L. Fryer, J. A. Rueda, and R. Ruffini, *Astrophys. J.* **812**, 100 (2015).
- [54] L. Becerra, C. L. Bianco, C. L. Fryer, J. A. Rueda, and R. Ruffini, *Astrophys. J.* **833**, 107 (2016).
- [55] L. Becerra, M. M. Guzzo, F. Rossi-Torres, J. A. Rueda, R. Ruffini, and J. D. Uribe, *Astrophys. J.* **852**, 120 (2018).
- [56] D. J. Price, SPLASH: An Interactive Visualization Tool for Smoothed Particle Hydrodynamics Simulations, Astrophysics Source Code Library (2011), <http://ascl.net/1103.004>.
- [57] R. Moradi, J. A. Rueda, R. Ruffini, L. Li, C. L. Bianco, S. Champion, C. Cherubini, S. Filippi, Y. Wang, and S. S. Xue, *Phys. Rev. D* **104**, 063043 (2021).
- [58] R. Ruffini, R. Moradi, J. A. Rueda, L. Li, N. Sahakyan, Y. C. Chen, Y. Wang, Y. Aimuratov, L. Becerra, C. L. Bianco, C. Cherubini, S. Filippi, M. Karlica, G. J. Mathews, M. Muccino, G. B. Pisani, and S. S. Xue, *Mon. Not. R. Astron. Soc.* **504**, 5301 (2021).
- [59] J. A. Rueda, R. Ruffini, M. Karlica, R. Moradi, and Y. Wang, *Astrophys. J.* **893**, 148 (2020).
- [60] Y. Wang, J. A. Rueda, R. Ruffini, L. Becerra, C. Bianco, L. Li, and M. Karlica, *Astrophys. J.* **874**, 39 (2019).
- [61] R. Ruffini, R. Moradi, J. A. Rueda, L. Becerra, C. L. Bianco, C. Cherubini, S. Filippi, Y. C. Chen, M. Karlica, N. Sahakyan, Y. Wang, and S. S. Xue, *Astrophys. J.* **886**, 82 (2019).
- [62] Y. Wang, J. A. Rueda, R. Ruffini, R. Moradi, L. Li, Y. Aimuratov, F. Rastegarnia, S. Eslamzadeh, N. Sahakyan, and Y. Zheng, *Astrophys. J.* **936**, 190 (2022).
- [63] J. A. Rueda and R. Ruffini, *Eur. Phys. J. C* **80**, 300 (2020).
- [64] R. Moradi, J. A. Rueda, R. Ruffini, and Y. Wang, *Astron. Astrophys.* **649**, A75 (2021).
- [65] F. Rastegarnia, R. Moradi, J. A. Rueda, R. Ruffini, L. Li, S. Eslamzadeh, Y. Wang, and S. S. Xue, *Eur. Phys. J. C* **82**, 778 (2022).
- [66] R. Ruffini, Y. Wang, Y. Aimuratov, U. Barres de Almeida, L. Becerra, C. L. Bianco, Y. C. Chen, M. Karlica, M. Kovacevic, L. Li, J. D. Melon Fuksman, R. Moradi, M. Muccino, A. V. Penacchioni, G. B. Pisani, D. Primorac, J. A. Rueda, S. Shakeri, G. V. Vereshchagin, and S.-S. Xue, *Astrophys. J.* **852**, 53 (2018).
- [67] J. A. Rueda, R. Ruffini, and R. P. Kerr, *Astrophys. J.* **929**, 56 (2022).
- [68] R. Ruffini, M. Karlica, N. Sahakyan, J. A. Rueda, Y. Wang, G. J. Mathews, C. L. Bianco, and M. Muccino, *Astrophys. J.* **869**, 101 (2018).
- [69] J. A. Rueda, R. Ruffini, R. Moradi, and Y. Wang, *Int. J. Mod. Phys. D* **30**, 2130007 (2021).
- [70] J. A. Rueda, *Astron. Rep.* **65**, 1026 (2021).
- [71] J. A. Rueda, R. Ruffini, and Y. Wang, *Universe* **5**, 110 (2019).
- [72] T. M. Tauris, N. Langer, T. J. Moriya, P. Podsiadlowski, S. C. Yoon, and S. I. Blinnikov, *Astrophys. J. Lett.* **778**, L23 (2013).
- [73] T. M. Tauris, N. Langer, and P. Podsiadlowski, *Mon. Not. R. Astron. Soc.* **451**, 2123 (2015).
- [74] T. M. Tauris, M. Kramer, P. C. C. Freire, N. Wex, H. T. Janka, N. Langer, P. Podsiadlowski, E. Bozzo, S. Chaty, M. U. Kruckow, E. P. J. van den Heuvel, J. Antoniadis, R. P. Breton, and D. J. Champion, *Astrophys. J.* **846**, 170 (2017).
- [75] K. De, M. M. Kasliwal, E. O. Ofek, T. J. Moriya *et al.*, *Science* **362**, 201 (2018).
- [76] L. Jiang, T. M. Tauris, W.-C. Chen, and J. Fuller, *Astrophys. J. Lett.* **920**, L36 (2021).
- [77] D. Vartanyan, E. Laplace, M. Renzo, Y. Götberg, A. Burrows, and S. E. de Mink, *Astrophys. J. Lett.* **916**, L5 (2021).
- [78] C. L. Fryer, S. Andrews, W. Even, A. Heger, and S. Safi-Harb, *Astrophys. J.* **856**, 63 (2018).
- [79] Y. B. Zel'dovich, L. N. Ivanova, and D. K. Nadezhin, *Sov. Astron.* **16**, 209 (1972), <https://ui.adsabs.harvard.edu/abs/1972SvA....16..209Z/abstract>.
- [80] C. L. Fryer, W. Benz, and M. Herant, *Astrophys. J.* **460**, 801 (1996).
- [81] C. L. Fryer, F. Herwig, A. Hungerford, and F. X. Timmes, *Astrophys. J. Lett.* **646**, L131 (2006).
- [82] C. L. Fryer, *Astrophys. J.* **699**, 409 (2009).
- [83] R. Ruffini and J. Wilson, *Phys. Rev. Lett.* **31**, 1362 (1973).
- [84] F. Cipolletta, C. Cherubini, S. Filippi, J. A. Rueda, and R. Ruffini, *Phys. Rev. D* **92**, 023007 (2015).
- [85] N. R. Sibgatullin and R. A. Sunyaev, *Astron. Lett.* **26**, 772 (2000).
- [86] F. Cipolletta, C. Cherubini, S. Filippi, J. A. Rueda, and R. Ruffini, *Phys. Rev. D* **96**, 024046 (2017).
- [87] J. Pétri, *Mon. Not. R. Astron. Soc.* **450**, 714 (2015).
- [88] J. B. Wei, A. Figura, G. F. Burgio, H. Chen, and H. J. Schulze, *J. Phys. G Nucl. Phys.* **46**, 034001 (2019).
- [89] C. Breu and L. Rezzolla, *Mon. Not. R. Astron. Soc.* **459**, 646 (2016).
- [90] J. P. Ostriker and J. E. Gunn, *Astrophys. J.* **157**, 1395 (1969).
- [91] K.-W. Lo and L.-M. Lin, *Astrophys. J.* **728**, 12 (2011).



# The structure of the ultrarelativistic prompt emission phase and the properties of the black hole in GRB 180720B

F. Rastegarnia<sup>1,2,3,4,a</sup>, R. Moradi<sup>1,2,5,b</sup>, J. A. Rueda<sup>1,2,3,4,6,c</sup>, R. Ruffini<sup>1,2,7,d</sup>, Liang Li<sup>1,2,7,e</sup>, S. Eslamzadeh<sup>1,2,3,4</sup>, Y. Wang<sup>1,2,5,f</sup>, S. S. Xue<sup>1,2</sup>

<sup>1</sup> ICRA, Dipartimento di Fisica, Sapienza Università di Roma, Piazzale Aldo Moro 5, I-00185 Rome, Italy

<sup>2</sup> International Center for Relativistic Astrophysics Network, Piazza della Repubblica 10, I-65122 Pescara, Italy

<sup>3</sup> ICRA-Net-Ferrara, Dipartimento di Fisica e Scienze della Terra, Università degli Studi di Ferrara, Via Saragat 1, I-44122 Ferrara, Italy

<sup>4</sup> Dipartimento di Fisica e Scienze della Terra, Università degli Studi di Ferrara, Via Saragat 1, I-44122 Ferrara, Italy

<sup>5</sup> INAF-Osservatorio Astronomico d'Abruzzo, Via M. Maggini snc, I-64100 Teramo, Italy

<sup>6</sup> INAF, Istituto di Astrofisica e Planetologia Spaziali, Via Fosso del Cavaliere 100, I-00133 Rome, Italy

<sup>7</sup> INAF, Viale del Parco Mellini 84, I-00136 Rome, Italy

Received: 1 June 2022 / Accepted: 23 August 2022  
© The Author(s) 2022

**Abstract** In analogy with GRB 190114C, we here analyze the ultrarelativistic prompt emission (UPE) of GRB 180720B observed in the rest-frame time interval  $t_{\text{rf}} = 4.84\text{--}10.89$  s by Fermi-GBM. We reveal the UPE hierarchical structure from the time-resolved spectral analysis performed in time sub-intervals: the spectrum in each shorter time interval is always fitted by a composite blackbody plus cutoff power-law model. We explain this structure with the *inner engine* of binary-driven hypernova (BdHN) model operating in a quantum electrodynamics (QED) regime. In this regime, the electric field induced by the gravitomagnetic interaction of the newborn Kerr BH with the surrounding magnetic field is overcritical, i.e.,  $|\mathbf{E}| \geq E_c$ , where  $E_c = m_e^2 c^3 / (e\hbar)$ . The overcritical field polarizes the vacuum leading to an  $e^+ e^-$  pair plasma that loads baryons from the surroundings during its expansion. We calculate the dynamics of the self-acceleration of the pair-electromagnetic-baryon (PEMB) pulses to their point of transparency. We characterize the quantum vacuum polarization process in the sequences of decreasing time bins of the UPE by determining the radiation timescale, Lorentz factors, and transparency radius of the PEMB pulses. We also estimate the strength of the surrounding magnetic field  $\sim 10^{14}$  G, and obtain a lower limit to the BH mass,  $M = 2.4 M_\odot$ , and correspondingly an upper limit to the spin,  $\alpha = 0.6$ ,

from the conditions that the UPE is powered by the Kerr BH extractable energy and its mass is bound from below by the NS critical mass.

## 1 Introduction

The binary-driven hypernova (BdHN) model has been proposed for the description of long-duration gamma-ray bursts (GRBs), following the induced gravitational collapse (IGC) scenario [51]. The progenitor is a binary system composed of a carbon-oxygen core ( $\text{CO}_{\text{core}}$ ) and a neutron star (NS) companion. These  $\text{CO}_{\text{core}}$ -NS binaries are expected to form in the late stages of the binary evolution of massive binaries, e.g.,  $\sim 15 + 12 M_\odot$  zero-age main-sequence (ZAMS) stars [53]. The more massive star undergoes core-collapse supernova (SN) and creates a NS when its thermonuclear evolution is over. After multiple common-envelope phases and binary interactions during the X-ray binary phase of the system (see, [23, 24], and references therein), the hydrogen and helium envelopes of the less massive main-sequence star are stripped, leading to the formation of the  $\text{CO}_{\text{core}}$  (see [23], and Fig. 1 and section 2 in [53]). The system at this point is a  $\text{CO}_{\text{core}}$ -NS binary in tight orbit, which is taken as the initial configuration of the BdHN model for long GRBs [4–6, 24, 53].

In the last decade, theoretical progress in the analysis of BdHNe, including three-dimensional numerical simulations, has identified their sequence of physical events [4–6, 23, 24, 29, 51]. The gravitational core-collapse event of the  $\text{CO}_{\text{core}}$  forms a newborn NS ( $\nu\text{NS}$ ) at its center and powers

<sup>a</sup> e-mail: [fatemeh.rastegarnia@edu.unife.it](mailto:fatemeh.rastegarnia@edu.unife.it)

<sup>b</sup> e-mail: [rahim.moradi@inaf.it](mailto:rahim.moradi@inaf.it) (corresponding author)

<sup>c</sup> e-mail: [jorge.rueda@icra.it](mailto:jorge.rueda@icra.it)

<sup>d</sup> e-mail: [ruffini@icra.it](mailto:ruffini@icra.it)

<sup>e</sup> e-mail: [liang.li@icranet.org](mailto:liang.li@icranet.org)

<sup>f</sup> e-mail: [yu.wang@uniroma1.it](mailto:yu.wang@uniroma1.it)

a type Ic SN explosion. The SN ejecta is partially accreted by the  $\nu$ NS because of matter fallback and partially by the NS companion at hypercritical (i.e., highly super-Eddington) rates due to a powerful neutrino emission process occurring on top the NS surface [4, 7]. The fallback accretion onto the  $\nu$ NS contribute to the energy of prompt emission and spins up the  $\nu$ NS (Becerra et al., submitted; see also [6] and Yu et al., in press). The  $\nu$ NS rotational energy powers the synchrotron emission leading to the afterglow [6, 24, 51, 55, 71]. For orbital periods of a few minutes, the NS companion reaches the critical mass for gravitational collapse leading to the formation of a rotating (Kerr) black hole (BH). These systems have been called BdHN I, which explain the subclass of energetic long GRBs with  $E_{\text{iso}} \gtrsim 10^{52}$  erg. Up to now, 380 long GRBs have been interpreted as BdHNe I [71]. Therefore, three pillars of BdHN I, responsible for different episodes of this subclass of long GRBs are: (1) SN, (2) BH, and (3)  $\nu$ NS. The interplay between these three components leads to different episodes of BdHN I. For longer orbital periods, the NS companion does not reach the critical mass and hold stable as a more massive, fast rotating NS. These systems have been called BdHN II, which explain the subclass of energetic long GRBs with  $E_{\text{iso}} \lesssim 10^{52}$  erg. The emergence of the optical SN naturally expected in the BdHN scenario (see e.g., [18, 43, 66, 68]) completes the BdHN approach.

The experimental verification of the entire sequence of Episodes in a BdHN I has been recently achieved in GRB 190114C [38] and GRB 180720B [36]. Thanks to the high quality of the data and the brightness of these sources, we have identified through a detailed time-resolved analysis the following Episodes of a BdHN I [36, 38]: the emission from the  $\nu$ NS (the  $\nu$ NS-rise); the BH formation, known as BH-rise, originating the ultrarelativistic prompt emission (UPE) phase; the formation of the *cavity* around the newborn BH, formed in the gravitational collapse of the companion NS to the BH, and further depleted by the UPE phase [59]; the soft and hard X-ray flares (SXF and HXF) originating from the interaction of the UPE phase with the expanding SN ejecta [67]; the X-ray afterglow powered by the rapidly rotating  $\nu$ NS [53, 58, 83], and the gigaelectronvolt (GeV) emission from the BH following the UPE [37, 69]. We discuss in Sect. 2 the observational identification of the above episodes in the case of GRB 180720B.

In this article, we perform a time-resolved spectral analysis of the UPE phase of GRB 180720B and interpret it in the context of the BH formation in a BdHN I. A most relevant result of this kind of analysis has been the discovery of the hierarchical structure of the UPE phase of GRB 190114C. The spectrum on rebinned shorter time intervals shows always a similar blackbody plus cutoff power-law (BB + CPL) model during the entire UPE phase [38]. The explanation of such a hierarchical structure of the UPE phase has been found in the sequence of microphysical elementary events,

in the quantum electrodynamics (QED) regime of vacuum polarization, that occurs in the formation of the BH in the inner engine of the GRB [69]. The inner engine is the system composed of the newborn rotating BH surrounded by a uniform magnetic field, aligned with the BH rotation axis, and the low-density ( $\sim 10^{-14}$  g cm $^{-3}$ ) matter of the SN ejecta in the cavity.

The physical process, which combines the pure general relativistic effect of *gravitomagnetism* and QED works as follows. The gravitomagnetic interaction of the Kerr BH with the magnetic field induces an electric field, and the structure of such an electromagnetic field has been modeled with the Papapetrou–Wald solution [82]. The intensity of the induced electric field is proportional to the BH spin parameter and the magnetic field strength. The newborn BH is not charged. The interaction of the gravitomagnetic field of the Kerr BH with the surrounding magnetic field,  $B_0$ , induces an electric field around the BH. This electric field is nearly radial, and despite its quadrupolar nature, decreases with distance roughly as  $1/r^2$ . Hence, it is possible to define an “effective charge”,  $Q_{\text{eff}}$ , as the proportionality constant of such a field, i.e.,  $E \approx Q_{\text{eff}}/r^2$ , where [37, 52, 69]

$$Q_{\text{eff}} = \frac{G}{c^3} 2B_0 J. \quad (1)$$

It can be shown that the Papapetrou–Wald solution, due to theorems by Ipser [26], Wald [81] and Carter [19], produces the unique solution which, at perturbative level, represents the transformation of the Kerr BH into a charged rotating Kerr–Newman BH, with effective charge given by the above equation, i.e., Eq. (1) of the paper. It can be indeed checked that for relatively low values of the spin parameter  $\alpha = cJ/(GM^2) \lesssim 0.6$ , the Papapetrou–Wald solution can be approximated by the Kerr–Newman solution [37]. We take advantage of the above property to estimate the energy and the QED effect with the Kerr–Newman geometry for which an analytic expression for the energy of the dyadoregion has been derived in Cherubini et al. [12]. In fact, the difficulty of the origin of a charged BH is overcome by the idea of the effective charge.

The inner engine in the UPE phase operates in an overcritical QED regime in which the induced electric field is larger than the critical field for vacuum polarization, i.e.,  $E > E_c$ , where

$$E_c = \frac{m_e^2 c^3}{e \hbar} \approx 1.32 \times 10^{16} \text{ V/cm}. \quad (2)$$

The MeV radiation of the UPE and its associated hierarchical structure is explained by the inner engine in this overcritical regime, and is powered by the rotational energy of the Kerr BH. In this article, we focus on the UPE phase of GRB 180720B.

The overcritical electric field of the inner engine generates an initially optically thick  $e^+e^-$  plasma that self-accelerates under its own internal pressure while engulf ambient baryons. The first numerical simulations of the expanding optically thick pair electromagnetic-baryon plasma, called *PEMB* pulse, were presented in [60]. For instance, for a BH mass  $10M_\odot$  and effective charge to mass ratio of  $\sim 0.1$ , adopted for GRB 991216 [57], the produced  $e^+e^-$  plasma pairs lie between the radii  $r_1 = 6 \times 10^6$  cm and  $r_2 = 2.3 \times 10^8$  cm, with total energy of  $E_{\text{tot}} = 4.8 \times 10^{53}$  erg, and the total number of pairs is  $N_{e^+e^-} = 2 \times 10^{58}$ . This leads to the pair number density of  $10^{32} \lesssim \bar{n}_{e^+e^-} \lesssim 10^{37}$  cm $^{-3}$  and the optical depth of  $\tau \sim \sigma_T \bar{n}_{e^+e^-} \times [r_2 - r_1] \sim 10^{16-10^{21}} \gg 1$ , being  $\sigma_T = 6.6 \times 10^{-25}$  cm $^{-2}$  the Thomson cross-section. Such an optically thick *PEMB* pulse self-accelerates outward reaching ultrarelativistic velocities [60, 61] up to Lorentz factors of  $\Gamma \sim 300$  at transparency and emits MeV photons. The observation of such thermal photons signs the first evidence of the Kerr BH formation, i.e., the BH-rise. The high Lorentz factor guarantees the avoidance of the so-called GRB compactness problem [44, 49].

In Rueda et al. [53] (see Sect. 7 therein), it has been discussed that numerical simulations of BdHN I point to the possible presence of a torus-like distribution of matter with higher density on the equatorial plane that can serve to anchor the magnetic field. The physical process leading to the UPE phase requires the presence of low-density ionized matter on the polar regions, i.e., above and below the BH. Therefore, the presence of matter with higher density on the equatorial plane, providing it is not as massive as to change the assumed spacetime geometry, does not interfere with the production of the pair plasma around the BH.

The emitted energy in the UPE phase is paid by the rotational energy of the BH, hence it reduces its angular momentum, and consequently the intensity of the induced electric field. This process continues until the electric field reaches the value  $E_c$  and no more pairs can be created via vacuum breakdown. We here analyze all the above process occurring during the UPE phase in the case of GRB 180720B, which is another BdHN I and its data quality allows us to perform a detailed time-resolved spectral analysis analogous to the one applied successfully to GRB 190114C in [38]. We confirm in this paper the presence in the 10 keV–10 MeV energy band the very same hierarchical structure of the UPE phase in GRB 180720B already found in GRB 190114C. We simulate the above physical process of the inner engine that explains the UPE energetics, luminosity and spectrum and infer from it the magnetic field strength, the initial mass and spin of the BH, and their time evolution.

The electro-vacuum Papapetrou–Wald solution used in the inner engine differs from other models of the electromagnetic field structure around astrophysical BHs (see, e.g., [32, 42]). A detailed theoretical review of such models is presented

by Komissarov [32]. In those models, the field structure and parameters enforce the condition  $\mathbf{E} \cdot \mathbf{B} \neq 0$ , while in the Papapetrou–Wald solution naturally exist regions where such a condition is naturally satisfied in the Kerr BH surroundings. In the BdHN I, the BH is surrounded by a very-low dense plasma in which the screening of the electric field is unlikely to occur, guaranteeing the stability of the Papapetrou–Wald electromagnetic field structure. This differs from the environment envisaged for describing the mechanism of generating powerful relativistic jets from a black hole system in AGNs and X-ray binary systems, e.g., in Komissarov [32] and Parfrey et al. [42], where the surrounding plasma has a much larger density and may cause the screening of the electric field. Therefore, the inner engine parameters and physical processes are different with respect to these models and have been guided by the GRB analysis. Specifically, our approach gives a theoretical explanation to the time-resolved spectral analysis of the UPE phase, and the MeV luminosity observed by Fermi-GBM.

The article is organized as follows. In Sect. 2, we present the observations of GRB 180720B by different satellites and then introduce the 6 Episodes of this GRB obtained from the observations. In Sect. 3, we perform the time-resolved spectral analysis during the UPE phase of GRB 180720B thanks to the recent progress in the understanding of the UPE phase of GRB 190114C [39], and the high signal-to-noise (S/N) ratio of the Fermi-GBM data during the UPE phase of GRB 180720B. In Sect. 4, we introduce the structure of the electromagnetic field used to study the properties of inner engine of GRB 180720B. We also discuss the physical differences of this electromagnetic field and the operation of the inner engine to extract the rotational energy of the BH with the existing literature on the subject. In Sect. 5, we determine the mass and spin of the BH in the inner engine of GRB 180720B during the UPE phase and in the subsequent evolution. In Sect. 6, we describe the vacuum polarization process in the inner engine and how it originates the UPE phase. In Sect. 7, we analyze the compactness problem and the general formulation of transparency condition during the UPE phase. In Sect. 8, we obtain the magnetic field and BH parameters at transparency point during the UPE phase. We follow the quantum vacuum polarization process down to a timescale of  $\tau \sim 10^{-9}$  s, marking the hierarchical structure of the UPE imposed by the observed luminosity and the electromagnetic configuration of the inner engine during the UPE phase. We compute the value of the magnetic field,  $B_0$ , the Lorentz factors, the baryon loads, the energy emitted and radii at the transparency of each *PEMB* pulse. We also discuss relevant differences between our approach and different models in the literature, e.g. by Komissarov [32] and Parfrey et al. [42]. In Sect. 9, we summarize the conclusions of this work.

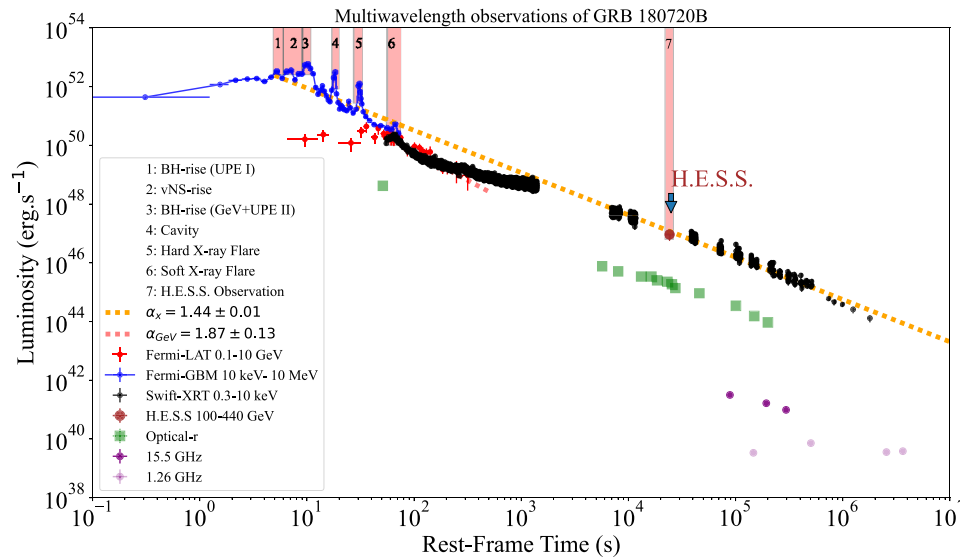


**Fig. 1** Luminosity of GRB 180720B in the cosmological rest-frame of the source. Blue circles: obtained from *Fermi*-GBM in the 10 keV–10 MeV energy band. Red circles: obtained from *Fermi*-LAT in the 0.1–10 GeV energy band. The Episode 1 shows the BH-rise (UPE I) from  $t_{\text{rf}} = 4.84$  s to  $t_{\text{rf}} = 6.05$  s. The Episode 2 shows the  $\nu$ NS-rise from  $t_{\text{rf}} = 6.05$  s to  $t_{\text{rf}} = 9.07$  s. The Episode 3 represents the second UPE phase (UPE II) from  $t_{\text{rf}} = 9.07$  s to  $t_{\text{rf}} = 10.89$  s. The Episode 4 shows the *Fermi*-GBM the cavity from  $t_{\text{rf}} = 16.94$  s

to  $t_{\text{rf}} = 19.96$  s. The Episode 5 the hard X-ray Flares (HXF), from  $t_{\text{rf}} = 28.95$  s to  $t_{\text{rf}} = 34.98$  s. The Episode 6, the soft X-ray Flares (SXF), from  $t_{\text{rf}} = 55$  s to  $t_{\text{rf}} = 75$  s. The rest-frame 0.1–100 GeV luminosity light-curve of GRB 180720B after UPE phase is best fitted by a power-law with slope of  $\alpha_X = 1.87 \pm 0.13$  and, amplitude of  $(4.6 \pm 2.9) \times 10^{53}$  erg s $^{-1}$ . The purple circles present the radio data from AMI-LA retrieved from Rhodes et al. [47]. The green squares represent the r-band optical data retrieved from Abdalla et al. [1]

## 2 Observational data of GRB 180720B

On July 20, 2018, GRB 180720B triggered the *Fermi*-GBM at 14:21:39.65 UT [48], the CALET Gamma-ray Burst Monitor at 14:21:40.95 UT [11], the *Swift*-BAT at 14:21:44 UT [76], the *Fermi*-LAT at 14:21:44.55 UT [9], and the *Konus-Wind* at 14:21:45.26 UT [22]. The X-ray telescope (XRT) on board the Neil Gehrels *Swift* Observatory (hereafter *Swift*), began observing 91 s after the *Fermi*-GBM trigger [76], *MAXI/GSC* started at 296 s [40] and *NuStar* covered later times from 243 to 318 ks [8]. Just 78 s after the *Fermi*-GBM trigger, the 1.5-m Kanata telescope performed optical and NIR imaging polarimetry of the source field and found a bright optical R-band counterpart within the the *Swift*-XRT error circle, observed by *HOWPol* and *HONIR* attached to the 1.5-m Kanata telescope [72]. Additional observations followed by optical, infrared and radio telescopes [1, 16, 17, 27, 28, 30, 31, 33, 35, 45, 73, 74, 84, 87].

Following the optical observation, redshift  $z = 0.654$  was identified from the Fe II and Ni II lines by the VLT/X-shooter telescope [34]. This allows to determine the cosmological rest frame time  $t_{\text{rf}} = t_{\text{obs}}/(1+z)$ , being  $t_{\text{obs}}$  the observed time, as well as the isotropic energy ( $E_{\text{iso}}$ ) and the isotropic luminosity ( $L_{\text{iso}}$ ) of this source. GRB 180720B has isotropic energy of  $E_{\text{iso}} = 5.92 \times 10^{53}$  erg during the  $T_{90}$  of the *Fermi*-GBM. The sub-TeV (100–440 GeV) observation by

the High Energy Stereoscopic System (H.E.S.S.) has been also reported for this GRB [1]. The diversity and the statistical significance of the observed data have made this GRB one of the proper candidates to test the GRB models. The luminosity light-curve in radio, optical, and gamma-rays of the GRB 180720B is shown in Fig. 1.

### 2.1 The episodes of GRB 180720B

Six different episodes relating to six different astrophysical processes have been recently identified in the time domain analysis of GRB 180720B [36]:

(I) Episode 1 (UPE I): the BH formation caused by hypercritical accretion onto the companion NS in BdHN I, and its subsequent UPE phase originated from vacuum polarization and expanding PEMB pulses with their characteristic Lorentz factor  $\Gamma \sim 100$  [60, 61]. This episode pinpoints the first manifestation of the BH (BH-rise) which is the subject of the current paper. The UPE I of GRB 180720B occurs from  $t_{\text{rf}} = 4.84$  s to  $t_{\text{rf}} = 6.05$  s. Its measured isotropic energy is  $E_{\text{UPEI}}^{\text{MeV}} = (6.37 \pm 0.48) \times 10^{52}$  erg, and its spectrum is best fitted by a CPL + BB model (index  $\alpha = -1.13$ , cutoff energy  $E_c = 2220.569$  keV, and blackbody (BB) temperature  $kT = 50.31$  keV in the observer's frame); see Fig. 2.

(II) Episode 2 ( $\nu$ NS-rise): the fallback of the SN ejecta onto the  $\nu$ NS spins it up ([6] and Becerra et al., submitted).

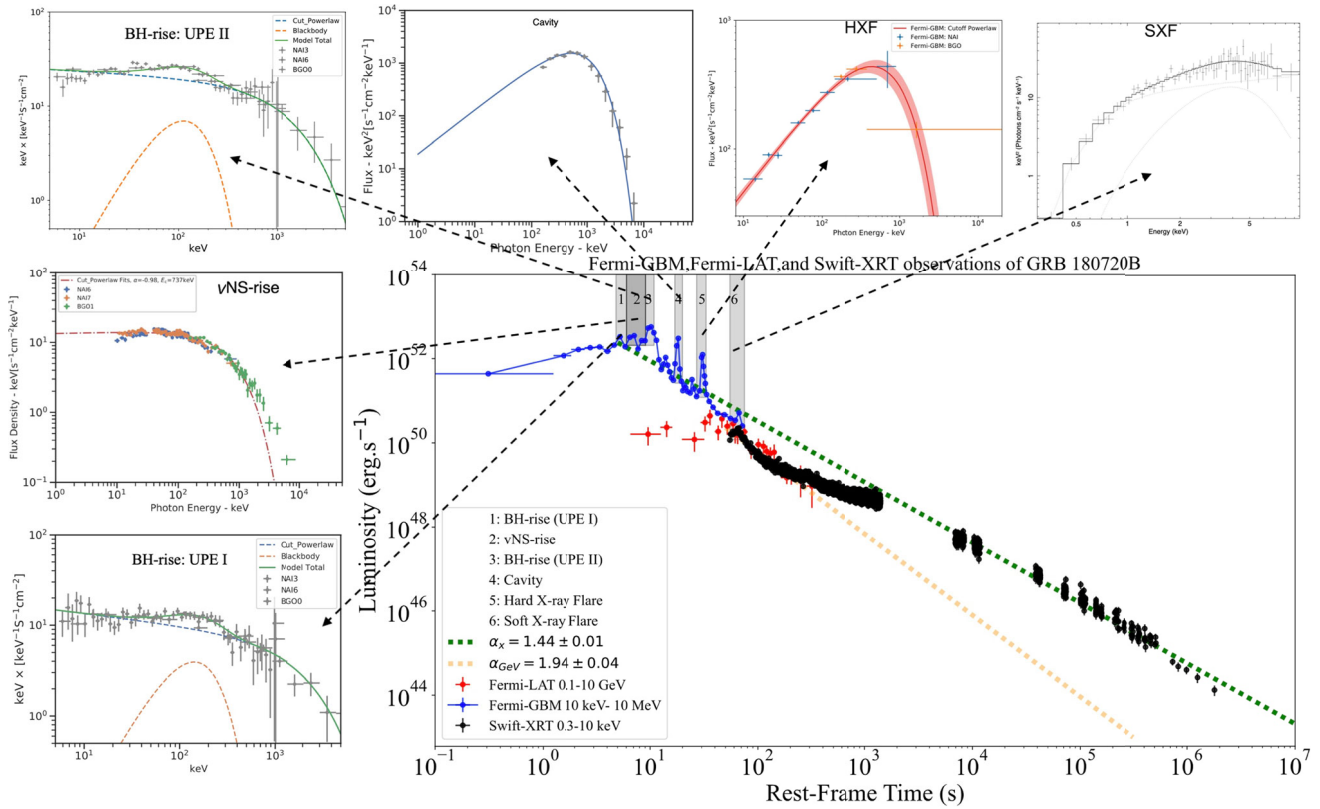


**Fig. 2** Luminosity light-curves and spectra related to the different Episodes identified in GRB 180720B. Plots and best fits are reproduced from [36] by the author’s permission

The first evidence of this interplay in GRB 180720B, referred to as the  $\nu$ NS-rise, spans from  $t_{\text{rf}} = 6, 05$  s to  $t_{\text{rf}} = 9.07$  s. The isotropic energy of this phase  $E_{\nu\text{Ns}}^{\text{MeV}} = (1.13 \pm 0.04) \times 10^{53}$  erg, and its spectrum is best fitted by a CPL model ( $\alpha = -0.98$ , and  $E_c = 737$  keV, in the observer’s frame); see Fig. 2.

(III) Episode 3 (UPE II): it is evidenced by the first significant observed GeV photon at  $t_{\text{rf}} = 7.06$  s. This phase also includes the continuation of the UPE phase (UPE II) from  $t_{\text{rf}} = 9.07$  s to  $t_{\text{rf}} = 10.89$  s, with an isotropic energy of  $E_{\text{UPEII}}^{\text{MeV}} = (1.6 \pm 0.95) \times 10^{53}$  erg. A CPL + BB model with model parameters of  $\alpha = -1.06^{+0.01}_{-0.01}$ ,  $E_c = 1502.5^{+88.6}_{-87.5}$  keV and  $kT = 39.8^{+1.6}_{-1.6}$  keV is the best fit for the spectrum of this phase; see Fig. 2.

(IV) Episode 4 (Cavity): the gravitational collapse of the NS and the consequent BH formation creates a cavity, which becomes further depleted by the expanding PEMB pulses [59]. The collision and partial reflection of the ultra-relativistic PEMB pulses from the cavity’s wall results in radiation with a CPL spectrum that has an energy of  $\sim 10^{52}$  erg and a luminosity of  $\sim 10^{51}$  erg s $^{-1}$ . These values are comparable to the UPE and  $\nu$ NS-rise energetics [59]. For GRB 180720B, this emission extends from  $t_{\text{rf}} = 16.94$  s to  $t_{\text{rf}} = 19.96$  s, with an isotropic energy of  $E_{\text{CV}}^{\text{MeV}} =$

$(4.32 \pm 0.19) \times 10^{52}$  erg, characterized by a CPL spectrum ( $\alpha = -1.16$ ,  $E_c = 607.96$  keV). Its luminosity and spectrum is given in Fig. 2.

(V) Episode 5 soft X-ray flare (SXF), and (VI) Episode 6 hard X-ray flare (HXF): HXF and SXF emissions result from the interaction of the PEMB pulses with the SN ejecta occurring at  $r = 10^{12}$  cm from the BH [67]. The HXF of GRB 180720B extends from  $t_{\text{rf}} = 28.95$  s to  $t_{\text{rf}} = 34.98$  s, with  $L_{\text{HXF,iso}}^{\text{MeV}} = (7.8 \pm 0.07) \times 10^{51}$  erg s $^{-1}$ . Its spectrum is best fitted by a CPL model with  $E_c = (5.5^{+0.8}_{-0.7}) \times 10^2$  keV,  $\alpha = -1.198 \pm 0.031$ . The SXF occurs from  $t_{\text{rf}} = 55$  s to  $t_{\text{rf}} = 75$  s, with  $L_{\text{SXF,iso}}^{\text{X}} = 1.45 \times 10^{50}$  erg s $^{-1}$ . Its spectrum is best fitted by a PL+BB model with  $\alpha = -1.79 \pm 0.23$ , and  $kT = 0.99 \pm 0.13$  keV; see Fig. 2.

The cavity, SXF, and HXF have energetics similar to the UPE phase because they are also created by the interaction of expanding PEMB pulses with SN ejecta; (see, [71], and references therein).

One-dimensional [23, 24], two-dimensional [5], and three-dimensional [4, 6] simulations of BdHN model clearly show that the accretion of the SN ejecta onto the  $\nu$ NS and NS companion transfers both mass and angular momentum to them. According to numerical simulations of the early evolution phase of BdHN I, the NS companion can reach its critical

**Table 1** The time-resolved spectral fit parameters for GRB 180720B (CPL + BB model) during the UPE I phase ( $t_{\text{rf}} = 4.84$  s to  $t_{\text{rf}} = 6.05$  s). This table summarizes the time intervals in the rest and observer frames, their significance ( $S$ ), the power-law index, cut-off energy, temperature,  $\Delta\text{DIC}$ , BB flux, total flux, BB to total flux ratio,  $F_{\text{BB}}/F_{\text{tot}}$ , and finally the isotropic energy. The first block (first row) in the table contains the spectral best-fit parameters for UPE I. The second block (second, third, fourth, and fifth rows) contains the time-resolved spectral best-fit

parameters for  $\Delta t_{\text{rf}} = 0.3$  s. To select the best model from two different given models, we adopt the deviance information criterion (DIC), defined as  $\text{DIC} = -2\log[p(\text{data}|\hat{\theta})] + 2p_{\text{DIC}}$ , where  $\hat{\theta}$  is the posterior mean of the parameters, and  $p_{\text{DIC}}$  is the effective number of parameters. The preferred model is the model with the lowest DIC score. Here we define  $\Delta\text{DIC} = (\text{CPL} + \text{BB}) - \text{CPL}$ , if  $\Delta\text{DIC}$  is negative, indicating the CPL + BB is better. After comparing the DIC, we find the CPL + BB model is the preferred model over the CPL and other models

$t_1 \sim t_2$	$t_{r,f,1} \sim t_{r,f,2}$	$S$	$\alpha$	$E_c$	$kT$	$\Delta\text{DIC}$	$F_{\text{BB}}$	$F_{\text{tot}}$	$F_{\text{ratio}}$	$E_{\text{tot}}$
(s)	(s)			(keV)	(keV)		( $10^{-6}$ )	( $10^{-6}$ )		( $10^{52}$ erg)
Obs	Rest-frame						( $\text{erg cm}^{-2} \text{s}^{-1}$ )	( $\text{erg cm}^{-2} \text{s}^{-1}$ )		
8.000~10.000	4.840~6.050	142.74	$-1.13^{+0.01}_{-0.01}$	$2221^{+184}_{-183}$	$50.3^{+2.8}_{-2.9}$	-108	$1.39^{+0.53}_{-0.35}$	$27.14^{+2.20}_{-2.04}$	0.05	9.53
8.000~8.500	4.840~5.142	82.61	$-1.06^{+0.02}_{-0.02}$	$2965^{+316}_{-313}$	$64.4^{+6.1}_{-6.0}$	-84	$2.44^{+1.43}_{-0.92}$	$43.61^{+4.78}_{-4.80}$	0.06	3.83
8.500~9.000	5.142~5.445	89.78	$-1.11^{+0.03}_{-0.03}$	$1898^{+266}_{-267}$	$56.2^{+5.0}_{-5.0}$	-51	$1.97^{+1.15}_{-0.75}$	$31.47^{+4.46}_{-4.26}$	0.06	2.76
9.000~9.500	5.445~5.747	72.53	$-1.07^{+0.06}_{-0.06}$	$953^{+265}_{-267}$	$34.2^{+10.3}_{-13.9}$	-23	$0.37^{+1.53}_{-0.34}$	$15.77^{+7.32}_{-3.93}$	0.02	1.38
9.500~10.000	5.747~6.050	60.82	$-1.19^{+0.05}_{-0.05}$	$1788^{+571}_{-582}$	$38.1^{+4.9}_{-4.9}$	-32	$0.76^{+0.67}_{-0.39}$	$15.42^{+4.80}_{-4.00}$	0.05	1.35

**Table 2** The parameters of the time-resolved spectral best fits of GRB 180720B (CPL + BB model) from the  $t_{\text{rf}} = 9.07$  s to  $t_{\text{rf}} = 10.89$  s. This table reports: the time intervals both in rest-frame and observer frame, the significance ( $S$ ) for each time interval, the power-law index,

cut-off energy, temperature,  $\Delta\text{DIC}$ , BB flux, total flux, the BB to total flux ratio,  $F_{\text{BB}}/F_{\text{tot}}$  and finally the isotropic energy. The  $\Delta\text{DIC}$ s are reported in column 6

$t_1 \sim t_2$	$t_{r,f,1} \sim t_{r,f,2}$	$S$	$\alpha$	$E_c$	$kT$	$\Delta\text{DIC}$	$F_{\text{BB}}$	$F_{\text{tot}}$	$F_{\text{ratio}}$	$E_{\text{tot}}$
(s)	(s)			(keV)	(keV)		( $10^{-6}$ )	( $10^{-6}$ )		( $10^{52}$ erg)
Obs	Rest-frame						( $\text{erg cm}^{-2} \text{s}^{-1}$ )	( $\text{erg cm}^{-2} \text{s}^{-1}$ )		
15.00~18.00	9.07~10.89	274.60	$-1.06^{+0.01}_{-0.01}$	$1502.5^{+88.6}_{-87.5}$	$39.8^{+1.6}_{-1.6}$	-226.4	$1.99^{+0.43}_{-0.34}$	$45.55^{+3.11}_{-2.70}$	$0.04^{+0.01}_{-0.01}$	$16.0^{+1.1}_{-0.952}$
15.00~16.50	9.07~9.98	190.63	$-1.04^{+0.01}_{-0.01}$	$1750.5^{+112.7}_{-111.1}$	$40.5^{+2.0}_{-2.0}$	-176.6	$2.08^{+0.58}_{-0.46}$	$48.03^{+3.28}_{-3.09}$	$0.04^{+0.01}_{-0.01}$	$8.46^{+0.577}_{-0.543}$
16.50~18.00	9.98~10.89	215.76	$-1.05^{+0.02}_{-0.02}$	$1151.3^{+117.3}_{-119.6}$	$37.1^{+2.8}_{-2.8}$	-78.7	$1.63^{+0.69}_{-0.54}$	$41.83^{+4.61}_{-4.04}$	$0.04^{+0.02}_{-0.01}$	$7.37^{+0.812}_{-0.712}$
15.00~15.75	9.07~9.53	105.93	$-1.07^{+0.03}_{-0.03}$	$1198.0^{+211.1}_{-217.8}$	$31.4^{+3.3}_{-3.3}$	-41.5	$0.94^{+0.70}_{-0.42}$	$23.84^{+4.65}_{-3.86}$	$0.04^{+0.03}_{-0.02}$	$2.1^{+0.41}_{-0.34}$
15.75~16.50	9.53~9.98	163.07	$-1.02^{+0.01}_{-0.01}$	$1949.4^{+126.1}_{-127.9}$	$46.2^{+2.68}_{-2.67}$	-15.4	$3.43^{+1.23}_{-0.84}$	$72.68^{+5.48}_{-5.31}$	$0.04^{+0.01}_{-0.01}$	$5.16^{+0.478}_{-0.423}$
16.50~17.25	9.98~10.44	155.67	$-1.15^{+0.02}_{-0.02}$	$2382.3^{+217.5}_{-221.3}$	$45.3^{+2.7}_{-2.7}$	-125.6	$2.85^{+1.00}_{-0.76}$	$53.96^{+4.55}_{-4.28}$	$0.05^{+0.02}_{-0.01}$	$4.75^{+0.401}_{-0.377}$
17.25~18.00	10.44~10.89	159.05	$-0.93^{+0.02}_{-0.02}$	$684.7^{+49.7}_{-49.2}$	$23.9^{+3.8}_{-4.0}$	-30.8	$0.63^{+0.93}_{-0.37}$	$35.74^{+3.28}_{-3.21}$	$0.02^{+0.03}_{-0.01}$	$3.15^{+0.289}_{-0.283}$
15.00~15.38	9.07~9.30	69.11	$-1.06^{+0.07}_{-0.08}$	$711.2^{+209.5}_{-215.5}$	$28.9^{+5.7}_{-5.6}$	-30.2	$0.78^{+1.14}_{-0.55}$	$14.27^{+6.80}_{-3.54}$	$0.05^{+0.08}_{-0.04}$	$0.628^{+0.299}_{-0.156}$
15.38~15.75	9.30~9.53	83.03	$-1.01^{+0.03}_{-0.03}$	$1319.4^{+210.9}_{-208.7}$	$31.0^{+5.2}_{-5.2}$	-28.9	$0.83^{+1.14}_{-0.48}$	$32.18^{+6.45}_{-5.45}$	$0.03^{+0.04}_{-0.02}$	$1.42^{+0.284}_{-0.24}$
15.75~16.12	9.53~9.75	109.59	$-1.02^{+0.02}_{-0.02}$	$1967.9^{+193.8}_{-194.9}$	$43.6^{+4.0}_{-4.0}$	-72.6	$2.63^{+1.51}_{-0.96}$	$62.61^{+6.83}_{-6.58}$	$0.04^{+0.02}_{-0.02}$	$2.76^{+0.301}_{-0.29}$
16.12~16.50	9.75~9.98	133.10	$-1.01^{+0.02}_{-0.02}$	$1919.4^{+162.1}_{-168.5}$	$47.9^{+3.5}_{-3.5}$	-107.5	$4.31^{+1.60}_{-1.38}$	$82.08^{+8.46}_{-7.17}$	$0.05^{+0.02}_{-0.02}$	$3.61^{+0.372}_{-0.316}$
16.50~16.88	9.98~10.21	133.12	$-1.09^{+0.02}_{-0.02}$	$2574.3^{+264.0}_{-267.2}$	$55.7^{+3.8}_{-3.7}$	-117.9	$5.16^{+2.03}_{-1.44}$	$83.97^{+8.79}_{-7.60}$	$0.06^{+0.02}_{-0.02}$	$3.7^{+0.387}_{-0.335}$
16.88~17.25	10.21~10.44	89.16	$-1.24^{+0.05}_{-0.05}$	$1537.9^{+522.7}_{-558.0}$	$31.9^{+3.4}_{-3.4}$	-27.8	$1.38^{+0.94}_{-0.57}$	$24.25^{+7.37}_{-6.29}$	$0.06^{+0.04}_{-0.03}$	$1.07^{+0.325}_{-0.277}$
17.25~17.62	10.44~10.66	125.76	$-0.86^{+0.03}_{-0.03}$	$696.1^{+59.2}_{-57.7}$	$22.5^{+3.8}_{-3.7}$	-27.3	$0.83^{+1.39}_{-0.48}$	$45.89^{+5.21}_{-4.69}$	$0.02^{+0.03}_{-0.01}$	$2.02^{+0.23}_{-0.206}$
17.62~18.00	10.66~10.89	102.97	$-1.02^{+0.04}_{-0.04}$	$622.4^{+77.4}_{-80.6}$	$25.7^{+8.4}_{-9.5}$	-25.5	$0.39^{+1.32}_{-0.34}$	$25.51^{+4.95}_{-3.40}$	$0.02^{+0.05}_{-0.01}$	$1.12^{+0.218}_{-0.15}$
15.00~15.19	9.07~9.19	51.57	$-1.01^{+0.14}_{-0.15}$	$805.3^{+449.1}_{-380.0}$	$33.0^{+13.1}_{-18.2}$	-288.8	$0.80^{+5.09}_{-0.77}$	$19.23^{+23.49}_{-7.86}$	$0.04^{+0.27}_{-0.04}$	$0.423^{+0.517}_{-0.173}$
15.19~15.38	9.19~9.30	42.03	$-1.19^{+0.09}_{-0.09}$	$1201.3^{+667.6}_{-595.4}$	$27.5^{+4.3}_{-4.2}$	-27.1	$0.97^{+1.06}_{-0.55}$	$12.89^{+8.98}_{-4.04}$	$0.08^{+0.1}_{-0.05}$	$0.284^{+0.198}_{-0.0889}$
15.38~15.56	9.30~9.41	53.84	$-1.00^{+0.04}_{-0.04}$	$1158.5^{+201.4}_{-200.2}$	$23.4^{+8.3}_{-8.3}$	-27.1	$0.29^{+1.66}_{-0.26}$	$27.59^{+7.34}_{-4.93}$	$0.01^{+0.06}_{-0.01}$	$0.608^{+0.162}_{-0.109}$
15.56~15.75	9.41~9.53	63.61	$-1.06^{+0.05}_{-0.05}$	$1839.8^{+434.0}_{-420.6}$	$39.4^{+7.6}_{-7.0}$	-32.2	$1.74^{+2.60}_{-1.11}$	$40.95^{+11.15}_{-9.24}$	$0.04^{+0.06}_{-0.03}$	$0.902^{+0.246}_{-0.203}$
15.75~15.94	9.53~9.64	72.54	$-1.04^{+0.04}_{-0.04}$	$1896.8^{+350.9}_{-351.5}$	$40.8^{+4.7}_{-4.7}$	-30.3	$2.78^{+2.13}_{-1.19}$	$51.44^{+12.23}_{-9.91}$	$0.05^{+0.04}_{-0.03}$	$1.13^{+0.269}_{-0.218}$
15.94~16.12	9.64~9.75	83.99	$-0.99^{+0.03}_{-0.03}$	$1950.2^{+231.8}_{-232.1}$	$47.5^{+7.6}_{-7.6}$	-34.3	$2.34^{+3.12}_{-1.29}$	$74.72^{+11.53}_{-9.35}$	$0.03^{+0.04}_{-0.02}$	$1.65^{+0.254}_{-0.206}$
16.12~16.31	9.75~9.87	85.09	$-0.95^{+0.04}_{-0.04}$	$1379.2^{+207.4}_{-203.8}$	$32.7^{+5.4}_{-5.3}$	-39.2	$1.84^{+2.29}_{-1.02}$	$63.06^{+12.29}_{-10.56}$	$0.03^{+0.04}_{-0.02}$	$1.39^{+0.271}_{-0.233}$



**Table 2** continued

$t_1 \sim t_2$	$t_{rf,1} \sim t_{rf,2}$	$S$	$\alpha$	$E_c$	$kT$	$\Delta DIC$	$F_{BB}$	$F_{tot}$	$F_{ratio}$	$E_{tot}$
(s)	(s)			(keV)	(keV)		( $10^{-6}$ )	( $10^{-6}$ )		( $10^{52}$ erg)
Obs	Rest-frame						( $\text{erg cm}^{-2} \text{s}^{-1}$ )	( $\text{erg cm}^{-2} \text{s}^{-1}$ )		
16.31~16.50	9.87~9.98	104.94	$-1.05^{+0.02}_{-0.02}$	$2304.7^{+260.1}_{-261.8}$	$62.1^{+2.8}_{-2.8}$	-85.4	$6.72^{+1.63}_{-1.29}$	$97.87^{+12.08}_{-9.75}$	$0.07^{+0.02}_{-0.01}$	$2.15^{+0.266}_{-0.215}$
16.50~16.69	9.98~10.10	107.18	$-1.04^{+0.03}_{-0.03}$	$2737.1^{+346.9}_{-340.9}$	$58.4^{+5.6}_{-5.6}$	-86.1	$6.57^{+3.89}_{-2.56}$	$119.20^{+16.65}_{-14.38}$	$0.06^{+0.03}_{-0.02}$	$2.62^{+0.367}_{-0.317}$
16.69~16.88	10.10~10.21	82.58	$-1.13^{+0.13}_{-0.08}$	$1910.0^{+709.1}_{-1074.0}$	$58.6^{+8.6}_{-9.2}$	-86.9	$3.67^{+4.06}_{-3.43}$	$53.29^{+28.29}_{-22.24}$	$0.07^{+0.08}_{-0.07}$	$1.17^{+0.623}_{-0.49}$
16.88~17.06	10.21~10.32	64.96	$-1.24^{+0.03}_{-0.03}$	$2412.4^{+580.9}_{-576.0}$	$34.7^{+4.0}_{-4.0}$	-28.1	$1.52^{+1.46}_{-0.72}$	$32.97^{+6.96}_{-5.49}$	$0.05^{+0.05}_{-0.02}$	$0.726^{+0.153}_{-0.121}$
17.06~17.25	10.32~10.44	62.39	$-1.06^{+0.08}_{-0.08}$	$480.3^{+112.6}_{-97.0}$	$21.1^{+8.8}_{-8.9}$	-125.2	$0.39^{+3.01}_{-0.35}$	$15.20^{+8.60}_{-3.47}$	$0.03^{+0.2}_{-0.02}$	$0.335^{+0.189}_{-0.0764}$
17.25~17.44	10.44~10.55	81.92	$-0.89^{+0.05}_{-0.05}$	$720.6^{+93.9}_{-92.3}$	$19.1^{+3.9}_{-3.8}$	-23.5	$0.82^{+1.62}_{-0.55}$	$38.20^{+8.11}_{-5.42}$	$0.02^{+0.04}_{-0.01}$	$0.841^{+0.179}_{-0.119}$
17.44~17.62	10.55~10.66	97.68	$-0.84^{+0.05}_{-0.05}$	$713.4^{+96.8}_{-97.0}$	$32.3^{+11.9}_{-10.7}$	-38.1	$1.05^{+5.66}_{-0.87}$	$55.49^{+13.70}_{-10.34}$	$0.02^{+0.1}_{-0.02}$	$1.22^{+0.302}_{-0.228}$
17.62~17.81	10.66~10.78	82.29	$-0.95^{+0.05}_{-0.05}$	$628.7^{+86.6}_{-86.2}$	$19.5^{+9.9}_{-7.8}$	-66.8	$0.33^{+4.15}_{-0.30}$	$33.47^{+9.11}_{-5.06}$	$0.01^{+0.12}_{-0.01}$	$0.737^{+0.201}_{-0.111}$
17.81~18.00	10.78~10.89	64.36	$-1.08^{+0.06}_{-0.06}$	$565.9^{+123.9}_{-118.5}$	$30.2^{+7.8}_{-10.3}$	-15.3	$0.36^{+1.63}_{-0.33}$	$17.96^{+6.32}_{-3.42}$	$0.02^{+0.09}_{-0.02}$	$0.395^{+0.139}_{-0.0752}$

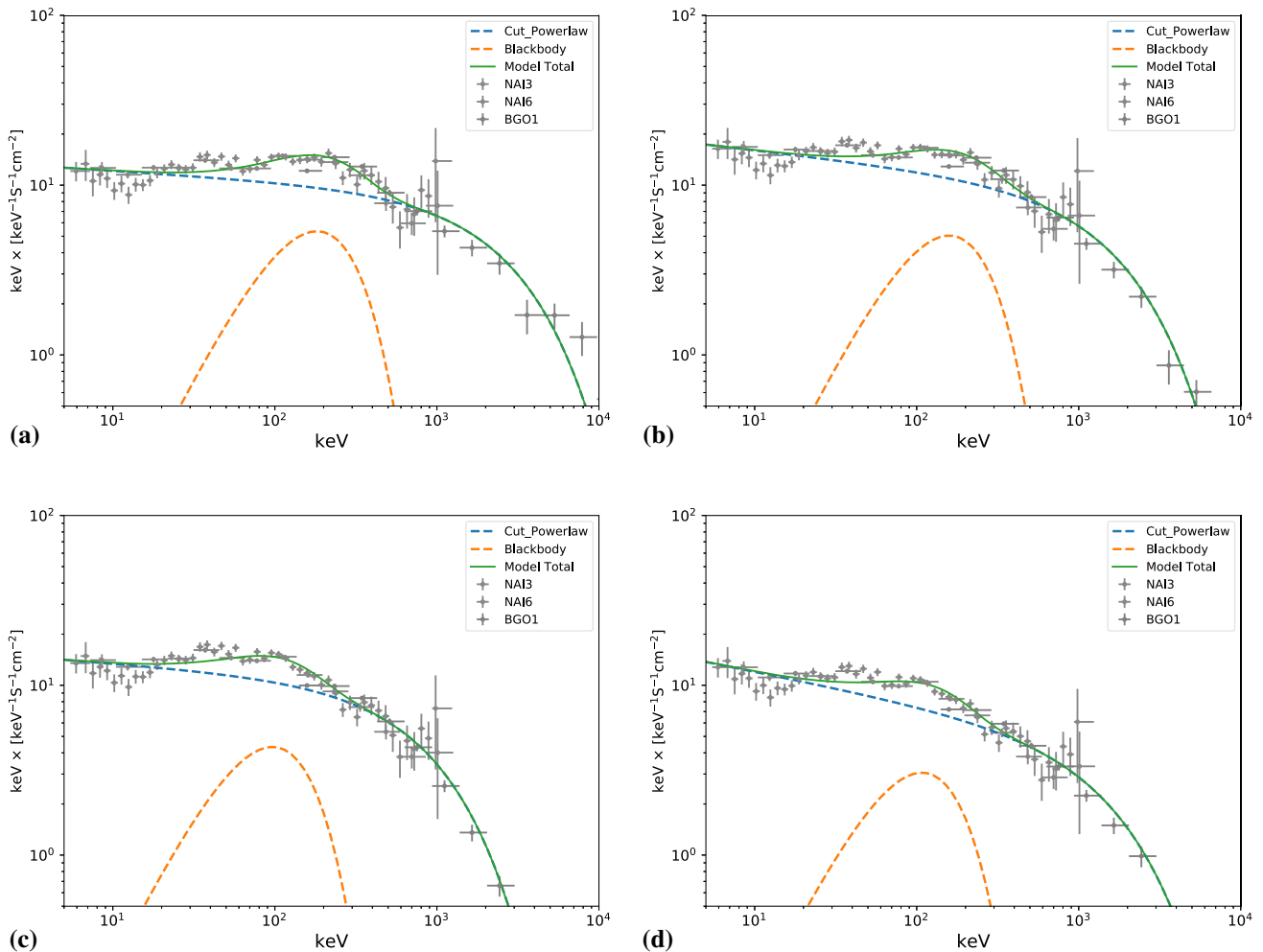


**Fig. 3** Time-resolved spectral analysis of the UPE I phase of GRB 180720B. This phase, extending from  $t_{rf} = 4.84$  to  $t_{rf} = 6.05$ , is divided into four time intervals with duration of  $\Delta t_{rf} \approx 0.3$  s. The spectra of the best fit for the rest-frame time intervals [4.840s–5.142s],

[5.142s–5.445s], [5.445s–5.747s], and [5.747s–6.050s] are shown in panels a–c, respectively. The CPL + BB is confirmed to be the best fit for each time interval. The best fit parameters are listed in Table 1

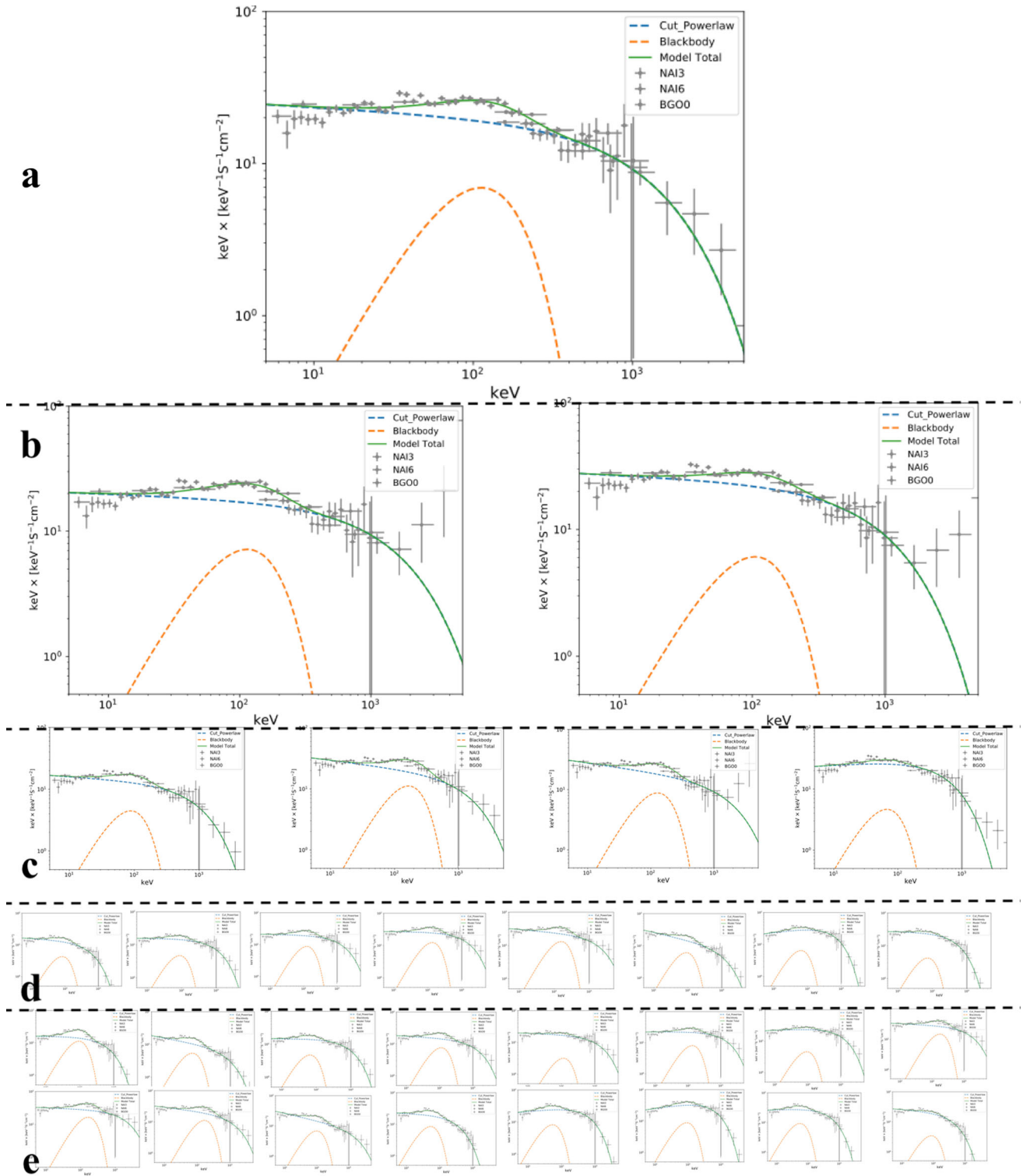


**Fig. 4** Time-resolved spectral analysis of UPE II phase of GRB 180720B. **a** The first iteration: spectrum of the entire UPE II phase extended from  $t_{\text{rf}} = 9.07$  s to  $t_{\text{rf}} = 10.89$  s. **b** The second iteration: spectral analysis carried out over two equal rest-frame time intervals of [9.07s–9.98s] and [9.98s–10.89s]. **c** The third iteration: spectral analysis performed over four equal rest-frame time intervals of [9.07s–9.53s], [9.53s–9.98s], [9.98s–10.44s] and [10.44s–10.89s]. **d** The fourth iteration: spectral analysis performed over eighth equal rest-frame time intervals of [9.07s–9.30s], [9.30s–9.53s], [9.53s–9.75s],

[9.75s–9.98s], [9.98s–10.21s], [10.21s–10.44s], [10.44s–10.66s] and [10.66s–10.98s]. Finally, **e** the fifth iteration: spectral analysis performed over sixteen equal rest-frame time intervals of [9.07s–9.19s], [9.19s–9.30s], [9.30s–9.41s], [9.41s–9.53s], [9.53s–9.64s], [9.64s–9.75s], [9.75s–9.87s], [9.87s–9.98s], [9.98s–10.10s], [10.10s–10.21s], [10.21s–10.32s], [10.32s–10.44s], [10.44s–10.55s], [10.55s–10.66s], [10.66s–10.78s] and, [10.78s–10.89s]. The CPL + BB is confirmed to be the best fit for each time interval. The spectral best fit parameters correspond to each iteration are reported in Table 2

mass for BH formation before the second peak of fallback accretion onto the  $\nu$ NS (Becerra et al., submitted; see also [6]). In some cases, this phenomenon allows the  $\nu$ NS-rise emission to superpose to the UPE. In GRB 180720B, the energy released by the  $\nu$ NS-rise dominates the UPE phase for about three seconds, resulting in split UPEs I and II. After that, the  $\nu$ NS-rise emission fades and the UPE becomes visible again.

The detailed explanation of Episodes 4 to 6 of GRB 180720B is presented in [36]. This work is devoted to the UPE I and UPE II phases of GRB 180720B. Following the explanation of the UPE phase in GRB 190114C [39], we first present the detailed spectral analysis of the UPE phase of GRB 180720B and then its astrophysical mechanism based on the inner engine of GRBs [69] and expanding PEMB pulses [38].

### 3 The time-resolved spectral analysis of the UPE phase

Due to the high signal-to-noise (S/N) ratio of the Fermi-GBM data acquired during the UPE phase, a refined spectral analysis is performed in the [4.84–6.05] time interval in three iterations, and in the [9.07–10.89] time interval in five iterations on decreasing time bins, while maintaining reliable statistical significance. The time intervals between iterations are halved.

For the final iteration of the UPE I, i.e., the third iteration, the UPE I is divided into four time intervals of  $\Delta t_{\text{rf}} \approx 0.3$  s: [4.840s–5.142s], [5.142s–5.445s], [5.445s–5.747s], [5.747s–6.050s].

For the last iteration of the UPE II where reliable statistical significance is still fulfilled, i.e., the fifth iteration, the UPE II is divided into 16 time intervals of  $\Delta t_{\text{rf}} \approx 0.11$  s: [9.07s–9.19s], [9.19s–9.30s], [9.30s–9.41s], [9.41s–9.53s], [9.53s–9.64s], [9.64s–9.75s], [9.75s–9.87s], [9.87s–9.98s], [9.98s–10.10s], [10.10s–10.21s], [10.21s–10.32s], [10.32s–10.44s], [10.44s–10.55s], [10.55s–10.66s], [10.66s–10.78s] and [10.78s–10.89s].

The spectral analysis is performed over each time interval. The presence of a cut-off power-law plus black body (CPL + BB) as the best spectral fit is confirmed in each time interval and for each iterative process. The time intervals both in rest-frame and observer frame, the significance ( $S$ ) for each time interval, the power-law index, cut-off energy, temperature,  $\Delta$ DIC, BB flux, total flux, the BB to total flux ratio,  $F_{\text{BB}}/F_{\text{tot}}$  and finally the isotropic energy of entire the UPE phase and its sub-intervals are shown in Table 1 and Table 2; see also Fig. 3 and Fig. 4. The evolution of the temperature and the luminosity during the UPE phase, as obtained by the time-resolved spectral analysis, are shown in Fig. 5.

The time-resolved spectral analysis over each iteration, reveals a common spectral feature for each time interval char-

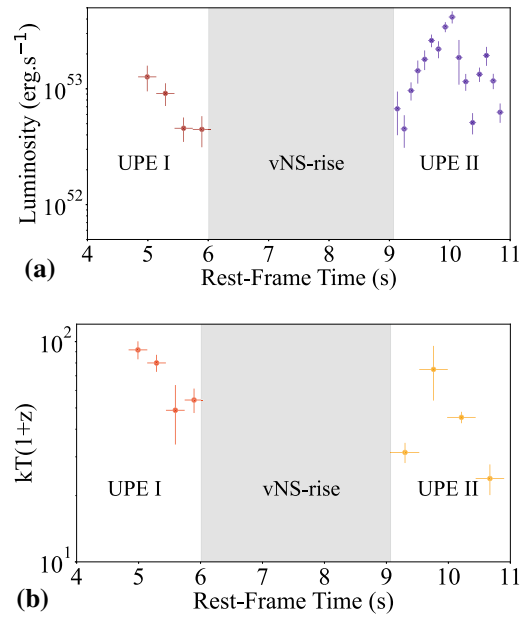


**Fig. 5** **a** The Luminosity during the UPE phase. **b** The rest-frame temperature during the UPE phase. The luminosity and temperature data points are obtained from analyses with  $\Delta t_{\text{rf}} = 0.3$  s time resolution reported in Table 1 (UPE I), and  $\Delta t_{\text{rf}} = 0.11$  s time resolution reported in Table 2 (UPE II)

acterized by the CPL+BB best-fit model with a rest-frame temperature of  $kT = 20\text{--}60$  keV and the ratio of blackbody flux ( $F_{\text{BB}}$ ) to the total flux ( $F_{\text{tot}}$ ) of

$$0.01 \lesssim \frac{F_{\text{BB}}}{F_{\text{tot}}} \lesssim 0.07. \tag{3}$$

In essence, the UPE II is a continuation of the UPE I, and there is no distinction between the two. The observed discontinuity in the UPE phase is caused by the simultaneous occurrence of the UPE phase and the  $\nu$ NS-rise in this GRB. The temporal coincidence of these two emissions in a BdHN depends on binary parameters, more relevant the orbital period (Rueda et al.; to be submitted). As a result, we assume in this paper that the UPE phase extends from  $t_{\text{rf}} = 4.84$  to  $t_{\text{rf}} = 10.89$  s.

The existence of the BB components in the spectrum of the UPE phase has been identified as the characteristic signature of  $e^+ e^-$  pair creation in presence of baryons (the PEMB pulse) originating from the vacuum polarization process [39, 60, 62–64]. This subject will be addressed in Sects. 6 and 7.

### 4 The properties of inner engine

The physics of inner engine was first described in [52, 69] for GRB 130427A and [37] for GRB 190114C. The Papapetrou–Wald solution [41, 82] is used to describe the newborn Kerr BH in the BdHNE I surrounded by a magnetic field and by the

low-density plasma in the cavity [59]. The gravitomagnetic interaction of the newborn Kerr BH with the magnetic field induces a strong electric field in the BH vicinity [54]. In [39], it was shown that the UPE phase of GRB 190114C can be originate by the QED process of vacuum polarization in an overcritical field, i.e.,  $|\mathbf{E}| > E_c$ , where  $E_c$  is the critical field for spontaneous  $e^+e^-$  pair creation in vacuum and is given by Eq. (2). Following this framework, we apply in this work the inner engine in the QED overcritical regime to explain the UPE phase of GRB 180720B observed by Fermi-GBM. We give the details of the physical process in Sect. 6.

In this section, we focus on the structure of the electromagnetic field around the BH to investigate the conditions under which the overcritical field regime can develop. The components of the electric and magnetic field (in the Carter’s orthonormal tetrad) in the approximation of small polar angles can be written as [52,69]

$$E_{\hat{r}} = -\frac{2B_0 J G}{c^3} \frac{(r^2 - \hat{a}^2)}{(r^2 + \hat{a}^2)^2} \tag{4}$$

$$E_{\hat{\theta}} = 0 \tag{5}$$

$$B_{\hat{r}} = \frac{B_0 \left( -\frac{4GJ^2r}{M(r^2 + \hat{a}^2)} + a^2 + r^2 \right)}{(r^2 + \hat{a}^2)} \tag{6}$$

$$B_{\hat{\theta}} = 0. \tag{7}$$

where  $\Sigma = r^2 + \hat{a}^2 \cos^2 \theta$ ,  $\Delta = r^2 - 2\hat{M}r + \hat{a}^2$ ,  $\hat{M} = GM/c^2$ ,  $\hat{a} = a/c = J/(Mc)$ , being  $M$  and  $J$  the mass and angular momentum of the Kerr BH. The (outer) event horizon is located at  $r_+ = (\hat{M} + \sqrt{\hat{M}^2 - \hat{a}^2})$ .

We can now introduce the effective charge [69]

$$Q_{\text{eff}} = \frac{G}{c^3} 2B_0 J, \tag{8}$$

which when is replaced in the charge of the Kerr–Newman solution, it leads to a radial electric field equal to the one of the Papapetrou–Wald solution given by Eq. (4) [39]. Therefore, up to linear order in  $\theta$  and in the dimensionless BH spin parameter  $\alpha \equiv \hat{a}/(GM/c^2)$ , the electric field can be written as

$$E_{\hat{r}} = -\frac{2B_0 J G}{c^3} \frac{(r^2 - \hat{a}^2)}{(r^2 + \hat{a}^2)^2} \approx -\frac{1}{2} \alpha B_0 \frac{r_+^2}{r^2}. \tag{9}$$

The specific value of the mass, spin parameter, and magnetic field in the inner engine will be determined as a function of operative astrophysical processes, which are presented in the next sections. We now discuss how the gravitational collapse of the NS in a BdHN I can lead to an engine with an electromagnetic field structure that can be approximately described by the Papapetrou–Wald solution. To the best of our knowledge, there are no numerical simulations dedicated

to demonstrating the formation of this specific configuration. Nevertheless, we refer to Sec. 7 of [53] which discusses the nature of the magnetic field around the newborn BH in a BdHN I and its support from numerical simulations of gravitational collapse.

Numerical simulations in [6] show that the magnetized NS companion of the CO<sub>core</sub>, in the accretion process, gains not only a considerable amount of mass but also angular momentum. Therefore, we conclude that the BH forms from the collapse of a magnetized ( $10^{12}$ – $10^{13}$  G), fast rotating (millisecond period) NS once it reaches the critical mass. The same simulations show that SN material remains bound around the nascent BH in a torus-like structure. This matter is essential to anchor the magnetic field outside the newborn BH. The matter density in the off-equatorial directions is low, as shown by numerical simulations in [59]. The above picture naturally leads to the inner engine: a rotating BH surrounded by a magnetic field and very low density ionized matter.

The numerical simulations of the magneto-rotational collapse of NS starting from the seminal simulations of J. Wilson in [85,86]. These early works already showed the amplification of the magnetic field in the gravitational collapse. This result is confirmed by simulations of NS binary mergers leading to a BH surrounded by an accretion disk, whose post-merger system show similarities with the inner engine picture and support the present scenario. Some relevant works on this subject are [20,21,46,75,77,78].

Equation (9) tells us that if the above processes occur and amplify the magnetic field strength to values  $B_0 \gtrsim (2/\alpha)B_c$  near the BH horizon, where  $B_c = E_c = 4.41 \times 10^{13}$  G, an overcritical electric field will develop and lead to the QED process of vacuum polarization.

### 5 Mass and spin of BH

The energy condition is obtained from the mass–energy formula of the Kerr BH [13,14,25]

$$M^2 = \frac{c^2 J^2}{4G^2 M_{\text{irr}}^2} + M_{\text{irr}}^2. \tag{10}$$

The extractable energy of a Kerr BH  $E_{\text{ext}}$  is given by the subtracting the irreducible mass,  $M_{\text{irr}}$ , from the total mass of the BH,  $M$ :

$$E_{\text{ext}} = (M - M_{\text{irr}})c^2 = \left( 1 - \sqrt{\frac{1 + \sqrt{1 - \alpha^2}}{2}} \right) M c^2. \tag{11}$$

which we use to obtain  $M$  as a function of  $\alpha$ ,  $M(\alpha)$ , by requesting the condition that observed UPE emission origi-

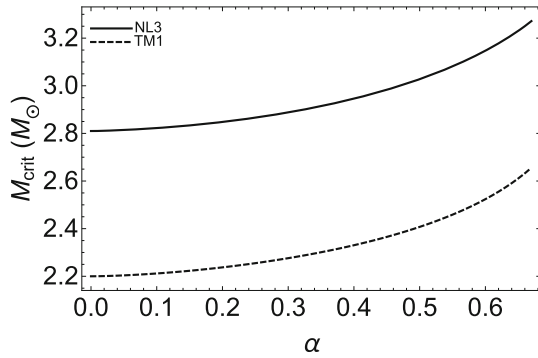


**Fig. 6** NS critical mass as a function of the spin parameter  $\alpha$  for the NL3 and TM1 EOS. We recall that the maximum spin parameter of a uniformly rotating NS is  $\alpha_{\max} \approx 0.71$ , independently of the NS EOS; see e.g. Cipolletta et al. [15]

nates from BH extractable energy, i.e.

$$E_{\text{UPE}} = E_{\text{ext}}. \tag{12}$$

The goal is to show that the Kerr BH extractable energy can explain the energetics of the UPE phase and, in turn, it leads to estimate the mass and spin of BH. Equation (11) has two parameters,  $M$  and  $\alpha$ , hence we must supply another equation to determine them.

In BdHNeI the BH originates from the hypercritical accretion of SN ejecta onto the NS, i.e., the BH forms when the NS reaches its critical mass. Therefore, the mass of the BH must satisfy the constraint

$$M \geq M_{\text{crit}}(\alpha), \tag{13}$$

where  $M_{\text{crit}}(\alpha)$  is the critical mass of a rotating NS with Kerr spin parameter  $\alpha$ . The NS critical mass value depends on the nuclear equation of state (EOS). In Cipolletta et al. [15], it was shown that, for instance, for the NL3, GM1 and TM1 EOS, the critical mass for rigidly rotating NS is fitted with a maximum error of 0.45% by the expression

$$M_{\text{crit}}(j) = M_{\text{crit}}^{J=0}(1 + kj^p), \tag{14}$$

where  $k$ ,  $p$ , and  $M_{\text{crit}}^{J=0}$  are parameters that depend upon the nuclear EOS, being the latter the critical mass in the non-rotating case, and  $j \equiv cJ/(GM_{\odot})^2$ . With the relation between  $j$  and  $\alpha$ , i.e.,  $j = \alpha(M/M_{\odot})^2$ , Eq. (14) becomes an implicit non-linear algebraic equation for the NS critical mass as a function of  $\alpha$ . For instance, we show in Fig. 6 the numerical solution of Eq. (14) for the NL3 ( $k = 0.006$ ,  $p = 1.68$ ) and TM1 ( $k = 0.017$ ,  $p = 1.61$ ) EOS. We limit the value of the spin parameter to  $\alpha_{\max} \approx 0.7$ , which has been found to be the maximum value attainable by rigidly rotating NS independent on the nuclear EOS (see [15] for details).

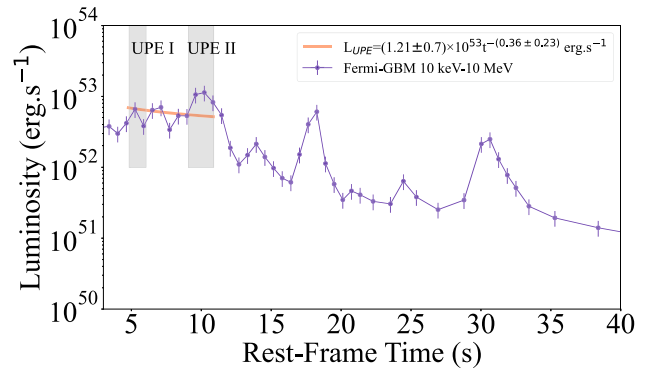


**Fig. 7** Luminosity of GRB 180720B in the cosmological rest-frame of the source. Blue circles: obtained from *Fermi*-GBM in the 10 keV–10 MeV energy band. The light grey parts represent the UPE phase; UPE I from  $t_{\text{rf}} = 4.84$  s to  $t_{\text{rf}} = 6.05$  s, and UPE II from  $t_{\text{rf}} = 9.07$  s to  $t_{\text{rf}} = 10.89$  s. The rest-frame luminosity light-curve of GRB 180720B during the UPE phase is fitted by a power-law with slope of  $\alpha_{\text{UPE}} = 0.36 \pm 0.23$  and, amplitude of  $(1.21 \pm 0.70) \times 10^{53} \text{ erg s}^{-1}$

We now proceed to estimate the mass and spin parameter of the BH at the beginning of the UPE phase, namely at  $t_{\text{rf}} = 4.84$  s. For this task, we solve Eq. (12) using  $E_{\text{UPE}} = E_{\text{UPEI}} + E_{\text{UPEII}} = 2.24 \times 10^{53} \text{ erg}$ , together with the inequality (13). We use the minimum possible value in the latter so to set a lower limit to the BH mass, and correspondingly an upper limit to the spin parameter. For the NS critical mass, we use Eq. (14) for the TM1 EOS. We obtain the lower limit to the BH mass,  $M = 2.40M_{\odot}$ , and the upper limit to the spin,  $\alpha = 0.60$ . The corresponding irreducible mass of the BH which is assumed to be constant during the radiation process is  $M_{\text{irr}} = 2.28 M_{\odot}$ .

Since the MeV emission during the UPE phase is powered by the extractable rotational energy of the Kerr BH [see Eq. (12)], the time derivative of Eq. (11) gives the luminosity

$$L_{\text{UPE}} = -\frac{dE_{\text{ext}}}{dt} = -\frac{dM}{dt}. \tag{15}$$

The rest-frame 10 keV–10 MeV luminosity light-curve of GRB 180720B during UPE phase is fitted by a power-law with slope of  $\alpha_{\text{UPE}} = 0.36 \pm 0.23$  and, amplitude of  $(1.21 \pm 0.70) \times 10^{53} \text{ erg s}^{-1}$ . From this luminosity (see Fig. 7), and using as initial BH mass and spin at  $t_{\text{rf}} = 4.84$  s the values estimated above, Eq. (15) can be integrated to obtain the time evolution of the BH mass and spin during the UPE phase which is shown in Fig. 8.

## 6 Vacuum polarization and its role in the formation of UPE phase

The UPE phase has been explained by introducing the concept of the the dyadosphere around the Reissner–Nordström

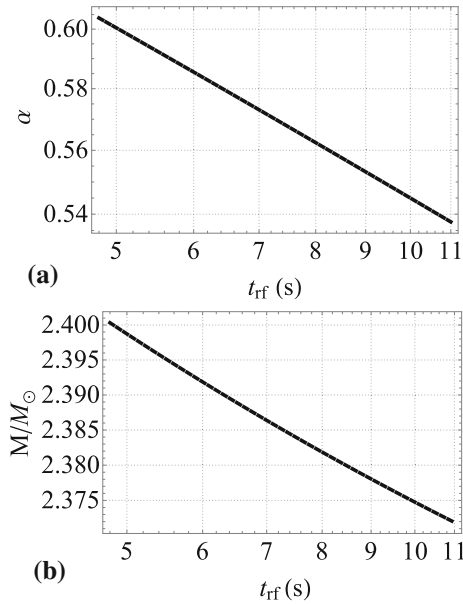


**Fig. 8** The evolution of the mass and spin of BH, as a function of rest-frame time ( $t_{\text{rf}}$ ) for GRB 180720B during the UPE phase ( $t_{\text{rf}} = 4.84\text{--}10.89$  s). The MeV energetic is paid by the extractable energy of the Kerr BH (Eq. 15), leading to the reduction of the mass and spin during the UPE phase

BH [56] and dyadotorous around the Kerr–Newman geometry [12]. The dyadoregion is the region around the BHs, characterised by the overcritical electric field  $|\mathbf{E}| > E_c$ , filled by the highly dense  $e^+ e^-$  pairs produced by vacuum polarization process (see [64] for more details).

Following Ref. [39], we use the dyadoregion framework in the Kerr–Newman geometry taking advantage of the effective charge defined by Eq. (8). For the calculation of the transparency properties of the  $e^+ e^-$  pair plasma formed from the vacuum polarization process (analyzed in Sect. 7), we need the initial energy of the pairs,  $E_{e^+e^-}$ , and the radius of the dyadoregion,  $r_d$ .

The dyadoregion extends from the BH horizon to the distance  $r_d$  at which the electric field has the critical value  $E_c$ . Applying this condition to the Kerr–Newman electric field one obtains [12]

$$\left(\frac{r_d}{\hat{M}}\right)^2 = \frac{1}{2} \frac{\lambda}{\mu\epsilon} - \alpha^2 + \left(\frac{1}{4} \frac{\lambda^2}{\mu^2\epsilon^2} - 2\frac{\lambda}{\mu\epsilon}\alpha^2\right)^{1/2} \quad (16)$$

with  $\epsilon = E_c M_\odot G^{3/2} / c^4 \approx 1.873 \times 10^{-6}$ , and

$$\lambda = \frac{Q_{\text{eff}}}{\sqrt{GM}} = \frac{2B_0 JG/c^3}{\sqrt{GM}}, \quad (17)$$

is the effective charge-to-mass ratio. Therefore, the width of the dyadoregion is

$$\Delta_d(t) = r_d(t) - r_+(t). \quad (18)$$

The energy of  $e^+ e^-$  pairs generated (at a given time) by the inner engine is estimated as the electromagnetic energy stored in the dyadoregion (see [12] for details), i.e.,  $E_{e^+e^-} = E_{(r_+,r_d)}$ , where

$$E_{(r_+,r_d)} = \frac{(2B_0 JG/c^3)^2}{4r_+} \left(1 - \frac{r_+}{r_d}\right) + \frac{(2B_0 JG/c^3)^2}{4\hat{a}} \times \left[ \left(1 + \frac{\hat{a}^2}{r_+^2}\right) \arctan\left(\frac{\hat{a}}{r_+}\right) - \left(1 + \frac{\hat{a}^2}{r_d^2}\right) \arctan\left(\frac{\hat{a}}{r_d}\right) \right]. \quad (19)$$

### 7 General formulation of transparency condition of the UPE phase

We follow the treatment of the transparency introduced in [39]. The existence of the overcritical electric field around the BH leads to the following sequence of events:

(1) The formation of an optically thick dyadoregion around BH dominated by the high density and pressure of the neutral  $e^+ e^- \gamma$  plasma [64], formed in a timescale  $\sim \hbar/(m_e c^2) \approx 10^{-21}$  s, with total energy  $E_{e^+e^-}^{\text{tot}} = E_{\text{iso}}$ . This plasma is endowed with a baryonic mass  $M_B$ , with baryon load parameter  $\mathcal{B} = M_B c^2 / E_{\text{iso}}$ . This optically thick pair electromagnetic-baryon pulse is known as the PEMB pulse first introduced by [60].

(2) The self-acceleration and expansion of the PEMB pulses due to their high internal pressure achieved by pair-plasma thermalization in a very short timescale ( $\sim 10^{-13}$  s). They reach ultra-relativistic velocities of up to  $\Gamma \sim 100$  in the case of long GRBs [2, 3, 60].

(3) Emission of thermal radiation. When the PEMB pulses expand with ultra-relativistic velocities, the  $e^+ e^- \gamma$  plasma becomes optically thin [60, 63]. The condition of transparency is

$$\begin{aligned} \tau &= \sigma_T (n_{e^+e^-} + \bar{Z} n_B) \Delta_d \approx \sigma_T (\bar{Z} n_B) \Delta_d, \\ &= \sigma_T \frac{\bar{Z} M_B}{m_N 4\pi R^2 \Delta_d} \Delta_d = 1, \end{aligned} \quad (20)$$

where  $\Delta_d$  is the thickness of the PEMB pulses,  $\sigma_T$  is the Thomson cross-section,  $\bar{Z}$  is the average atomic number of baryons ( $\bar{Z} = 1$  for Hydrogen atom and  $\bar{Z} = 1/2$  for general baryonic matter),  $m_N$  is nucleon mass and  $M_B$  is the baryon mass. For the values of  $\mathcal{B}$  considered in the present work, i.e.,  $\mathcal{B} = 10^{-3}\text{--}10^{-2}$ , we can safely assume  $n_{e^+e^-} \ll n_B$ . Therefore, from Eq. (20) the lower bound of transparency radius is

$$R^{\text{tr}} = \left(\frac{\sigma_T M_B}{8\pi m_N}\right)^{1/2} = \left(\frac{\sigma_T \mathcal{B} E_{\text{iso}}}{8\pi m_N c^2}\right)^{1/2}. \quad (21)$$

This emission at transparency, previously known as P-GRB, is characterised by a thermal component observed in the spectral analysis of prompt emission of GRBs. The energy of this blackbody component that signs the occurrence of the UPE phase is

$$E_{\text{P-GRB}}^{\text{obs}} = aT_{\text{obs}}^4 \Gamma^4 (1 - v/c)^3 4\pi R_{\text{tr}}^2 \Delta_d, \tag{22}$$

where  $a = 4\sigma/c$ , being  $\sigma$  the Stefan-Boltzmann constant.

The most efficient process to create the  $e^+e^-$  plasma around BH is the vacuum polarization, which proceeds on a quantum timescale of the order of the Compton time,  $\hbar/(m_e c^2) \approx 10^{-21}$  s [61]. The electric field screening time is given by the time it takes to charged particles to induce a field that opposites to the original field. This timescale, of the order of  $r_+/c \approx 10^{-5}$  s ( $r_+$  is the BH horizon radius), is 16 orders of magnitudes larger than quantum time scale. This guarantees that the formation of the  $e^+e^-$  pair plasma and its self-expansion by internal pressure starts before any screening process of the electric field could be at work. The dynamics of the expanding plasma from the vicinity of the BH up to the transparency point depends upon the plasma energy,  $E_{e^+e^-}^{\text{tot}}$ , and the baryon load parameter,  $\mathcal{B}$  [60,63].

As discussed in Sec. XI in [38] and in Sects. 8 and 9 of this paper, the BH extractable energy powers the energy for the creation of the  $e^+e^-$  plasma around the BH, which is then used in the kinetic energy of expansion of the PEMB pulse and in the radiation released at transparency. Therefore, in each of these processes, the Kerr BH loses a fraction of its mass-energy and angular momentum. This implies that the BH mass and angular momentum, at the time  $t_0 + \Delta t$ , are  $M = M_0 - \Delta M$  and  $J = J_0 - \Delta J$ , where  $\Delta M$  and  $\Delta J$  are the BH mass-energy and angular momentum extracted by the PEMB pulse expansion and emission process. We estimate that each process extracts  $\Delta M/M \sim \Delta J/J \sim 10^{-9}$ . Since the induced electric field depends linearly on  $J$ , see Eq. (4), the new value of the induced electric field,  $E$ , is lower than the previous value,  $E_0$ , fulfilling  $E = E_0(1 - \Delta J/J)$ . As a result, the system begins a new process in presence of the same magnetic field  $B_0$ , which is kept constant, and a new, lower effective charge  $Q_{\text{eff}} = Q_{\text{eff},0} - \Delta Q_{\text{eff}}$ , where  $\Delta Q_{\text{eff}} = 2B_0\Delta J$ . Therefore, we assume that the spacetime evolves from one stationary axially symmetric metric to the next, and at each step the electromagnetic field structure of the inner engine is given by the Papapetrou-Wald solution, and the latter can be approximated by the Kerr-Newman metric of charge  $Q_{\text{eff}}$ . Once the plasma is formed, it self-accelerates, expanding to the point of transparency. We recall that the dynamics of the plasma depends only on the initial conditions of energy and baryon load, which in turn depend only on  $M$ ,  $J$  and  $Q_{\text{eff}}$ . This means that the plasma dynamics at times  $t > t_0$ , being  $t_0$  the time of its formation and beginning of the expansion, depends only on the values at  $t_0$  of  $M$ ,  $J$  and  $B_0$ . Thus, the QED process of  $e^+e^-$  formation and

its dynamics leading to transparency of the PEMB pulses efficiently extracts the BH energy without being affected by any screening process of the electric field. Therefore, the decrease of the electric field with time is driven by the BH energy extraction which lowers the BH angular momentum, not because of an electric field screening. This ensures that the above process can repeat over time until the electric field reaches the critical value. For GRB 180720B, this occurs at  $t_{\text{tr}} = 10.89$  s. After this time, the vacuum polarization process does not occur any longer.

The corresponding value of the Lorentz factor at the instant of transparency,  $\Gamma$ , and the baryon load parameter can be inferred from UPE observables as follows. The calculation involves the following quantities: (a) the isotropic energy of PEMB pulses,  $E_{\text{iso}}$ ; (b) the ratio of the blackbody energy of the P-GRB to the isotropic energy,  $E_{\text{P-GRB}}^{\text{obs}}/E_{\text{iso}}$ ; (c) the observed value of the blackbody temperature of the P-GRB,  $T_{\text{obs}}$ ; (d) the width of the dyadoregion at decoupling,  $\Delta_d$ , obtained from Eq. (18). The properties of the plasma at transparency are obtained from the solution of the following equations simultaneously.

The first equation is obtained by substituting Eq. (21) into Eq. (22), and dividing it by  $E_{\text{iso}}$

$$\frac{E_{\text{P-GRB}}^{\text{obs}}}{E_{\text{iso}}} = \frac{aT_{\text{obs}}^4}{16\Gamma^2} \sigma_T \frac{\mathcal{B}}{m_N c^2} \Delta_d, \tag{23}$$

and the second equation is obtained from the energy conservation

$$1 = \frac{E_{\text{P-GRB}}^{\text{obs}}}{E_{\text{iso}}} + \frac{E_{\text{Kinetic}}}{E_{\text{iso}}} \tag{24}$$

where  $E_{\text{Kinetic}}$  is the kinetic energy of the baryonic PEMB pulses

$$E_{\text{Kinetic}} = (\Gamma - 1)M_B c^2. \tag{25}$$

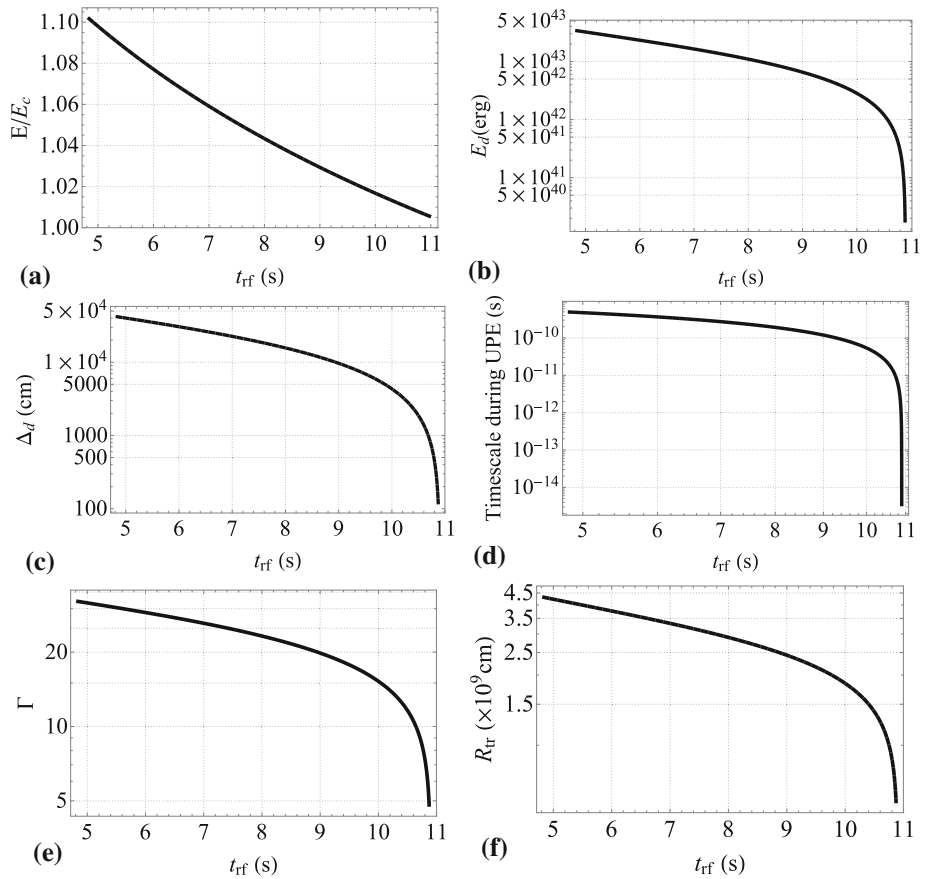
By substituting Eq. (25) in Eq. (24) we have

$$\mathcal{B} = \frac{1}{\Gamma - 1} \left( 1 - \frac{E_{\text{P-GRB}}^{\text{obs}}}{E_{\text{iso}}} \right). \tag{26}$$

### 8 Magnetic field and transparency condition and timescale of radiation during the UPE phase

The time evolution of the mass and spin of BH during the UPE was discussed in in Sec 5; see Fig. 8. In order to calculate the magnetic field during the UPE phase, i.e., in the time interval  $4.84 < t_{\text{tr}} < 10.89$  s, we assume that the electric field therein is overcritical, which guarantees the occurrence of the UPE phase. Therefore, we infer a magnetic field strength  $B_0 =$

**Fig. 9** **a** The evolution of the overcritical electric field reaching its critical value at the end of UPE phase ( $t_{\text{rf}} = 10.89$  s). **b** The energy stored in dyadoregion obtained from Eq. (19). **c** The width of dyadoregion obtained from Eq. (18). **d** Repetition time scale of the inner engine from Eq. (27). **e** The Lorentz factor,  $\Gamma$  which tends to unity at  $t_{\text{rf}} = 10.89$  s confirming the the end of UPE. **[f]** The transparency radius; see Sect. 8. All values are plotted as a function of rest-frame time for GRB 180720B during the UPE phase ( $t_{\text{rf}} = 4.84\text{--}10.89$  s)



$2.14 \times 10^{14}$  G such that the electric field given by Eq. (9), at the end of the UPE phase at  $t_{\text{rf}} = 10.89$  s, fulfills  $|E_{r+}| = E_c$ .

For this magnetic field, the dyadoregion energy at  $t_{\text{rf}} = 4.84$  is  $5 \times 10^{43}$  erg obtained from Eq. (19). Figures 9[a] and 9[b] show the evolution of magnitude of electric field and the dyadoregion energy during the UPE phase. The total isotropic energy of the UPE phase is  $E_{\text{iso}}^{\text{UPE}} = 2.23 \times 10^{53}$  erg, consequently, there exist  $\sim 10^9$  PEMB pulses during UPE phase.

For the first PEMB pulse, assuming  $B_0 = 1.87 \times 10^{14}$  G, the width of the dyadoregion at transparency point is  $\Delta_d = 4.1 \times 10^4$  cm; obtained from Eq. (18). From the hierarchical structure of UPE phase in this GRB presented by Eq. 3, we have  $E_{\text{P-GRB}}^{\text{obs}}/E_{\text{iso}} \sim 0.03$  and the temperature  $kT_{\text{obs}} \sim 50$  keV; see Table. 2.

With these and following the previous section the transparency radius  $R^{\text{tr}} = 4.5 \times 10^9$  cm, the baryon load parameter  $\mathcal{B} = 3.1 \times 10^{-2}$ , and finally the Lorentz factor  $\Gamma = 38$ , are obtained.

After the first PEMB pulse, whose energetics ( $\Delta E$ ) is paid by the rotational energy of the BH (by reducing the  $\Delta J$  from the angular momentum of the BH), the system starts over with the new value of the BH mass, angular momentum and effective charge, as explained above.

We infer from the MeV luminosity, the evolution of the radiation timescale  $\tau_q(t)$  of the PEMB pulses by requiring it

**Table 3** The parameters of the inner engine and the transparency point, obtained from the starting time of the UPE phase for GRB 180720B ( $t_{\text{rf}} = 4.84$  s) and GRB 190114C ( $t_{\text{rf}} = 1.9$  s)

	GRB180720B	GRB190114C
$R^{\text{tr}}$ (cm)	$4.5 \times 10^9$	$9.4 \times 10^9$
$\mathcal{B}$	$3.1 \times 10^{-2}$	$5.1 \times 10^{-3}$
$\Gamma$	30	139
$\tau_q$ (s)	$5 \times 10^{-10}$	$3.1 \times 10^{-9}$
$\Delta_d$ (cm)	$4.1 \times 10^4$	$1.8 \times 10^5$
$B_0$ (G)	$1.87 \times 10^{14}$	$2.3 \times 10^{14}$
$ E /E_c$	1.11	1.25

to explain the MeV emission energetics, i.e.:

$$\tau_q(t) = \frac{E_{(r_+(t), r_d(t))}}{L_{\text{MeV}}}, \tag{27}$$

where the  $E_{(r_+(t), r_d(t))}$  is the energy of dyadoregion from Eq. (19), determined from the new values of  $J$  and  $M$  for each PEMB pulse, and  $L_{\text{MeV}}$  is the MeV luminosity obtained from the best fit in Sect. 5.

These parameters obtained from the starting time of the UPE phase, are similar to those of GRB 190114C; see Table 3. The evolution of the PEMB pulse timescale, the



Lorentz  $\Gamma$  factor, transparency radius, are shown in Fig. 9d–f, respectively.

We recall that the inner engine model has been first motivated to explain the GeV emission of GRBs as powered by an electro-dynamical process that extracts the rotational energy of the newborn Kerr BH [37, 54, 59], and in [38] for GRB 190114C and here for GRB 180720B it has been extended to explain the UPE phase. Following [37, 38], we summarize some key takeaways of our approach with respect to existing literature on this subject, in particular from numerical simulations.

There is a vast literature about magnetic fields around BHs and how they may act in a mechanism that could extract the mass–energy of a Kerr BH. Ruffini and Wilson [65] made an early attempt using a matter-dominated magnetized plasma accreting in a disk around a pre-existing Kerr BH. They used the infinite conductivity condition,  $F_{\alpha\beta}u^\beta = 0$ , where  $F_{\alpha\beta}$  is the electromagnetic field tensor and  $u^\beta$  is the plasma four-velocity, leading to  $\mathbf{E} \cdot \mathbf{B} = 0$ . Under these conditions, the acceleration of particles and processes of energy extraction were not possible. This work was further developed by Blandford and Znajek [10], who introduced the concept of gaps and spontaneous  $e^+e^-$  pair creation in the context of a BH, closely following the pulsar theory by Sturrock [79] and Ruderman and Sutherland [50], to have regions in the magnetosphere where  $\mathbf{E} \cdot \mathbf{B} \neq 0$ . They imposed a force-free condition,  $F_{\alpha\beta}J^\beta = 0$ , where  $J^\beta$  is the current density. Their aim was to produce an ultrarelativistic matter-dominated plasma whose bulk kinetic energy could be used to explain the energetics of a jet at large distances from the BH. The alternative view of Thorne and MacDonald [80] extended the work of Blandford and Znajek [10] and analyzed the problem of matter-dominated accretion in a magnetic field anchored to a rotating surrounding disk. The physical system, however, remained the same of Blandford and Znajek [10].

More recently, numerical simulations based on different models with respect to the one used in this article have been developed with the premise that the background electric field of an electro-vacuum solution (like the Papapetrou–Wald solution) might be screened from the surrounding plasma in the magnetosphere (see e.g. Komissarov [32] and Parfrey et al. [42]). These simulations have mainly addressed the physics of relativistic jets of plasma emerging from active galactic nuclei and X-ray binary systems and a especially detailed treatment and review of their theoretical models is presented by Komissarov [32]. The choice of parameters and physical processes are different from the ones we have used for the GRB analysis. In our approach, we have been guided by the theoretical explanation of the following crucial observations of GRBs: (1) the time-resolved spectral analysis of the UPE phase; and (2) the MeV luminosity observed by Fermi-GBM. From this, we have identified the physical processes and parameters that have to be fulfilled in order to

fit the vast amount of high-quality observational data. Their parameters enforce the condition  $\mathbf{E} \cdot \mathbf{B} \neq 0$ , while we use the Papapetrou–Wald solution which naturally possesses regions fulfilling such a condition in the BH vicinity.

In our model, the magnetic field inherited from the collapsed NS is rooted in the surrounding material, and the electric field is created by the interaction of the gravitomagnetic field of the rotating BH with the external magnetic field. Since the electric field is assumed to be overcritical at the beginning, in a very short timescale of the order of the Compton time,  $\hbar/(m_e c^2) \sim 10^{-21}$  s, which is much shorter than any electromagnetic process, it is originated a region dominated by the high density and high pressure of the neutral PEMB pulse. The PEMB pulse self-accelerates to the ultrarelativistic regime and finally reaches transparency at a radius  $\sim 10^{10}$  cm.

As soon as the BH forms, the first and the most efficient process in action to produce the  $e^+e^-$  plasma and, consequently decreasing the rotational energy of BH, occurs through the Schwinger critical field pair production. Since an overwhelming amount of pair plasma is created in quantum timescales, the plasma expansion by its internal pressure starts well before any electric field screening. This process takes a fraction of angular momentum of the Kerr BH. The BH then is left with a slightly smaller angular momentum  $J^* = J - \Delta J$ , with  $\Delta J/J \sim 10^{-9}$ , being  $\Delta J$  the angular momentum extracted to the BH and the same magnetic field. This process leads to a new, lower value of the induced electric field. This process continues up to the moment when the electric field becomes undercritical.

The expanding  $e^+e^-$  photon plasma sweeps matter in the cavity reducing the density of the latter to values as low as  $\sim 10^{-14}$  g cm $^{-3}$ , as shown by numerical simulations in Ruffini et al. [59]. This low-density ionized plasma is needed to fulfill an acceleration of charged particles leading to the electro-dynamical process around a newborn BH. This density is much lower the Goldreich-Julian density, for instance  $\rho_{\text{GJ}} \sim 10^{-11}$  g cm $^{-3}$ , obtained for the present inner engine parameters. Moreover, the matter energy density inside the cavity is negligible comparing to the electromagnetic energy density, namely  $\rho_M/(B^2 - E^2) \sim 10^{-14}$ , while in Komissarov [32] (see also [42]), this ratio is 0.05 or higher.

## 9 Discussion and conclusions

Following a new paradigm opened by the theoretical understanding and data analysis of GRB 190114C [39, 70], we have analyzed in this paper the UPE phase of GRB 180720B. We have here shown that also in GRB 180720B, a time-resolved spectral analysis conducted on shorter and shorter time intervals reveals the hierarchical structure of the UPE. Namely, the spectrum of the UPE phase, obtained in multiply rebinned

time intervals, holds its features and is always fitted by a BB+CPL model (see Fig. 4). We have shown the statistical significance of such a structure down to a time resolution of 0.11 s.

We have then linked the above hierarchical structure of the UPE phase to a sequence of microphysical elementary events in the QED regime of the inner engine, occurring on a timescale of  $\tau_q \sim 10^{-9}$  s. The understanding of the underlying quantum nature is not possible without the discovery of the observed hierarchical structure of the UPE phase.

The inner engine is composed of a Kerr BH rotating in a uniform magnetic field  $B_0$ , aligned with the BH rotation axis, described by the Papapetrou–Wald solution, immersed in a rarefied plasma. The gravitomagnetic interaction of the rotating BH with the magnetic field induces an electric field. The process that originates the 10 keV–10 MeV radiation is triggered by the vacuum polarization that occurs when the induced electric field in the inner engine is overcritical, i.e.,  $|\mathbf{E}| > E_c$ . This process forms around the BH an optically thick pair  $e^+ e^- \gamma$  plasma whose high internal pressure drives its self-accelerating expansion. During the expansion, the plasma is loaded with baryons forming the PEMB pulse that reaches ultrarelativistic regime with  $\Gamma \sim 30$  and the transparency point where the radiation becomes observable [64]. We assume that the magnetic field  $B_0 \sim 10^{14}$  G is constant during the UPE phase.

In the radiation timescale of the PEMB pulses,  $\tau_q \sim 10^{-9}$  s, the above process extracts  $\Delta J \sim 10^{-9} J$  of angular momentum of the Kerr BH, leaving it with a new, lower angular momentum  $J^* = J - \Delta J$ . Since the magnetic field is assumed constant during the UPE phase, the new value of the induced electric field is lower. Then, the system starts a new vacuum polarization process in the presence of the same magnetic field  $B_0$ , and a new effective charge of  $Q_{\text{eff}}^* = Q_{\text{eff}} - \Delta Q_{\text{eff}}$ , where  $\Delta Q_{\text{eff}} = 2B_0 \Delta J$ . It leads to the production of approximately  $10^9$  PEMB pulses, which one after another reach the transparency point and their radiations form the UPE phase. This process continues till the electric field lowers to  $|\mathbf{E}| < E_c$ .

The magnetic field in this scenario is inherited from the NS and is amplified in the gravitational collapse to a BH. Consequently, the electric field and consequent effective charge,  $Q_{\text{eff}} = 2B_0 J G/c^3$ , are induced by the gravitomagnetic interaction of the rotating BH with the external magnetic field [53, 54]. The electric field is overcritical during the UPE phase. In a quantum timescale,  $\hbar/(m_e c^2) \approx 10^{-21}$  s, the dyadoregion characterized by the high density and high pressure of the  $e^+ e^- \gamma$  plasma develops and dominates over any other electromagnetic process [64].

**Acknowledgements** We thank the Referee for the deep remarks and comments which have improved the presentation of the results and readability of the paper.

**Data Availability Statement** This manuscript has no associated data or the data will not be deposited. [Authors' comment: The spectral data are represented in the current manuscript. The data for luminosity light curves are reproduced from Reference [36].]

**Open Access** This article is licensed under a Creative Commons Attribution 4.0 International License, which permits use, sharing, adaptation, distribution and reproduction in any medium or format, as long as you give appropriate credit to the original author(s) and the source, provide a link to the Creative Commons licence, and indicate if changes were made. The images or other third party material in this article are included in the article's Creative Commons licence, unless indicated otherwise in a credit line to the material. If material is not included in the article's Creative Commons licence and your intended use is not permitted by statutory regulation or exceeds the permitted use, you will need to obtain permission directly from the copyright holder. To view a copy of this licence, visit <http://creativecommons.org/licenses/by/4.0/>.

Funded by SCOAP<sup>3</sup>. SCOAP<sup>3</sup> supports the goals of the International Year of Basic Sciences for Sustainable Development.

## References

1. H. Abdalla, R. Adam, F. Aharonian et al., *Nature* **575**, 464 (2019). <https://doi.org/10.1038/s41586-019-1743-9>
2. A.G. Aksenov, R. Ruffini, G.V. Vereshchagin, *Phys. Rev. Lett.* **99**, 125003 (2007). <https://doi.org/10.1103/PhysRevLett.99.125003>
3. A.G. Aksenov, R. Ruffini, G.V. Vereshchagin, *Phys. Rev. D* **79**, 043008 (2009). <https://doi.org/10.1103/PhysRevD.79.043008>
4. L. Becerra, C.L. Bianco, C.L. Fryer, J.A. Rueda, R. Ruffini, *ApJ* **833**, 107 (2016). <https://doi.org/10.3847/1538-4357/833/1/107>
5. L. Becerra, F. Cipolletta, C.L. Fryer, J.A. Rueda, R. Ruffini, *ApJ* **812**, 100 (2015). <https://doi.org/10.1088/0004-637X/812/2/100>
6. L. Becerra, C.L. Ellinger, C.L. Fryer, J.A. Rueda, R. Ruffini, *ApJ* **871**, 14 (2019). <https://doi.org/10.3847/1538-4357/aaf6b3>
7. L. Becerra, M.M. Guzzo, F. Rossi-Torres et al., *ApJ* **852**, 120 (2018). <https://doi.org/10.3847/1538-4357/aaa296>
8. E.C. Bellm, *GRB Coord. Netw.* **23041**, 1 (2018)
9. E. Bissaldi, *GRB Coord. Netw.* **22980**, 1 (2018)
10. R.D. Blandford, R.L. Znajek, *MNRAS* **179**, 433 (1977). <https://doi.org/10.1093/mnras/179.3.433>
11. M.L. Cherry, *GRB Coord. Netw.* **23042**, 1 (2018)
12. C. Cherubini, A. Gerialico, H.J.A. Rueda, R. Ruffini, *Phys. Rev. D* **79**, 124002 (2009). <https://doi.org/10.1103/PhysRevD.79.124002>
13. D. Christodoulou, *Phys. Rev. Lett.* **25**, 1596 (1970). <https://doi.org/10.1103/PhysRevLett.25.1596>
14. D. Christodoulou, R. Ruffini, *Phys. Rev. D* **4**, 3552 (1971). <https://doi.org/10.1103/PhysRevD.4.3552>
15. F. Cipolletta, C. Cherubini, S. Filippi, J.A. Rueda, R. Ruffini, *Phys. Rev. D* **92**, 023007 (2015). <https://doi.org/10.1103/PhysRevD.92.023007>
16. S. Covino, *GRB Coord. Netw.* **23021**, 1 (2018)
17. N. Crouzet, *GRB Coord. Netw.* **22988**, 1 (2018)
18. A. de Ugarte Postigo, L. Izzo, C.C. Thoene et al., *GRB Coord. Netw.* **25677**, 1 (2019)
19. C. DeWitt, B.S. DeWitt, eds. *Les Houches Summer School, Vol. 23, Proceedings, Ecole d'Été de Physique Théorique: Les Astres Occlus* (Gordon and Breach, New York, 1973)
20. M.D. Duez, Y.T. Liu, S.L. Shapiro, M. Shibata, B.C. Stephens, *Phys. Rev. Lett.* **96**, 031101 (2006). <https://doi.org/10.1103/PhysRevLett.96.031101>
21. M.D. Duez, Y.T. Liu, S.L. Shapiro, M. Shibata, B.C. Stephens, *Phys. Rev. D* **73**, 104015 (2006). <https://doi.org/10.1103/PhysRevD.73.104015>

22. D. Frederiks, GRB Coord. Netw. **23011**, 1 (2018)
23. C.L. Fryer, F.G. Oliveira, J.A. Rueda, R. Ruffini, Phys. Rev. Lett. **115**, 231102 (2015). <https://doi.org/10.1103/PhysRevLett.115.231102>
24. C.L. Fryer, J.A. Rueda, R. Ruffini, ApJL **793**, L36 (2014). <https://doi.org/10.1088/2041-8205/793/2/L36>
25. S.W. Hawking, Phys. Rev. Lett. **26**, 1344 (1971). <https://doi.org/10.1103/PhysRevLett.26.1344>
26. J.R. Ipser, Phys. Rev. Lett. **27**, 529 (1971). <https://doi.org/10.1103/PhysRevLett.27.529>
27. R. Itoh, GRB Coord. Netw. **22983**, 1 (2018)
28. L. Izzo, GRB Coord. Netw. **23040**, 1 (2018)
29. L. Izzo, J.A. Rueda, R. Ruffini, A&A **548**, L5 (2012). <https://doi.org/10.1051/0004-6361/201219813>
30. M. Jelinek, GRB Coord. Netw. **23024**, 1 (2018)
31. D.A. Kann, GRB Coord. Netw. **22985**, 1 (2018)
32. S.S. Komissarov, Mon. Not. R. Astron. Soc. **359**, 801 (2005). <https://doi.org/10.1111/j.1365-2966.2005.08974.x>
33. L. Lipunov, GRB Coord. Netw. **23023**, 1 (2018)
34. D. Malesani, GRB Coord. Netw. **22996**, 1 (2018)
35. R. Martone, GRB Coord. Netw. **22976**, 1 (2018)
36. R. Moradi, L. Li, J. A. Rueda, et al. arXiv e-prints (2021). [arXiv:2103.09158](https://arxiv.org/abs/2103.09158)
37. R. Moradi, J.A. Rueda, R. Ruffini, Y. Wang, A&A **649**, A75 (2021). <https://doi.org/10.1051/0004-6361/201937135>
38. R. Moradi, J.A. Rueda, R. Ruffini et al., Phys. Rev. D **104**, 063043 (2021). <https://doi.org/10.1103/PhysRevD.104.063043>
39. R. Moradi, J.A. Rueda, R. Ruffini et al., Phys. Rev. D **104**, 063043 (2021). <https://doi.org/10.1103/PhysRevD.104.063043>
40. H. Negoro, GRB Coord. Netw. **22993**, 1 (2018)
41. A. Papapetrou, Annales de L'Institut Henri Poincare Section (A) Physique Theorique **4**, 83 (1966)
42. K. Parfrey, A. Philippov, B. Cerutti, Phys. Rev. Lett. **122**, 035101 (2019). <https://doi.org/10.1103/PhysRevLett.122.035101>
43. D.A. Perley, A.M. Cockeram, GRB Coord. Netw. **25657**, 1 (2019)
44. T. Piran, Rev. Mod. Phys. **76**, 1143 (2004). <https://doi.org/10.1103/RevModPhys.76.1143>
45. A. Pozanenko, GRB Coord. Netw. **23020**, 1 (2018)
46. L. Rezzolla, B. Giacomazzo, L. Baiotti et al., ApJL **732**, L6 (2011). <https://doi.org/10.1088/2041-8205/732/1/L6>
47. L. Rhodes, A.J. van der Horst, R. Fender et al., MNRAS **496**, 3326 (2020). <https://doi.org/10.1093/mnras/staa1715>
48. O.J. Roberts, GRB Coord. Netw. **22981**, 1 (2018)
49. M. Ruderman, in *Seventh Texas Symposium on Relativistic Astrophysics*, ed. by P.G. Bergman, E.J. Fenyves, L. Motz **262**, 164–180 (1975). <https://doi.org/10.1111/j.1749-6632.1975.tb31430.x>
50. M.A. Ruderman, P.G. Sutherland, ApJ **196**, 51 (1975). <https://doi.org/10.1086/153393>
51. J.A. Rueda, R. Ruffini, ApJL **758**, L7 (2012). <https://doi.org/10.1088/2041-8205/758/1/L7>
52. J.A. Rueda, R. Ruffini, Eur. Phys. J. C **80**, 300 (2020). <https://doi.org/10.1140/epjc/s10052-020-7868-z>
53. J.A. Rueda, R. Ruffini, M. Karlica, R. Moradi, Y. Wang, ApJ **893**, 148 (2020). <https://doi.org/10.3847/1538-4357/ab80b9>
54. J.A. Rueda, R. Ruffini, R.P. Kerr, ApJ **929**, 56 (2022). <https://doi.org/10.3847/1538-4357/ac5b6e>
55. J.A. Rueda, R. Ruffini, R. Moradi, Y. Wang, Int. J. Mod. Phys. D **30**, 2130007 (2021). <https://doi.org/10.1142/S021827182130007X>
56. R. Ruffini, in *49th Yamada Conference, Kyoto, Japan, April 6–10, 1998*, astro (1998). [arXiv:astro-ph/9811232](https://arxiv.org/abs/astro-ph/9811232)
57. R. Ruffini, C.L. Bianco, S.-S. Xue et al., Int. J. Mod. Phys. D **13**, 843 (2004). <https://doi.org/10.1142/S0218271804004980>
58. R. Ruffini, M. Karlica, N. Sahakyan et al., ApJ **869**, 101 (2018). <https://doi.org/10.3847/1538-4357/aaac8>
59. R. Ruffini, J.D. Melon Fuksman, G.V. Vereshchagin, ApJ **883**, 191 (2019). <https://doi.org/10.3847/1538-4357/ab3c51>
60. R. Ruffini, J.D. Salmonson, J.R. Wilson, S.-S. Xue, A&A **350**, 334 (1999)
61. R. Ruffini, J.D. Salmonson, J.R. Wilson, S.-S. Xue, A&A **350**, 334 (1999)
62. R. Ruffini, J.D. Salmonson, J.R. Wilson, S.-S. Xue, Astron. Astrophys. Suppl. **138**, 511 (1999)
63. R. Ruffini, J.D. Salmonson, J.R. Wilson, S.-S. Xue, A&A **359**, 855 (2000)
64. R. Ruffini, G. Vereshchagin, S. Xue, PhysRep **487**, 1 (2010). <https://doi.org/10.1016/j.physrep.2009.10.004>
65. R. Ruffini, J.R. Wilson, Phys. Rev. D **12**, 2959 (1975). <https://doi.org/10.1103/PhysRevD.12.2959>
66. R. Ruffini, C.L. Bianco, M. Enderli et al., GRB Coord. Netw. **14526**, 1 (2013)
67. R. Ruffini, L. Becerra, C.L. Bianco et al., ApJ **869**, 151 (2018). <https://doi.org/10.3847/1538-4357/aaec68>
68. R. Ruffini, R. Moradi, Y. Aimuratov et al., GRB Coord. Netw. **23715**, 1 (2019)
69. R. Ruffini, R. Moradi, J.A. Rueda et al., ApJ **886**, 82 (2019). <https://doi.org/10.3847/1538-4357/ab4ce6>
70. R. Ruffini, L. Li, R. Moradi, et al., arXiv e-prints (2019). [arXiv:1904.04162](https://arxiv.org/abs/1904.04162)
71. R. Ruffini, R. Moradi, J.A. Rueda et al., MNRAS **504**, 5301 (2021). <https://doi.org/10.1093/mnras/stab724>
72. M. Sasada, GRB Coord. Netw. **22977**, 1 (2018)
73. M. Sasada, T. Nakaoka, M. Kawabata et al., GRB Coord. Netw. **22977**, 1 (2018)
74. I. Sfaradi, GRB Coord. Netw. **23037**, 1 (2018)
75. M. Shibata, M.D. Duez, Y.T. Liu, S.L. Shapiro, B.C. Stephens, Phys. Rev. Lett. **96**, 031102 (2006). <https://doi.org/10.1103/PhysRevLett.96.031102>
76. M.H. Siegel, GRB Coord. Netw. **22973**, 1 (2018)
77. B.C. Stephens, M.D. Duez, Y.T. Liu, S.L. Shapiro, M. Shibata, Class. Quantum Gravity **24**, S207 (2007). <https://doi.org/10.1088/0264-9381/24/12/S14>
78. B.C. Stephens, S.L. Shapiro, Y.T. Liu, Phys. Rev. D **77**, 044001 (2008). <https://doi.org/10.1103/PhysRevD.77.044001>
79. P.A. Sturrock, ApJ **164**, 529 (1971). <https://doi.org/10.1086/150865>
80. K.S. Thorne, D. MacDonald, Mon. Not. R. Astron. Soc. **198**, 339 (1982). <https://doi.org/10.1093/mnras/198.2.339>
81. R.M. Wald, Ph.D. thesis, (unpublished) (1972)
82. R.M. Wald, Phys. Rev. D **10**, 1680 (1974). <https://doi.org/10.1103/PhysRevD.10.1680>
83. Y. Wang, J.A. Rueda, R. Ruffini et al., ApJ **874**, 39 (2019). <https://doi.org/10.3847/1538-4357/ab04f8>
84. A.M. Watson, GRB Coord. Netw. **23017**, 1 (2018)
85. J.R. Wilson, in *Seventh Texas symposium on relativistic astrophysics*, ed. by P.G. Bergman, E.J. Fenyves, L. Motz, Ann. N. Y. Acad. Sci. **262** (1975), pp. 123–132. <https://doi.org/10.1111/j.1749-6632.1975.tb31425.x>
86. J.R. Wilson, in *Physics and Astrophysics of Neutron Stars and Black Holes*, ed. by R. Giacconi, R. Ruffini, 2nd edn. (Cambridge Scientific Publishers, UK, 1978), pp. 644–675
87. W. Zheng, GRB Coord. Netw. **23033**, 1 (2018)



# GRB 190829A—A Showcase of Binary Late Evolution

Yu Wang<sup>1,2,3</sup> , J. A. Rueda<sup>1,2,4,5,6</sup>, R. Ruffini<sup>1,2,7</sup> , R. Moradi<sup>1,2,3</sup> , Liang Li<sup>1,2,3</sup> , Y. Aimuratov<sup>1,2,8,15</sup>, F. Rastegarnia<sup>2,5,9</sup>,  
S. Eslamzadeh<sup>2,5,10</sup>, N. Sahakyan<sup>11</sup> , and Yunlong Zheng<sup>2,12,13,14</sup>

<sup>1</sup> ICRA, Dip. di Fisica, Università di Roma “La Sapienza”, Piazzale Aldo Moro 5, I-00185 Roma, Italy; [yu.wang@uniroma1.it](mailto:yu.wang@uniroma1.it), [jorge.rueda@icra.it](mailto:jorge.rueda@icra.it), [ruffini@icra.it](mailto:ruffini@icra.it),  
[rahim.moradi@inaf.it](mailto:rahim.moradi@inaf.it), [liang.li@icranet.org](mailto:liang.li@icranet.org)

<sup>2</sup> ICRA/INAF, Piazza della Repubblica 10, I-65122 Pescara, Italy

<sup>3</sup> INAF—Osservatorio Astronomico d’Abruzzo, Via M. Maggini snc, I-64100 Teramo, Italy

<sup>4</sup> ICRA/INAF-Ferrara, Dip. di Fisica e Scienze della Terra, Università degli Studi di Ferrara, Via Saragat 1, I-44122 Ferrara, Italy

<sup>5</sup> Dip. di Fisica e Scienze della Terra, Università degli Studi di Ferrara, Via Saragat 1, I-44122 Ferrara, Italy

<sup>6</sup> INAF, Istituto di Astrofisica e Planetologia Spaziali, Via Fosso del Cavaliere 100, I-00133 Rome, Italy

<sup>7</sup> INAF, Viale del Parco Mellini 84, I-00136 Rome, Italy

<sup>8</sup> Fesenkov Astrophysical Institute, Observatory 23, 050020 Almaty, Kazakhstan

<sup>9</sup> Department of Physics, Faculty of Physics and Chemistry, Alzahra University, Tehran, Iran

<sup>10</sup> Department of Theoretical Physics, Faculty of Basic Sciences, University of Mazandaran, P.O. Box 47416-95447, Babolsar, Iran

<sup>11</sup> ICRA/INAF-Armenia, Marshall Baghramian Avenue 24a, Yerevan 0019, Armenia

<sup>12</sup> Department of Astronomy, School of Physical Sciences, University of Science and Technology of China, Hefei, Anhui 230026, People’s Republic of China

<sup>13</sup> CAS Key Laboratory for Researches in Galaxies and Cosmology, University of Science and Technology of China, Hefei, Anhui 230026, People’s Republic of China

<sup>14</sup> School of Astronomy and Space Science, University of Science and Technology of China, Hefei, Anhui 230026, People’s Republic of China

<sup>15</sup> al-Farabi Kazakh National University, al-Farabi Avenue 71, 050040 Almaty, Kazakhstan; [rahim.moradi@inaf.it](mailto:rahim.moradi@inaf.it)

Received 2022 March 3; revised 2022 June 4; accepted 2022 June 29; published 2022 September 14

## Abstract

GRB 190829A is the fourth-closest gamma-ray burst to date ( $z = 0.0785$ ). Owing to its wide range of radio, optical, X-ray, and very-high-energy observations by HESS, it has become an essential new source that has been examined by various models with complementary approaches. Here, we show in GRB 190829A that the double prompt pulses and the three multiwavelength afterglows are consistent with the type II binary-driven hypernova model. The progenitor is a binary composed of a carbon–oxygen (CO) star and a neutron star (NS) companion. The gravitational collapse of the iron core of the CO star produces a supernova (SN) explosion and leaves behind a new NS ( $\nu$ NS) at its center. The accretion of the SN ejecta onto the NS companion and onto the  $\nu$ NS via matter fallback spins up the NSs and produces the double-peak prompt emission. The synchrotron emission from the expanding SN ejecta, with energy injection from the rapidly spinning  $\nu$ NS and its subsequent spindown, leads to the afterglow in the radio, optical, and X-ray bands. We model the sequence of physical and related radiation processes in BdHNe, and focus on individuating the binary properties that play the relevant roles.

*Unified Astronomy Thesaurus concepts:* Gamma-ray bursts (629); Black hole physics (159); Neutron stars (1108); Supernovae (1668); Type Ic supernovae (1730)

## 1. Introduction

As one of the closest gamma-ray bursts (GRBs; Dichiarà et al. 2019; Heintz et al. 2019; Hu et al. 2021), GRB 190829A has been the subject of one of the most extensive observational campaigns, including but not limited to the Fermi satellite (Fermi GBM Team 2019), the Neil Gehrels Swift Observatory (Perley & Cockeram 2019), the High Energy Stereoscopic System (HESS; Abdalla et al. 2021), the Gran Telescopio Canarias (GTC; de Ugarte Postigo et al. 2019), and the Gamma-Ray Burst Optical/Near-Infrared Detector (GROND; Bolmer et al. 2019). GRB 190829A has become a key source for testing details of alternative GRB models. The conventional concept of GRBs postulates that when the core of a single massive star collapses, a relativistic jet-like outflow forms and propagates. The internal shock in the outflow produces prompt emissions. The outflow then interacts with the interstellar medium, generating the afterglow via the synchrotron process, as well as the very-high-energy (VHE) emission via the

synchrotron self-Compton (SSC) process (Mészáros 2002; Piran 2004; Zhang 2018; Abdalla et al. 2019; MAGIC Collaboration et al. 2019; Zhang 2019; Abdalla et al. 2021). Here, we present an alternative approach: the progenitor is a binary system composed of a carbon–oxygen core (CO<sub>core</sub>) and a companion neutron star (NS) in a tight orbit with an orbital period of a few minutes. The iron core of the CO<sub>core</sub> collapses and generates a supernova (SN) at the end of its thermonuclear evolution, with a new NS ( $\nu$ NS) being left at the SN’s center. The accretion of SN ejecta onto the companion NS and the fallback accretion onto the  $\nu$ NS contribute to the energy of prompt emission, spinning up the  $\nu$ NS. The rotational energy from the  $\nu$ NS spindown powers the afterglow of the synchrotron emission (Rueda & Ruffini 2012; Fryer et al. 2014; Becerra et al. 2019; Rueda et al. 2021; Ruffini et al. 2021). The observed optical SN (Perley & Cockeram 2019; de Ugarte Postigo et al. 2019) completes this alternative self-consistent approach.

Specifically, Abdalla et al. (2021) presented the HESS observations of VHE photons of hundreds of GeV, lasting  $10^5$  s. The VHE photons exhibit a luminosity decaying index and a spectral shape similar to the ones of the X-ray afterglow emission. The standard forward-shock model was applied to the afterglow, revealing its difficulties in explaining these

observations. Rhodes et al. (2020) showed that the radio observations could be explained within the synchrotron forward-shock model. Hu et al. (2021) presented the optical observations, analyzed the multiwavelength data, and compared this burst with GRB 180728A. Fraija et al. (2021) modeled the optical and X-ray observations in the afterglow using the synchrotron forward-shock model, and the VHE observations with SSC scattering. Zhang et al. (2021a) interpreted the VHE observations using the external inverse-Compton scenario, with the seed photons coming from prompt emission pulses. Chand et al. (2020) analyzed various episodes of this burst and concluded that the shockwave breakout model could not explain the entire burst. Sato et al. (2021) proposed that this GRB was being viewed from an off-axis angle, in an attempt to solve the dilemma of the VHE photons being produced in a low-luminosity GRB. Zhang et al. (2021b) proposed that the interaction of the hard X-ray photons in the first prompt pulse with the dusty medium produces the second prompt pulse, as well as a medium rich in electron–positron pairs, in which the SSC process produces the VHE emission. Dichiaro et al. (2021) focused on the early afterglow, with their multiwavelength studies purporting the existence of both forward and reverse shocks.

The above articles present detailed observations, including radio, optical, X-ray, and VHE, and give a variety of interpretations of the different emission episodes: they all generally assume a single progenitor and ultrarelativistic shock waves. In this article, we start by focusing on the nature of the binary progenitor, and far from describing a single leading ultrarelativistic process, we emphasize the existence of a number of episodes with different emission processes, which we examine in their rest-frames. We do not evidence any ultrarelativistic emission. On the contrary, we evidence: (1) the special role of two early pulses, observed by Fermi and Swift, relating to the progenitors of binary components; (2) the crucial role of synchrotron electromagnetic radiation from the mild-relativistic expanding SN ejecta in describing the afterglow composed of radio, optical, and X-ray emissions; and (3) we finally address the appearance of the SN, for which the optical emission is brighter than the synchrotron emission. Therefore, in our approach, we model the sequence of the physical and related radiation processes, and focus on individuating the binary properties that play the relevant roles.

The binary model was proposed in 2012 (Rueda & Ruffini 2012), and it has been in development for one decade. The physical picture and the modeling of the SN ejecta accretion onto the NS companion have been gradually extended to include the required physics, allowing the study of a wide range of binary parameters, based on detailed analysis of multiple well-observed GRBs and statistical analysis of different GRB components (Ruffini et al. 1999, 2000, 2010, 2015; Wang et al. 2015; Ruffini et al. 2018a, 2018b, 2018c; Wang et al. 2018; Ruffini et al. 2019; Wang et al. 2019b; Rueda et al. 2020; Rueda & Ruffini 2020; Moradi et al. 2021b; Ruffini et al. 2021). The numerical simulations of the occurring physical processes have been upgraded from one dimension (Fryer et al. 2014) to two dimensions (Becerra et al. 2015) to three dimensions (Becerra et al. 2016, 2019). The latest simulations (Becerra et al. 2019) implemented a smoothed particle hydrodynamics method, and examined a large selection of the initial conditions and outcomes of the binary system after the SN explosion. Rueda

et al. (2019) and Rueda et al. (2021) have reviewed the entire development process. In this article, we have the scenario—namely, a type II binary-driven hypernova (BdHN II)—that the NS does not accrete enough matter to reach the critical mass for black hole (BH) formation, meaning that it remains stable as a more massive NS (MNS).

Unlike the traditional fireball model, the BdHN model considers a central engine arising in the final evolutionary stage of the  $\text{CO}_{\text{core}}$  in the presence of a binary companion. An SN explosion occurs, which triggers the GRB emission and generates a  $\nu\text{NS}$ . Therefore, in addition to the physical processes of single-star collapse models, we need to consider not only the binary interactions, but also the appearance of the  $\nu\text{NS}$ . The most influential interactions are the accretion of the SN ejecta onto the NS companion, with the fallback accretion onto the  $\nu\text{NS}$  spinning it up. The afterglow is produced by the mildly relativistic expanding SN ejecta, which contain a large number of electrons accelerated by the kinetic energy of the SN and the energy injection from the rapidly spinning  $\nu\text{NS}$  and its subsequent spindown. In this article, we will model the afterglow of GRB 190829A, following the above picture. An additional advantage is that it naturally accounts for the observed association of GRBs with type Ic SNe (Rueda & Ruffini 2012), as well as indicating the peak luminosity of the optical SN emission well above the synchrotron optical emission.

This article is structured as follows. In Section 2, we present the physical picture and the emission episodes that our model predicts. In Section 3, we introduce the observational data. In Section 4, we analyze the prompt emission and explain the prompt pulses by means of the SN explosion and the accretion of SN ejecta onto the companion NS and  $\nu\text{NS}$ . In Section 5, we analyze the afterglow, then model the radio, optical, and X-ray emissions using the synchrotron emission from the SN ejecta. In Section 6, we present the conclusions of the article.

## 2. Physical Picture and Expectations

As recalled in the introduction, we consider a binary system composed of a  $\text{CO}_{\text{core}}$  and an NS with an orbital period of a few tens of minutes (Ruffini et al. 2021). At a given time, the  $\text{CO}_{\text{core}}$  collapses, forms a  $\nu\text{NS}$  at its center, and induces an SN explosion. Most of the SN energy ( $\sim 10^{53}$  erg) is deposited in the neutrino, while a small percentage of the energy goes to the kinetic energy of the SN ejecta ( $\sim 10^{51}$ – $10^{52}$  erg), which expands outward at velocities of around  $0.1c$  (Arnett 1996; Branch & Wheeler 2017; Cano et al. 2017). The low-density outermost layer has the highest speed, while the denser regions expand with slower velocities. After a few minutes, the SN ejecta reach the companion NS, and the hypercritical accretion starts. In the meantime, some matter falls back, leading to an accretion process onto the  $\nu\text{NS}$ . This fallback accretion is significantly amplified by the companion NS, which alters the trajectory of the partial SN ejecta that flow back to the  $\nu\text{NS}$  (Becerra et al. 2019; J. A. Rueda et al. 2022, in preparation). The accretion rate onto the companion NS rises exponentially and peaks in a few minutes. The numerical simulations presented in Fryer et al. (2014), Becerra et al. (2016, 2019), and J. A. Rueda et al. (2022, in preparation) show that the entire hypercritical accretion process may last for hundreds of minutes, while the peak accretion rate of  $\sim 10^{-3} M_{\odot} \text{ s}^{-1}$ , supplied by the high-density and slow-moving part of the SN ejecta, holds only for tens of seconds to tens of minutes, depending on the binary separation, with the energy release being in the order of  $10^{48}$ – $10^{49}$  erg  $\text{ s}^{-1}$ . The accretion onto

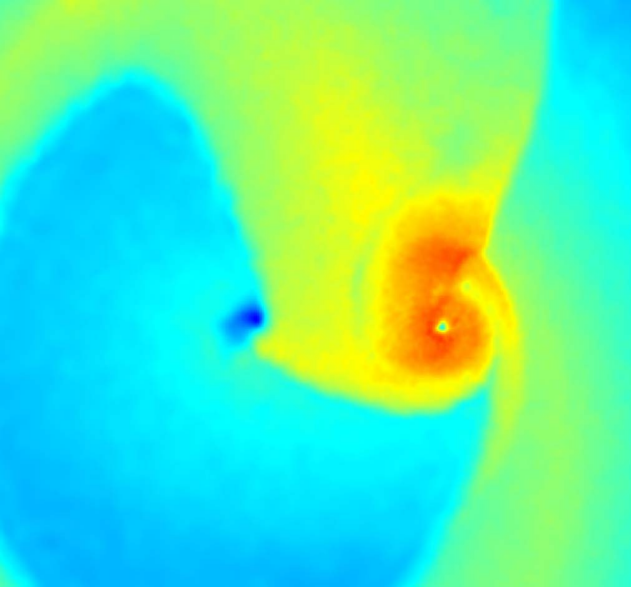


**Figure 1.** The ongoing accretion process onto the  $\nu$ NS and the NS companion, as simulated in Becerra et al. (2019). The  $\nu$ NS is located at the center of the dark blue spot, and is accreting the surrounding material. The SN ejecta are also being accreted by the NS companion, which is located at the center of the green spot. We also notice that the expansion of the SN ejecta is distorted by the companion NS and that some of the SN ejecta are flowing back to the  $\nu$ NS. This process creates a unique feature of BdHNe: the fallback accretion onto the  $\nu$ NS is enhanced, creating a second peak of accretion at about an orbital period of time after the SN explosion (see, e.g., Figure 5 in Becerra et al. 2019 for more details).

the  $\nu$ NS has two components. The first is the typical fallback matter, analogous to the case of the SN of a single star, which leads the accretion rate to reach a peak, then to decay nearly as a power law with time,  $\propto t^{-5/3}$ . The peak luminosity produced by it is weak,  $<10^{48}$  erg s $^{-1}$ , and can hardly be for cosmological distances. The second component is the unique feature of the binary system that is induced by the interaction of the SN ejecta with the NS companion. The presence of the companion enhances the fallback onto the  $\nu$ NS, creating a second peak of accretion (Becerra et al. 2019; see, e.g., Figure 1). The second part contributes the most to the accreting mass, with an accretion rate of  $\sim 10^{-3} M_{\odot}$  s $^{-1}$  at about an orbital period of time after the SN explosion (J. A. Rueda et al. 2022, in preparation). The fallback accretion also transfers angular momentum to the  $\nu$ NS, spinning it up to a rotation period of a few milliseconds (Bhattacharyya & Chakrabarty 2017). The peak luminosity from the fallback accretion is of the order of  $10^{48}$ – $10^{49}$  erg s $^{-1}$ , and occurs at minutes to tens of minutes after the SN explosion. As we show below, the fallback accretion will continue as a source of energy that powers the afterglow. The SN produces  $\sim 0.4 M_{\odot}$  nickel, whose radioactive decay energy is emitted mainly at optical wavelengths, with a corresponding flux that peaks at around  $\sim 13$  days in the source rest-frame (Cano et al. 2017). This optical signal can be observed from some low-redshift sources ( $\sim z < 1$ ) that are less affected by the absorption (Woosley & Bloom 2006).

In summary, from the observational point of view, a few minutes after the SN explosion, we first expect to observe the signal from the accretion onto the companion NS and the  $\nu$ NS, whose peak times may overlap or be separate, depending on the binary separation, hence there will be one or two pulses with luminosities of the order of  $10^{48}$  erg s $^{-1}$  to  $10^{49}$  erg s $^{-1}$ . We will then observe the afterglow emission due to the synchrotron emission from the SN ejecta, with a luminosity that decays as a

power law, and at  $\sim 13$  days we will observe an optical bump from the radioactive decay of nickel.

### 3. Observations

At 19:55:53 UT, on 2019 August 29, GRB 190829A triggered the Fermi-Gamma-Ray Burst Monitor (GBM; Fermi GBM Team 2019). Swift-Burst Alert Telescope (BAT) was triggered 51 s later, but fortunately GRB 190829A was in the Swift-BAT field of view before the trigger. Here, in this paper, we take the GBM trigger time as  $T_0$ . The Swift-X-Ray Telescope (XRT) started to observe at time  $T_0 + 148.3$  s (Dichiara et al. 2019). The redshift of  $z = 0.0785 \pm 0.005$  was proposed by Swift-UVOT (Dichiara et al. 2019), the Half Meter Telescope (Xu et al. 2019), and the Nordic Optical Telescope (Heintz et al. 2019), via associating to a nearby galaxy, and was later confirmed by the spectroscopic observations of GTC (Hu et al. 2021). GRB 190829A is one of the nearest GRBs ever observed. The SN association has been found and confirmed by the Liverpool Telescope, GTC (Perley & Cockeram 2019; de Ugarte Postigo et al. 2019), and GROND (Bolmer et al. 2019).

We retrieve the Fermi data from the Fermi Science Support Center,<sup>16</sup> and they were analyzed using the Multi-Mission Maximum Likelihood framework (3ML; Vianello et al. 2015).<sup>17</sup> The spectrum fitting is performed by a Bayesian analysis with Markov Chain Monte Carlo iterations within the 3ML framework, and the results are double-checked by implementing the Fermi GBM Data Tools (Goldstein et al. 2021). For a detailed Bayesian analysis of the data and the reduction procedure applied to a GRB spectrum, we refer to Li et al. (2019), Li (2019a, 2019b), Li et al. (2021), and Li & Zhang (2021). We retrieve the Swift data from the UK Swift Science Data Centre,<sup>18</sup> and the analyzing and fitting are carried out by HEASoft<sup>19</sup> and 3ML. The VHE data observed by HESS are from Chand et al. (2020), the optical data observed by GTC are taken from Hu et al. (2021), and the radio emission observed by the Arcminute Microkelvin Imager—Large Array (AMI-LA) are taken from Rhodes et al. (2020).

### 4. Prompt Emission: SN Explosion and NS Accretion

Both the GBM and BAT light curves show two pulses—see, e.g., the Fermi-GBM light curves in Figures 2 and 3. The first pulse starts to rise at time  $-0.75$  s, peaks at 1.02 s, and fades at 8.05 s. The cutoff power-law function gives a best fit over the power law and band functions. We also tested the addition of a blackbody component to the above models, but this did not lead to a statistical improvement of the fit. As shown in Figure 4, the fit of the spectrum is characterized by the power-law index  $\alpha = -1.15 \pm 0.06$  and peak energy  $E_p = 144.28 \pm 50.67$  keV. The integrated isotropic energy<sup>20</sup> from 1 keV to 10 MeV gives  $4.25 \pm 1.02 \times 10^{49}$  erg s $^{-1}$ . The averaged luminosity is  $4.84 \pm 1.16 \times 10^{48}$  erg s $^{-1}$ . After 38.45 s, the second, larger pulse rises at 46.50 s, peaks at 51.65 s, and fades at 64.00 s. This pulse is best fitted by a band function with a low peak

<sup>16</sup> <https://fermi.gsfc.nasa.gov/ssc/>

<sup>17</sup> <https://three.ml.readthedocs.io>

<sup>18</sup> <https://www.swift.ac.uk>

<sup>19</sup> <https://heasarc.gsfc.nasa.gov/lheasoft/>

<sup>20</sup> For the calculation of the luminosity distance, we use a Friedman–Lemaître–Robertson–Walker metric, Hubble constant  $H_0 = 67.4 \pm 0.5$  km/s/Mpc, and matter density  $\Omega_M = 0.315 \pm 0.007$  (Planck Collaboration et al. 2020).

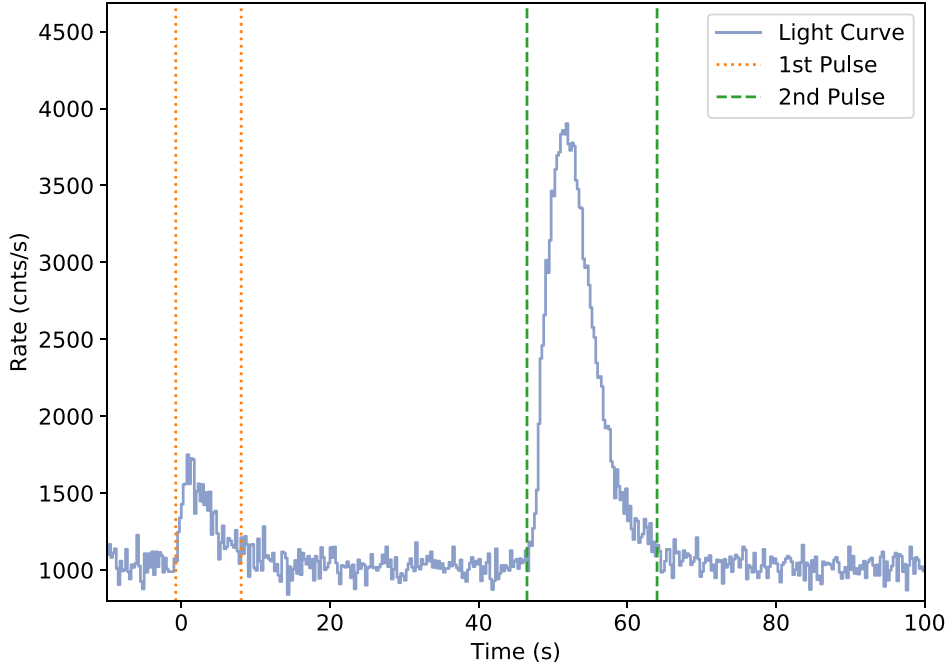


**Figure 2.** The count rate of the GRB 190829A prompt emission from the raw data of Fermi-GBM: the first pulse is from  $-0.75$  s to  $8.05$  s, indicated by the orange dotted line, and the second pulse is from  $46.50$  s to  $64.00$  s, indicated by the green dashed line.

energy  $E_p = 13.58 \pm 0.42$  keV, which almost touches the lower edge of the Fermi-GBM energy band. Because of the small amount of data of energy lower than  $E_p$ , the low energy is unconstrained; in fact, we obtain  $\alpha = 0.50 \pm 1.01$ . The high-energy index  $\beta = -2.53 \pm 0.02$  appears to be a typical value. The total energy in the second pulse is  $3.56 \pm 0.50 \times 10^{50}$  erg, and the averaged luminosity is  $2.05 \pm 0.29 \times 10^{49}$  erg  $s^{-1}$ . Our spectral fit is consistent with the analysis of Hu et al. (2021).

We interpret these two pulses as being due to the accretion onto the companion NS and the fallback accretion onto the  $\nu$ NS. The observed energy and luminosity are consistent with our expectation that the emission from the accretion processes with a luminosity of  $\sim 10^{48} \sim 10^{49}$  erg  $s^{-1}$ .

Numerical simulations of BdHNe show that the time evolution of the  $\nu$ NS fallback accretion rate has a two-peak structure, the second peak being a unique feature of the binary interactions, while the accretion onto the MNS companion shows a single-peak structure (see, e.g., Figure 5 in Becerra et al. 2019). The first peak of the  $\nu$ NS fallback accretion is probably not observable, because, before it occurs, the star has little rotational energy to be released. Therefore, we assume that the two observed pulses are related to the second peak of the  $\nu$ NS accretion and the peak of the MNS accretion. The simulations show that the fallback accretion rate onto the  $\nu$ NS weakly depends on the binary parameters, while the time of occurrence and intensity of the accretion peak onto the MNS crucially depends on the orbital period and the initial angular momentum of the MNS at the beginning of the accretion. The larger the orbital period, the lower the MNS accretion peak, and the later it occurs, the more it approaches the time of occurrence of the second accretion peak of the  $\nu$ NS. The relatively short time separation between the two observed peaks in GRB 190829A suggests a binary period of the order of tens of minutes. This is also suggested by the energy released in the emission. For an orbital period in the range of 20–40 minutes, we expect a peak accretion rate of the MNS in the range of  $10^{-4} \sim 10^{-5} M_\odot s^{-1}$  (see Figure 5 in Becerra et al. 2019), which translates into an accretion power of

$10^{48} \sim 10^{49}$  erg  $s^{-1}$ , assuming 10% efficiency in the conversion from gravitational to radiation energy. If we assume that the energy release is powered by the rotational energy gained during the accretion process, then we end up with similar figures. The star gains angular momentum at a rate of  $\dot{J} \sim 2\sqrt{3} GMM/c \sim 4 \times 10^{45}$  g  $cm^2 s^{-1}$ , for  $1.5M_\odot$  and the above accretion rate, which implies a spinup rate of about 40 Hz  $min^{-1}$ . The simulations show that the MNS accretion peaks at about one-tenth of the orbit, therefore, for the above range of orbital periods, at the time of the accretion the MNS could rotate with a frequency of 80–160 Hz, which implies a rotation power of  $\Omega \dot{J} \sim (2\text{--}5) \times 10^{48}$  erg  $s^{-1}$ , where  $\Omega$  is the stellar angular velocity.

## 5. Afterglow: Synchrotron and $\nu$ NS Pulsar Radiation

Figure 3 shows the multiwavelength luminosity light curves. We notice the continuity of the Swift-BAT and Swift-XRT observations, and a soft X-ray depression at  $\sim 10^2 \sim 10^3$  s after the prompt emission, then from  $3 \times 10^5$  s the soft X-rays decay as a power law of index  $-1.26 \pm 0.06$ . The optical and radio afterglows also have a power-law decay behavior. The VHE emission evolves similarly to the X-rays, with a luminosity of  $\sim 25\%$  of the absorption-corrected X-ray luminosity, similar to other GRBs with VHE observations (Abdalla et al. 2019; MAGIC Collaboration et al. 2019; Zhang 2019; Abdalla et al. 2021).

The optical observations show an additional bump after  $10^6$  s (Perley & Cockeram 2019; de Ugarte Postigo et al. 2019), which indicates the SN optical emission powered by nickel decay.

We here follow and extend the treatment of the GRB afterglow by Ruffini et al. (2018a) within the BdHN scenario. In this picture, the afterglow originates from the synchrotron radiation produced by the expansion of the SN ejecta in the presence of the magnetic field of the  $\nu$ NS. We now estimate the emission generated by the synchrotron mechanism in the X-rays, in the optical, and in the radio, together with the pulsar emission of the  $\nu$ NS. The  $\nu$ NS contributes the energy of

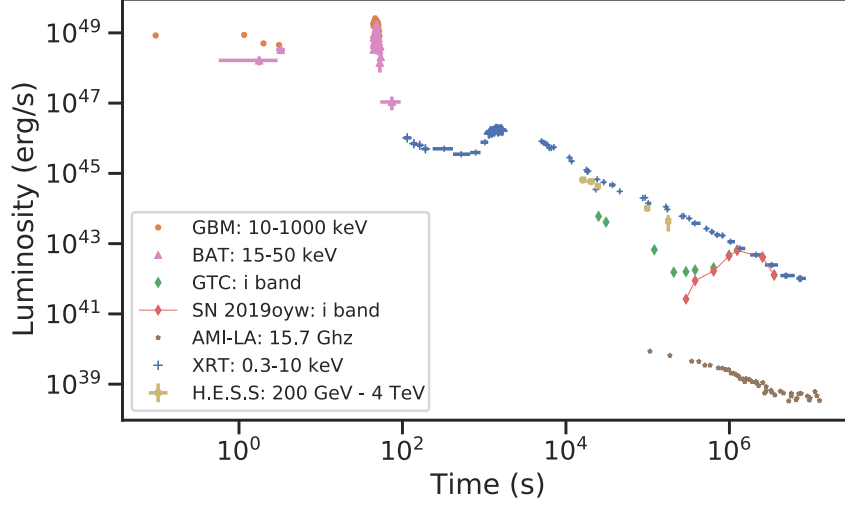


**Figure 3.** The luminosity of GRB 190829A, including the data from HESS (yellow) for TeV; Fermi-GBM (orange dots); Swift-BAT (purple triangles) for the prompt emission of hard X-rays and gamma-rays; Swift-XRT (blue crosses) for the soft X-rays (absorbed); GTC (green diamonds) for the optical  $i$  band, from which the SN 2019oyw is extracted (red diamonds)—the optical signal of the SN overshoots the synchrotron optical emission; and AMI-LA (brown stars) for the radio observation.

afterglow by two means: first, the fallback accretion of surrounding matter, the energy from which dominates the early afterglow; and second, the release of rotation energy from its spindown, which produces the late-time X-ray afterglow. This model predicts that the VHE emission is not directly emitted by this synchrotron emission, although it seems to be related to the  $\nu$ NS activity (see Section 6).

### 5.1. Synchrotron Emission by the Expanding Ejecta

Because the electrons lose their energy from synchrotron radiation very efficiently, we can apply a one-zone model, assuming that the radiation originates from the ejecta, say  $r = R_*$ . We assume that the ejecta expand at a constant velocity  $v_{*,0}$ , so the radius evolves as

$$R_*(t) = R_{*,0} \hat{t}, \quad (1)$$

where  $\hat{t} \equiv t/t_*$  and  $t_* \equiv R_{*,0}/v_{*,0}$ .

In agreement with pulsar theory (see, e.g., Goldreich & Julian 1969; Ostriker & Gunn 1969), we assume that, at large distances from the  $\nu$ NS, beyond its light cylinder, the magnetic field decreases linearly with distance. This implies that the magnetic field strength felt by the expanding ejecta evolves with time as

$$B_*(t) = B_{*,0} \frac{R_{*,0}}{R_*} = \frac{B_{*,0}}{\hat{t}}, \quad (2)$$

where  $B_*^{(0)}$  is the magnetic field strength at  $r = R_{*,0}$ , and we have used Equation (1).

The evolution of the distribution of radiating electrons per unit energy,  $N(E, t)$ , is obtained from the solution of the well-known classical kinetic equation (see, e.g., Kardashev 1962),

$$\frac{\partial N(E, t)}{\partial t} = -\frac{\partial}{\partial E} [\dot{E} N(E, t)] + Q(E, t), \quad (3)$$

which accounts for the particle energy losses, where  $Q(E, t)$  is the number of injected electrons per unit time, per unit energy, and  $\dot{E}$  is the electron energy-loss rate. In the present case, the electrons are subjected to adiabatic losses, due to the ejecta expansion, and to synchrotron radiation losses, because of the magnetic field.

Therefore, the electron energy evolves with time, according to the classical energy balance equation (Kardashev 1962):

$$-\dot{E} = \frac{E}{t} + P_{\text{syn}}(E, t), \quad (4)$$

where

$$P_{\text{syn}}(E, t) = \beta B_*^2(t) E^2 \quad (5)$$

is the bolometric synchrotron power and  $\beta = 2e^4/(3m_e^4 c^7)$  (for details, see, e.g., Longair 2011).

We adopt a distribution of the injected particles following a power-law behavior (see, e.g., Kardashev 1962; Rybicki & Lightman 1979; Longair 2011):

$$Q(E, t) = Q_0(t) E^{-\gamma}, \quad 0 \leq E \leq E_{\text{max}}, \quad (6)$$

where  $\gamma$  and  $E_{\text{max}}$  are parameters to be determined from the observational data. We now address the function determining the rate of particle injection,  $Q_0(t)$ , which is related to the power injected by the  $\nu$ NS into the ejecta, i.e., the injected electrons are accelerated by the energy from the fallback accretion onto the  $\nu$ NS. We assume that the bolometric power released by the  $\nu$ NS is given by

$$L_{\text{inj}}(t) = L_0 \left(1 + \frac{t}{t_q}\right)^{-k}, \quad (7)$$

where  $L_0$ ,  $t_q$ , and  $k$  are model parameters. Because the ejecta surround the  $\nu$ NS, the power released by the  $\nu$ NS is injected into the ejecta, so the function  $Q_0(t)$  can be found from energy conservation as

$$L_{\text{inj}}(t) = \int_0^{E_{\text{max}}} E Q(E, t) dE = Q_0(t) \frac{E_{\text{max}}^{2-\gamma}}{2-\gamma}, \quad (8)$$

which, via Equation (7), leads to

$$Q_0(t) = q_0 \left(1 + \frac{t}{t_q}\right)^{-k}, \quad (9)$$

where  $q_0 \equiv (2 - \gamma)L_0/E_{\text{max}}^{2-\gamma}$ .

With the specification of the ejecta evolution given by Equation (1), that of the magnetic field given by Equation (2), and the rate of particle injection given by Equations (6) and (9),



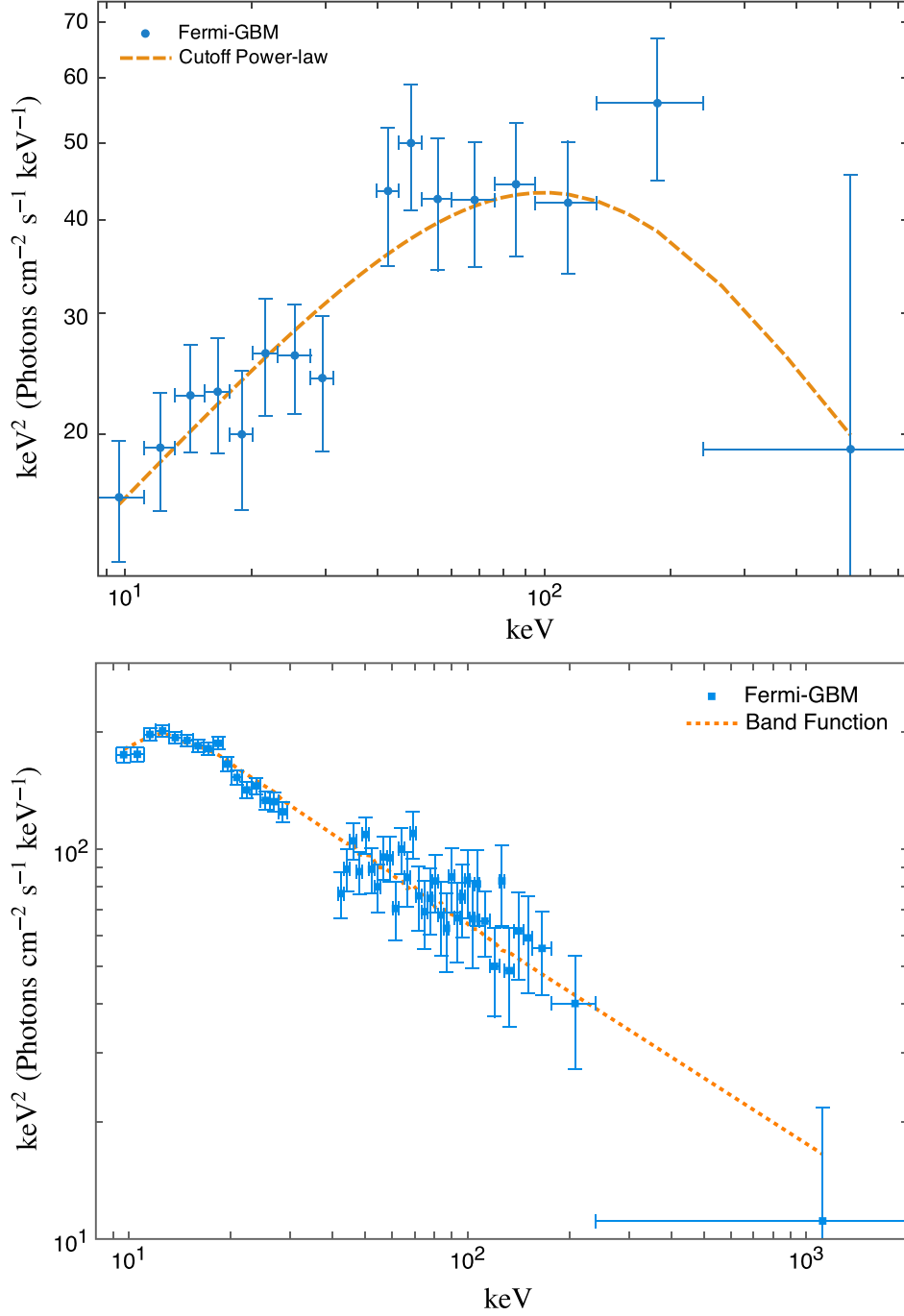


**Figure 4.** Top: the spectrum of the first pulse observed by Fermi-GBM. The blue points are the data and the orange curve indicates the fitting by a cutoff power law with power-law index  $\alpha = -1.45$  and the peak energy  $E_p = 144.28$  keV. Bottom: the spectrum of the second pulse. The blue points are the data and the orange curve indicates a band function fitting, with the low-energy index  $\alpha = 0.50$ , the high-energy index  $\beta = -2.53$ , and the peak energy  $E_p = 13.58$  keV.

we proceed to integrate the kinetic Equation (3). For this task, we must first find the time evolution of the energy of a generic electron injected at time  $t = t_i$  with initial energy  $E_i$ . With all the above, Equation (4) is a Riccati differential equation that has the following analytic solution (Rueda et al. 2022; Rueda 2022):

$$E = \frac{E_i(t_i/t)}{1 + \mathcal{M}E_it_i\left(\frac{1}{\hat{t}_i^2} - \frac{1}{\hat{t}^2}\right)}, \quad (10)$$

where  $\mathcal{M} \equiv \beta B_{*0}^2/2$ .

Following Pacini & Salvati (1973), we write the solution to Equation (3) as

$$N(E, t) = \int_E^\infty Q[E_i, t_i(t, E_i, E)] \frac{\partial t_i}{\partial E} dE_i, \quad (11)$$

where  $t_i(t, E_i, E)$  is obtained from Equation (10). The solution  $N(E, t)$  can be written as a piecewise function of time, depending upon the behavior of the energy injection in Equation (9); i.e., at times  $t < t_q$ , it can be approximated as a constant, while at longer times it is well approximated by a

pure power-law function. In addition, as we shall show below, the GRB afterglow data is well explained by a regime in which synchrotron radiation losses dominate over adiabatic losses. Under these conditions, the solution of Equation (11) can be written as (Rueda et al. 2022)

$$N(E, t) \approx \begin{cases} \frac{q_0}{\beta B_{*,0}^2 (\gamma - 1)} \hat{t}^2 E^{-(\gamma+1)}, & t < t_q \\ \frac{q_0 (t_q/t_*)^k}{\beta B_{*,0}^2 (\gamma - 1)} \hat{t}^{2-k} E^{-(\gamma+1)}, & t_q < t < t_b, \end{cases} \quad (12)$$

where the electron energy is in the range  $E_b < E < E_{\max}$ , being

$$E_b = \frac{\hat{t}}{\mathcal{M} t_*}, \quad t_b = t_*^2 \mathcal{M} E_{\max}. \quad (13)$$

The synchrotron luminosity radiated in the frequencies  $[\nu_1, \nu_2]$  can then be obtained as

$$L_{\text{syn}}(\nu_1, \nu_2; t) = \int_{\nu_1}^{\nu_2} J_{\text{syn}}(\nu, t) d\nu, \quad (14)$$

where  $J_{\text{syn}}(\nu, t)$  is the synchrotron spectral density (energy per unit time, per unit frequency),  $\nu_1 = \nu$ , and  $\nu_2 = \nu + \Delta\nu$ , with  $\Delta\nu$  being the bandwidth. The synchrotron power is mostly emitted at radiation frequencies close to the so-called critical frequency  $\nu_{\text{crit}} = \alpha B_* E^2$ , where  $\alpha = 3e/(4\pi m_e^3 c^5)$  (see, e.g., Rybicki & Lightman 1979). Therefore, the bolometric synchrotron power of Equation (5) can be readily written in terms of the radiation frequency  $\nu$  as

$$P_{\text{syn}}(E, t) \approx P_{\text{syn}}(\nu, t) = \frac{\beta}{\alpha} B_* \nu = \frac{\beta B_{*,0}}{\alpha \hat{t}} \nu, \quad (15)$$

and, within the same approximation (see, e.g., Longair 2011),

$$J_{\text{syn}} d\nu \approx P_{\text{syn}}(\nu, t) N(E, t) dE. \quad (16)$$

We now replace this into Equation (14) and obtain the synchrotron luminosity

$$L_{\text{syn}}(\nu, t) = \frac{\beta}{2} \alpha^{\frac{p-3}{2}} \eta B_{*,0}^{\frac{p+1}{2}} \hat{t}^{\frac{2l-p-1}{2}} \nu^{\frac{3-p}{2}}, \quad (17)$$

where we have used the approximation  $\Delta\nu/\nu \ll 1$  in the integration of Equation (14) in view of the power-law behavior of  $J_{\text{syn}}$ , and we have written the electron distribution as  $N(E, t) = \eta \hat{t}^l E^{-p}$ , with  $\eta$ ,  $l$ , and  $p$  being known constants from Equation (12).

Therefore, the synchrotron power has a power-law dependence in both time and radiation frequency; see Equation (17). If, over time, the system remains in the same physical regime in which the energy losses of the electrons are dominated by synchrotron radiation, the luminosities in the X-ray, optical, and radio wavelengths decrease with the *same* power-law index (see Figure 5). For the parameters of GRB 190829A (see Table 1), we found that this condition is fulfilled; i.e., the afterglow data remains at times  $t < t_b$  and is explained by electron energies that hold in the range  $E_b < E < E_{\max}$ —see Equation (13). In this case, the ratio of the synchrotron luminosity at different frequencies is constant in time, because it depends only on the power-law

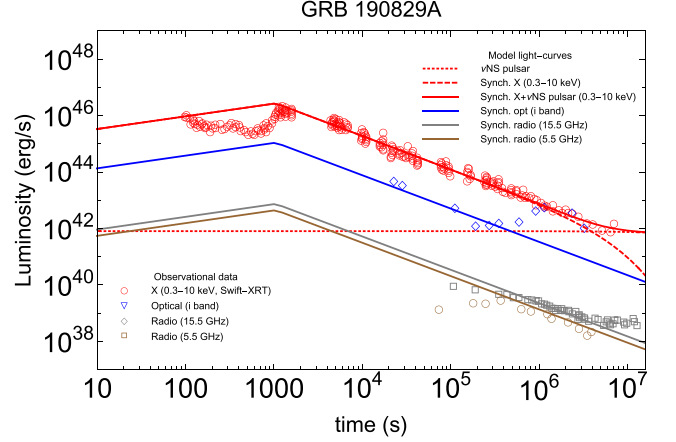


**Figure 5.** The luminosity of GRB 190829A in the X-ray (0.3–10 keV), optical (*i* band; Hu et al. 2021), and radio (5.5 and 15.5 GHz) energy bands (Rhodes et al. 2020).

**Table 1**

Numerical Values of the Theoretical Model of Synchrotron Radiation that Fit the Multiwavelength Observational Data of GRB 190829A, as Shown in Figure 5

Parameter	Value
$\gamma$	1.01
$k$	1.63
$L_0$ ( $10^{46}$ erg $s^{-1}$ )	8.00
$E_{\max}$ ( $10^4 m_e c^2$ )	5.00
$t_q$ (s)	1050.00
$R_{*,0}$ ( $10^{11}$ cm)	1.00
$v_{*,0}$ ( $10^9$ cm $s^{-1}$ )	1.00
$B_{*,0}$ ( $10^6$ G)	5.01
$\xi$	100.00
$B_{\text{dip}}$ ( $10^{12}$ G)	5.00
$P$ (ms)	8.00

index of the injection rate as (Rueda 2022)

$$\frac{L_{\text{syn}}(\nu_1, t)}{L_{\text{syn}}(\nu_2, t)} = \left( \frac{\nu_1}{\nu_2} \right)^{\frac{3-p}{2}} = \left( \frac{\nu_1}{\nu_2} \right)^{\frac{2-\gamma}{2}}. \quad (18)$$

In practice, we fix the value of  $\gamma$  from the X-rays to the optical luminosity ratio. Having fixed  $\gamma$ , the ratio of the optical (or X-rays) to radio luminosity is fixed, too. Figure 5 shows that this procedure leads to a synchrotron luminosity in the radio band that also agrees with the observations. This result implies that this model correctly describes the afterglow in the wide range of energies, including the radio and the optical, in addition to X-rays, giving strong support to the proposed scenario for afterglow emission.

## 5.2. $\nu$ NS Evolution and Pulsar Emission

As the synchrotron luminosity fades with time, the pulsar-like emissions of the  $\nu$ NS and the MNS companion become observable in the X-ray afterglow. We expect the magnetic field of the younger  $\nu$ NS to dominate over that of the much older MNS companion. By the time of the BdHN event, the MNS magnetic field could have decayed with respect to its

birth value. Although microphysical mechanisms leading to magnetic field decay in pulsars have been debated, a relevant mechanism for such a decay is that, during the evolution, the binary passes through common envelope and X-ray binary phases, in which the magnetic field is reduced by long-term accretion episodes (see, e.g., Payne & Melatos 2007, and references therein, for numerical simulations).

Bearing the above in mind, we assume that the pulsar emission observable in the afterglow is driven by the magnetic field of the  $\nu$ NS. We calculate this pulsar emission following the dipole + quadrupole magnetic field model presented in Pétri (2015). The total pulsar (spindown) luminosity is obtained by summing the dipole and quadrupole contributions:

$$\begin{aligned} L_{\text{sd}} &= L_{\text{dip}} + L_{\text{quad}} \\ &= \frac{2}{3c^3} \Omega^4 B_{\text{dip}}^2 R^6 \sin^2 \chi_1 \left( 1 + \xi^2 \frac{16}{45} \frac{R^2 \Omega^2}{c^2} \right), \end{aligned} \quad (19)$$

with  $R$  being the  $\nu$ NS radius and  $\xi$  defining the quadrupole-to-dipole strength ratio

$$\xi \equiv \sqrt{\cos^2 \chi_2 + 10 \sin^2 \chi_2} \frac{B_{\text{quad}}}{B_{\text{dip}}}, \quad (20)$$

where the modes can be separated as:  $\chi_1 = 0$  and any value of  $\chi_2$  for the  $m=0$  mode;  $(\chi_1, \chi_2) = (90^\circ, 0^\circ)$  for the  $m=1$  mode; and  $(\chi_1, \chi_2) = (90^\circ, 90^\circ)$  for the  $m=2$  mode.

The evolution of the  $\nu$ NS is calculated by integrating the energy balance equation,

$$-(\dot{W} + \dot{T}) = L_{\text{tot}} = L_{\text{inj}} + L_{\text{sd}}, \quad (21)$$

where  $W$  and  $T$  are, respectively, the  $\nu$ NS gravitational and the rotational energy.

Table 1 lists the model parameters that fit the afterglow of GRB 190829A in the X-ray, optical (Hu et al. 2021), and radio energy bands (Rhodes et al. 2020), as shown in Figure 5. The power-law luminosity observed in the multiwavelength data after  $10^3$  s is well explained by the synchrotron emission. We do not find evidence up to times of  $10^7$  s of a change in the power-law index, which implies that the system up to these times has not yet transitioned to the physical regime of the dominance of adiabatic losses over synchrotron losses. Although there is a good agreement of the model with the data after  $10^3$  s, the fit of the emission  $<10^3$  s is complicated. At those times, the behavior of the light curve is far from smooth, which is likely due to factors other than the synchrotron alone. The modeling of this early part of the afterglow is challenging for the presently simplified synchrotron picture, and probably needs very detailed information on the density profile of the ejecta and the absorption processes that we are not considering. The light curve at early times may catch short-timescale details of the evolution, so the accurate evaluation of the absorption and/or scattering processes (e.g., synchrotron self-absorption or Thomson scattering), leading to the evolution of the optical depth, might need a detailed radiative-transfer calculation, including possible deviations of the density and the expansion velocity from spherical symmetry (e.g., polar-angle dependence and filaments arising from Rayleigh–Taylor instability) and/or possible deviations of the thermodynamics variables (e.g., temperature and composition) that are needed for the evaluation of the opacity at every photon energy, position, and time. In addition, the early evolution of the  $\nu$ NS could be highly complex, leading to

an energy injection that deviates from the law assumed in Equation (7). The latter implies a constant injection rate at times  $t \lesssim \tau_q \approx 10^3$  s (see Table 1), leading to the rising synchrotron luminosity following a power law at those times (see Figure 5).

The VHE emission observed in the 0.2–4 TeV energy band of HESS is not explained by the above synchrotron model. We now estimate whether the SSC radiation could originate such an emission. The SSC emission is produced by synchrotron photons that upscatter off the relativistic electrons that produce them. The upscattering increases the energy of those photons by a factor equal to the square of the electron Lorentz factor, leading to a spectrum with a shape similar to the synchrotron spectrum, but at higher energies (Dermer & Menon 2009; Zhang 2018; Wang et al. 2019a; Nigro et al. 2022). Figure 6 shows as an example the first observational epoch of HESS ( $17438.5 \pm 805.5$  s) and our estimate of the SSC emission for the parameters of our synchrotron model. The SSC emission peaks at a few hundreds of MeV, cuts off at  $<10$  GeV, and has a lower luminosity with respect to that observed in the HESS energy bandwidth. Therefore, we conclude that neither the synchrotron nor the SSC radiation explain the VHE emission of GRB 190829A as observed by HESS. However, the similar power-law behavior of the VHE and the X-ray light curves suggests that the former could be related to some (presently unexplored) transient activity of the  $\nu$ NS. We notice that the HESS team expressed a similar conclusion, that the traditional afterglow model, including SSC radiation, does not explain their observations, and they expected a multizone emission model (Abdalla et al. 2021).

We turn now to the synchrotron emission. The critical synchrotron radiation energy ( $h\nu_{\text{crit}}$ ) decreases with time, so the peak of the synchrotron radiation shifts to lower energies with time. Around  $10^6$  s, the critical radiation energy falls below the keV range, leading to the exponential decay of the synchrotron emission in the X-rays after that time. Subsequently, the pulsar emission from the  $\nu$ NS dominates the observed X-ray emission. We have taken advantage of this behavior to infer the strength of the dipole and quadrupole components of the magnetic field, as well as the rotational period of the  $\nu$ NS.

The bump observed in the optical data at about  $10^6$  s is explained by the SN emission powered by the energy released from nickel decay (Arnett 1996), where, in this specific GRB, the type Ic SN 2019oyw optical signal overshoots the synchrotron optical emission. For the detailed SN observations and analysis, we refer the reader to the article from GTC (Hu et al. 2021).

The radio emission shows some excess over the synchrotron emission, from a few  $10^6$  s to  $10^7$  s. This feature may be a signature from the  $\nu$ NS pulsar, although further observational data and theoretical analysis are needed to confirm this hypothesis.

## 6. Discussion and Conclusion

The BdHN scenario describes the late evolution of a  $\text{CO}_{\text{core}}\text{-NS}$  binary. In particular, it predicts the electromagnetic signals that can be observed from a sequence of episodes that are triggered when the  $\text{CO}_{\text{core}}$  undergoes gravitational collapse at the end of its thermonuclear evolution, generating an SN and forming a  $\nu$ NS at its center. The ejected material from the SN accretes onto the companion NS and also onto the  $\nu$ NS, via matter fallback. The fate of the

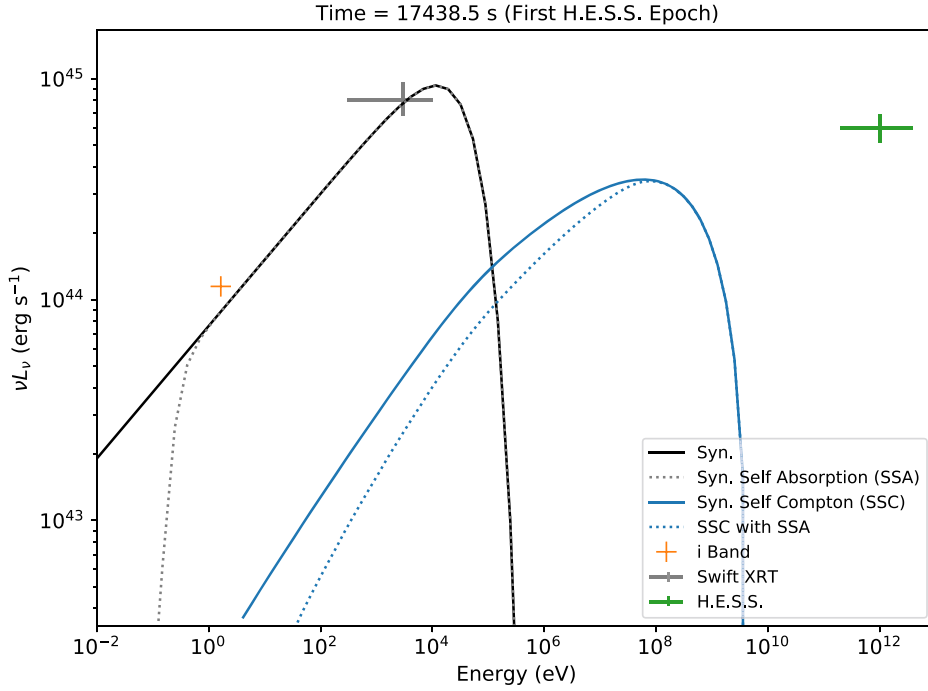


**Figure 6.** The synchrotron and SSC spectra of the first HESS observational epoch. The synchrotron spectrum well fits the optical and X-ray data. Neither the synchrotron nor the SSC spectra are able to reproduce the HESS observations.

companion NS depends on the initial mass and, crucially, on the binary separation (i.e., the orbital period) that sets the accretion rate. BdHNe I are characterized by short orbital periods of the order of a few minutes, where the NS reaches by accretion the critical mass for gravitational collapse into a BH. We refer the reader to Ruffini et al. (2021) for a comprehensive analysis of 380 BdHN I. In this article, we have analyzed GRB 190829A, which is classified as a BdHN II. These sources are characterized by longer orbital periods, i.e., larger binary separations, with lower accretion rates, and therefore the companion NS does not reach the critical mass for gravitational collapse.

GRB 190829A, at the close distance of redshift 0.0785, was observed by multiband telescopes and satellites on the ground and in space. These detailed observations have given us the opportunity to find the emissions that correspond to the episodes that are expected to occur in a BdHN II. The initial X-ray pulse of energy  $\sim 4.25 \times 10^{49}$  erg and the second pulse of energy  $\sim 3.56 \times 10^{50}$  erg represent the accretion of the SN ejecta onto the companion NS and the  $\nu$ NS; see Figures 2 and 4 for their light curves and spectra.

We explained the radio, optical, and X-ray afterglow emissions as being due to the synchrotron radiation from the SN ejecta expanding into the magnetic field of the  $\nu$ NS. The  $\nu$ NS continuously injects energy into the SN ejecta, from fallback accretion and spindown, owing to magnetic braking. From the fitting of afterglow synchrotron emission—see Figure 5—we infer the  $\nu$ NS spinning at an 8 ms period, with a dipole field of  $5 \times 10^{12}$  G. The observed VHE emission is explained neither by this synchrotron radiation process nor by SSC radiation. However, the fact that the VHE light curve shows a similar power-law decay to the X-rays, with a lower luminosity being released, but at higher photon energy, is suggestive of a process relating to a transient activity of the  $\nu$ NS, e.g., *glitches*, which shares a portion of the rotational

energy and leads to a narrow-angle emission near the light cylinder. The modeling of such a complex physical phenomenon needs further theoretical work and simulations, and, as such, goes beyond the scope of the present article. This same VHE emission parallel to the X-ray afterglow has also been observed in GRB 180720B (Moradi et al. 2021a) and GRB 190114C (R. Ruffini et al., to be submitted).

The BdHN model naturally contains an SN, and indeed in GRB 190829A the SN association was observed. The peak of the SN standard optical luminosity (R. Moradi et al., to be submitted) is higher than the synchrotron optical emission—see Figure 3—which makes the optical SN signal distinguishable.

In general, this article presents an evolutionary picture of the late stage of a binary system, which produces a GRB induced by an SN. We have observed two pulses of luminosity  $\sim 10^{49}$  erg  $s^{-1}$  from the accretion of the SN ejecta onto the NS and the  $\nu$ NS, as well as the NS spindown. From the observations, we infer that the  $\nu$ NS has an initial spin of 8 ms and a dipole magnetic field  $5 \times 10^{12}$  G.

Y.A. acknowledges funding from the Science Committee of the Ministry of Education and Science of the Republic of Kazakhstan (grant No. AP08855631).

#### ORCID iDs

Yu Wang <https://orcid.org/0000-0001-7959-3387>  
 R. Ruffini <https://orcid.org/0000-0003-0829-8318>  
 R. Moradi <https://orcid.org/0000-0002-2516-5894>  
 Liang Li <https://orcid.org/0000-0002-1343-3089>  
 N. Sahakyan <https://orcid.org/0000-0003-2011-2731>



#### References

Abdalla, H., Adam, R., Aharonian, F., et al. 2019, *Natur*, 575, 464  
 Abdalla, H., Aharonian, F., Benkhali, F. A., et al. 2021, *Sci*, 372, 1081

- Arnett, D. 1996, *Supernovae and Nucleosynthesis: An Investigation of the History of Matter from the Big Bang to the Present* (Princeton, NJ: Princeton Univ. Press)
- Becerra, L., Bianco, C. L., Fryer, C. L., Rueda, J. A., & Ruffini, R. 2016, *ApJ*, **833**, 107
- Becerra, L., Cipolletta, F., Fryer, C. L., Rueda, J. A., & Ruffini, R. 2015, *ApJ*, **812**, 100
- Becerra, L., Ellinger, C. L., Fryer, C. L., Rueda, J. A., & Ruffini, R. 2019, *ApJ*, **871**, 14
- Bhattacharyya, S., & Chakrabarty, D. 2017, *ApJ*, **835**, 4
- Bolmer, J., Greiner, J., & Chen, T. W. 2019, GCN, **25651**, 1
- Branch, D., & Wheeler, J. C. 2017, *Supernova Explosions* (Berlin: Springer)
- Cano, Z., Wang, S.-Q., Dai, Z.-G., & Wu, X.-F. 2017, *AdAst*, **2017**, 8929054
- Chand, V., Banerjee, A., Gupta, R., et al. 2020, *ApJ*, **898**, 42
- de Ugarte Postigo, A., Izzo, L., Thoene, C. C., et al. 2019, GCN, **25677**, 1
- Dermer, C. D., & Menon, G. 2009, *High Energy Radiation from Black Holes: Gamma Rays, Cosmic Rays, and Neutrinos* (Princeton, NJ: Princeton Univ. Press)
- Dichiara, S., Bernardini, M. G., Burrows, D. N., et al. 2019, GCN, **25552**, 1
- Dichiara, S., Troja, E., Lipunov, V., et al. 2021, *MNRAS*, **512**, 2337
- Fermi GBM Team 2019, GCN, **25551**, 1
- Frajia, N., Veres, P., Beniamini, P., et al. 2021, *ApJ*, **918**, 12
- Fryer, C. L., Rueda, J. A., & Ruffini, R. 2014, *ApJL*, **793**, L36
- Goldreich, P., & Julian, W. H. 1969, *ApJ*, **157**, 869
- Goldstein, A., Cleveland, W. H., & Kocevski, D. 2021, Fermi GBM Data Tools: v1.1.0, <https://fermi.gsfc.nasa.gov/ssc/data/analysis/gbm>
- Heintz, K. E., Fynbo, J. P. U., Jakobsson, P., et al. 2019, GCN, **25563**, 1
- Hu, Y. D., Castro-Tirado, A. J., Kumar, A., et al. 2021, *A&A*, **646**, A50
- Kardashev, N. S. 1962, *SvA*, **6**, 317
- Li, L. 2019a, *ApJS*, **242**, 16
- Li, L. 2019b, *ApJS*, **245**, 7
- Li, L., Ryde, F., Pe'er, A., Yu, H.-F., & Acuner, Z. 2021, *ApJS*, **254**, 35
- Li, L., & Zhang, B. 2021, *ApJS*, **253**, 43
- Li, L., Geng, J.-J., Meng, Y.-Z., et al. 2019, *ApJ*, **884**, 109
- Longair, M. S. 2011, *High Energy Astrophysics* (Cambridge: Cambridge Univ. Press)
- MAGIC Collaboration, Acciari, V. A., Ansoldi, S., et al. 2019, *Natur*, **575**, 455
- Mészáros, P. 2002, *ARA&A*, **40**, 137
- Moradi, R., Li, L., Rueda, J. A., et al. 2021a, arXiv:2103.09158
- Moradi, R., Rueda, J. A., Ruffini, R., & Wang, Y. 2021b, *A&A*, **649**, A75
- Nigro, C., Sitarek, J., Gliwny, P., et al. 2022, *A&A*, **660**, A18
- Ostriker, J. P., & Gunn, J. E. 1969, *ApJ*, **157**, 1395
- Pacini, F., & Salvati, M. 1973, *ApJ*, **186**, 249
- Payne, D. J. B., & Melatos, A. 2007, *MNRAS*, **376**, 609
- Perley, D. A., & Cockeram, A. M. 2019, GCN, **25657**, 1
- Pétri, J. 2015, *MNRAS*, **450**, 714
- Piran, T. 2004, *RvMP*, **76**, 1143
- Planck Collaboration, Aghanim, N., Akrami, Y., et al. 2020, *A&A*, **641**, A6
- Rhodes, L., van der Horst, A. J., Fender, R., et al. 2020, *MNRAS*, **496**, 3326
- Rueda, J. A. 2022, arXiv:2202.00316
- Rueda, J. A., & Ruffini, R. 2012, *ApJL*, **758**, L7
- Rueda, J. A., & Ruffini, R. 2020, *EPJC*, **80**, 300
- Rueda, J. A., Ruffini, R., Karlica, M., Moradi, R., & Wang, Y. 2020, *ApJ*, **893**, 148
- Rueda, J. A., Ruffini, R., Li, L., et al. 2022, *IJMPD*, **31**, 2230013
- Rueda, J. A., Ruffini, R., Moradi, R., & Wang, Y. 2021, *IJMPD*, **30**, 2130007
- Rueda, J. A., Ruffini, R., & Wang, Y. 2019, *Univ*, **5**, 110
- Ruffini, R., Karlica, M., Sahakyan, N., et al. 2018a, *ApJ*, **869**, 101
- Ruffini, R., Salmonson, J. D., Wilson, J. R., & Xue, S. S. 1999, *A&A*, **350**, 334
- Ruffini, R., Salmonson, J. D., Wilson, J. R., & Xue, S.-S. 2000, *A&A*, **359**, 855
- Ruffini, R., Vereshchagin, G., & Xue, S. 2010, *PhR*, **487**, 1
- Ruffini, R., Wang, Y., Enderli, M., et al. 2015, *ApJ*, **798**, 10
- Ruffini, R., Wang, Y., Aimuratov, Y., et al. 2018b, *ApJ*, **852**, 53
- Ruffini, R., Becerra, L., Bianco, C. L., et al. 2018c, *ApJ*, **869**, 151
- Ruffini, R., Moradi, R., Rueda, J. A., et al. 2019, *ApJ*, **886**, 82
- Ruffini, R., Moradi, R., Rueda, J. A., et al. 2021, *MNRAS*, **504**, 5301
- Rybicki, G. B., & Lightman, A. P. 1979, *Radiative Processes in Astrophysics* (New York: Wiley)
- Sato, Y., Obayashi, K., Yamazaki, R., Murase, K., & Ohira, Y. 2021, *MNRAS*, **504**, 5647
- Vianello, G., Lauer, R. J., Younk, P., et al. 2015, arXiv:1507.08343
- Wang, X.-Y., Liu, R.-Y., Zhang, H.-M., Xi, S.-Q., & Zhang, B. 2019a, *ApJ*, **884**, 117
- Wang, Y., Aimuratov, Y., Moradi, R., et al. 2018, *MmSAI*, **89**, 293
- Wang, Y., Rueda, J. A., Ruffini, R., et al. 2019b, *ApJ*, **874**, 39
- Wang, Y., Ruffini, R., Kovacevic, M., et al. 2015, *ARep*, **59**, 667
- Woosley, S. E., & Bloom, J. S. 2006, *ARA&A*, **44**, 507
- Xu, D., Yu, B. Y., Zhu, Z. P., et al. 2019, GCN, **25555**, 1
- Zhang, B. 2018, *The Physics of Gamma-ray Bursts* (Cambridge: Cambridge Univ. Press)
- Zhang, B. 2019, *Natur*, **575**, 448
- Zhang, B. T., Murase, K., Veres, P., & Mészáros, P. 2021a, *ApJ*, **920**, 55
- Zhang, L.-L., Ren, J., Huang, X.-L., et al. 2021b, *ApJ*, **917**, 9



# Gravitomagnetic Interaction of a Kerr Black Hole with a Magnetic Field as the Source of the Jetted GeV Radiation of Gamma-Ray Bursts

J. A. Rueda<sup>1,2,3,4,5</sup> , R. Ruffini<sup>1,2,6,7</sup> , and R. P. Kerr<sup>1,2,8</sup>

<sup>1</sup> ICRA, Dipartimento di Fisica, Sapienza Università di Roma, Piazzale Aldo Moro 5, I-00185 Roma, Italy; [jorge.rueda@icra.it](mailto:jorge.rueda@icra.it), [ruffini@icra.it](mailto:ruffini@icra.it), [roy.kerr@canterbury.ac.nz](mailto:roy.kerr@canterbury.ac.nz)

<sup>2</sup> ICRANet, Piazza della Repubblica 10, I-65122 Pescara, Italy

<sup>3</sup> ICRANet-Ferrara, Dipartimento di Fisica e Scienze della Terra, Università degli Studi di Ferrara, Via Saragat 1, I-44122 Ferrara, Italy

<sup>4</sup> Dipartimento di Fisica e Scienze della Terra, Università degli Studi di Ferrara, Via Saragat 1, I-44122 Ferrara, Italy

<sup>5</sup> INAF, Istituto di Astrofisica e Planetologia Spaziali, Via Fosso del Cavaliere 100, I-00133 Rome, Italy

<sup>6</sup> Université de Nice Sophia-Antipolis, Grand Château Parc Valrose, Nice, CEDEX 2, France

<sup>7</sup> INAF, Viale del Parco Mellini 84, I-00136 Rome, Italy

<sup>8</sup> University of Canterbury, Christchurch, New Zealand

Received 2022 January 17; revised 2022 March 4; accepted 2022 March 5; published 2022 April 12

## Abstract

We show that the gravitomagnetic interaction of a Kerr black hole (BH) with a surrounding magnetic field induces an electric field that accelerates charged particles to ultra-relativistic energies in the vicinity of the BH. Along the BH rotation axis, these electrons/protons can reach energies of even thousands of petaelectronvolts, so stellar-mass BHs in long gamma-ray bursts (GRBs) and supermassive BHs in active galactic nuclei can contribute to the ultrahigh-energy cosmic rays through this mechanism. At off-axis latitudes, the particles accelerate to energies of hundreds of gigaelectronvolts and emit synchrotron radiation at gigaelectronvolt energies. This process occurs within  $60^\circ$  around the BH rotation axis, and due to the equatorial symmetry, it forms a double-cone emission. We outline the theoretical framework describing these acceleration and radiation processes, how they extract the rotational energy of the Kerr BH and the consequences for the astrophysics of GRBs.

*Unified Astronomy Thesaurus concepts:* [Black hole physics \(159\)](#); [Gamma-ray bursts \(629\)](#); [Active galactic nuclei \(16\)](#); [Ultra-high-energy cosmic radiation \(1733\)](#)

## 1. Introduction

In the absence of any observational evidence, the process of gravitational collapse was studied in the simplest possible mathematical solution of the Einstein equations, i.e., for a spherically symmetric and vacuum spacetime (Oppenheimer & Snyder 1939; Finkelstein 1958; Kruskal 1960). The renaissance of the physics of general relativity started with the new era of relativistic astrophysics heralded by three discoveries:

1. On 1962 June 12, the first evidence of an X-ray source outside the solar system, Sco X1 (Giacconi et al. 1962), whose nature as a binary system was identified by Shklovskii (1968). This was the first source of a long number of binary X-ray sources discovered later (see, e.g., Giacconi & Ruffini 1978). The identification of the detailed nature of Sco X1 stills today represents an open problem (see, e.g., Jia et al. 2020).
2. On 1963 July 26, the discovery by Kerr (1963) of an algebraically special metric, among the solutions of the Einstein field equations in vacuum, that describes the gravitational field of a spinning mass. The *Kerr solution* introduced a theoretical formalism of unprecedented complexity in general relativity to describe the effect of the rotation in the black hole (BH) geometry. From an observational point of view, the Kerr metric offered, in principle, since 1971 (see below) an unprecedented

energy source for an astrophysical system, alternative, e.g., to nuclear energy sources.

3. On 1963 March 16, the epochal discovery of the quasar nature of the radio source 3C 273 by Schmidt (1963), at  $z = 0.158$ , i.e., at a distance of about 760 Mpc, implying energies of  $10^{59}$  erg originating from the nuclear region of a galaxy. The explanation of the energy source in terms of the rotational energy of the BH is among the leading open astrophysical problems still today, and gaining additional crucial observations from closer active galactic nuclei (AGNs) as M87 at  $z = 0.00436$  (Bird et al. 2010) and IC 310 at  $z = 0.0189$  (Bernardi et al. 2002).

The authentic shock of the pulsar discovery, the very quick identification of its nature as the first observed gravitationally collapsed object, and the long awaited explanation of the nature of the supernova (SN), marked the real birth of relativistic astrophysics and of the physics of gravitational collapse. The discovery of the Crab Nebula pulsar by Hewish et al. (1968) allowed:

1. The first, unequivocal observational identification of a pulsar as a rapidly rotating NS (Gold 1968; Pacini 1968; Finzi & Wolf 1969).
2. The possibility to confirm the hypothesis of Baade & Zwicky (1934) that NSs originate in SNe. In this case, the Crab pulsar had originated in the SN observed by Chinese astronomers in the year 1054 (Shklovskii 1953; Shklovskij 1969).
3. To conceptually realize that, the process of gravitational collapse leading to NS formation is not an isolated event in time, but followed by a long-lasting emission of thousands of years. The conceptual role of this prolonged



Original content from this work may be used under the terms of the [Creative Commons Attribution 4.0 licence](#). Any further distribution of this work must maintain attribution to the author(s) and the title of the work, journal citation and DOI.

emission, traditionally neglected, is now acquiring a special role in the context of gamma-ray bursts (GRBs), where both the collapse to a NS and to a BH are observed daily with a long-lasting X-ray and gigaelectronvolt emission (see Ruffini et al. 2021, references therein, and Equations (1) and (2) in this article).

In Princeton, John A. Wheeler’s group proceeded ahead in the study of BHs adopting as a background the geometry of the Kerr solution. This research program soon materialized in three steps:

1. The introduction in 1969 of the effective potential technique to determine the properties of corotating and counter-rotating orbits, including the often quoted last stable circular orbits in the Kerr metric (see Ruffini & Wheeler in Section 104 of Landau & Lifshitz 1975).
2. The identification, among these trajectories, of the ones corresponding to reversible and irreversible transformations presented in Christodoulou (1970). The derivation by Demetrios Christodoulou of the mass-energy formula of a Kerr BH was made possible by introducing the concept of *irreducible* mass  $M_{\text{irr}}$  (from the Italian *irreducibile*) following the definition of *ergosphere* introduced in Christodoulou (1970) by Ruffini and Wheeler. The further relation between the irreducible mass and the horizon area was soon shown in Christodoulou & Ruffini (1971) and Hawking (1971). These results were obtained practicing on the *gedanken* Penrose process, see Figure 2 in Christodoulou (1970), which we found to be physically not implementable, as confirmed later by Penrose & Floyd (1971).<sup>9</sup>
3. The publication of *Introducing the Black Hole* (Ruffini & Wheeler 1971a), where the BH was introduced as a physical system characterized by three parameters, the total mass,  $M$ , the angular momentum,  $J$ , and the irreducible mass,  $M_{\text{irr}}$ , with the geometry given by the Kerr metric.

A first step in this novel domain established the absolute upper limit to the value of the critical mass of a nonrotating NS,  $3.2M_{\odot}$ , generalizing the first established value of  $0.7M_{\odot}$  by Oppenheimer & Volkoff (1939). The result was obtained, out of first principles, imposing the non-violation of causality, a fiducial nuclear density, and adopting the validity of general relativity (Rhoades & Ruffini 1974). A second step was the discovery of the first BH in our galaxy, Cygnus X1 (Leach & Ruffini 1973; Ruffini 1974; Giacconi 2003), using X-ray and optical data and imposing the above critical mass limit for BH formation. Nevertheless, the discovery of such a Galactic object, although of great interest, did not offer any evidence for the new physics of the irreducible mass. It was clear that a binary X-ray source evolves on a timescale of  $10^8$  yr, so we initially thought that we would have to wait for too long to see what occurs next in their evolution. But this was a big mistake. The gravitational collapse releases about  $10^{52}$  erg, so such an event would be visible from any place in the universe, and from the number of binary X-ray sources, that would lead to the observation of these events almost everyday. We had to wait a third gigantic step following the launch of Beppo-Sax and the

discovery of the extragalactic origin of GRBs (Costa et al. 1997; van Paradijs et al. 1997). It was then started an unprecedented experimental effort of observing these most unique sources in the vastest range of wavelengths, from the radio to the kiloelectronvolt, to the megaelectronvolt, to the gigaelectronvolt, to teraelectronvolt, to the ultrahigh-energy cosmic rays (UHECRs). As a result, we have the opportunity to observe these sources up to high values of the cosmological redshift, e.g.,  $z = 10$ , allowing us to witness on a daily basis the birth of NSs and BHs. This new unprecedented condition allows us, for the first time, to submit also our own theoretical analysis to the scrutiny of direct observations and to verify which one of our theoretical assumptions, introduced 49 yr ago, were made just for the sake of simplicity or mathematical convenience.

In parallel, a novel path of theoretical research was gaining attention, diverging from a pure gravitational analysis of an isolated BH, in vacuum and stationary. Interest was called on the electrodynamics and magneto-hydrodynamics around BHs and on BH gravito-hydrodynamics (see Punsly 2009, and references therein). The BH theory based on the above theoretical developments and on the vastest multiwavelength observations has been started to be constructed, with necessary changes of paradigm, and new ones that we infer in this article.

This article is dedicated to the development of the theoretical framework of the *inner engine* originating the gigaelectronvolt radiation of GRBs within the binary-driven hypernova (BdHN) scenario (see Ruffini et al. 2019b, references therein, and Section 2 for details). It emphasizes the special role of the interaction of the *gravitomagnetic* field of a Kerr BH with a uniform, asymptotically aligned background test magnetic field, following the mathematical solution of the Einstein–Maxwell equations by Papapetrou (1966) and Wald (1974), hereafter referred to as the Papapetrou–Wald solution (see Sections 3–6 for details). As we shall show, the above leads to a mechanism of particle acceleration and radiation in the BH vicinity, leading to UHECRs along the BH rotation axis, and to gigaelectronvolt radiation at off-axis latitudes within  $60^\circ$  of the polar axis, with equatorial symmetry, i.e., there is a double-cone emission structure. The theory equations and their solution describing the particle acceleration and radiation processes, how they extract the rotational energy of the Kerr BH, as well as the consequences for the astrophysics of GRBs and AGN are outlined here.

The article is organized as follows. In Section 2, we outline the observational features of the formation of a Kerr BH in a BdHN of type I, using GRB 190114C as a prototype. Section 3 describes the structure of the electromagnetic field of the Papapetrou–Wald solution. In Section 3, we present the general relativistic equations of motion for charged particles including radiation losses. We show in Section 4 specific results of the numerical integration of the equations of motion. In Section 5, we analyze the properties of the photon four-momentum observed at infinity to infer the properties of the observed radiation. Section 6 is devoted to give quantitative estimates of the radiation power and the spectrum. In Section 7, we describe how the energy of the Kerr BH is extracted in the present mechanism. Finally, we present in Section 8 our conclusions.

<sup>9</sup> The negative results on the Penrose process have in no way affected the derivation of the irreducible mass, uniquely based on the reversible and irreversible transformations, which never attracted Penrose’s attention.

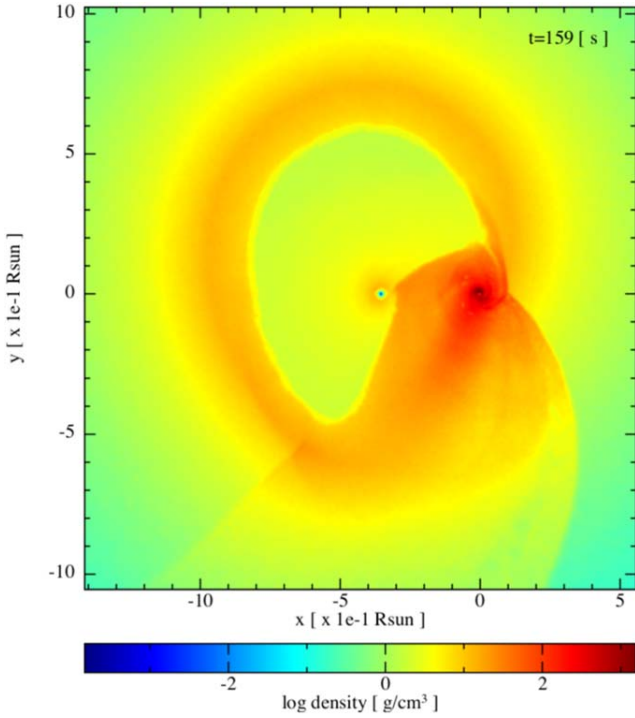


**Figure 1.** Numerical simulation of a BdHN I from Becerra et al. (2019; Model “25m1p08E” from Table 2 therein). The CO star of mass  $M_{\text{CO}} = 6.85 M_{\odot}$  explodes as SN in presence of a binary companion NS of mass  $M_{\text{NS}} = 2 M_{\odot}$ . At the center of the SN, it is formed as a  $\nu\text{NS}$  of mass  $1.85 M_{\odot}$ . The orbital period of the binary system is 4.8 minutes. This plot shows a snapshot of the mass density on the binary equatorial plane at a time 159 s from the SN explosion. The reference system is rotated and translated so that the  $x$ -axis is along the line that joins the  $\nu\text{NS}$  and the NS, and the axis origin (0, 0) is located at the NS position. In this simulation, the NS reaches the point of gravitational collapse with a mass of  $2.26 M_{\odot}$  and angular momentum  $1.24 GM_{\odot}^2/c$ . This binary system kept bound up the final time of the simulation despite the orbit widens, reaching an orbital period of 16.5 minutes and an eccentricity of  $\epsilon = 0.6$ . In this simulation, the collapse of the NS into a BH occurs at  $t = 21.6$  minutes.

## 2. BH Formation in a BdHN I: GRB 190114C as a Prototype

Prior to the year 2000, GRBs were traditionally considered as single objects originating their energy from a Kerr BH (see, e.g., Rees & Meszaros 1992; Woosley 1993; Piran 1999). Since then, a new scenario has been gradually developing in which GRBs originate in binary systems leading to their classification in nine GRB subclasses (see, e.g., Ruffini et al. 2016; Wang et al. 2019; Rueda et al. 2020). What has become clear is that a BH is generated only in some short GRBs originating in NS–NS mergers, and only in some long GRBs originating in binaries composed of a carbon–oxygen (CO) star and a NS companion in tight orbit.

We here focus on the latter special subclass of long GRBs that originate in short-period CO–NS binaries. The GRB ignition works as follows. As the CO star gravitationally collapses, it gives origin to a SN explosion and to a new NS (hereafter  $\nu\text{NS}$ ) at its center. The ejected matter in the SN produces a hypercritical (i.e., highly super-Eddington) accretion process both onto the  $\nu\text{NS}$  (via matter fallback) and onto the companion NS. For short orbital periods of the order of a few minutes, the accretion process onto the NS companion is sufficiently massive to lead it to the critical mass, hence forming a BH (see Figure 1). We have called these systems

BdHN of type I (see, e.g., Wang et al. 2019). Until now, 380 of BdHN I have been identified, with their evolution following a precise sequence of episodes, which we here indicate using GRB 190114C as a prototype (Moradi et al. 2021a, 2021b).

The time  $t = 0$  coincides with the trigger of GRB 190114C given by the Fermi satellite. The progenitor is a CO–NS binary with an inferred orbital period of 5 minutes (Rueda et al. 2020). The appearance of the  $\nu\text{NS}$ , hereafter  $\nu\text{NS}$  rise (formerly called SN rise), following the CO star core collapse, occurs between 0.79 and 1.18 s in the rest frame of the source. The  $\nu\text{NS}$  rise triggers the entire BdHN I evolution. In the SN explosion, as usual, a  $\nu\text{NS}$  is created, which operates in addition to the binary companion NS (see Figure 1). The spectrum of the  $\nu\text{NS}$  rise, observed in the gamma rays by the Fermi–GBM detector, is shown in Figure 2 (upper left panel). The energy of the  $\nu\text{NS}$  rise in GRB 190114C is  $E_{\nu\text{NS-rise}} = 2.82 \times 10^{52}$  erg (Ruffini et al. 2021).

The SN ejecta now accrete at hypercritical rates onto the binary companion NS. At 1.9 s, the NS companion reaches its critical mass and collapses creating a Kerr BH, highlighted by the onset of the giga-electronvolt emission (see Figure 2; lower left panel). Between 1.9 and 3.9 s in the source rest frame, the ultra-relativistic prompt emission (UPE) occurs, characterized by a cutoff power-law plus blackbody (CPL + BB) spectrum and the energetics reported in Figure 2 (upper right panel). The energy released observed in the UPE phase is  $E_{\text{UPE}} = 1.47 \times 10^{53}$  erg (Moradi et al. 2021b).

At 47.83 s, the Neil Gehrels Swift satellite turns on and allows performing the observations of the ongoing emission of the X-ray afterglow. One of the major successes of the BdHN I theory has been the identification in the SN accretion onto the rapidly rotating  $\nu\text{NS}$ , with a spinning period of 2.1 ms (Rueda et al. 2020), the energy source of the afterglow of GRB 190114C (see Figure 2; lower right panel). The observations of GRB 190114C and of its *twin* source GRB 180427A have further allowed to explain the observed spectra of the afterglow characterized by the synchrotron emission originating from the rapidly rotating  $\nu\text{NS}$ , interacting with the SN ejecta. Further examples of afterglows fulfilling this approach and leading to the determination of the  $\nu\text{NS}$  rotation period have been the cases of GRB 180728A with a  $\nu\text{NS}$  spin of 3.5 ms, GRB 130427A with 0.95 ms, GRB 160625B with 0.5 ms, GRB 160509A with 0.75 ms, and GRB 090926A with 1.1 ms (Rueda et al. 2020).

The most significant result has been that all 378 identified BdHN I have an afterglow characterized by a decreasing luminosity with time, that expressed in the rest frame of the source is well fitted by a power-law function

$$L_X = A_X t^{-\alpha_X}, \quad (1)$$

which for GRB 190114C  $A_X = (5.14 \pm 2.03) \times 10^{52}$  erg s $^{-1}$  and  $\alpha_X = 1.37 \pm 0.05$  (Ruffini et al. 2021). The observed energy released in the X-ray emission is  $E_X = 2.11 \times 10^{52}$  erg.

We have identified above the role of the SN in creating a magnetized rapidly rotating  $\nu\text{NS}$ , as well as its role in producing a hypercritical accretion process onto the  $\nu\text{NS}$  which helps to power the X-ray afterglow. There are three main conclusions on the afterglow:

1. The initial rotational energy of the  $\nu\text{NS}$  with the observed power-law luminosity given by Equation (1) may well justify an afterglow emission occurring for an infinite time.



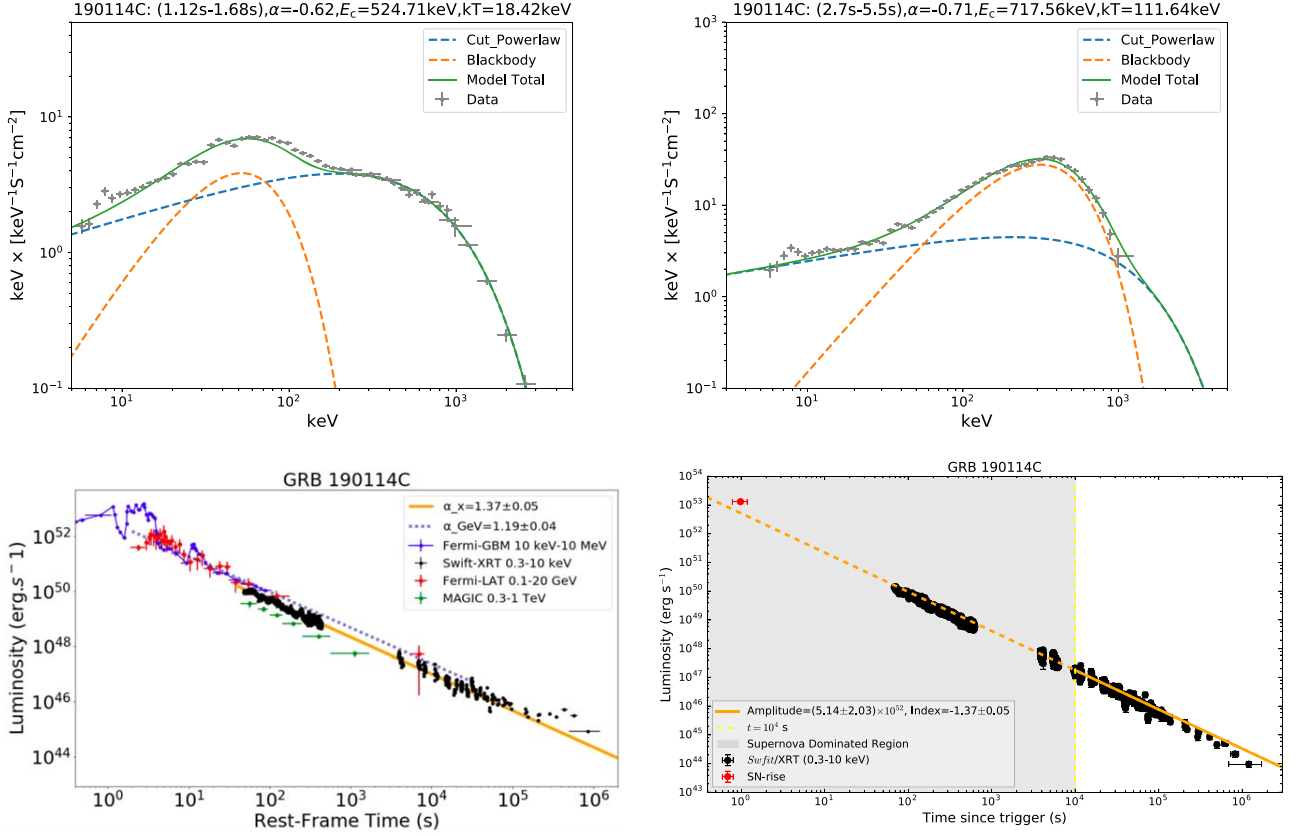


**Figure 2.** Upper left panel:  $\nu$ NS rise spectrum of BdHN I 190114C, corresponding to a time interval from  $t = 1.12$  s ( $t_{\text{rf}} = 0.79$  s) to  $t = 1.68$  s ( $t_{\text{rf}} = 1.18$  s). The best-fit model is a CPL+BB with parameters (in the observer’s frame): low-energy photon index  $-0.71$ , peak energy  $E_c = 524.7$  keV, and blackbody temperature  $kT = 18.42$  keV. The energy of the  $\nu$ NS rise is  $E_{\nu\text{NS-rise}} = 2.82 \times 10^{52}$  erg. Upper right panel: spectral analysis of the UPE phase of GRB 190114C, i.e., in the time interval from  $t = 2.7$  s ( $t_{\text{rf}} = 1.9$  s) to  $t = 5.5$  s ( $t_{\text{rf}} = 3.9$  s). The best-fit model is a CPL+BB with the following parameters: power-law index  $\alpha = -0.71^{+0.02}_{-0.02}$ , cutoff energy  $E_c = 717.6^{+25.4}_{-25.4}$  keV, temperature  $kT = 111.64^{+2.3}_{-2.3}$  keV. The observed energy released in the UPE is  $E_{\text{UPE}} = 1.47 \times 10^{53}$  erg (Moradi et al. 2021b). Lower left panel: multiwavelength luminosity of BdHN I 190114C. The blue points are the rest frame 10 keV–10 MeV luminosity from Fermi-GBM. The black points are the rest frame 0.3–10 keV luminosity from Swift-XRT. The red points are the rest frame 0.1–20 GeV luminosity from Fermi-LAT. It follows a decaying power law with amplitude  $(4.6 \pm 0.6) \times 10^{52}$  erg s $^{-1}$ , and index  $\alpha_{\text{GeV}} = 1.19 \pm 0.04$ . The green points are the rest frame 0.3–1 TeV luminosity from MAGIC. Lower right panel: luminosity of GRB 190114C observed by the Swift-XRT in the 0.3–10 keV energy band. The luminosity is well fitted by a power-law function given by Equation (1), with  $A_X = (5.14 \pm 2.03) \times 10^{52}$  erg s $^{-1}$  and  $\alpha_X = 1.37 \pm 0.05$ . The observed energy released in the X-ray emission is  $E_X = 2.11 \times 10^{52}$  erg (Moradi et al. 2021b).

2. These results open a new scenario with respect to the usually assumed ultra-relativistic blast waves in the traditional GRB model, which has been shown to contradict model-independent constraints (Ruffini et al. 2018) and imply unacceptable energetic requirements for the system.
3. The presence of a rapidly spinning  $\nu$ NS in the afterglow can lead to the possibility of relating  $\nu$ NS *glitches* to the emission of teraelectronvolt emission, e.g., in GRB 180720B (Moradi et al. 2022, submitted).

At 3.9 s, at the end of the UPE phase, the gigaelectronvolt radiation observed by LAT is emitted following a decreasing power-law luminosity (see Figure 2; lower left panel)

$$L_{\text{GeV}} = A_{\text{GeV}} t^{-\alpha_{\text{GeV}}}, \quad (2)$$

with  $A_{\text{GeV}} = 7.75 \pm 0.44 \times 10^{52}$  erg s $^{-1}$  and  $\alpha_{\text{GeV}} = 1.2 \pm 0.04$ . The energy of the gigaelectronvolt emission is  $E_{\text{GeV}} = 8.3 \times 10^{52}$  erg (Moradi et al. 2021a).

The existence of the above-mentioned power laws in the X-ray emission observed by the Swift satellite, originating from the rotational energy extraction from a spinning  $\nu$ NS, see Equation (1), and the analogous one in the gigaelectronvolt

observed by the Fermi-LAT satellite, originating from the rotational energy extraction Kerr BH, see Equation (2), are the two conceptually new observables characterizing GRBs. Every gravitational collapse episode occurring within a GRB, either leading to a rotating NS or to a rotating BH, is not an isolated event in space and time. On the contrary, it is the beginning of a process characterized by a decreasing power-law luminosity that, in principle, may last the entire life of the universe. What is clear is that, currently, we are observing all *alive* Kerr BHs and not *dead* Schwarzschild BHs. The crucial characterization of this difference resides in the *jetted* emission and the possible presence of trapped surface and of shadows cannot be meaningfully addressed on the ground of this physics.

In order to approach in the following sections the physics of the *inner engine*, we have first to introduce three main new paradigms:

1. The rotational energy extraction from a Kerr BH and the associated acceleration process originates in the *gravitomagnetic* interaction of the Kerr BH with a uniform background magnetic field (Ruffini et al. 2019b). Necessarily, the conditions of stationarity of the Kerr solution, as well as assuming such a solution in vacuum

and all the considerations of the geodesics of uncharged particles have to be superseded, see Section 3.

2. The geodesic equations of motion of massive particles around a Kerr BH (Ruffini & Wheeler 1971a, 1971b) are superseded by the equation of motion of positively and negatively charged particles in the field of a Papapetrou–Wald solution, taking into due account the radiation-reaction forces; see Sections 4 and 5, as well as Appendices A–C.
3. The fundamental role of the reversible transformations stands, indeed, the irreducible mass  $M_{\text{irr}}$  is the fundamental regulator of the energy extraction process from the Kerr BH and the emission of the radiation power and spectrum; see Sections 6 and 7.

### 3. The Electromagnetic Field Structure

The *inner engine* of the high-energy emission of long GRBs was presented in Ruffini et al. (2019b), and applied there to GRB 130427A. It is composed of a Kerr BH (Boyer & Lindquist 1967; Carter 1968), embedded in a test, asymptotically aligned magnetic field, described by the Papapetrou–Wald (Papapetrou 1966; Wald 1974) solution of the Einstein–Maxwell equations.

We here present a full (numerical) integration of the equations of motion of a charged particle in the electromagnetic field of the Papapetrou–Wald solution, accounting for radiation in the background of the Kerr metric. We use geometric units  $c = G = 1$ , unless otherwise specified.

Denoting by  $\eta = \partial/\partial t$  and  $\psi = \partial/\partial \phi$ , respectively the time-like and space-like Killing vectors for the Kerr metric (see Appendix A), the electromagnetic four-potential is given by (Wald 1974)

$$A_\mu = \frac{B_0}{2} \psi_\mu + a B_0 \eta_\mu, \quad (3)$$

where  $B_0$  is the asymptotic value of the magnetic field strength. Because of  $\eta^\mu = \delta^\mu_t$  and  $\psi^\mu = \delta^\mu_\phi$ , the nonvanishing components of the four-potential, in the Boyer–Lindquist coordinate basis of the Kerr metric (see Appendix A), read a

$$A_t = -aB_0 \left[ 1 - \frac{Mr}{\Sigma} (1 + \cos^2 \theta) \right], \quad (4)$$

$$A_\phi = \frac{1}{2} B_0 \sin^2 \theta \left[ r^2 + a^2 - \frac{2Mr a^2}{\Sigma} (1 + \cos^2 \theta) \right]. \quad (5)$$

As in Damour et al. (1978), we introduce a local Lorentz observer, specifically a *locally nonrotating* (LNR) observer (Bardeen 1970; Bardeen et al. 1972), in order to analyze the electromagnetic field properties and the equations of motion.

The LNR observer carries a tetrad basis with vectors  $e_{\hat{a}}$ ; see Appendix A for details on the tetrad and related framework of the subsequent calculations. We use a hat to distinguish components (projections) in the LNR frame from the ones in coordinate frame. Latin alphabet (e.g.,  $a$ ) and Greek indexes (e.g.,  $\mu$ ) run over the spacetime coordinates, i.e., from 0–3 ( $t$ ,  $r$ ,  $\theta$ , and  $\phi$ ), while Latin indexes (e.g.,  $i$ ) run only over the spatial coordinates.

In the LNR frame, the electric and magnetic field components are given by

$$E_{\hat{i}} = E_\mu e_{\hat{i}}^\mu = F_{\hat{i}\hat{t}}, \quad (6a)$$

$$B_{\hat{i}} = B_\mu e_{\hat{i}}^\mu = \epsilon_{\hat{i}\hat{j}\hat{k}} F^{\hat{j}\hat{k}}, \quad (6b)$$

where  $F_{\mu\nu}$  is the electromagnetic field tensor in the coordinate basis. Expressed in Boyer–Lindquist coordinates, the electric and magnetic field are (Damour et al. 1978)

$$E_{\hat{r}} = -\frac{B_0 a M}{\Sigma^2 A^{1/2}} [(r^2 + a^2)(r^2 - a^2 \cos^2 \theta)(1 + \cos^2 \theta) - 2r^2 \sin^2 \theta \Sigma], \quad (7a)$$

$$E_{\hat{\theta}} = B_0 a M \frac{\Delta^{1/2}}{\Sigma^2 A^{1/2}} 2ra^2 \sin \theta \cos \theta (1 + \cos^2 \theta), \quad (7b)$$

$$B_{\hat{r}} = -\frac{B_0 \cos \theta}{\Sigma^2 A^{1/2}} \{ 2Mr a^2 [2r^2 \cos^2 \theta + a^2 (1 + \cos^4 \theta)] - (r^2 + a^2) \Sigma^2 \}, \quad (8a)$$

$$B_{\hat{\theta}} = -\frac{\Delta^{1/2} B_0 \sin \theta}{\Sigma^2 A^{1/2}} [Ma^2 (r^2 - a^2 \cos^2 \theta)(1 + \cos^2 \theta) + r \Sigma^2]. \quad (8b)$$

For completeness, we give the expressions of the electric and magnetic field in the Boyer–Lindquist coordinate basis (see Equation (B2))

$$\mathbf{E} = E_{\hat{r}} \mathbf{e}_{\hat{r}} + E_{\hat{\theta}} \mathbf{e}_{\hat{\theta}} = E_{\hat{r}} \sqrt{\frac{\Delta}{\Sigma}} \mathbf{e}_r + E_{\hat{\theta}} \frac{1}{\sqrt{\Sigma}} \mathbf{e}_\theta, \quad (9a)$$

$$\mathbf{B} = B_{\hat{r}} \mathbf{e}_{\hat{r}} + B_{\hat{\theta}} \mathbf{e}_{\hat{\theta}} = B_{\hat{r}} \sqrt{\frac{\Delta}{\Sigma}} \mathbf{e}_r + B_{\hat{\theta}} \frac{1}{\sqrt{\Sigma}} \mathbf{e}_\theta. \quad (9b)$$

Figures 3 and 4 show the electric and magnetic field lines as seen by the LNR observer, in the  $x$ – $z$  plane in Kerr–Schild coordinates (see Appendix A). We describe now the physical situation in the northern hemisphere since because of the equatorial symmetry, the situation in southern hemisphere will be exactly the same. Electrons move outwardly where the electric field is inwardly directed. Clearly, the opposite happens for protons, they move outwardly where the electric field is outwardly directed. In Figure 3, we show the case of an asymptotically parallel magnetic field to the BH spin. The electric field is inwardly directed in the cone of semi-aperture angle  $\theta_\pm \approx 55^\circ$  from the polar axis. Therefore, in this situation we have a *polar electronic jet*. At  $\theta = \theta_\pm$ , the electric field vanishes and reverse direction, i.e., the electric field becomes outwardly directed. In Figure 4, we show the case of an asymptotically antiparallel magnetic field to the BH spin. In this case, the electric field is outwardly directed in the cone of semi-aperture angle  $\theta_\pm \approx 55^\circ$  from the polar axis, creating a *polar electronic jet*.

For moderate spin values (i.e.,  $a/M \lesssim 0.7$ ), the electric and magnetic fields are accurately represented by the lowest order of their expansions in the dimensionless spin parameter  $a/M$ , i.e., up to first order we have

$$E_{\hat{r}} \approx -\frac{B_0 a M}{r^2} (3 \cos^2 \theta - 1), \quad (10a)$$

$$E_{\hat{\theta}} \approx 0, \quad (10b)$$

$$B_{\hat{r}} \approx B_0 \cos \theta, \quad (10c)$$

$$B_{\hat{\theta}} \approx -B_0 \sqrt{1 - \frac{2M}{r}} \sin \theta. \quad (10d)$$

We can see that within this approximation, the electric field reverses sign at  $\cos \theta_\pm = \sqrt{3}/3$ , i.e.,  $\theta_\pm \approx 54.74^\circ$ , in agreement

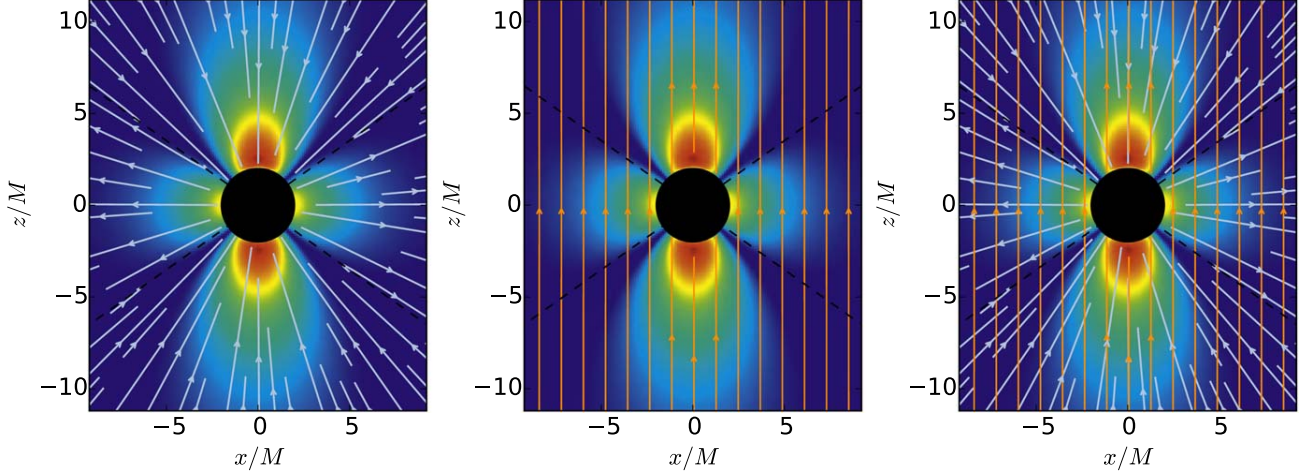


**Figure 3.** Electromagnetic field configuration for a *polar electronic jet*. Left panel: electric field lines (blue-colored lines) of the Papapetrou–Wald solution for a BH spin parameter  $a/M = 0.3$ , in the  $xz$  plane in Kerr–Schild coordinates. Center panel: magnetic field lines (gold-colored lines). Right panel: electric and magnetic field lines together. It can be directly checked from the slow-rotation expressions of the fields, Equation (10), that the electric field intensity decreases from the polar axis to the equator along a contour of constant radial distance. The magnetic field is asymptotically (at infinity) parallel to the BH spin. The colored background is a density plot of the electric field energy density, which decreases from red to blue. The BH horizon is represented by the black filled disk. Distances are in units of  $M$  and the fields in units of  $B_0$ . Electron acceleration (outward photon emission) occurs in the region where the electric field is inwardly directed. This region, limited by the dashed-black lines, is defined in the northern hemisphere by the spherical polar angles (measured clockwise from the rotation axis)  $-\theta_{\pm} < \theta < \theta_{\pm}$ , and by equatorial symmetry, in the southern hemisphere by  $\pi - \theta_{\pm} < \theta < \pi + \theta_{\pm}$ . At the angle  $\theta_{\pm}$ , the electric field reverses direction, i.e.,  $\mathbf{E} \cdot \mathbf{B} = 0$ . For the above parameters,  $\theta_{\pm} \approx 55^\circ$ . We have used the general transformation from Boyer–Lindquist to Kerr–Schild coordinates (A6); see Appendix A for details.

with the full numerical result. It can be checked that the magnetic field is asymptotically directed along the  $z$ -direction. Evaluating the Kerr–Schild components (see Appendix B), e.g., on the plane  $\phi = 0$ , we obtain

$$\begin{aligned} B_{\hat{x}} &= B_{\hat{r}} \sin \theta + B_{\hat{\theta}} \cos \theta \\ &= B_0 \sin \theta \cos \theta \left( 1 - \sqrt{1 - \frac{2M}{r}} \right), \end{aligned} \quad (11a)$$

$$B_{\hat{y}} = B_{\hat{\phi}} \frac{a}{r} \cos \theta = -B_0 \sin \theta \cos \theta \frac{a}{r} \sqrt{1 - \frac{2M}{r}}, \quad (11b)$$

$$\begin{aligned} B_{\hat{z}} &= B_{\hat{r}} \cos \theta - B_{\hat{\theta}} \sin \theta \\ &= B_0 \left( \cos^2 \theta + \sin^2 \theta \sqrt{1 - \frac{2M}{r}} \right). \end{aligned} \quad (11c)$$

It is then clear that for radial distances  $r \gg 2M$ , we have  $B_{\hat{x}} \rightarrow 0$ ,  $B_{\hat{y}} \rightarrow 0$ , and  $B_{\hat{z}} \rightarrow B_0$ . The dominance of the  $z$ -component actually occurs everywhere and for any value of the BH spin parameter  $a$ , as can be seen from Figure 3, which shows the electric and magnetic field lines without any approximation.

The electric field (Equation (7)) is induced by interaction of the magnetic field and the BH gravitomagnetic field. In fact, it is easy to check that it vanishes for  $a = 0$ . As we have seen in Figures 3 and 4, the electric field has a quadrupolar nature. Thus, although the BH has a zero net charge, we can think of this field as produced by a quadrupolar distribution of charges of surface density (Thorne et al. 1986)

$$\sigma = \frac{1}{4\pi} B_0 a r_+ (r_+ - M) \frac{r_+ \sin^4 \theta - M \cos^2 \theta (1 + \cos^2 \theta)}{(r_+^2 + a^2 \cos^2 \theta)}, \quad (12)$$

which in the slow-rotation approximation becomes

$$\sigma \approx \frac{B_0}{16\pi M} a (1 - 3 \cos^2 \theta). \quad (13)$$

From this expression it is clear that it equals  $E_{\hat{r}}/(4\pi)$ , where the electric field is given by Equation (10), as expected. From this expression, we have that the surface charge vanishes at  $\cos \theta_{\pm} = \sqrt{3}/3$ , which leads to  $\theta_{\pm} = 54^\circ.74$ , consistent with the value already obtained directly from the electric field expression and shown in Figures 3 and 4.

By introducing the dimensionless radius and the spin parameter in units of  $M$ , it can be seen that the surface charge  $\sigma$  does not depend explicitly on  $M$ , but only on  $B_0$  and  $a/M$ . Figure 5 shows the surface charge (Equation (12)) as a function of  $\theta$ , for a BH spin parameter  $a/M = 0.3$ , the same as used in Figure 3. This surface charge  $\sigma$  in fact agrees with the electric field lines in the upper row plots of Figure 3. In the first patch,  $\theta = [0, \theta_{\pm}]$  (the angle  $\theta$  is measured clockwise from the polar axis), the electric field lines are inwardly directed as expected from  $\sigma < 0$ ; the electric field lines in the region  $\theta = [\theta_{\pm}, \pi - \theta_{\pm}]$  point outward in agreement with  $\sigma > 0$ . A similar analysis for the other patches confirm the self-consistency of the scenario. The angle  $\theta_{\pm}$  is the one for which  $\sigma$  vanishes. For this numerical example,  $\theta_{\pm} \approx 54^\circ.95$ .

We can compute the charge induced on a surface patch of the horizon as

$$Q_{\text{patch}} = \iint \sigma \sqrt{|h_{ij}|} dx^i dx^j = \iint \sigma \sqrt{|h_{\theta\theta} h_{\phi\phi}|} d\theta d\phi, \quad (14)$$

where  $h_{ij}$  is the induced metric on the horizon,  $ds^2 = h_{ij} dx^i dx^j = h_{\theta\theta} d\theta^2 + h_{\phi\phi} d\phi^2$ , being  $h_{\theta\theta} = \Sigma_+ = r_+^2 + a^2 \cos^2 \theta$ , and  $h_{\phi\phi} = (2Mr_+)^2 \sin^2 \theta / \Sigma_+$ , obtained by taking constant slices  $t$  and  $r = r_+$  in the Kerr

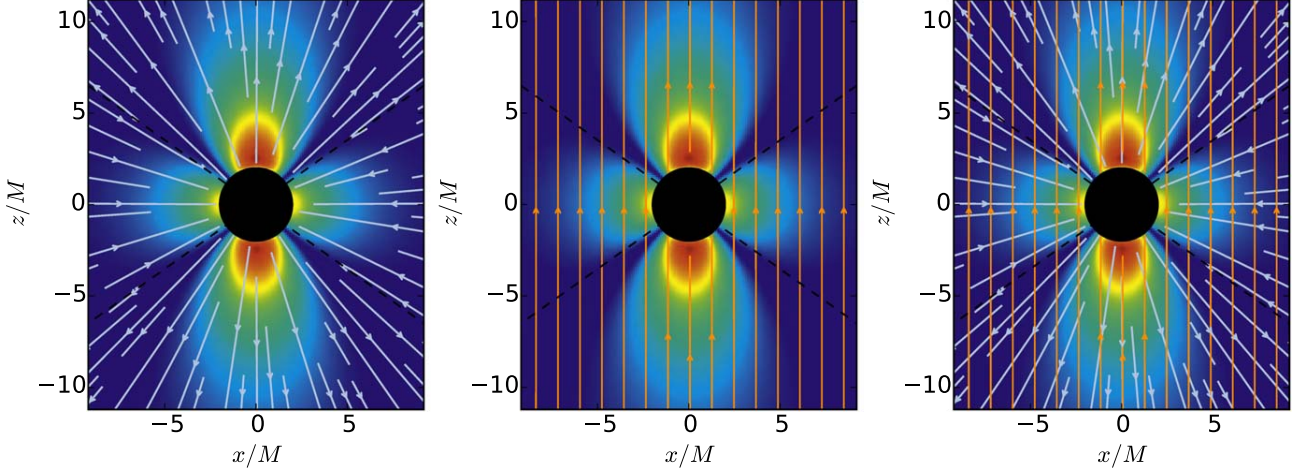


**Figure 4.** Electromagnetic field configuration for a *polar protonic jet*. Similar to Figure 3 but for a magnetic field asymptotically (at infinity) antiparallel to the BH spin. In this case, protons move outward where electrons do in Figure 3, namely, in the double cone of angle  $\theta_{\pm} \approx 55^\circ$  from the polar axis.

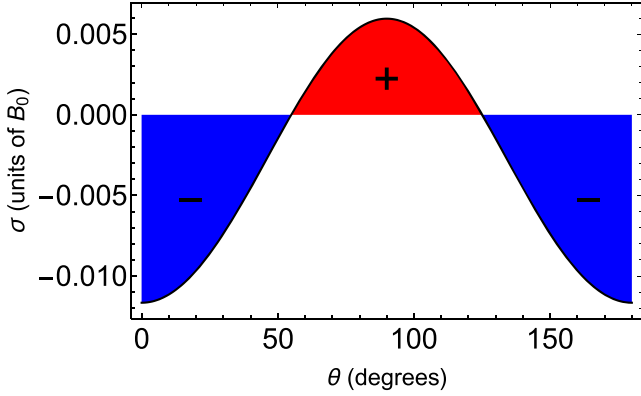


**Figure 5.** Surface charge (Equation (12)) in units of  $B_0$  as a function of the spherical polar angle  $\theta$ , and for a BH spin parameter  $a/M = 0.3$ . The blue and red colors indicate, respectively, the regions with negative and positive surface charge density.

metric (A3). Therefore, Equation (14) becomes

$$Q_{\text{patch}} = 4\pi Mr_{\pm} \int_{\Delta\theta} \sigma(\theta) \sin\theta d\theta, \quad (15)$$

where we have already performed the integral over  $\phi$  taking advantage of the axial symmetry and  $\Delta\theta$  denotes the angular region subtended by two spherical polar angles. The integral in Equation (15) from 0 to  $\pi$  vanishes, so the net charge of the BH is zero. In the example of Figure 5, the charge of the negatively charged patches is obtained by summing the integrals in the regions  $\theta = [0, \theta_{\pm}]$  and  $\theta = [\pi - \theta_{\pm}, \pi]$ , while the positively charged one is obtained from the integral in the region  $\theta = [\theta_{\pm}, \pi - \theta_{\pm}]$ . For the case of  $a/M = 0.3$ , we obtain

$$Q_{\pm} = \pm 0.1119 \times M^2 B_0, \quad (16)$$

and therefore,  $Q_- + Q_+ = 0$ , as expected.

We can obtain an analytic expression of the patch charge in the *slow-rotation* regime. By replacing  $\sigma$  given by Equation (13) into Equation (15), we obtain the charge on any patch,

$$Q_{\text{patch}} \approx \frac{1}{2} M^2 B_0 \frac{a}{M} \cos\theta (\cos^2\theta - 1) |_{\Delta\theta}. \quad (17)$$

We can now evaluate the total negative and positive charge as we proceeded before, which leads us to

$$Q_{\pm} = \pm \frac{2\sqrt{3}}{9} M^2 B_0 \frac{a}{M} = \pm \frac{2\sqrt{3}}{9} B_0 J, \quad (18)$$

where in the last equality we have used the BH angular momentum via the relation  $a = J/M$ . Turning to the previous numerical example, i.e.,  $a/M = 0.3$ , Equation (18) gives  $Q_{\pm} = \pm 0.1155 M^2 B_0$ , which is pretty close to the value given by Equation (16), validating once more the accuracy of the *slow-rotation* approximation.

#### 4. Equations of Motion

In the LNR frame, the particle equations of motion can be written as

$$\frac{Du^{\hat{a}}}{d\tau} = \frac{du^{\hat{a}}}{d\tau} + \omega^{\mu\hat{a}}_{\hat{c}\hat{b}} u^{\hat{b}} u^{\hat{c}} = \frac{q}{m} F^{\hat{a}}_{\hat{b}\hat{c}} u^{\hat{b}} - \mathcal{F}^{\hat{a}}, \quad (19)$$

where  $u^{\hat{a}}$  and  $F^{\hat{a}}_{\hat{b}\hat{c}}$  and  $\mathcal{F}^{\hat{a}}$  are, respectively, the components of the particle's four-velocity and the electromagnetic field tensor, projected onto the observer's tetrad, see Equations (B6) and (B5),  $\tau$  is the particle's proper time along its worldline, and  $\omega^{\mu\hat{a}}_{\hat{c}\hat{b}}$  are the *spin coefficients* given by Equation (B14). The last term on the right-hand side are the components of the radiation-reaction *force* (see, e.g., Landau & Lifshitz 1975) per unit mass, projected onto the LNR frame, i.e.,

$$\mathcal{F}^{\hat{a}} = \frac{2}{3} \left( \frac{q}{m} \right)^2 \frac{q^2}{m} (F^{\hat{a}}_{\hat{c}\hat{d}} F^{\hat{d}}_{\hat{e}} u^{\hat{c}} u^{\hat{e}}) u^{\hat{a}} + \frac{2}{3} \left( \frac{q}{m} \right)^2 \frac{q^2}{m} F^{\hat{a}}_{\hat{b}\hat{c}} F^{\hat{b}}_{\hat{d}\hat{e}} u^{\hat{c}} u^{\hat{e}} + \frac{2}{3} \left( \frac{q}{m} \right)^2 q \frac{DF^{\hat{a}}_{\hat{b}\hat{c}}}{dx^{\hat{c}}} u^{\hat{b}} u^{\hat{c}}, \quad (20)$$

where in the last term the covariant derivative of the electromagnetic tensor in the LNR frame can be computed via Equation (B12).

The radiation-reaction force (20) is largely dominated by the first term; hence,

$$\mathcal{F}^{\hat{a}} \approx \frac{2}{3} \left( \frac{q}{m} \right)^2 \frac{q^2}{m} (F^{\hat{a}}_{\hat{c}\hat{d}} F^{\hat{d}}_{\hat{e}} u^{\hat{c}} u^{\hat{e}}) u^{\hat{a}} = -\frac{\mathcal{P}}{m} v^{\hat{a}}, \quad (21)$$

where we have defined the radiated off power

$$\mathcal{P} \equiv \frac{2}{3} \left( \frac{q}{m} \right)^2 q^2 \hat{\gamma}^3 [(\mathbf{E} + \mathbf{v} \times \mathbf{B})^2 - (\mathbf{v} \cdot \mathbf{E})^2]. \quad (22)$$

We can work in the slow-rotation regime, which provides sufficient accuracy for our purpose. Within this approximation, Equation (19) becomes

$$\frac{d\hat{\gamma}}{d\tau} = -\frac{e}{m} E^{\hat{r}} v^{\hat{r}} \hat{\gamma} - \frac{\mathcal{P}}{m} + \left[ \frac{M}{r^2 \sqrt{1 - 2M/r}} - \frac{6Ma \sin \theta}{r^3} v^{\hat{\theta}} \right] \hat{\gamma} v^{\hat{r}}, \quad (23)$$

and

$$\begin{aligned} \frac{dv^{\hat{i}}}{d\tau} = & -\frac{e}{m} [(E^{\hat{r}} - v^{\hat{\phi}} B^{\hat{\theta}}) \delta_{\hat{r}}^{\hat{i}} + v^{\hat{\theta}} B^{\hat{r}} \delta_{\hat{\theta}}^{\hat{i}} + (v^{\hat{r}} B^{\hat{\theta}} - v^{\hat{\theta}} B^{\hat{r}}) \delta_{\hat{\phi}}^{\hat{i}} \\ & - E^{\hat{r}} v^{\hat{r}} v^{\hat{i}}] - \frac{\mathcal{P} v^{\hat{i}}}{m \hat{\gamma}} - \left( \frac{M r}{\sqrt{1 - 2M/r}} - 6Ma \sin \theta v^{\hat{\theta}} \right) \frac{\hat{\gamma} v^{\hat{r}} v^{\hat{i}}}{r^3} \\ & - \left[ 6Ma \sin \theta v^{\hat{\phi}} + \frac{M r (v^{\hat{\theta}})^2}{(1 - \frac{2M}{r})^{5/2}} + r^2 \sqrt{1 - \frac{2M}{r}} (v^{\hat{\phi}})^2 \right] \frac{\hat{\gamma} \delta}{r^3} \\ & + \left[ \frac{M}{(1 - 2M/r)^{5/2}} v^{\hat{r}} v^{\hat{\theta}} - \frac{r \cos \theta}{\sin \theta} (v^{\hat{\phi}})^2 \right] \frac{\hat{\gamma} \delta_{\hat{\theta}}^{\hat{i}}}{r^2} \\ & - \left[ 6Ma \sin \theta v^{\hat{r}} - r^2 \sqrt{1 - \frac{2M}{r}} v^{\hat{r}} v^{\hat{\phi}} - \frac{r^2 \cos \theta}{\sin \theta} v^{\hat{\theta}} v^{\hat{\phi}} \right] \frac{\hat{\gamma} \delta_{\hat{\phi}}^{\hat{i}}}{r^3}, \end{aligned} \quad (24)$$

where  $E^{\hat{r}}$ ,  $B^{\hat{r}}$ , and  $B^{\hat{\theta}}$  are given by their corresponding slow-regime expressions given by Equation (10).

It is worth assessing the relative importance of the purely gravitational terms in the dynamics of the particle. It is clear that the contribution of the square brackets on the right-hand side of Equation (23) is dominated by the first term inside them. Then, because of  $E^{\hat{r}} \propto 1/r^2$ , the order of magnitude of the ratio between the electric field term and the gravitational one is given by  $\omega_B a/M$ , where  $\omega_B \equiv eB_0/m$  is the so-called gyration angular frequency. Therefore, since the largest value of the spin parameter is  $a=M$ , the largest value that the electric to gravitational contributions ratio can attain is  $\omega_B$ , which becomes of the order of unity only for an extremely weak magnetic field of the order of microgauss. This implies that, for a magnetic field  $10^{11}$  G, the electric field term is  $10^{17}$  bigger than the gravitational one. Only in the limit  $r \rightarrow r_+$ , the gravitational attraction can play some role against such a huge electric force. Therefore, we expect the evolution of  $\gamma$  to be dictated only by the first term on the right-hand side of Equation (23). A similar analysis can be done for the evolution of the spatial velocity, which we therefore expect to be fully dominated by the terms in the first row of Equation (24).

#### 4.1. A Specific Numerical Solution

We turn now to show specific examples of numerical solutions to the equations of motion (23) and (24), for *inner engine* parameters:  $M = 4.4M_{\odot}$ ,  $a/M = 0.3$ ,  $B_0 = 10^{11}$  G (so  $\omega_B \approx 1.8 \times 10^{18}$  rad s $^{-1}$ ).

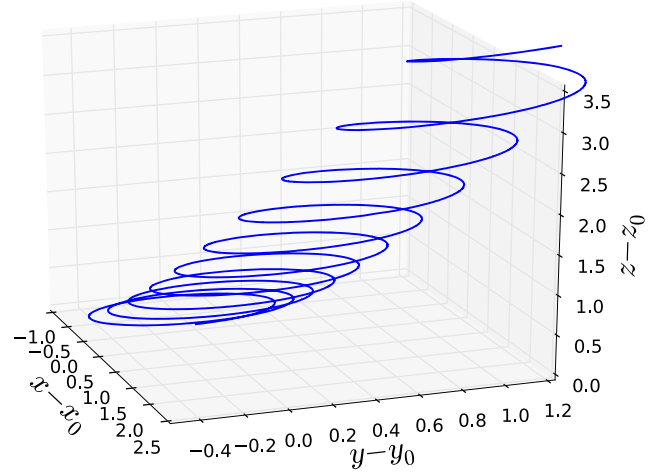


**Figure 6.** Example of numerical solution of the equations of motion in the slow-rotation regime, given by Equations (23) and (24). The figure shows the electron's trajectory in Kerr–Schild Cartesian coordinates, for which we have used the transformation from Boyer–Lindquist coordinates given by Equation (B15). The *inner engine* parameters in this case are  $M = 4.4M_{\odot}$ ,  $a/M = 0.3$ , and  $B_0 = 10^{11}$  G (so  $\omega_B \approx 1.8 \times 10^{18}$  rad s $^{-1}$ ). We have set as initial conditions the location  $r_0 = 2r_+ = 4M$ ,  $\theta(0) = 20^\circ$ ,  $\phi(0) = 0$ , and velocity components  $v^{\hat{r}}(0) = v^{\hat{\theta}}(0) = 0$ , and  $v^{\hat{\phi}}(0) = \sqrt{\hat{\gamma}_0^2 - 1}/\hat{\gamma}_0$ , with  $\hat{\gamma}_0 = 2$ . For the sake of illustration, the trajectory is shown here at times  $0 \leq \omega_B \tau \leq 65$ , in which the spiraling behavior is better appreciated. The displacements in the  $x$  and  $y$  directions are in units of  $10^{-13}M$  and, the one in the  $z$ -direction, in units of  $10^{-12}M$ .

Figure 6 shows an example of the trajectory of an electron initially located at  $r_0 = 2r_+ \approx 4M$ ,  $\theta(0) = 20^\circ$ ,  $\phi(0) = 0$ . The initial values of the electron's velocity components were, in this specific example, set to have a spiraling electron motion, that is setting up an initially dominating azimuthal velocity; in particular, we have chosen  $v^{\hat{r}}(0) = v^{\hat{\theta}}(0) = 0$  and  $v^{\hat{\phi}}(0) = \sqrt{\hat{\gamma}_0^2 - 1}/\hat{\gamma}_0$ , with  $\hat{\gamma}_0 = 2$ . The trajectory is shown at times  $\omega_B \tau \leq 65$ , when the spiraling behavior is better appreciated. At longer times, the electron follows closely the magnetic field lines, which are nearly  $z$ -directed (see Figure 3), so the  $z$ -component of the velocity becomes dominant (see also Figure 7).

In Figure 6, the position displacements in the  $x$  and  $y$  direction are in units of  $10^{-13}M$  and the one in the  $z$ -direction in units of  $10^{-12}M$ . Indeed, a dimensionless proper time  $\omega_B \tau = 65$  corresponds to  $\tau \approx 3.7 \times 10^{-17}$  s, so the observer measures a displacement  $\Delta z \sim \hat{\gamma} c \tau \approx 2.2 \times 10^{-6}$  cm  $\approx 4 \times 10^{-12}M$ , for the chosen BH mass. The displacements in the  $x$ - $y$  plane are  $\sim 1/\hat{\gamma}$  smaller since the particle's velocity is dominated by the  $z$ -component.

Figure 7 shows the evolution of the position and velocity components  $v^{\hat{i}}$  of an electron located at  $r(0) = 2r_+$ ,  $\theta(0) = 0^\circ 0001$  (upper row),  $\theta(0) = 20^\circ$  (lower row), and  $\phi(0) = 0$ . The electron has been set initially at rest, i.e.,  $v^{\hat{r}}(0) = v^{\hat{\theta}}(0) = v^{\hat{\phi}}(0) = 0$ , so  $\hat{\gamma}(0) = 1$ . This figure shows that, in general, the motion along the  $z$ -direction is dominant, and it is even more pronounced for small spherical polar angles (motion nearly attached to the BH rotation axis).

## 5. Photon Four-momentum Measured at Infinity

We refer the reader to Appendix B for the general equations between the four-momentum measured by the observer at rest at infinity, the LNR observer and the comoving observer. We

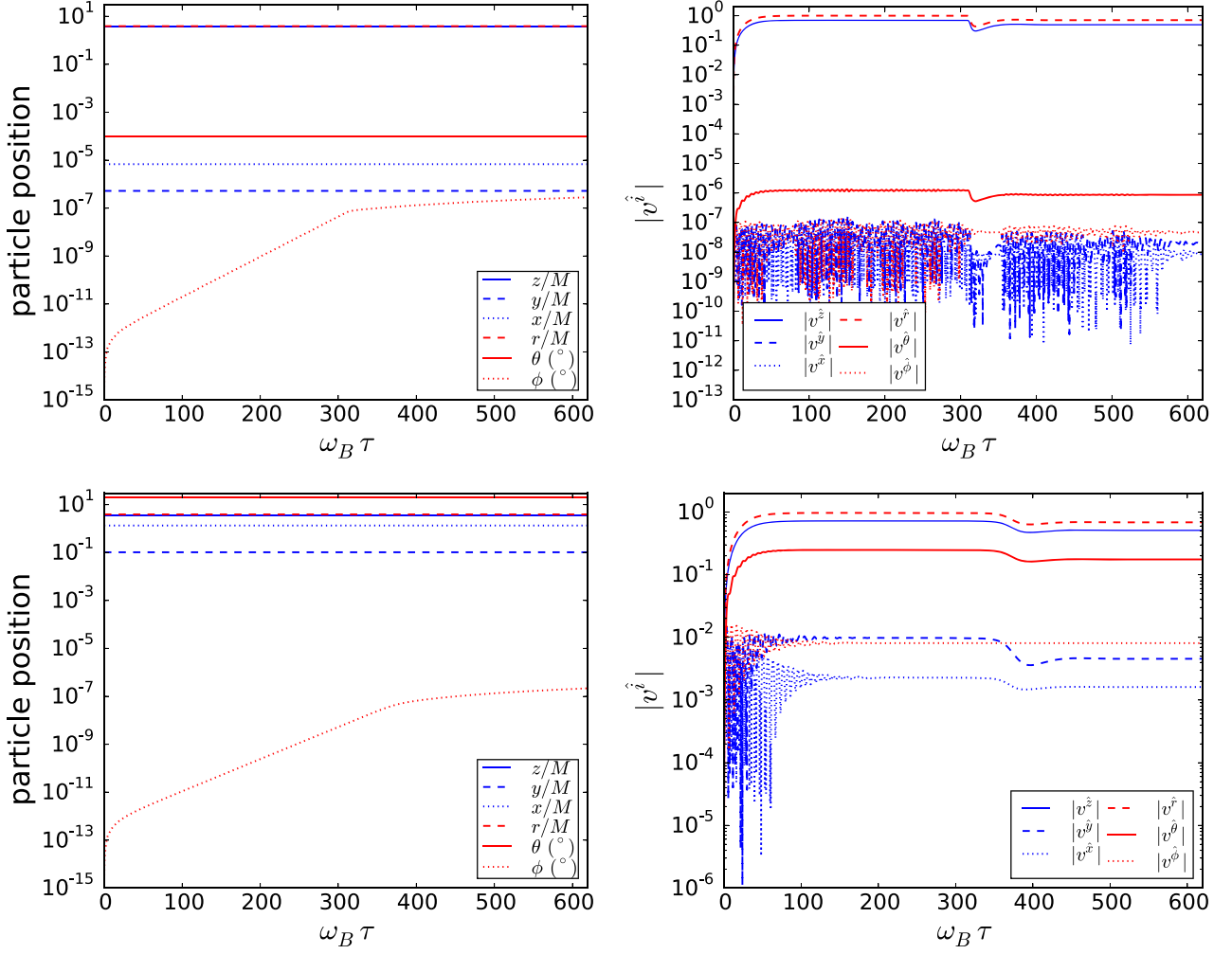


**Figure 7.** Electron’s position (coordinate frame) and velocity (LNR frame), as a function of dimensionless proper time,  $\omega_B \tau$ . The electron is initially located at Boyer–Lindquist coordinates  $r(0) = 2r_+$ ,  $\theta(0) = 0.0001$  (upper row),  $\theta(0) = 20^\circ$  (lower row), and  $\phi(0) = 0$ . The electron is initially at rest, i.e.,  $v^{\hat{r}}(0) = v^{\hat{\theta}}(0) = v^{\hat{\phi}}(0) = 0$ , i.e.,  $\hat{\gamma}(0) = 1$ . The particle position and the velocity components are shown in both Boyer–Lindquist and (Kerr–Schild) coordinates. The *inner engine* parameters are the same as in Figure 6. Notice that in Figure 6 we represent displacements, namely, the relative particle position with respect to the initial position, while here we represent the actual position of the particle, namely, the position with respect to the coordinates origin. In addition, in Figure 6 the displacement in the  $x$  and  $y$  directions is in units of  $10^{-13}M$  and the one in the  $z$ -direction is in units  $10^{-12}M$ , while in this figure the  $x$ ,  $y$ , and  $z$  position are in units of  $M$ .

can gain some (analytical) insight into the features of the photon emission by assuming  $v^{\hat{r}} \approx 1$ ,  $v^{\hat{\theta}} \approx 0$  and  $v^{\hat{\phi}} \approx 0$ . In this one-dimensional approximation of motion, Equation (C6) reduces to

$$k^0 = k^{(0)} \hat{\gamma} e^{-\nu} [1 + v^{\hat{r}} n^{(1)}], \quad n^r = e^{\nu - \mu_1} \frac{v^{\hat{r}} + n^{(1)}}{1 + v^{\hat{r}} n^{(1)}}, \quad (25a)$$

$$n^\theta = \frac{e^{\nu - \mu_2} n^{(2)}}{\hat{\gamma} [1 + v^{\hat{r}} n^{(1)}]}, \quad n^\phi = \omega + \frac{e^{\nu - \Psi} n^{(3)}}{\hat{\gamma} [1 + v^{\hat{r}} n^{(1)}]}, \quad (25b)$$

which in the slow-rotation regime can be written as

$$k^0 = \frac{k^{(0)}}{\sqrt{1 - 2M/r}} \hat{\gamma} (1 + \hat{\beta} \cos \Theta), \quad (26a)$$

$$n^r = \left(1 - \frac{2M}{r}\right) \frac{\cos \Theta + \hat{\beta}}{1 + \hat{\beta} \cos \Theta}, \quad (26b)$$

$$r n^\theta = \sqrt{1 - \frac{2M}{r}} \left( \frac{\sin \Theta \cos \Phi}{1 + \hat{\beta} \cos \Theta} \right) \frac{1}{\hat{\gamma}}, \quad (26c)$$

$$r \sin \theta n^\phi = \frac{2Ma \sin \theta}{r^2} + \sqrt{1 - \frac{2M}{r}} \left( \frac{\sin \Theta \sin \Phi}{1 + \hat{\beta} \cos \Theta} \right) \frac{1}{\hat{\gamma}}, \quad (26d)$$

where we have introduced the notation  $\hat{\beta} = v^{\hat{r}}$ . We have also parameterized the spatial components of the photon four-

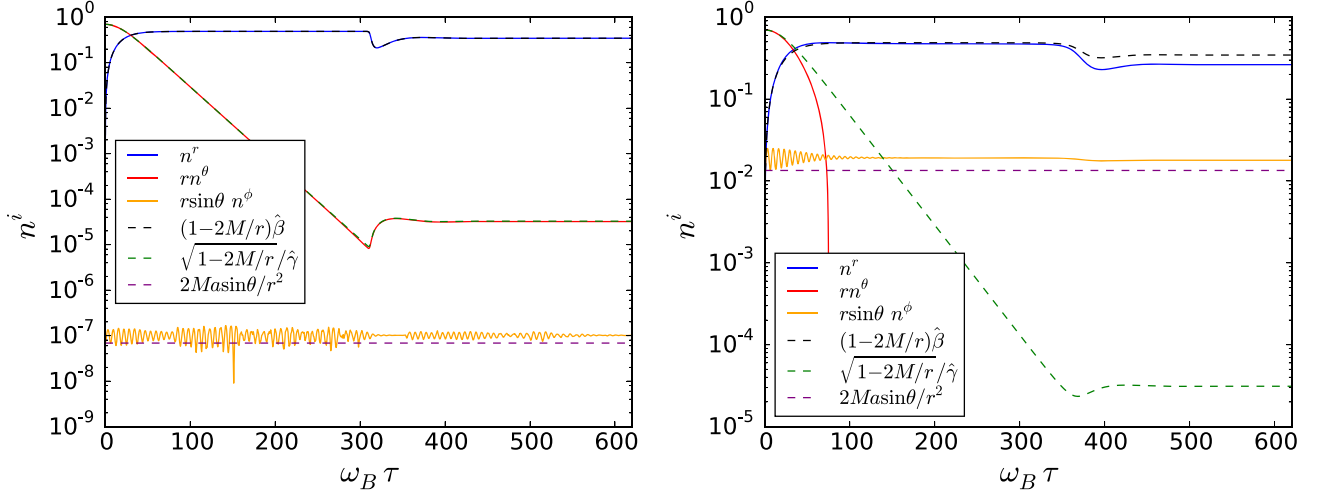


**Figure 8.** Spatial components of the photon four-momentum measured by an observer at rest at infinity. The emitter (electron) is initially located at Boyer–Lindquist coordinates  $r(0) = 2r_+$ ,  $\theta(0) = 0.0001$  (left) and  $\theta(0) = 20^\circ$  (right), and  $\phi(0) = 0$ . The comoving frame emission angles have been set to  $\Phi = 0$  and  $\Theta = \pi/2$ . The solid curves are obtained from the full expressions given by Equation (C6), while the dashed curves are the corresponding components of the four-momentum given by the approximate expressions given by Equation (25); see also Table 1. The approximate expressions remain accurate for the entire evolution only for an emitter moving along the BH rotation axis, or for small departures of the spherical polar angle. The azimuth component of the four-momentum remains nearly constant and is a purely general relativistic effect of dragging of inertial frames.

**Table 1**

Photon Four-momentum Components Calculated with Equation (26), for Specific Angles of Emission,  $\Theta$  and  $\Phi$ , as Measured by the Comoving Observer

	$\Phi = 0$ : plane $e_{(z)}-e_{(x)}$			$\Phi = \pi/2$ : plane $e_{(z)}-e_{(y)}$		
	$\Theta = 0$	$\Theta = \pi/2$	$\Theta = \pi$	$\Theta = 0$	$\Theta = \pi/2$	$\Theta = \pi$
$k^0$	$\frac{k^{(0)}}{\sqrt{1-2M/r}} \sqrt{\frac{1+\hat{\beta}}{1-\hat{\beta}}}$	$k^{(0)}\gamma$	$\frac{k^{(0)}}{\sqrt{1-2M/r}} \sqrt{\frac{1-\hat{\beta}}{1+\hat{\beta}}}$	$\frac{k^{(0)}}{\sqrt{1-2M/r}} \sqrt{\frac{1+\hat{\beta}}{1-\hat{\beta}}}$	$k^{(0)}\gamma$	$\frac{k^{(0)}}{\sqrt{1-2M/r}} \sqrt{\frac{1-\hat{\beta}}{1+\hat{\beta}}}$
$n^r$	$1 - 2M/r$	$(1 - 2M/r)\hat{\beta}$	$-(1 - 2M/r)$	$1 - 2M/r$	$(1 - 2M/r)\hat{\beta}$	$-(1 - 2M/r)$
$n^\theta$	0	$(1/\gamma)(1/r)$	0	0	0	0
$n^\phi$	$2Ma/r^3$	$2Ma/r^3$	$2Ma/r^3$	$2Ma/r^3$	$2Ma/r^3 + (1/\gamma)(1/r \sin \theta)$	$2Ma/r^3$

**Note.** We have used the relation between the Lorentz factor  $\hat{\gamma}$  and  $\gamma$  given by Equation (C7).

momentum in the orthonormal comoving frame as

$$n^{(1)} = \cos \Theta, \quad n^{(2)} = \sin \Theta \cos \Phi, \quad n^{(3)} = \sin \Theta \sin \Phi, \quad (27)$$

where  $\Theta$  and  $\Phi$  are spherical polar and azimuth angles measured by this local observer. This choice satisfies  $n^{(i)}n_{(i)} = 1$ , which derives from  $k^{(a)}k_{(a)} = 0$ .

Thus, by assigning values to these angles in their corresponding range, i.e.,  $\Theta \in [0, \pi]$  and  $\Phi \in [0, 2\pi]$ , we can compute from Equation (26) the corresponding normalized components of the photon four-momentum in the coordinate frame. Figure 8 compares and contrasts the photon four-momentum components calculated with the general Equation (C6) with the ones obtained from the approximate Equation (26). In this example, the photons are emitted from the two positions  $(r, \theta)$  of Figure 7, and make angles  $\Phi = 0$  and  $\Theta = \pi/2$  as measured by the comoving observer.

Table 1 shows the photon four-momentum components as measured by the observer at rest at infinity, i.e.,  $k^\mu$ , for photons emitted in the plane  $\Phi = 0$  of the comoving observer (i.e.,  $e_{(z)}-e_{(x)}$ ), and in the plane  $\Phi = \pi/2$  (i.e.,  $e_{(z)}-e_{(y)}$ ), in the directions  $\Theta = 0, \pi/2$ , and  $\pi$ .

It can be seen from the above equations (see also their summary in Table 1) that

1. There is a purely general relativistic effect: the azimuthal photon four-momentum component,  $n^\phi$ , has a contribution from the angular velocity  $\omega$  associated with the *frame-dragging* effect. This contribution vanishes only for photons emitted by electrons accelerated along the BH rotation axis ( $\theta = 0$ ). For off-axis motion, it does not vanish and it can be even larger than the polar component,  $n^\theta$  (see Table 1 and Figure 8).
2. The above implies that *relativistic aberration* by which photons are measured at infinity as confined within an angle  $1/\gamma$  around the direction of motion of the emitter (see, e.g., Landau & Lifshitz 1975), strictly holds only along the BH rotation axis. However, the radial component of the four-momentum is still dominant and the traditional relativistic aberration can be assumed for practical purposes.

## 6. Radiation Power and Spectrum

The above result allows us to estimate the radiation by acceleration using known results from special relativity. Most of the synchrotron power is radiated around the peak of the spectrum, which occurs near the characteristic angular

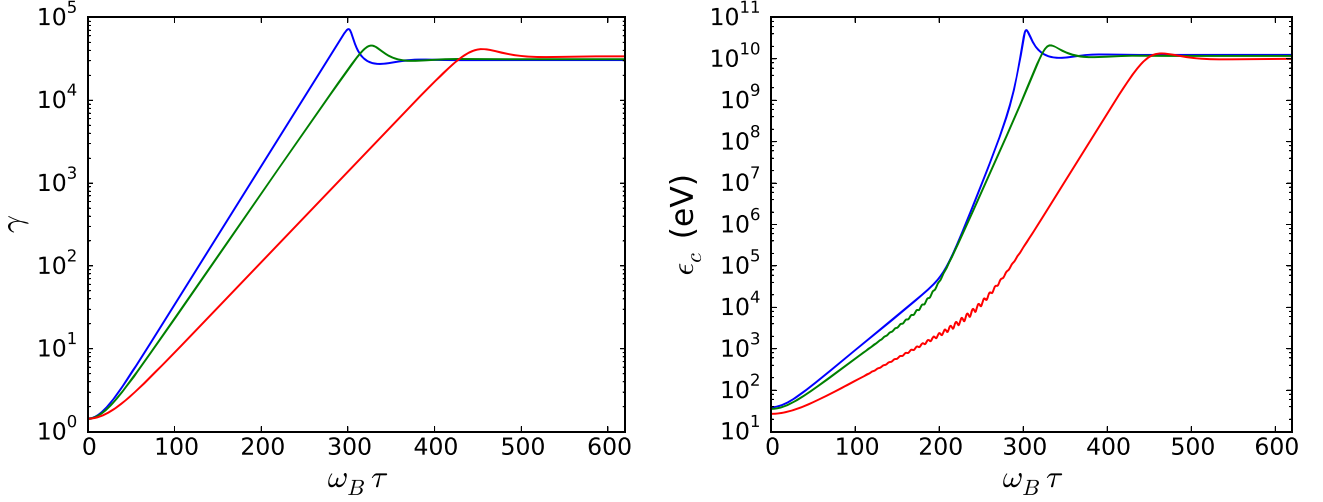


**Figure 9.** Electron Lorentz factor  $\gamma$ , given by Equation (C7), and photon critical energy  $\epsilon_c$ , given by Equation (28), as a function of the emitter (electron) proper time,  $\omega_B \tau$ . In this example, the electron starts its motion at rest at the position  $r(0) = 2r_+$ ,  $\phi(0) = 0$ , and  $\theta(0) = 1^\circ$  (blue),  $14^\circ$  (green), and  $27^\circ$  (red).

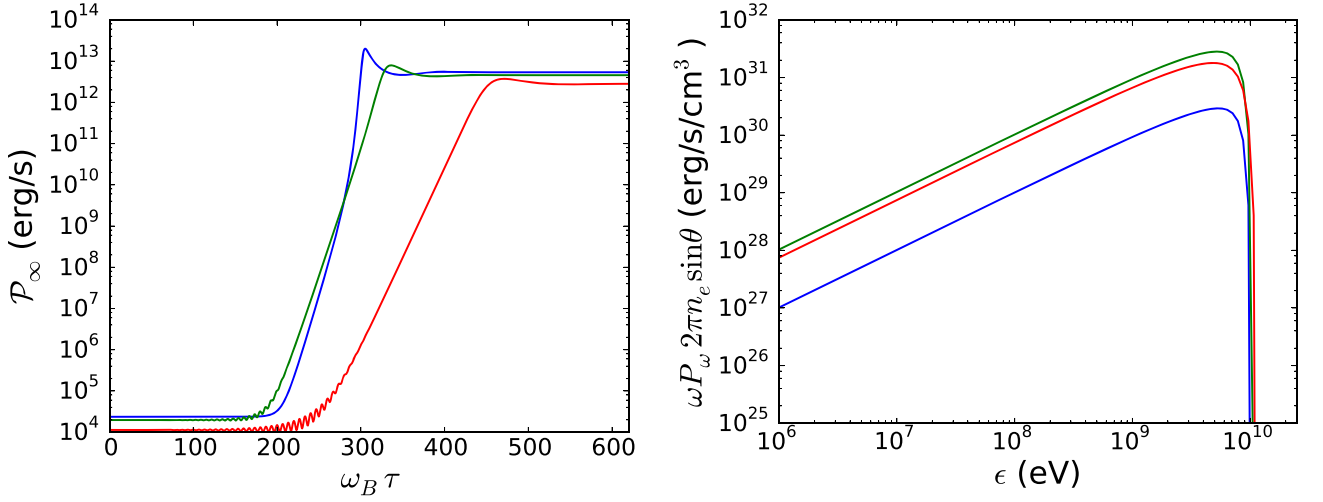


**Figure 10.** Left panel: power radiated off to infinity as a function of the dimensionless proper time. Right panel: energy distribution of the synchrotron power per unit volume,  $\omega P_\omega n_e \sin \theta$ , where  $n_e$  is given by Equation (31). This gives an estimate of the energy radiated to infinity per unit time, per unit volume. In this example, the electron starts its motion at rest at three different selected positions  $(r, \theta, \phi)$ :  $r(0) = 2r_+$ ,  $\phi(0) = 0$ , and  $\theta(0) = 1^\circ$  (blue),  $14^\circ$  (green), and  $27^\circ$  (red).

frequency (Landau & Lifshitz 1975)

$$\omega_c = \frac{c}{\rho} \gamma^3, \quad (28)$$

where  $\rho$  is the relativistic curvature radius

$$\rho = \frac{mc^2 \gamma}{|q|} [(E + \mathbf{v} \times \mathbf{B})^2 - (\mathbf{v} \cdot \mathbf{E})^2]^{-1/2}. \quad (29)$$

The left panel of Figure 9 shows the electron Lorentz factor as a function of the dimensionless proper time, and the right panel the characteristic photon energy,  $\epsilon_c = \hbar \omega_c$ . We show the results for three different initial conditions: the electron starts its motion at rest at  $[r(0), \theta(0), \phi(0)]$ , where  $r(0) = 2r_+$ ,  $\phi(0) = 0$ , and  $\theta(0) = 1^\circ$  (blue curves),  $\theta(0) = 14^\circ$  (green curves), and  $\theta(0) = 27^\circ$ .

The electron reaches an asymptotic value when acceleration and radiation losses balance each other. At small values of the spherical polar angle, the electron experiences less radiation losses reaching a higher Lorentz factor and higher photon energy. Furthermore, the photon characteristic energy falls in

the gigaelectronvolt regime at the asymptotic Lorentz factor. Therefore, most of the radiation is emitted at gigaelectronvolt energies.

We now turn to the energy distribution of the radiation. The synchrotron power radiated by an electron, per unit angular frequency  $\omega$ , and integrated over the solid angle is (see, e.g., Landau & Lifshitz 1975)

$$P_\omega = \frac{\sqrt{3}}{2\pi} \frac{e^2}{\rho} \gamma F_\omega(x), \quad F_\omega(x) \equiv x \int_x^\infty K_{5/3}(y) dy, \quad (30)$$

where  $x \equiv \omega/\omega_c$ , and  $K_{5/3}$  is the modified Bessel function of the second kind.

We plot in Figure 10 the (bolometric) power radiated off to infinity (left panel),  $\mathcal{P}_\infty$ , as a function of dimensionless proper time. The obtained power per electrons shows that to emit, for instance, a luminosity of  $L = 10^{51} \text{ erg s}^{-1}$ , we must accelerate about  $N_e \sim L/\mathcal{P}_\infty \sim 10^{38}$  electrons. Since the acceleration occurs in the proximity of the BH horizon, these electrons occupy a volume  $\mathcal{V}_e \sim 4\pi r_+^3/3 \sim 10^{19} \text{ cm}^3$ , implying a number density  $n_e \sim N_e/\mathcal{V}_e \sim 10^{38}/10^{19} = 10^{19} \text{ cm}^{-3}$ . In fact, for the



LNR observer the *inner engine* can accelerate the following number of electrons per unit volume

$$n_e = \frac{E^2}{8\pi \hat{\gamma} m_e c^2}, \quad (31)$$

where  $E$  is given by Equation (7). The electric field near the horizon is  $E \approx \alpha B_0/2$ , where  $\alpha = a/M$ , so Equation (31) gives  $n_e \approx 3(\alpha B_0)^2/(32\pi \hat{\gamma} m_e c^2)$ . For the present quantitative example, so using  $\hat{\gamma} \approx 10^4$  (see Figure 9), Equation (31) gives  $n_e \approx 10^{19} \text{ cm}^{-3}$ , as expected from our previous estimate. The number of electrons around the Kerr BH can be either lower and higher than this value, but the *inner engine* can accelerate at most the above number of electrons. The density in the *cavity* created around the Kerr BH formed from the gravitational collapse of the NS in a BdHN is of the same order as the above value (see Becerra et al. 2019; Ruffini et al. 2019a, for numerical simulations). This implies that the *inner engine* in BdHNe works efficiently using its full energy reservoir.

The right panel of Figure 10 shows the spectrum density, i.e., the radiated power per unit volume,  $\omega P_\omega 2\pi n_e \sin \theta$ , as a function of the photon energy (calculated as  $\epsilon = \hbar\omega$ ). Here,  $n_e$  is given by Equation (31). This plot confirms that most of the energy is emitted in the giga-electronvolt domain, and the above-mentioned value of the electron density of particles that can be accelerated; in fact,  $\mathcal{P}_\infty \times n_e \sim 10^{13} \times 10^{18} = 10^{31} \text{ erg s}^{-1} \text{ cm}^{-3}$ .

Summarizing, the gravitomagnetic interaction of the Kerr BH with the surrounding magnetic field efficiently accelerate electrons from the ionized environment in the BH vicinity. This acceleration and radiation process emits photons in the giga-electronvolt regime for magnetic fields in the  $10^{10}$ – $10^{11}$  G and stellar-mass Kerr BHs. The emission originates in proximity of the BH horizon and within  $60^\circ$  from the BH rotation axis with equatorial symmetry, hence generating a double-cone *jetted* high-energy ( $\gtrsim \text{GeV}$ ) emission.

## 7. The BH Energy Extraction

It is clear that the energy radiated off to infinity must necessarily come from the BH extractable energy

$$E_{\text{extr}} \equiv (M - M_{\text{irr}})c^2, \quad (32)$$

where the total mass  $M$  is given by the BH mass-energy formula (Christodoulou 1970; Christodoulou & Ruffini 1971; Hawking 1971)

$$M^2 = \frac{c^2 J^2}{4G^2 M_{\text{irr}}^2} + M_{\text{irr}}^2, \quad (33)$$

where  $J$ ,  $M$ , are respectively the angular momentum and the mass of the BH.

In order to understand better how the BH rotational energy is extracted, it is useful to recall the *inner engine* operation:

1. The magnetic field and the BH rotation induce an electric field as given by the Papapetrou–Wald solution (see Section 2). For aligned and parallel magnetic field to the BH spin, the electric field is nearly radial and inwardly around the BH rotation axis within an angle  $\theta_\pm \approx 60^\circ$  (see Figure 3).
2. The induced electric field accelerates electrons outwardly. The number of electrons that can be accelerated is set by

the energy of the electric field

$$\mathcal{E} \approx \frac{1}{2} E_{\hat{r}}^2 r_+^3 \approx \frac{G B_0^2 J^2}{c^4 M}, \quad (34)$$

where we have used Equation (10).

3. The maximum possible electron acceleration/energy is set by the electric potential energy difference from the horizon to infinity

$$\Delta\Phi = \frac{1}{c} e a B_0. \quad (35)$$

4. Along the polar axis, radiation losses by acceleration are absent because the electric and magnetic fields are parallel. Therefore, electrons accelerated on the BH rotation axis can gain the full potential energy difference (Equation (35)).
5. At off-axis latitudes, the accelerated electrons emit synchrotron radiation. In order to explain the observed luminosity,  $L_{\text{GeV}}$ , the radiation timescale,  $t_{\text{rad}}$ , must fulfill

$$L_{\text{GeV}} = \frac{dE_{\text{GeV}}}{dt} \leq \frac{dE_{\text{extr}}}{dt} \approx \frac{\mathcal{E}}{t_{\text{rad}}}, \quad (36)$$

where  $\mathcal{E}$  is given by Equation (34), and we assume most of this energy is radiated off in high-energy photons, as we have shown in Section 6. We take here into account that the energy reservoir is the rotational energy of the BH; therefore, the extractable energy must satisfy

$$E_{\text{extr}} \geq E_{\text{GeV}}, \quad (37)$$

where  $E_{\text{extr}}$  is given by Equation (32) and  $E_{\text{GeV}}$  is the energy observed at high energies, i.e.,

$$E_{\text{GeV}} = \int L_{\text{GeV}} dt. \quad (38)$$

6. Once the energy  $\mathcal{E}$  has been emitted, the BH is left with new values of mass and angular momentum, which have been reduced by amounts  $dM$  and  $dJ$ , respectively. The change in the BH mass is

$$c^2 dM = dE_{\text{extr}} \approx dE_{\text{GeV}} \approx \mathcal{E}. \quad (39)$$

According to the BH mass-energy formula (33), if in the energy extraction process the irreducible mass is kept constant, the change in the BH angular momentum is

$$dJ = \frac{c^2 dM}{\Omega_+}. \quad (40)$$

7. The above steps are repeated, with the same efficiency, if the density of plasma is sufficient, namely, if the number of the particles is enough to cover the new electric energy. Therefore, the *inner engine* evolves in a sequence of *elementary processes*, each emitting a well-defined, precise amount of BH rotational energy.

Therefore, the total fractional changes of mass and angular momentum in the whole emission process are

$$\frac{\Delta M}{M} = 1 - \frac{M_{\text{irr}}}{M}, \quad (41)$$

$$\frac{\Delta J}{J} = \left(1 + \frac{M_{\text{irr}}}{M}\right)^{-1}, \quad (42)$$

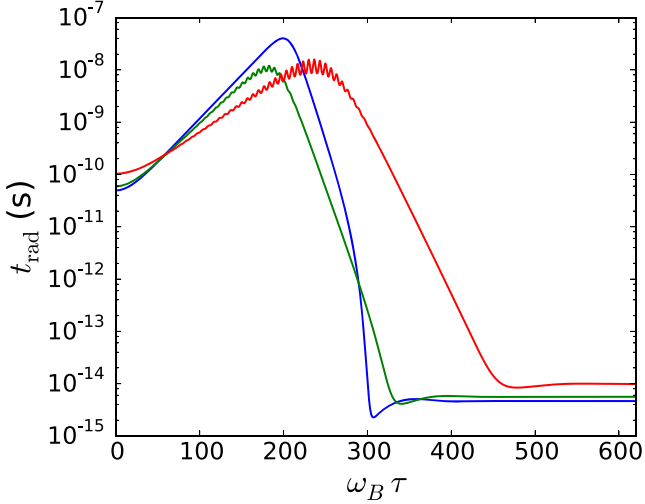


**Figure 11.** Radiation timescale  $t_{\text{rad}}$  given by Equation (44), as a function of the dimensionless proper time  $\omega_B \tau$ . It can be seen how  $t_{\text{rad}}$  becomes as short as  $10^{-14}$  s when the electrons reach the peak radiation power at  $\omega_B \tau \sim 300$  (see Figure 9).

where we have used Equations (33), (39), and (40), and the relation between the BH irreducible mass and the horizon:

$$r_+ = \frac{G}{c^2} \frac{2M_{\text{irr}}^2}{M}. \quad (43)$$

As a quantitative example, let us use our present fiducial parameters  $B_0 = 10^{11}$  G,  $M = 4.4M_\odot$ , and  $\alpha = 0.3$ . In this case, the electric energy is  $\mathcal{E} \approx 2.04 \times 10^{37}$  erg. The radiated luminosity is set by the timescale at which  $\mathcal{E}$  is radiated off. Figures 9 and 10 show that electrons reach a Lorentz factor  $\gamma \approx 3 \times 10^4$ , so an energy of nearly  $\epsilon_e = \gamma m_e c^2 \approx 10^{11}$  eV  $\approx 10^{-1}$  erg, which is then radiated off at a rate  $\mathcal{P}_\infty \approx 10^{13}$  erg s $^{-1}$ , leading to a radiation timescale

$$t_{\text{rad}} = -\frac{p_\mu \eta^\mu}{\mathcal{P}_\infty}, \quad (44)$$

of the order of  $\approx 10^{-14}$  s. We recall that  $p_\mu$  is the four-momentum of the particle measure by an observer at rest at infinity and  $\eta^\mu$  is the time-like Killing vector. This estimate of the timescale is confirmed by Figure 11, which shows the time evolution of  $t_{\text{rad}}$ . This radiation timescale implies that the system radiates off with a power  $\mathcal{E}/t_{\text{rad}} \approx 10^{51}$  erg s $^{-1}$ . This energy is mainly radiated at photon of energies  $\epsilon_c$  of the order of giga-electronvolt (see right panels of Figures 9 and 10).

For these parameters, in each elementary emission, the BH mass and angular momentum experience fractional changes  $dM/M \approx 2.59 \times 10^{-18}$  and  $dJ/J \approx 1.12 \times 10^{-16}$ , respectively. The BH irreducible mass can be readily obtained from Equation (43), i.e.,  $M_{\text{irr}} \approx 4.35 M_\odot$ . Therefore, the total extractable energy is  $E_{\text{extr}} = \Delta M c^2 \approx 0.012 M c^2 \approx 9.12 \times 10^{52}$  erg. If  $E_{\text{extr}}$  is emitted, the total fractional changes in the BH mass and angular momentum will be, respectively,  $\Delta M/M \approx 0.012$  and  $\Delta J/J \approx 0.50$ .

## 8. Discussion and Conclusions

Summarizing, all BdHN I are powered by three independent sources of energy:

1. The BdHN I is triggered by the  $\nu$ NS rise produced in the core collapse of the CO star generating a  $\nu$ NS at its center. The  $\nu$ NS rotational energy powers the synchrotron emission from the expanding SN that originates the X-ray afterglow (see Rueda et al. 2020, and references therein).
2. The hypercritical accretion of the SN material onto the binary companion NS leads to the formation of the BH when it reaches the critical mass for gravitational collapse (see, e.g., Becerra et al. 2016, 2019). This *smooth* accretion leading to BH formation does not emit any detectable signal of gravitational waves and is alternative to the direct gravitational collapse of a massive star (*collapsar*).
3. The gravitomagnetic interaction of the Kerr BH with the surrounding magnetic field, in presence of ionized matter of the SN ejecta, leads to the process of extraction of the BH rotational energy, generating the *jetted* high-energy ( $\gtrsim$  GeV) emission. We have here shown that this radiation is emitted in the vicinity of the BH horizon within  $60^\circ$  from the BH rotation axis (see Sections 2 and 6).

We have focused in this article on the *inner engine* of the high-energy emission, which as we have shown drives a new paradigm in the theory of GRBs:

1. *There is no need for bulk motion.* The traditional GRB model uses the gravitational pull to accelerate matter in bulk up to very large distances  $\sim 10^{16}$ – $10^{18}$  cm, where the ultra-relativistic blastwave becomes transparent to high-energy photons. The *inner engine*, instead, radiates at horizon scales the kinetic energy rapidly gained by single-particle acceleration (Sections 3–6). As shown in Moradi et al. (2021a) and Ruffini et al. (2019b), the radiated high-energy photons are transparent to magnetic pair production, likely the most important opacity source of this system.
2. *There is no need for massive accretion.* The density of ionized matter needed for the *inner engine* to explain the giga-electronvolt emission of a long GRB is much lower than the corresponding one requested by traditional matter accretion. For example, an accretion disk produces a luminosity  $L_{\text{disk}} = \eta \dot{M} c^2$ , where  $\eta$  is a parameter accounting for the efficiency in converting gravitational energy into radiation. Adopting a fiducial value  $\eta = 0.1$ , in order to get a luminosity of  $10^{50}$  erg s $^{-1}$ , the BH must accrete matter at a rate  $\dot{M} = 10^{-3} M_\odot$  s $^{-1}$ . This implies a consumption of protons by the BH at a rate of  $\dot{N}_p \sim \dot{M}/m_p \sim 10^{31}$  s $^{-1}$ , or a proton number density rate  $\dot{n}_p = \dot{N}_p/(4\pi r_+^3/3) \sim 10^{33}$  cm $^{-3}$  s $^{-1}$ . Clearly, smaller values of  $\eta$  require larger accretion rates. The *inner engine*, instead, produces the same luminosity by accelerating electrons with a rate  $\dot{N}_e \sim N_e/\tau_{\text{rad}} = \mathcal{E}/(\Delta\Phi \tau_{\text{rad}}) \sim 10^{47}$  s $^{-1}$ , i.e.,  $\dot{M} \sim m_p \dot{N}_e \sim 10^{-7} M_\odot$  s $^{-1}$  (for fully ionized matter), or an electron density of  $\dot{n}_e \sim 10^{29}$  cm $^{-3}$  s $^{-1}$ ; see discussion of Equation (31) in Section 6 for further details. This implies that the geodesic equations of motion of massive particles around a Kerr BH, traditionally applied to the problem of gravitational matter accretion, are superseded by the equation of motion of charged particles, accounting for the radiation reaction, accelerated in the electromagnetic field of the Papapetrou–Wald solution (see Sections 4–6).

3. *The BH is responsible only for the high-energy radiation.* During the acceleration region, the electrons radiate mainly at high energies, e.g.,  $\gtrsim 0.1$  GeV (see Section 6). The fundamental role of the reversible transformations holds. Indeed, the energy budget is paid by the BH extractable energy (Rueda & Ruffini 2020), and the irreducible mass  $M_{\text{irr}}$  of the BH mediates the energy extraction process (see Section 7).

On the occasion of this 50th anniversary of the publication of *Introducing the Black Hole*, we would like to thank all the people who have contributed during these 50 years to finally identifying the energy extraction process of a Kerr BH. We are most grateful to Prof. Robert Jantzen for insightful discussions on the general relativistic framework presented in this article. We thank Dr. Li Liang for the preparation of the upper left, upper right, and lower right panels of Figure 2.

## Appendix A The Kerr Metric

### A.1. The Original Kerr Metric and the Boyer–Lindquist Coordinates Form

The Kerr spacetime metric, which is stationary and axially symmetric, describes the exterior field of a rotating BH. In Eddington–Finkelstein-like coordinates  $(u, r, \theta, \phi)$ , it reads as

$$\begin{aligned} ds^2 = & -\left(1 - \frac{2Mr}{\Sigma}\right) du^2 \\ & + 2du dr + \Sigma d\theta^2 + \frac{A}{\Sigma} \sin^2 \theta d\phi^2 \\ & - 2a \sin^2 \theta dr d\phi - \frac{4a M r \sin^2 \theta}{\Sigma} du d\phi, \end{aligned} \quad (\text{A1})$$

where  $\Sigma = r^2 + a^2 \cos^2 \theta$ ,  $\Delta = r^2 - 2Mr + a^2$ , and  $A = (r^2 + a^2)^2 - \Delta a^2 \sin^2 \theta$ , with  $M$  and  $a = J/M$ , respectively, the BH mass and angular momentum per unit mass. This form of the Kerr metric differs from the original one presented by Kerr (1963), in the signs of the  $u$  coordinate and of the BH spin parameter  $a$  (see Kerr 2007 in Wiltshire et al. 2009, for details).

The current most used form of the Kerr metric uses the *spheroidal* Boyer–Lindquist coordinates (Boyer & Lindquist 1967), which is obtained via the coordinate transformation (Carter 1968; Kerr 2007)

$$du \rightarrow dt + \frac{r^2 + a^2}{\Delta} dr, \quad d\phi \rightarrow d\phi + \frac{a}{\Delta} dr, \quad (\text{A2})$$

while  $r$  and  $\theta$  hold the same. In these coordinates, the Kerr metric reads (Carter 1968; Kerr 2007) as

$$\begin{aligned} ds^2 = & -\left(1 - \frac{2Mr}{\Sigma}\right) dt^2 + \frac{\Sigma}{\Delta} dr^2 + \Sigma d\theta^2 \\ & + \frac{A}{\Sigma} \sin^2 \theta d\phi^2 - \frac{4a M r \sin^2 \theta}{\Sigma} dt d\phi, \end{aligned} \quad (\text{A3})$$

and the (outer) event horizon is located at  $r_+ = M + \sqrt{M^2 - a^2}$ .

Computations are facilitated by writing the metric in the general form of an asymptotically flat, stationary, axisymmetric metric, which using the notation of Bardeen (1970) and

Bardeen et al. (1972) reads as

$$\begin{aligned} ds^2 = & -e^{2\nu} dt^2 + e^{2\psi} (d\phi - \omega dt)^2 \\ & + e^{2\mu_1} dr^2 + e^{2\mu_2} d\theta^2, \end{aligned} \quad (\text{A4})$$

where

$$\begin{aligned} e^{2\nu} = \frac{\Sigma \Delta}{A}, \quad e^{2\psi} = \frac{A}{\Sigma} \sin^2 \theta, \quad e^{2\mu_1} = \frac{\Sigma}{\Delta}, \\ e^{2\mu_2} = \Sigma, \quad \omega = \frac{2Mar}{A}. \end{aligned} \quad (\text{A5})$$

### A.2. Kerr–Schild Coordinates

The Kerr metric was also presented by Kerr (1963) in Kerr–Schild spacetime coordinates  $(t, x, y, z)$  which are related to the Boyer–Lindquist ones by (see Kerr 1963, 2007, for details)

$$\begin{aligned} x &= (r \cos \phi - a \sin \phi) \sin \theta, \\ y &= (r \sin \phi + a \cos \phi) \sin \theta, \\ z &= r \cos \theta, \end{aligned} \quad (\text{A6})$$

whose inverse transformation can be written as

$$\begin{aligned} r^2 &= \frac{r_f^2 - a^2 + \sqrt{(r_f^2 - a^2)^2 + 4a^2 z^2}}{2}, \\ \theta &= \arctan\left(\frac{r}{z} \sqrt{\frac{x^2 + y^2}{r^2 + a^2}}\right), \\ \phi &= \arctan\left(\frac{y}{x}\right) + \arctan\left(\frac{a}{r}\right), \end{aligned} \quad (\text{A7})$$

where  $r_f = \sqrt{x^2 + y^2 + z^2}$ , and we have given the expressions for  $\theta$  and  $\phi$  in terms of arctan functions which give the right angle sign on any quadrant. In these coordinates, the Kerr metric reads (Kerr 1963) as

$$\begin{aligned} ds^2 = & -dt^2 + dx^2 + dy^2 + dz^2 \\ & + \frac{2Mr^3}{r^4 + a^2 z^2} \left[ dt + \frac{z}{r} dz + \frac{r}{r^2 + a^2} (x dx + y dy) \right. \\ & \left. - \frac{a}{r^2 + a^2} (x dy - y dx) \right]^2, \end{aligned} \quad (\text{A8})$$

which explicitly show the *quasi-Minkowskian* character of the metric (see Kerr 2007, for details).

## Appendix B Locally Nonrotating Observers

### B.1. Observer’s Frame using the Boyer–Lindquist Coordinate Basis

We denote coordinate basis vectors by  $e_a = \partial/\partial x^a$ , and dual one-form basis vectors by  $e^a = dx^a$ . Thus, the tetrad carried by the LNR observer (Bardeen 1970; Bardeen et al. 1972) has the following dual 1-form basis vectors:

$$\begin{aligned} e^{\hat{t}} &= \sqrt{\frac{\Sigma \Delta}{A}} e^t, \quad e^{\hat{r}} = \sqrt{\frac{\Sigma}{\Delta}} e^r, \quad e^{\hat{\theta}} = \sqrt{\Sigma} e^\theta, \\ e^{\hat{\phi}} &= -\frac{2Mra \sin \theta}{\sqrt{\Sigma} A} e^t + \sqrt{\frac{A}{\Sigma}} \sin \theta e^\phi, \end{aligned} \quad (\text{B1})$$

which are naturally identified from the metric (A4), and tetrad vectors given by

$$\begin{aligned} e_{\hat{t}} &= \sqrt{\frac{A}{\Sigma \Delta}} e_t + \frac{2Mar}{\sqrt{\Sigma \Delta A}} e_\phi, & e_{\hat{r}} &= \sqrt{\frac{\Delta}{\Sigma}} e_r, \\ e_{\hat{\theta}} &= \frac{1}{\sqrt{\Sigma}} e_\theta, & e_{\hat{\phi}} &= \sqrt{\frac{\Sigma}{A}} \frac{1}{\sin \theta} e_\phi, \end{aligned} \quad (\text{B2})$$

where in the second equality of each covector and vector, we have used the definitions (A5).

It is also useful to write the coordinate basis 1-forms in terms of the observer's basis ones, i.e.,

$$\begin{aligned} e^t &= \sqrt{\frac{A}{\Sigma \Delta}} e^{\hat{t}}, & e^r &= \sqrt{\frac{\Delta}{\Sigma}} e^{\hat{r}}, \\ e^\theta &= \frac{1}{\sqrt{\Sigma}} e^{\hat{\theta}}, & e^\phi &= \frac{2Mar}{\sqrt{\Sigma \Delta A}} \frac{1}{\sin \theta} e^{\hat{t}} + \sqrt{\frac{\Sigma}{A}} \frac{1}{\sin \theta} e^{\hat{\phi}}, \end{aligned} \quad (\text{B3})$$

and the corresponding relation among basis vectors

$$\begin{aligned} e_t &= \sqrt{\frac{\Sigma \Delta}{A}} e_{\hat{t}} - \frac{2Mar}{\sqrt{\Sigma A}} e_{\hat{\phi}}, & e_r &= \sqrt{\frac{\Sigma}{\Delta}} e_{\hat{r}}, \\ e_\theta &= \sqrt{\Sigma} e_{\hat{\theta}}, & e_\phi &= \sqrt{\frac{A}{\Sigma}} \sin \theta e_{\hat{\phi}}. \end{aligned} \quad (\text{B4})$$

For the formulation of the equations of motion in the LNR frame, we must know the components of the involved four-vectors and tensors projected onto the observer's tetrad. The covariant (contravariant) components of a vector and a tensor in the observer's frame are given by

$$\begin{aligned} A_{\hat{a}} &= e_{\hat{a}}^\mu A_\mu, & A^{\hat{a}} &= e^{\hat{a}}_\mu A^\mu \\ B_{\hat{a}\hat{b}} &= e_{\hat{a}}^\mu e_{\hat{b}}^\nu B_{\mu\nu}, & B^{\hat{a}\hat{b}} &= e^{\mu\hat{a}} e^{\nu\hat{b}} B^{\mu\nu}, \end{aligned} \quad (\text{B5})$$

where we recall the Greek indexes label the components in the coordinate frame. Thus, the four-velocity velocity of a particle with respect to the observer's frame is

$$u^{\hat{a}} = u^\mu e^{\mu\hat{a}}, \quad (\text{B6})$$

and the spatial components

$$v^{\hat{i}} = \frac{u^\mu e^{\mu\hat{i}}}{u^\mu e^{\mu\hat{t}}}, \quad (\text{B7})$$

so we can write the velocity four-vector of the particle as  $\hat{\mathbf{u}} = (\hat{\gamma}, \hat{\gamma}\mathbf{v})$ , where  $\hat{\gamma} = (1 - v^{\hat{i}}v_{\hat{i}})^{-1/2}$  is the Lorentz factor of the particle measured by the LNR observer. The four-velocity of the LNR observer,  $e_{\hat{t}}$ , with respect to an *observer at rest at infinity* can be written as

$$u_{\text{Inr}}^{\hat{a}} = \Gamma e_{\hat{t}} + \Gamma V e_{\hat{\phi}}, \quad (\text{B8})$$

where

$$\Gamma = e^{-\nu} = \sqrt{\frac{A}{\Sigma \Delta}}, \quad V = \omega = \frac{2Mar}{A}. \quad (\text{B9})$$

In the *slow-rotation* regime, at first order in the spin parameter, the spatial velocity of the observer becomes

$$V = \frac{2Ma}{r^3}. \quad (\text{B10})$$

This expression is much accurate than expected; indeed, for a spin parameter  $a \lesssim 0.7$ , it overestimates the full expression by less than 5% for radial distances  $r \gtrsim 2r_+$  and for any polar angle. Of course, the expression increases the accuracy for the lower spin values and for the larger distances.

The spatial velocity of the LNR observer, as seen by a *locally static observer*, is instead given by

$$V_{\text{Inr,s}} = \frac{2Mar \sin \theta}{\Sigma \sqrt{\Delta}} \approx \frac{2Ma \sin \theta}{r^2 \sqrt{1 - 2M/r}}, \quad (\text{B11})$$

where the last approximation corresponds to the slow-rotation regime. The tetrad basis carried by this observer is not used in this article; hence, it is not here presented.

In a non-coordinate frame, the covariant derivative of a tensor is given by

$$\frac{DB_{\hat{b}}^{\hat{a}}}{dx^{\hat{c}}} = \frac{\partial B_{\hat{b}}^{\hat{a}}}{\partial x^{\hat{c}}} + \omega_{\hat{c}\hat{d}}^{\hat{a}} B_{\hat{b}}^{\hat{d}} - \omega_{\hat{c}\hat{b}}^{\hat{d}} B_{\hat{d}}^{\hat{a}}, \quad (\text{B12})$$

where the *spin connection* coefficients,  $\omega_{\hat{c}\hat{d}}^{\hat{a}}$ , play the role of the *affine connection* coefficients. For the present LNR observer, the spin coefficients can be obtained directly from the rotation vectors (Bardeen et al. 1972)

$$\omega_{\hat{a}\hat{b}} = \omega_{\hat{a}\hat{b}\hat{c}} e^{\hat{c}}, \quad (\text{B13})$$

where

$$\begin{aligned} \omega_{\hat{t}\hat{r}\hat{t}} &= -\omega_{\hat{r}\hat{t}\hat{t}} = -\nu_{,r} e^{-\mu_1}, \\ \omega_{\hat{t}\hat{r}\hat{\phi}} &= -\omega_{\hat{r}\hat{t}\hat{\phi}} = -\frac{\omega_{,r}}{2} e^{\Psi-\nu-\mu_1}, \end{aligned} \quad (\text{B14a})$$

$$\begin{aligned} \omega_{\hat{t}\hat{\theta}\hat{t}} &= -\omega_{\hat{\theta}\hat{t}\hat{t}} = -\nu_{,\theta} e^{-\mu_2}, \\ \omega_{\hat{t}\hat{\theta}\hat{\phi}} &= -\omega_{\hat{\theta}\hat{t}\hat{\phi}} = -\frac{\omega_{,\theta}}{2} e^{\Psi-\nu-\mu_2}, \end{aligned} \quad (\text{B14b})$$

$$\omega_{\hat{t}\hat{\phi}\hat{t}} = -\omega_{\hat{\phi}\hat{t}\hat{t}} = -\frac{\omega_{,r}}{2} e^{\Psi-\nu-\mu_1}, \quad (\text{B14c})$$

$$\omega_{\hat{t}\hat{\phi}\hat{\theta}} = -\omega_{\hat{\phi}\hat{t}\hat{\theta}} = -\frac{\omega_{,\theta}}{2} e^{\Psi-\nu-\mu_2}, \quad (\text{B14d})$$

$$\begin{aligned} \omega_{\hat{t}\hat{\theta}\hat{r}} &= -\omega_{\hat{\theta}\hat{t}\hat{r}} = \mu_{1,\theta} e^{-\mu_2}, \\ \omega_{\hat{t}\hat{\theta}\hat{\theta}} &= -\omega_{\hat{\theta}\hat{t}\hat{\theta}} = -\mu_{2,r} e^{-\mu_1}, \end{aligned} \quad (\text{B14e})$$

$$\begin{aligned} \omega_{\hat{t}\hat{\phi}\hat{\phi}} &= -\omega_{\hat{\phi}\hat{t}\hat{\phi}} = -\Psi_{,r} e^{-\mu_1}, \\ \omega_{\hat{r}\hat{\phi}\hat{t}} &= -\omega_{\hat{\phi}\hat{r}\hat{t}} = \frac{1}{2} \omega_{,r} e^{\Psi-\nu-\mu_1}, \end{aligned} \quad (\text{B14f})$$

$$\begin{aligned} \omega_{\hat{\theta}\hat{\phi}\hat{\phi}} &= -\omega_{\hat{\phi}\hat{\theta}\hat{\phi}} = -\Psi_{,\theta} e^{-\mu_2}, \\ \omega_{\hat{\theta}\hat{\phi}\hat{t}} &= -\omega_{\hat{\phi}\hat{\theta}\hat{t}} = \frac{1}{2} \omega_{,\theta} e^{\Psi-\nu-\mu_2}, \end{aligned} \quad (\text{B14g})$$

with the colon notation  $f_{,\sigma} \equiv \partial f / \partial x^\sigma$ , and we have used the antisymmetric property  $\omega_{\hat{a}\hat{b}} = -\omega_{\hat{b}\hat{a}}$ .

### B.2. Observer's Frame Using the Kerr–Schild Coordinate Basis

The relation between the spatial coordinate basis vectors in Boyer–Lindquist and coordinates is therefore given by

$$\mathbf{e}_r = \sin \theta \cos \phi \mathbf{e}_x + \sin \theta \sin \phi \mathbf{e}_y + \cos \theta \mathbf{e}_z, \quad (\text{B15a})$$

$$\begin{aligned} \mathbf{e}_\theta &= (r \cos \theta \cos \phi - a \cos \theta \sin \phi) \mathbf{e}_x \\ &+ (r \cos \theta \sin \phi + a \cos \theta \cos \phi) \mathbf{e}_y - r \sin \theta \mathbf{e}_z, \end{aligned} \quad (\text{B15b})$$

$$\begin{aligned} \mathbf{e}_\phi &= -(r \sin \theta \sin \phi + a \sin \theta \cos \phi) \mathbf{e}_x \\ &+ (r \sin \theta \cos \phi - a \sin \theta \sin \phi) \mathbf{e}_y, \end{aligned} \quad (\text{B15c})$$

while the vectors of the inverse transformation are

$$\begin{aligned} \mathbf{e}_x &= \left( \frac{r^2}{\Sigma} \sin \theta \cos \phi - \frac{a r}{\Sigma} \sin \theta \sin \phi \right) \mathbf{e}_r \\ &+ \left( \frac{r}{\Sigma} \cos \theta \cos \phi - \frac{a}{\Sigma} \cos \theta \sin \phi \right) \mathbf{e}_\theta \\ &- \left( \frac{r}{\Sigma \sin \theta} \sin \phi + \frac{a}{\Sigma \sin \theta} \cos^2 \theta \cos \phi \right) \mathbf{e}_\phi, \end{aligned} \quad (\text{B16a})$$

$$\begin{aligned} \mathbf{e}_y &= \left( \frac{r^2}{\Sigma} \sin \theta \sin \phi + \frac{a r}{\Sigma} \sin \theta \cos \phi \right) \mathbf{e}_r \\ &+ \left( \frac{r}{\Sigma} \cos \theta \sin \phi + \frac{a}{\Sigma} \cos \theta \cos \phi \right) \mathbf{e}_\theta \\ &+ \left( \frac{r}{\Sigma \sin \theta} \cos \phi - \frac{a}{\Sigma \sin \theta} \cos^2 \theta \sin \phi \right) \mathbf{e}_\phi, \end{aligned} \quad (\text{B16b})$$

$$\mathbf{e}_z = \frac{r^2 + a^2}{\Sigma} \cos \theta \mathbf{e}_r - \frac{r}{\Sigma} \sin \theta \mathbf{e}_\theta + \frac{a}{\Sigma} \cos \theta \mathbf{e}_\phi. \quad (\text{B16c})$$

In the limit  $a \rightarrow 0$ , or in the weak-field limit  $r \rightarrow \infty$  (so  $a/r \rightarrow 0$ ), the above transformation reduce to the ones from traditional spherical to coordinates:

$$\mathbf{e}_r = \sin \theta \cos \phi \mathbf{e}_x + \sin \theta \sin \phi \mathbf{e}_y + \cos \theta \mathbf{e}_z, \quad (\text{B17a})$$

$$\mathbf{e}_\theta = r \cos \theta \cos \phi \mathbf{e}_x + r \cos \theta \sin \phi \mathbf{e}_y - r \sin \theta \mathbf{e}_z, \quad (\text{B17b})$$

$$\mathbf{e}_\phi = -r \sin \theta \sin \phi \mathbf{e}_x + r \sin \theta \cos \phi \mathbf{e}_y \quad (\text{B17c})$$

and

$$\mathbf{e}_x = \sin \theta \cos \phi \mathbf{e}_r + \frac{1}{r} \cos \theta \cos \phi \mathbf{e}_\theta - \frac{1}{r \sin \theta} \sin \phi \mathbf{e}_\phi, \quad (\text{B18a})$$

$$\mathbf{e}_y = \sin \theta \sin \phi \mathbf{e}_r + \frac{1}{r} \cos \theta \sin \phi \mathbf{e}_\theta + \frac{1}{r \sin \theta} \cos \phi \mathbf{e}_\phi, \quad (\text{B18b})$$

$$\mathbf{e}_z = \cos \theta \mathbf{e}_r - \frac{1}{r} \sin \theta \mathbf{e}_\theta. \quad (\text{B18c})$$

Using the coordinate basis relation (B15), one can express the observer's tetrad (B2) in the coordinate basis.

### Appendix C

#### Photon Four-momentum Measured by Different Observers

We are interested in determining the photon four-momentum measured by an observer at rest at infinity. To do so, we have to express it in terms of the four-momentum measured by an

observer comoving with the emitter (i.e., the radiating electron), which sees an isotropic radiation field.

First, we relate the comoving and the LNR frames via a Lorentz boost:

$$\mathbf{e}_{(a)} = \Lambda_{(a)}^{\hat{b}} \mathbf{e}_{\hat{b}}, \quad (\text{C1})$$

where the components of the Lorentz boost are

$$\Lambda_{(0)}^{\hat{0}} = \hat{\gamma}, \quad \Lambda_{(i)}^{\hat{0}} = \hat{\gamma} v_i, \quad \Lambda_{(j)}^{\hat{i}} = \delta_j^i + \frac{\hat{\gamma}^2}{\hat{\gamma} + 1} v^i v_j, \quad (\text{C2})$$

where we denote vector components in the comoving frame with round brackets, and we recall  $\hat{\gamma} = (1 - v^i v_i)^{-1/2}$  is the Lorentz factor of the emitter measured by the LNR observer.

The tetrad basis of the LNR frame is related to the one of the coordinate frame by

$$\mathbf{e}_{\hat{b}} = e_{\hat{b}}^{\mu} \mathbf{e}_{\mu}, \quad (\text{C3})$$

where the transformation components  $e_{\hat{b}}^{\mu}$  are given by Equations (B2).

Therefore, the relations between the comoving tetrad basis and the basis of the observer at rest at infinity are

$$\mathbf{e}_{(a)} = \Lambda_{(a)}^{\hat{b}} e_{\hat{b}}^{\mu} \mathbf{e}_{\mu}, \quad \mathbf{e}_{\mu} = \Lambda^{\hat{b}(a)} e^{\mu \hat{b}} \mathbf{e}_{(a)}, \quad (\text{C4})$$

where  $\Lambda^{\hat{b}(a)}$  can be obtained from Equation (C2) by changing the sign of the velocity components, i.e.,  $v^i \rightarrow -v^i$ , and the transformation components  $e^{\mu \hat{b}}$  are given by Equations (B1).

The photon four-momentum in the coordinate frame,  $k^{\mu}$ , is therefore related to the photon four-momentum in the comoving frame,  $k^{(a)}$ , by

$$k^{\mu} = e_{\hat{b}}^{\mu} \Lambda_{(a)}^{\hat{b}} k^{(a)}, \quad (\text{C5})$$

and we recall that for photons the above four-momenta satisfy, respectively,  $k^{\mu} k_{\mu} = 0$  and  $k^{(a)} k_{(a)} = 0$ . Thus, the four-momenta are related by

$$k^0 = k^{(0)} \hat{\gamma} e^{-\nu} [1 + v_i n^{(i)}], \quad (\text{C6a})$$

$$n^r = \frac{k^{(0)}}{k^0} e^{-\mu_1} \left[ \hat{\gamma} v^{\hat{r}} + n^{(1)} + \frac{\hat{\gamma}^2}{\hat{\gamma} + 1} v^{\hat{r}} v_j n^{(j)} \right], \quad (\text{C6b})$$

$$n^{\theta} = \frac{k^{(0)}}{k^0} e^{-\mu_2} \left[ \hat{\gamma} v^{\hat{\theta}} + n^{(2)} + \frac{\hat{\gamma}^2}{\hat{\gamma} + 1} v^{\hat{\theta}} v_j n^{(j)} \right], \quad (\text{C6c})$$

$$\begin{aligned} n^{\phi} &= \frac{k^{(0)}}{k^0} e^{-\Psi} \left\{ e^{\Psi - \nu} \omega \hat{\gamma} [1 + v_j n^{(j)}] \right. \\ &\left. + \hat{\gamma} v^{\hat{\phi}} + n^{(3)} + \frac{\hat{\gamma}^2}{\hat{\gamma} + 1} v^{\hat{\phi}} v_j n^{(j)} \right\}, \end{aligned} \quad (\text{C6d})$$

where we have introduced the normalized four-momenta by  $n^{\mu} = k^{\mu}/k^0$  and  $n^{(a)} = k^{(a)}/k^{(0)}$ . We recall that the Lorentz factor measured by the comoving and the observer at rest at infinity are related by

$$\gamma = u^0 = u^{\hat{0}} e_0^{\hat{0}} = \hat{\gamma} e^{-\nu}. \quad (\text{C7})$$

For the sake of completeness, we also present the components of the inverse relation

$$k^{(a)} = e^{\mu \hat{b}} \Lambda^{\hat{b}(a)} k^{\mu}, \quad (\text{C8})$$

which leads to the explicit components

$$k^{(0)} = k^0 \hat{\gamma} e^\nu [1 - e^{\mu_1 - \nu} v^{\hat{r}} n^r - e^{\mu_2 - \nu} v^{\hat{\theta}} n^\theta - e^{\Psi - \nu} v^{\hat{\phi}} (n^\phi - \omega)], \quad (\text{C9a})$$

$$n^{(1)} = \frac{k^0}{k^{(0)}} e^\nu \left\{ -\hat{\gamma} v^{\hat{r}} + e^{\mu_1 - \nu} n^r + \frac{\hat{\gamma} - 1}{\hat{v}^2} v^{\hat{r}} \right. \\ \left. \times [e^{\mu_1 - \nu} v^{\hat{r}} n^r + e^{\mu_2 - \nu} v^{\hat{\theta}} n^\theta + e^{\Psi - \nu} v^{\hat{\phi}} (n^\phi - \omega)] \right\}, \quad (\text{C9b})$$

$$n^{(2)} = \frac{k^0}{k^{(0)}} e^\nu \left\{ -\hat{\gamma} v^{\hat{\theta}} + e^{\mu_2 - \nu} n^\theta + \frac{\hat{\gamma} - 1}{\hat{v}^2} v^{\hat{\theta}} \right. \\ \left. \times [e^{\mu_1 - \nu} v^{\hat{r}} n^r + e^{\mu_2 - \nu} v^{\hat{\theta}} n^\theta + e^{\Psi - \nu} v^{\hat{\phi}} (n^\phi - \omega)] \right\}, \quad (\text{C9c})$$

$$n^{(3)} = \frac{k^0}{k^{(0)}} e^\nu \left\{ -\hat{\gamma} v^{\hat{\phi}} + e^{\Psi - \nu} (n^\phi - \omega) + \frac{\hat{\gamma} - 1}{\hat{v}^2} v^{\hat{\phi}} \right. \\ \left. \times [e^{\mu_1 - \nu} v^{\hat{r}} n^r + e^{\mu_2 - \nu} v^{\hat{\theta}} n^\theta + e^{\Psi - \nu} v^{\hat{\phi}} (n^\phi - \omega)] \right\}. \quad (\text{C9d})$$

### ORCID iDs


J. A. Rueda  <https://orcid.org/0000-0002-3455-3063>

R. Ruffini  <https://orcid.org/0000-0003-0829-8318>

### References

- Baade, W., & Zwicky, F. 1934, *PhRv*, **46**, 76
- Bardeen, J. M. 1970, *ApJ*, **162**, 71
- Bardeen, J. M., Press, W. H., & Teukolsky, S. A. 1972, *ApJ*, **178**, 347
- Becerra, L., Bianco, C. L., Fryer, C. L., Rueda, J. A., & Ruffini, R. 2016, *ApJ*, **833**, 107
- Becerra, L., Ellinger, C. L., Fryer, C. L., Rueda, J. A., & Ruffini, R. 2019, *ApJ*, **871**, 14
- Bernardi, M., Alonso, M. V., da Costa, L. N., et al. 2002, *AJ*, **123**, 2990
- Bird, S., Harris, W. E., Blakeslee, J. P., & Flynn, C. 2010, *A&A*, **524**, A71
- Boyer, R. H., & Lindquist, R. W. 1967, *JMP*, **8**, 265
- Carter, B. 1968, *PhRv*, **174**, 1559
- Christodoulou, D. 1970, *PhRvL*, **25**, 1596
- Christodoulou, D., & Ruffini, R. 1971, *PhRvD*, **4**, 3552
- Costa, E., Frontera, F., Heise, J., et al. 1997, *Natur*, **387**, 783
- Damour, T., Hanni, R. S., Ruffini, R., & Wilson, J. R. 1978, *PhRvD*, **17**, 1518
- Finkelstein, D. 1958, *PhRv*, **110**, 965
- Finzi, A., & Wolf, R. A. 1969, *ApJL*, **155**, L107
- Giacconi, R., & Ruffini, R. (ed.) 1978, *Physics and Astrophysics of Neutron Stars and Black Holes* (Amsterdam: North-Holland)
- Giacconi, R. 2003, *RvMP*, **75**, 995
- Giacconi, R., Gursky, H., Paolini, F. R., & Rossi, B. B. 1962, *PhRvL*, **9**, 439
- Gold, T. 1968, *Natur*, **218**, 731
- Hawking, S. W. 1971, *PhRvL*, **26**, 1344
- Hewish, A., Bell, S. J., Pilkington, J. D. H., Scott, P. F., & Collins, R. A. 1968, *Natur*, **217**, 709
- Jia, S. M., Bu, Q. C., Qu, J. L., et al. 2020, *JHEAp*, **25**, 1
- Kerr, R. P. 1963, *PhRvL*, **11**, 237
- Kerr, R. P. 2007, arXiv:0706.1109
- Kruskal, M. D. 1960, *PhRv*, **119**, 1743
- Landau, L. D., & Lifshitz, E. M. 1975, *The Classical Theory of Fields* (Oxford: Pergamon)
- Leach, R. W., & Ruffini, R. 1973, *ApJL*, **180**, L15
- Moradi, R., Rueda, J. A., Ruffini, R., & Wang, Y. 2021a, *A&A*, **649**, A75
- Moradi, R., Rueda, J. A., Ruffini, R., et al. 2021b, *PhRvD*, **104**, 063043
- Oppenheimer, J. R., & Snyder, H. 1939, *PhRv*, **56**, 455
- Oppenheimer, J. R., & Volkoff, G. M. 1939, *PhRv*, **55**, 374
- Pacini, F. 1968, *Natur*, **219**, 145
- Papapetrou, A. 1966, *AHHPA*, **4**, 83
- Penrose, R., & Floyd, R. M. 1971, *NPhS*, **229**, 177
- Piran, T. 1999, *PhR*, **314**, 575
- Punsly, B. 2009, *Black Hole Gravitohydrodynamics* (Berlin: Springer)
- Rees, M. J., & Meszaros, P. 1992, *MNRAS*, **258**, 41P
- Rhoades, C. E., & Ruffini, R. 1974, *PhRvL*, **32**, 324
- Rueda, J. A., & Ruffini, R. 2020, *EPJC*, **80**, 300
- Rueda, J. A., Ruffini, R., Karlica, M., Moradi, R., & Wang, Y. 2020, *ApJ*, **893**, 148
- Ruffini, R. 1974, in *Astrophysics and Gravitation*, 349
- Ruffini, R., Melon Fuksman, J. D., & Vereshchagin, G. V. 2019a, *ApJ*, **883**, 191
- Ruffini, R., Moradi, R., Rueda, J. A., et al. 2019b, *ApJ*, **886**, 82
- Ruffini, R., Moradi, R., Rueda, J. A., et al. 2021, *MNRAS*, **504**, 5301
- Ruffini, R., Rueda, J. A., Muccino, M., et al. 2016, *ApJ*, **832**, 136
- Ruffini, R., Wang, Y., Aimuratov, Y., et al. 2018, *ApJ*, **852**, 53
- Ruffini, R., & Wheeler, J. A. 1971a, *PhT*, **24**, 30
- Ruffini, R., & Wheeler, J. A. 1971b, *ESRO*, **52**, 45
- Schmidt, M. 1963, *Natur*, **197**, 1040
- Shklovskii, I. S. 1953, *DoSSR*, **90**, 983
- Shklovskii, I. S. 1968, *SvA*, **11**, 749
- Shklovskij, I. S. 1969, *Supernovae* (New York: Interscience)
- Thorne, K. S., Price, R. H., & MacDonald, D. A. 1986, *Black Holes: The Membrane Paradigm* (New Haven, CT: Yale Univ. Press)
- van Paradijs, J., Groot, P. J., Galama, T., et al. 1997, *Natur*, **386**, 686
- Wald, R. M. 1974, *PhRvD*, **10**, 1680
- Wang, Y., Rueda, J. A., Ruffini, R., et al. 2019, *ApJ*, **874**, 39
- Wiltshire, D. L., Visser, M., & Scott, S. M. 2009, *The Kerr Spacetime* (Cambridge: Cambridge Univ. Press)
- Woosley, S. E. 1993, *ApJ*, **405**, 273

# What does lie at the Milky Way centre? Insights from the S2-star orbit precession

C. R. Argüelles,<sup>1,2,3★</sup> M. F. Mestre,<sup>1,4</sup> E. A. Becerra-Vergara,<sup>2,3,5★</sup> V. Crespi,<sup>1</sup> A. Krut,<sup>2,3</sup>  
J. A. Rueda<sup>6</sup> <sup>2,3,6,7★</sup> and R. Ruffini<sup>2,3,6,7</sup>

<sup>1</sup>Facultad de Ciencias Astronómicas y Geofísicas, Universidad Nacional de La Plata, Paseo del Bosque, B1900FWA La Plata, Argentina

<sup>2</sup>ICRANet, Piazza della Repubblica 10, I-65122 Pescara, Italy

<sup>3</sup>ICRA, Dipartimento di Fisica, Sapienza Università di Roma, P.le Aldo Moro 5, I-00185 Rome, Italy

<sup>4</sup>Instituto de Astrofísica de La Plata, UNLP & CONICET, Paseo del Bosque, B1900FWA La Plata, Argentina

<sup>5</sup>GIRG, Escuela de Física, Universidad Industrial de Santander, Bucaramanga 680002, Colombia

<sup>6</sup>ICRANet-Ferrara, Dipartimento di Fisica e Scienze della Terra, Università degli Studi di Ferrara, Via Saragat 1, I-44122 Ferrara, Italy

<sup>7</sup>INAF, Istituto de Astrofisica e Planetologia Spaziali, Via Fosso del Cavaliere 100, I-00133 Rome, Italy

Accepted 2021 November 30. Received 2021 November 29; in original form 2021 September 10

## ABSTRACT

It has been recently demonstrated that both, a classical Schwarzschild black hole (BH), and a dense concentration of self-gravitating fermionic dark matter (DM) placed at the Galaxy centre, can explain the precise astrometric data (positions and radial velocities) of the S-stars orbiting Sgr A\*. This result encompasses the 17 best resolved S-stars, and includes the test of general relativistic effects such as the gravitational redshift in the S2-star. In addition, the DM model features another remarkable result: The dense core of fermions is the central region of a continuous density distribution of DM whose diluted halo explains the Galactic rotation curve. In this Letter, we complement the above findings by analysing in both models the relativistic periapsis precession of the S2-star orbit. While the Schwarzschild BH scenario predicts a unique prograde precession for S2, in the DM scenario, it can be either retrograde or prograde, depending on the amount of DM mass enclosed within the S2 orbit, which, in turn, is a function of the DM fermion mass. We show that all the current and publicly available data of S2 cannot discriminate between the two models, but upcoming S2 astrometry close to next apocentre passage could potentially establish if Sgr A\* is governed by a classical BH or by a quantum DM system.

**Key words:** stars: kinematics and dynamics – Galaxy: centre – Galaxy: structure – dark matter.

## 1 INTRODUCTION

The most effective method to explore the nature of the supermassive compact object at the centre of our Galaxy, Sgr A\*, has been the tracing of the orbits of the S-cluster stars. This astrometric data acquisition has been performed by two leading groups, one of which started a significant progress in constraining the central object mass (Eckart & Genzel 1997; Schödel et al. 2002; Gillessen et al. 2009, 2017; Genzel et al. 2010). More recently, this group has incorporated the GRAVITY instrument of the VLT, allowing us to detect the gravitational redshift of the S2-star (Gravity Collaboration et al. 2018a), to detect flares or hotspots close to Sgr A\* (Gravity Collaboration et al. 2018b), and to detect the relativistic precession of the S2-star orbit of about 12 arcmin cycle<sup>-1</sup> as predicted by the Schwarzschild BH (Gravity Collaboration et al. 2020). In parallel, a second group reached similar constraints to the mass of the central compact object in Sgr A\* (Ghez et al. 1998, 2005, 2008; Boehle et al. 2016), mainly operating with the Keck, Gemini North, and Subaru Telescopes, using the Adaptive Optics technique. This group has recently confirmed the detection of the S2-star relativistic redshift

(Do et al. 2019), converging with the first group in an estimate of the central object mass of about  $4 \times 10^6 M_{\odot}$ .

From these two observational campaigns, the inference on the nature of Sgr A\* has been reached on the ground of novel theoretical understandings. A recent important result has been obtained in Matsumoto, Chan & Piran (2020) (see also Tursunov et al. 2020), by re-considering the flare emissions around Sgr A\*, emphasizing both, that their motion is not purely geodesic, and establishing a limit on the spin of a putative Kerr BH mass of  $|a| < 0.5$ . Soon after, in Becerra-Vergara et al. (2020), it was introduced an alternative model to the classical BH in Sgr A\* by re-interpreting it as a high concentration of quantum self-gravitating DM made of fermions of about  $56 \text{ keV } c^{-2}$  rest mass. This alternative approach can explain the astrometric data of both the S2-star and the G2 object with similar accuracy than the Schwarzschild BH scenario, but without introducing a drag force on G2 which is needed in the BH case to reconcile it with the G2 post-pericentre passage velocity data. An underlying assumption about the nature of such a DM quantum core is its absence of rotation, which is well supported by recent upper bounds on the spin of the central BH of  $a < 0.1$ , based on the spatial distribution of the S-stars (Ali et al. 2020; Fragione & Loeb 2020; Peißker et al. 2020). The first results obtained in Becerra-Vergara et al. (2020) within the DM scenario have been further extended in Becerra-Vergara et al. (2021) by considering the 17 best resolved stars orbiting Sgr A\*, achieving

\* E-mail: [carguelles@fcaglp.unlp.edu.ar](mailto:carguelles@fcaglp.unlp.edu.ar) (CRA); [eduar.becerra@icranet.org](mailto:eduar.becerra@icranet.org) (EAB-V); [jorge.rueda@icra.it](mailto:jorge.rueda@icra.it) (JAR)

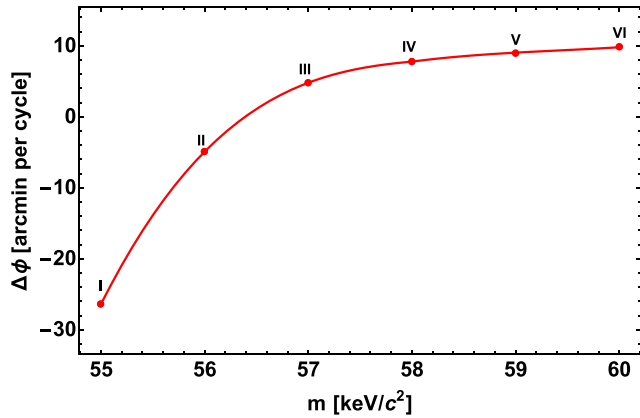


**Figure 1.** Relativistic periapsis precession  $\Delta\phi$  per orbit as a function of the *darkino* mass as predicted by the RAR DM models for the S2-star. The precession is retrograde for  $m < 56.4 \text{ keV c}^{-2}$  while it becomes prograde for  $m > 56.4 \text{ keV c}^{-2}$  (see also Table 1).

an equally good fit than in the BH paradigm. Remarkably, such a dense DM core is the central region of a continuous distribution of DM whose diluted halo explains the Galactic rotation curves (Argüelles et al. 2018; Becerra-Vergara et al. 2020, 2021). Core-halo DM distributions of this kind are obtained from the solution of the Einstein equations for a self-gravitating, finite-temperature fluid of fermions in equilibrium following the Ruffini–Argüelles–Rueda (RAR) model (Ruffini, Argüelles & Rueda 2015; Argüelles et al. 2016, 2018, 2019, 2021; Gómez et al. 2016; Gómez & Rueda 2017; Becerra-Vergara et al. 2020, 2021; Penacchioni et al. 2020; Yunis et al. 2020). These novel core-halo DM profiles, as the ones applied in this Letter, have been shown to form and remain stable in cosmological time-scales, when accounting for the quantum nature of the particles within proper relaxation mechanisms of collisionless fermions (Argüelles et al. 2021). There are other alternative scenarios for Sgr A\* involving a compact object of quantum nature, e.g. a boson star composed of ultralight scalars (see e.g. Torres et al. 2000). However, unlike the  $\sim 50\text{--}345 \text{ keV c}^{-2}$  fermionic DM RAR solutions, those boson stars do not explain the Galaxy rotation curves.

In this Letter, we focus the attention solely on the S2-star, which has been continuously monitored in the last 27 yr, and shows one of the most compact orbits around Sgr A\* with an orbital period of about 16 yr and a pericentre of 0.56 mpc (i.e. about 1450 Schwarzschild radii of the  $4 \times 10^6 M_{\odot}$  central object). Even though it is relatively far from Sgr A\* where relativistic effects are feeble and hard to detect, S2 is currently considered the best tracer of the Sgr A\* gravitational potential. Being its most precise astrometric data taken around pericentre passages, see e.g. Gravity Collaboration et al. (2018a, 2020) and Do et al. (2019).

With the aim of making progress in disentangling the nature of Sgr A\*, we analyse here the relativistic periapsis precession of the S2-star in the above BH and DM scenarios. As the main result of this work, it is shown that the precession of the S2-star within the RAR DM model can be either retrograde or prograde depending on the amount of DM mass enclosed within the orbit. The latter is shown to be a function of the mass of the DM fermion (hereafter *darkino*). In particular, we show that for a  $56 \text{ keV c}^{-2}$  *darkino* mass, the RAR model predicts a retrograde S2 orbit precession, while for a slightly larger *darkino* mass of  $58 \text{ keV c}^{-2}$ , it predicts a prograde precession. The latter very much similar to the Schwarzschild BH case. By fitting all the publicly available S2 astrometric data, we conclude that none of the above scenarios about the nature of

Sgr A\* can be currently discriminated. This is mainly due to the large eccentricity of the S2 orbit, implying that its cumulative precession has a better chance of detectability away from the pericentre passage and closer to apocentre (Parsa et al. 2017). Consequently, we assess at which epoch during the S2 orbital motion these scenarios can be disentangled, being the S2 high precision data beyond 2019 of utmost importance for this task.

## 2 PRECESSION OF THE S2 ORBIT

In both models here considered for Sgr A\*, the spherically symmetric space–time metric can be written as  $ds^2 = A(r)c^2 dt^2 - B(r)dr^2 - r^2(d\theta^2 + \sin^2\theta d\phi^2)$ , where  $(r, \theta, \phi)$  are the spherical coordinates,  $c$  is the speed of light, and  $A(r), B(r)$  are the metric functions to be found by solving the Einstein field equations. For the Schwarzschild BH model, such equations can be solved analytically leading to:  $A(r) = 1 - 2GM_{\text{BH}}/(c^2 r)$  and  $B(r) = 1/A(r)$ , where  $G$  is the gravitational constant and  $M_{\text{BH}}$  is the BH mass. For the RAR DM model, the system of Einstein equations is solved numerically for  $A(r)$  and  $B(r)$ , together with the Tolman and Klein thermodynamic equilibrium conditions, and the (particle) energy conservation along geodesics (Argüelles et al. 2018). These metric potentials are not analytic and their radial dependence depend on the boundary-value problem specified to have solutions that agree with the galaxy observables. A solution of the RAR DM model for the case of the Milky Way, with specific boundary conditions that agree either with the overall rotation curve, the orbits of the 17 best resolved S-cluster stars, and the G2 object, was presented in Becerra-Vergara et al. (2020, 2021) for a *darkino* mass of  $56 \text{ keV c}^{-2}$ .

A necessary condition to be fulfilled by the RAR DM profiles in order to explain the S2 orbit, is that the corresponding DM core radius ( $r_c$ ) be smaller than the S2 pericentre (which for the case of  $m = 56 \text{ keV c}^{-2}$  is  $r_c \approx 0.4 \text{ mpc} < r_{p(S_2)} = 0.56 \text{ mpc}$ ). However, as first understood in Argüelles et al. (2018), and further detailed here, more compact DM cores with  $r_c < r_{p(S_2)}$  (under fixed Milky Way halo boundary conditions) can also explain the S-cluster stellar orbits for different *darkino* masses. Thus, in this Letter, we explore other Milky Way RAR profiles from  $m = 55$  to  $60 \text{ keV c}^{-2}$ , which will be essential to compare the properties of the S2 orbit precession for different central DM concentrations.

The equations of motion (e.o.m.) of a test particle in the above space–time metric, assuming without loss of generality the motion on the plane  $\theta = \pi/2$ , are  $\dot{t} = E/(c^2 A(r))$ ;  $\dot{\phi} = L/r^2$ ;  $\ddot{r} = [-A'(r) c^2 \dot{t}^2 - B'(r) \dot{r}^2 + 2 r \dot{\phi}^2]/(2 B(r))$ , where  $E$  and  $L$  are, respectively, the conserved energy and the angular momentum of the test particle per unit mass, the overdot stands for derivative with respect to the proper time  $\tau$ , while the superscript comma (') denotes derivative with respect to the radial coordinate  $r$ . We perform the numerical integration of the e.o.m. with a Dormand–Prince algorithm (Strehmel 1988). In addition, the appropriate initial conditions have been chosen in such a way that the test particle motion starts at the apocentre, i.e.  $t(\tau_0) = 0$ ,  $\phi(\tau_0) = \pi$ ,  $r(\tau_0) = r_a$ , and  $\dot{r}(\tau_0) = 0$ . We integrate the equations for a sufficiently long time, which assures that the particle performs more than two consecutive orbits, so we can compute the net precession of the real orbit over two consecutive cycles. For instance, denoting the time of apocentre in two consecutive orbits, respectively, as  $t_{\text{apo1}}$  and  $t_{\text{apo2}}$ , the precession of the real orbit over those two cycles is  $\Delta\phi = \phi(t_{\text{apo2}}) - \phi(t_{\text{apo1}})$ .

We start by analysing the effects of different DM core concentrations with corresponding *darkino* masses, on the precession  $\Delta\phi$  (as defined above) for the S2-star. For this task, we use all the publicly available astrometric measurements (Do et al. 2019) that include



**Table 1.** Comparison of the BH and RAR DM models that best fit of all the publicly available data of the S2 orbit.

	Model	$M_{\text{CO}}$ [ $10^6 M_{\odot}$ ]	$r_c$ [mpc]	$\Delta M_{\text{DM}}/M_{\text{CO}}$	$r_p$ [as]	$r_a$ [as]	$\langle \chi^2 \rangle$	$\Delta\phi$ [arcmin]	$\Delta\phi_{\text{sky}}$ [arcmin]
I	RAR ( $m = 55 \text{ keV } c^{-2}$ )	3.55	0.446	$1.39 \times 10^{-2}$	0.01417	0.23723	2.9719	-26.3845	-32.1116
II	RAR ( $m = 56 \text{ keV } c^{-2}$ )	3.50	0.427	$5.99 \times 10^{-3}$	0.01418	0.23618	3.0725	-4.9064	-5.9421
III	RAR ( $m = 57 \text{ keV } c^{-2}$ )	3.50	0.407	$2.21 \times 10^{-3}$	0.01417	0.23617	3.2766	4.8063	5.8236
IV	RAR ( $m = 58 \text{ keV } c^{-2}$ )	3.50	0.389	$7.13 \times 10^{-4}$	0.01424	0.23609	3.2814	7.7800	9.4243
V	RAR ( $m = 59 \text{ keV } c^{-2}$ )	3.50	0.371	$2.93 \times 10^{-4}$	0.01418	0.23613	3.3356	9.0456	10.9613
VI	RAR ( $m = 60 \text{ keV } c^{-2}$ )	3.50	0.355	$1.08 \times 10^{-4}$	0.01423	0.23610	3.3343	9.8052	11.8764
	BH	4.07	$3.89 \times 10^{-4}$	0	0.01427	0.23623	3.3586	11.9501	14.4947

The second column shows the central object mass,  $M_{\text{CO}}$ . For the Schwarzschild BH model,  $M_{\text{CO}} = M_{\text{BH}}$ , while for the RAR model,  $M_{\text{CO}} = M_c$ , with  $M_c$  the DM core mass. The third column shows the radius of the central object,  $r_c$ . For the Schwarzschild BH model,  $r_c$  is given by the event horizon radius,  $R_{\text{Sch}} = 2GM_{\text{BH}}/c^2$ . The fourth column shows the DM mass enclosed within the S2 orbit,  $\Delta M_{\text{DM}}/M_{\text{CO}}$ . The best-fitting pericentre and apocentre radii of the S2 orbit are given, respectively, in the fifth and sixth columns. The values of the average reduced- $\chi^2$  of the best fits, defined as in Becerra-Vergara et al. (2020), are given in the seventh column. The last two columns show, respectively, the model predictions of the periastron precession of the real orbit,  $\Delta\phi$ , and of the sky-projected orbit,  $\Delta\phi_{\text{sky}}$ .

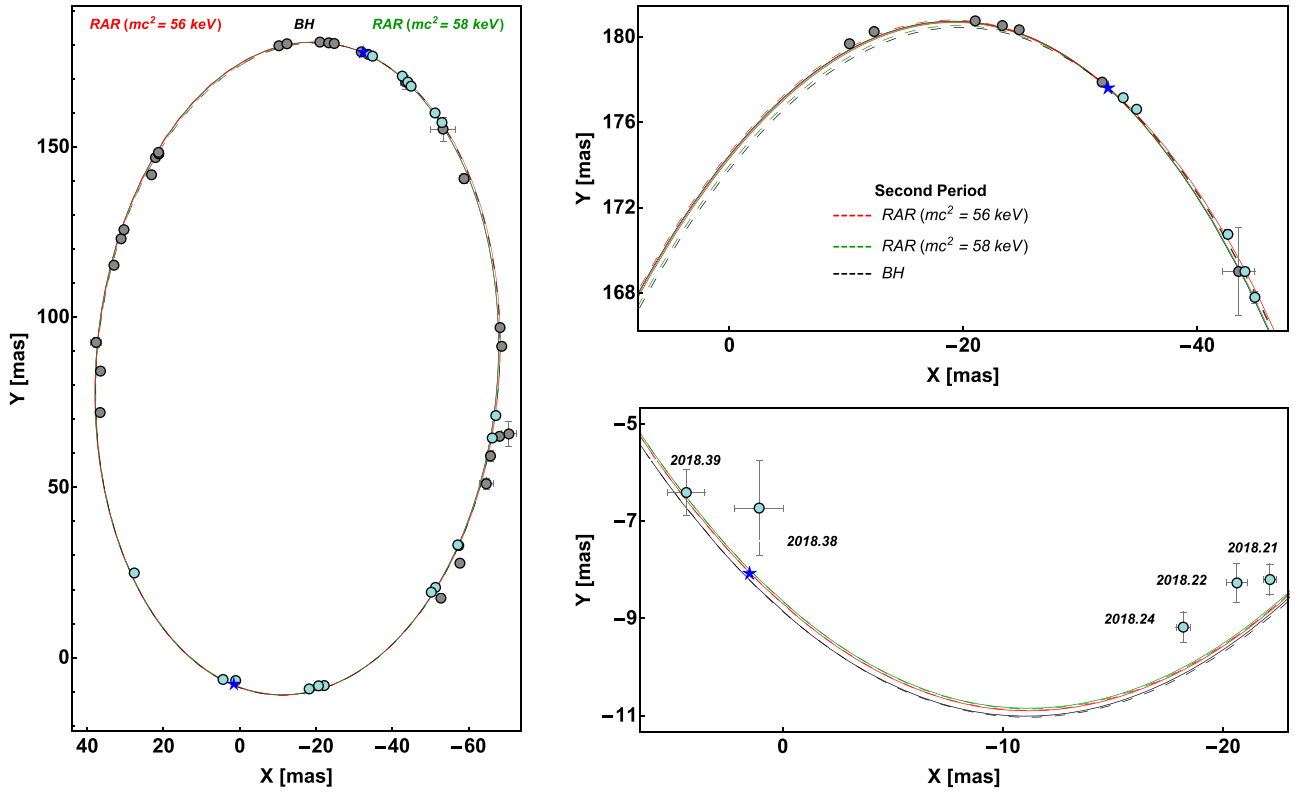


**Figure 2.** Relativistic precession of S2 in the projected orbit on the plane of the sky as predicted in the BH and RAR DM models. While it is prograde for the BH and RAR ( $m = 58 \text{ keV } c^{-2}$ ) (in dashed black and green, respectively), it is retrograde for the RAR DM model ( $m = 56 \text{ keV } c^{-2}$ ) (in dashed red). The solid (theoretical) curves and grey (data) points correspond to the first period ( $\approx 1994$ –2010) while the dashed (theoretical) curves and cyan (data) points to the second period ( $\approx 2010$ –2026). Right-hand panels: zoom of the region around apocentre (top panel) and pericentre (bottom panel). The astrometric measurements are taken from Do et al. (2019).

data obtained from the instruments NIRC on Keck I (1995–2005) and NIRC2 on Keck II (2005–2018). In Fig. 1, we show  $\Delta\phi$  as a function of the *darkino* mass  $m$ , within a narrow particle mass range around  $56 \text{ keV } c^{-2}$ . In the BH case, the precession of the orbit per cycle is given by the well-known expression  $\Delta\phi_{\text{BH}} = 6\pi GM_{\text{BH}}/[c^2 a(1 - e^2)]$ , which is always prograde ( $\Delta\phi > 0$ ) and for a  $4.07 \times 10^6 M_{\odot}$  BH mass and the S2 orbital parameters gives  $\approx 12$  arcmin. In the DM case,  $\Delta\phi$  has no analytic expression, but the numerical solutions show that it increases non-linearly from negative to positive (i.e. from retrograde to prograde) with the *darkino* mass (see Fig. 1).

Given the DM quantum core is surrounded by an extended and more diluted DM mass, there are two competing effects in the RAR model which lead to three different possibilities for the S2 orbit precession. The effects can be roughly separated into a prograde effect caused by the gravitational potential of the DM core lying inside the S2 pericentre (similar to a relativistic point-like source), and a retrograde effect caused by the gravitational potential generated by the extended mass between the pericentre radius  $r_p$ , and the apocentre radius  $r_a$ , i.e.  $\Delta M_{\text{DM}} = \int_{r_p}^{r_a} 4\pi r^2 \rho_{\text{DM}}(r) dr$ . Due to the scaling behaviour of the core-halo RAR profiles with the underlying

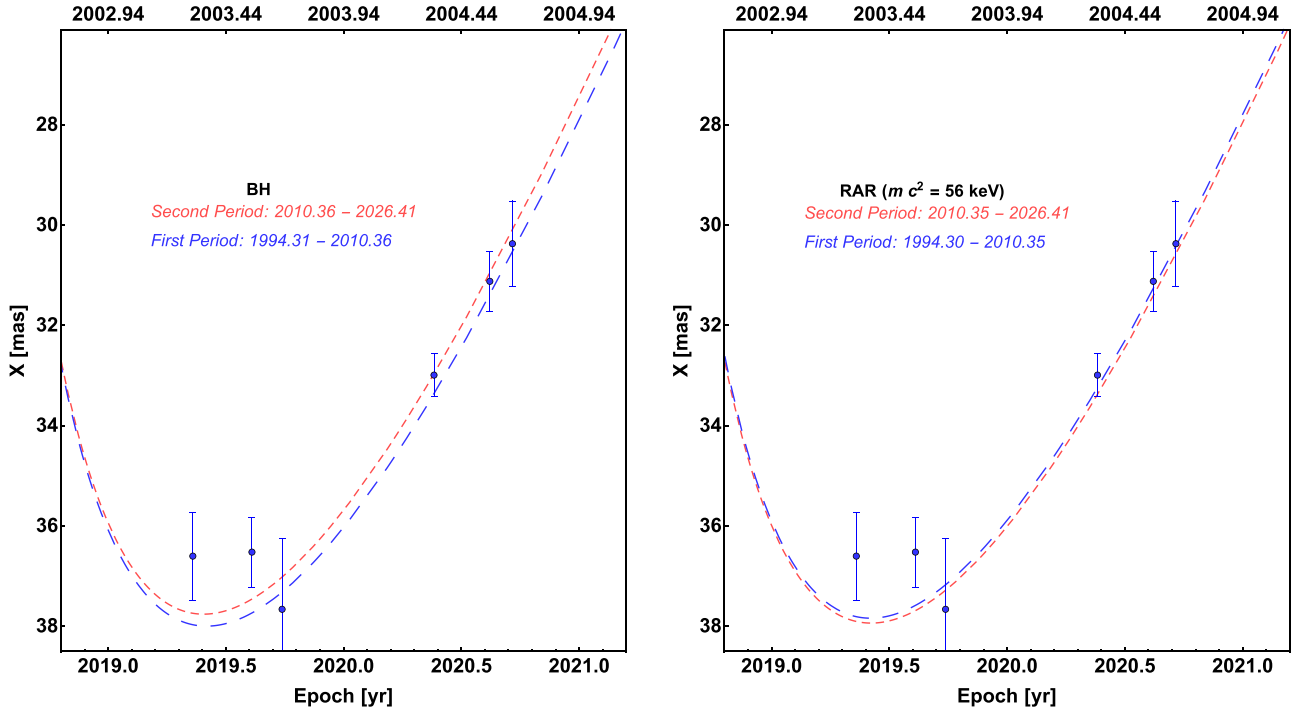


**Figure 3.** Relativistic precession of S2 as manifested in the right ascension as a function of time after last pericentre passage, where effects are more prominent. BH model (Left-hand panel) and RAR model for  $m = 56 \text{ keV c}^{-2}$  (Right-hand panel).

four free parameters of the theory (Argüelles et al. 2018, 2019), both effects are related to each other. That is, the larger the *darkino* mass is, the more compact the DM core is (resembling more and more the BH case; Argüelles et al. 2018), with consequent less extended mass fraction  $\Delta M_{\text{DM}}/M_c$ . The above leads to: (i) Prograde precession ( $\Delta\phi > 0$ ) as shown in Fig. 1 and occurring for  $m > 56.4 \text{ keV c}^{-2}$  with a corresponding DM core mass of  $M_c = 3.50 \times 10^6 M_\odot$ . In this case, the retrograde effect due to the extended DM mass  $\Delta M_{\text{DM}}/M_c$  is not enough to compensate for the prograde one. For larger fermion masses, this prograde trend gets closer to the Schwarzschild value of 11.95 arcmin, and is approached for  $m \approx 345 \text{ keV c}^{-2}$ , the mass value for which the DM core becomes unstable against gravitational collapse into a  $\sim 4.2 \times 10^6 M_\odot$  BH (Argüelles et al. 2018). (ii) Null precession ( $\Delta\phi = 0$ ) occurring for  $m = 56.4 \text{ keV c}^{-2}$  with  $M_c = 3.50 \times 10^6 M_\odot$  when the above two effects balance each other. (iii) Retrograde precession ( $\Delta\phi < 0$ ), as shown in Fig. 1 for  $m < 56.4 \text{ keV c}^{-2}$  when the fraction of the DM core mass  $\Delta M_{\text{DM}}/M_c$  between  $r_{\text{p}(S_2)}$  and  $r_{\text{a}(S_2)}$  is large enough. As detailed in Table 1, such a threshold value of  $\Delta M_{\text{DM}}/M_c$  below which its associated retrograde effect becomes negligible (and thus the precession is always prograde) is  $\sim 0.1$  per cent. Moreover, for  $m > 57 \text{ keV c}^{-2}$ , the fraction of extended mass,  $M_{\text{DM}}/M_{\text{CO}}$ , falls below 0.1 per cent, in agreement with the current bounds for an extended mass within the S2 orbit in the Schwarzschild BH case (Gravity Collaboration et al. 2020).

Then, we proceed to compare the predictions on the periastron precession of the S2-orbit analogous to that of Fig. 1, i.e. calculated at apocentre, but in the plane of the sky ( $\Delta\phi_{\text{sky}}$ ) for seven different models: one Schwarzschild BH and six RAR DM models for the Milky Way (i.e. already reproducing its rotation curve) with  $m$  from 55 and up to 60  $\text{keV c}^{-2}$ . The obtained values of  $\Delta\phi_{\text{sky}}$  are given in the last column of Table 1, together with each set of free model parameters (e.g.  $M_{\text{BH}}$  for the BH model and  $M_c$  for RAR at each given

$m$ ) that best fits the astrometry data of S2. Some a posteriori model properties including the DM core radius  $r_c$  and the extended DM mass fraction  $\Delta M_{\text{DM}}/M_c$  are included in the table. The best-fitting models are obtained following the procedure of Becerra-Vergara et al. (2020), where the full set of best-fitting orbital parameters of S2 (for  $m = 56 \text{ keV c}^{-2}$ ) can also be found.

Fig. 2 shows the relativistic precession of S2 projected orbit, in a *right ascension–declination* plot. It can be there seen that while the positions in the plane of the sky nearly coincide about the last pericentre passage in the three models, they can be differentiated close to next apocentre. Specifically, the upper right-hand panel evidences the difference at apocentre between the prograde case (as for the BH and RAR model with  $m = 58 \text{ keV c}^{-2}$ ) and the retrograde case (i.e. RAR model with  $m = 56 \text{ keV c}^{-2}$ ).

The same conclusion can be better evidenced, and quantified, by showing the S2 orbit precession effects in right ascension (X) as a function of time, as predicted by each of the above two models. This is plotted in Fig. 3 showing the clear difference in X between two consecutive periods, each one starting at about the pericentre passage. The first period is shown by the long-dashed blue curve, and the second period is shown by the short-dashed red curve which extends beyond the last pericentre passage, where the predicted precession in each model is more evident. Indeed, the BH case (left-hand panel) shows a prograde trend with a maximal shift of  $\Delta X \approx 0.7 \text{ mas}$  at 2026.0 with respect to the former period (and being  $\approx 0.4 \text{ mas}$  at 2021.2), while the RAR ( $m = 56 \text{ keV c}^{-2}$ ) case (right-hand panel) shows a retrograde trend with a maximal shift of  $\Delta X \approx 0.3 \text{ mas}$  at 2026.3 with respect to the former period (being  $\Delta X \approx 0.2 \text{ mas}$  at 2021.2).

Unfortunately, the publicly available data in the relevant time-window of Fig. 3 are only a few data points within the first period [shown in blue dots and obtained from Do et al. (2019)], where the large error bars impede to discriminate between the models. Even if

the improved S2 astrometric resolution obtained by the GRAVITY Collaboration between 2018 and 2019.7 reaches the 0.1 mas, it covers the range around pericentre passage where the predicted  $\Delta X$  in both models is too low to safely discriminate between these models.

### 3 DISCUSSION AND CONCLUSIONS

In this Letter, we have demonstrated that unlike the classical Schwarzschild BH prograde precession for the S2 orbit, when assuming a quantum DM nature for Sgr A\* according to the RAR model, it can be either retrograde or prograde depending on the amount of DM mass enclosed within the S2 orbit. Such a trend, in turn, depends on the *darkino* mass. We have shown that within the current astrometric resolution for S2, upcoming data close to the next apocentre passage have a good chance to validate one of the above predicted directions of the orbital precession. Additional constraints to the *darkino* mass could arise from the orbits of the faint stars S62 and S4714 whose pericenters have been estimated to be about one order of magnitude smaller than that of S2 (Peißker et al. 2020). If confirmed, the fermion mass would need to be larger ( $\sim 100 \text{ keV } c^{-2}$ ) for the quantum core to be compact enough to lie inside those pericentre distance and produce such elliptic orbits.

Finally, we outline some astrophysical and cosmological consequences of the RAR DM model, in addition to the present results. The RAR model predicts a mechanism for supermassive BH formation in the high-redshift Universe when the dense core of DM reaches its critical mass for gravitational collapse (Argüelles et al. 2021). For a *darkino* mass of about  $50 \text{ keV } c^{-2}$ , such a critical mass is  $\sim 10^8 M_{\odot}$ . This numerical value can be affected by the additional accretion of baryonic matter on the *darkino* core. Furthermore, the RAR model provides as well the quantum nature and mass of the DM particles, and the morphology of the DM profiles on inner halo scales. As recently shown in Argüelles et al. (2021), the formation of *core-halo* RAR DM profiles is predicted within violent relaxation mechanisms with the following key properties. (i) They form and remain stable within cosmological time-scales. (ii) They are *universal*, ranging from the scales of dwarfs up to the galaxy cluster scales (Argüelles et al. 2019). (iii) On inner halo scales, the RAR density profiles develop an extended plateau (similar to Burkert profiles), thereby not suffering from the core-cusp problem associated with the standard Lambda cold dark matter cosmology (see e.g. Bullock & Boylan-Kolchin 2017).

### ACKNOWLEDGEMENTS

CRA was supported by the Consejo Nacional de Investigaciones Científicas y Técnicas (CONICET) Argentina, Agencia Nacional de Promoción Científica y Tecnológica (grant PICT-2018-03743), and the International Center for Relativistic Astrophysics Network. EAB-V thanks financial support from COLCIENCIAS, ICRANet-IRAP-PhD, and Universidad Industrial de Santander (UIS).

### DATA AVAILABILITY

The astrometric data used here were obtained from Do et al. (2019). The data generated here are available in Table 1.

### REFERENCES

- Ali B. et al., 2020, *ApJ*, 896, 100  
 Argüelles C. R., Mavromatos N. E., Rueda J. A., Ruffini R., 2016, *J. Cosmol. Astropart. Phys.*, 2016, 038  
 Argüelles C. R., Krut A., Rueda J. A., Ruffini R., 2018, *Phys. Dark Universe*, 21, 82  
 Argüelles C. R., Krut A., Rueda J. A., Ruffini R., 2019, *Phys. Dark Universe*, 24, 100278  
 Argüelles C. R., Díaz M. I., Krut A., Yunis R., 2021, *MNRAS*, 502, 4227  
 Becerra-Vergara E. A., Argüelles C. R., Krut A., Rueda J. A., Ruffini R., 2020, *A&A*, 641, A34  
 Becerra-Vergara E. A., Argüelles C. R., Krut A., Rueda J. A., Ruffini R., 2021, *MNRAS*, 505, L64  
 Boehle A. et al., 2016, *ApJ*, 830, 17  
 Bullock J. S., Boylan-Kolchin M., 2017, *ARA&A*, 55, 343  
 Do T. et al., 2019, *Science*, 365, 664  
 Eckart A., Genzel R., 1997, *MNRAS*, 284, 576  
 Fragione G., Loeb A., 2020, *ApJ*, 901, L32  
 Genzel R., Eisenhauer F., Gillessen S., 2010, *Rev. Mod. Phys.*, 82, 3121  
 Ghez A. M., Klein B. L., Morris M., Becklin E. E., 1998, *ApJ*, 509, 678  
 Ghez A. M., Salim S., Hornstein S. D., Tanner A., Lu J. R., Morris M., Becklin E. E., Duchêne G., 2005, *ApJ*, 620, 744  
 Ghez A. M. et al., 2008, *ApJ*, 689, 1044  
 Gillessen S., Eisenhauer F., Trippe S., Alexander T., Genzel R., Martins F., Ott T., 2009, *ApJ*, 692, 1075  
 Gillessen S. et al., 2017, *ApJ*, 837, 30  
 Gómez L. G., Rueda J. A., 2017, *Phys. Rev.*, 96, 063001  
 Gómez L. G., Argüelles C. R., Perlick V., Rueda J. A., Ruffini R., 2016, *Phys. Rev.*, 94, 123004  
 Gravity Collaboration et al., 2018a, *A&A*, 615, L15  
 Gravity Collaboration et al., 2018b, *A&A*, 618, L10  
 Gravity Collaboration et al., 2020, *A&A*, 636, L5  
 Matsumoto T., Chan C.-H., Piran T., 2020, *MNRAS*, 497, 2385  
 Parsa M., Eckart A., Shahzamanian B., Karas V., Zjacek M., Zensus J. A., Straubmeier C., 2017, *ApJ*, 845, 22  
 Peißker F., Eckart A., Zjacek M., Ali B., Parsa M., 2020, *ApJ*, 899, 50  
 Penacchioni A. V., Civitaresse O., Argüelles C. R., 2020, *Eur. Phys. J.*, 80, 183  
 Ruffini R., Argüelles C. R., Rueda J. A., 2015, *MNRAS*, 451, 622  
 Schödel R. et al., 2002, *Nature*, 419, 694  
 Strehmel K., 1988, *J. Appl. Math. Mech.*, 68, 260  
 Torres D. F., Capozziello S., Lambiase G., 2000, *Phys. Rev.*, 62, 104012  
 Tursunov A., Zjacek M., Eckart A., Kološ M., Britzen S., Stuchlík Z., Czerny B., Karas V., 2020, *ApJ*, 897, 99  
 Yunis R., Argüelles C. R., Mavromatos N. E., Moliné A., Krut A., Carinci M., Rueda J. A., Ruffini R., 2020, *Phys. Dark Universe*, 30, 100699

This paper has been typeset from a  $\text{\TeX}/\text{\LaTeX}$  file prepared by the author.

## The white dwarf binary merger model of GRB 170817A\*

J. A. Rueda<sup>†,‡,§,¶,††,¶¶</sup>, R. Ruffini<sup>†,‡,||,\*\*</sup>, Liang Li<sup>†,‡,‡‡</sup>,  
 R. Moradi<sup>†,‡,‡‡</sup>, N. Sahakyan<sup>§§</sup> and Y. Wang<sup>†,‡,‡‡</sup>

<sup>†</sup>*ICRANet, Piazza della Repubblica 10, I-65122 Pescara, Italy*

<sup>‡</sup>*ICRA, Dipartimento di Fisica, Sapienza Università di Roma,  
 Piazzale Aldo Moro 5, I-00185 Roma, Italy*

<sup>§</sup>*ICRANet-Ferrara, Dipartimento di Fisica e Scienze della Terra,  
 Università degli Studi di Ferrara, Via Saragat 1,  
 I-44122 Ferrara, Italy*

<sup>¶</sup>*Dipartimento di Fisica e Scienze della Terra,  
 Università degli Studi di Ferrara,  
 Via Saragat 1, I-44122 Ferrara, Italy*

<sup>||</sup>*Université de Nice Sophia-Antipolis,  
 Grand Château Parc Valrose, Nice, CEDEX 2, France*

<sup>\*\*</sup>*INAF, Viale del Parco Mellini 84,  
 00136 Rome, Italy*

<sup>††</sup>*INAF, Istituto di Astrofisica e Planetologia Spaziali,  
 Via Fosso del Cavaliere 100, 00133 Rome, Italy*

<sup>‡‡</sup>*INAF – Osservatorio Astronomico d'Abruzzo,  
 Via M. Maggini snc, I-64100 Teramo, Italy*

<sup>§§</sup>*ICRANet-Armenia, Marshall Baghramian Avenue 24a,  
 Yerevan 0019, Republic of Armenia*

<sup>¶¶</sup>*jorge.rueda@icra.it*

Received 10 January 2022

Accepted 11 January 2022

Published 16 February 2022

Following the GRB 170817A prompt emission lasting a fraction of a second,  $10^8$  s of data in the X-rays, optical, and radio wavelengths have been acquired. We here present a model that fits the spectra, flux, and time variability of all these emissions, based on the thermal and synchrotron cooling of the expanding matter ejected in a binary white dwarf merger. The  $10^{-3}M_{\odot}$  of ejecta, expanding at velocities of  $10^9$  cm s $^{-1}$ , are powered by the newborn massive, fast rotating, magnetized white dwarf with a mass of  $1.3M_{\odot}$ , a rotation period of  $\gtrsim 12$  s, and a dipole magnetic field  $\sim 10^{10}$  G, born in the merger of a  $1.0 + 0.8M_{\odot}$  white dwarf binary. Therefore, the long-lasting mystery of the GRB

\*Based on a talk presented at the Sixteenth Marcel Grossmann Meeting on Recent Developments in Theoretical and Experimental General Relativity, Astrophysics and Relativistic Field Theories, online, July 2021.

170817A nature is solved by the merger of a white dwarf binary that also explains the prompt emission energetics.

*Keywords:* Gamma-ray bursts; white dwarfs; white dwarf mergers.

## 1. Introduction

GRB 170817A is a short gamma-ray burst (GRB) whose prompt emission lasts less than a second, as was detected by the gamma-ray burst monitor (GBM) onboard the NASA Fermi Gamma-ray Space Satellite,<sup>1,2</sup> and confirmed by *INTEGRAL*.<sup>3</sup> It was subsequently associated with GW170817, a gravitational wave signal reported by the LIGO/Virgo Collaboration about 40 min after the Fermi-GBM circular.<sup>4</sup> These initial data were then associated with the optical-infrared-ultraviolet source AT 2017gfo, which started to be observed about 12 h ( $\approx 4 \times 10^4$  s) after the GRB trigger.<sup>5–8</sup> Further data of GRB 170817A have been in the mean time acquired in the X-rays and in the radio from  $10^6$  s after the GRB trigger, and still ongoing.

It has been well established that short GRBs are produced by neutron star binary (NS-NS) mergers.<sup>9–11</sup> Therefore, it is not surprising that GRB 170817A was labeled as such from the very beginning,<sup>1,4,12</sup> despite the fact that it had been soon recognized that GRB 170817A was observationally very different from typical short GRBs.<sup>2</sup> Indeed, a comparison of GRB 170817A in the gamma-rays, X-rays and in the optical with typical short GRBs led<sup>13</sup> to suggest that GRB 170817A looks more like a white dwarf binary (WD-WD) merger rather than an abnormal, special or unique NS-NS merger.<sup>14</sup> Identified additional sources similar to GRB 170817A and have proposed an alternative interpretation of them as WD-WD mergers.

In the mean time,  $10^8$  s of data of GRB 170817A have been acquired in the X-rays, in the optical, and in the radio wavelengths, besides just the MeV radiation of the prompt emission. These observations have indeed led to alternative explanations. In fact

- The NS-NS merger interprets the associated optical counterpart AT 2017gfo as a nuclear *kilonova* produced by the decay of *r*-process, which yields in the matter ejected in the merger.<sup>5–8</sup>
- The experimental confirmation of the nuclear *kilonova* needs a univocal spectroscopic identification of the atomic species present in the ejecta.<sup>15–19</sup> This has not been achievable in view of lack of available accurate models of atomic spectra, the nuclear reaction network, density profile, and details of the radiative transport (opacity). Other mechanisms can also explain the photometric properties of AT 2017gfo, for instance the cooling of the expanding ejecta of a WD-WD merger.<sup>13,20</sup> We will further elaborate this scenario in this paper.
- The NS-NS merger leading to a jet propagating throughout the ejected matter appears in conflict with recent data by the *Chandra* X-ray Telescope at  $10^7$ – $10^8$  s after the GRB trigger.<sup>21,22</sup>

In view of all the above, we here explore further and extend the suggestion by Ref. 13 of GRB 170817A being the product of a WD-WD merger, adding new observations all the way up to  $10^8$  s.

- The possibly observed re-brightening in the X-ray afterglow of GRB 170817A at 1000 days agrees with the predicted appearance of the pulsar-like activity of the newborn WD from a WD-WD merger.<sup>13,20</sup>
- The rate of GRB 170817A-like events is well explained by the rate of WD-WD mergers.<sup>13,20</sup>
- Interestingly, the host galaxy of GRB 170817, NGC 4993 distant at about 40 Mpc, is an old elliptical galaxy.<sup>1</sup> Elliptical old galaxies are amply recognized as preferred sites of type Ia supernovae produced by the so-called double-degenerate scenario, namely, by WD-WD mergers.<sup>23,24</sup>

The aim of this paper is to extend the treatment of Ref. 20 on WD-WD mergers, and exploit the analogy with the synchrotron emission in the X-rays, optical and radio bands in the afterglow of long GRBs<sup>25–28</sup> to determine the emission of WD-WD mergers across the electromagnetic spectrum. Then, we apply the above considerations to the luminosity in the X-rays, optical and radio wavelengths observed in the afterglow of GRB 170817A.

We here show the prominent role of rotation and its effect on the synchrotron emission from the interaction of the newborn rotating object with the ejected matter in the merger. This process is energetically predominant and has been neglected in traditional simulations of these merging systems. The ejected matter expands in the magnetic field of the newborn fast rotating WD, which injects rotational and accretion energy into the expanding ejecta. While expanding, the ejecta radiate energy across the electromagnetic spectrum due to thermal cooling and synchrotron emission. We evidence that the newborn WD becomes observable as a pulsar when the synchrotron radiation fades off. The amount of mass ejected, the mass, rotation period, and strength of the magnetic field of the newborn WD are the most important features that determine the electromagnetic emission of the system.

We show that the above process leads to a hard-to-soft evolution of the emitted radiation with specific decreasing luminosities that approach a distinct power-law behavior. The late-time luminosity is dominated by the pulsar activity of the newborn object, therefore the asymptotic power-law gives information on the parameters of the newborn central object. The total energy radiated during the whole evolution is dominated by the energy injected and radiated from the central WD, so it is covered by its rotational energy.<sup>29</sup> Energy and angular momentum conservation allow to infer, for instance, the spin and magnetic field of the newborn WD directly from the light-curve of the source, prior to any detailed fit of the observational data with the theoretical model (see Refs. 26–28, for the case of long GRBs).

We apply the above considerations to GRB 170817A and show the agreement of the WD-WD merger scenario with all the available observational multiwavelength data from the gamma-rays all the way down to the radio wavelengths. This paper is

organized as follows. In Sec. 2, we formulate the general physical conditions of the WD-WD coalescence that constrain the parameters of the newborn WD formed at merger. Section 3 presents an estimate of a possible mechanism leading to a gamma-ray prompt emission in these mergers, and how it compares with GRB 1780817A. Section 4 is devoted to the analysis of the WD-WD post-merger early optical-infrared-ultraviolet emission by thermal cooling, and how it compares with AT 2017gfo. In Sec. 5, we present the theoretical model of the synchrotron emission powered by the newborn WD, and how it leads to a multiwavelength emission (from the radio to the gamma-rays). A comparison with the emission of GRB 170817A  $t \gtrsim 10^6$  s is presented. We outline our conclusions in Sec. 6. We use cgs units throughout.

## 2. Merging Binary and Post-Merger Remnant

The fate of the central remnant of a WD-WD merger with a total mass near (below or above) the Chandrasekhar mass limit can be one of the three possibilities: (i) a stable newborn WD, (ii) a type Ia supernova, or (iii) a newborn neutron star. Sub-Chandrasekhar remnants can lead either to (i) and (ii), while super-Chandrasekhar remnants produce either (ii) or (iii). Super-Chandrasekhar remnants are supported by angular momentum, so they are less dense and metastable objects whose final fate is delayed until the excess of angular momentum is lost, e.g. via magnetic braking, inducing its compression.<sup>30,31</sup>

We are here interested in WD-WD mergers leading to stable, massive, sub-Chandrasekhar newborn WDs with a mass  $\gtrsim 1.0M_{\odot}$ . These WDs can have rotation periods as short as  $\sim 0.5$  s (see Ref. 32) and can also avoid the trigger of unstable burning leading to type Ia supernova providing its central density is kept under some critical value of a few  $10^9$  g cm<sup>-3</sup>.<sup>31</sup>

Numerical simulations of WD-WD mergers show that the merged configuration has in general three distinct regions:<sup>31,33-39</sup> a rigidly rotating, central WD, on top of which there is a hot, convective corona with differential rotation, surrounded by a rapidly rotating Keplerian disk. Roughly, half of the mass of the secondary star, which is totally disrupted, goes to the corona while the other half goes to the disk. The above implies that little mass is ejected in the merger. Numerical simulations show that the amount of expelled mass is approximated by Ref. 39

$$m_{\text{ej}} \approx h(q) M, \quad h(q) = \frac{0.0001807}{-0.01672 + 0.2463q - 0.6982q^2 + q^3}, \quad (1)$$

where

$$M = m_1 + m_2 = \left( \frac{1+q}{q} \right) m_2, \quad (2)$$

is the total binary mass, and  $q \equiv m_2/m_1 \leq 1$  is the binary mass ratio. Equation (1) tells us that for a fixed total binary mass, the larger the mass symmetry, the smaller the mass that is ejected. Thus, for a fully symmetric mass ratio,  $q = 1$ , the amount of expelled matter becomes  $m_{\text{ej}} \approx 3.4 \times 10^{-4}M$ .

WD-WD merger simulations show two important ingredients for our model. First, the central remnant (the newborn WD) is degenerate, namely, massive ( $\gtrsim 1.0M_\odot$ ), fast rotating, and magnetized.<sup>31</sup> Second, although the amount of expelled matter is negligible with respect to the total mass of the system, the ejecta are crucial for the electromagnetic emission in the post-merger evolution.

We start with a double WD with components of mass  $m_1$  and  $m_2$ , with corresponding radii  $R_1$  and  $R_2$ . We shall make use of the analytic mass-radius relation<sup>40</sup>

$$\frac{R_i}{R_\odot} = \frac{0.0225}{\bar{\mu}} \frac{\sqrt{1 - (m_i/M_{\text{crit}})^{4/3}}}{(m_i/M_{\text{crit}})^{1/3}}, \quad (3)$$

where  $\bar{\mu} \approx 2$  is the molecular weight, and

$$M_{\text{crit}} \approx \frac{5.816M_\odot}{\bar{\mu}^2} \approx 1.4 M_\odot, \quad (4)$$

is the critical mass of (carbon) WDs,  $M_\odot$  and  $R_\odot$  are the solar mass and radius. Since little mass is expelled, we estimate the newborn WD mass as

$$m_{\text{wd}} \approx M - m_d = m_1 + m_2 - m_d \approx \left(\frac{2+q}{2q}\right) m_2, \quad (5)$$

where we have approximated the disk mass by  $m_d \approx m_2/2$ , according to numerical simulations. Combining Eqs. (2) and (5), we obtain

$$M \approx 2 \left(\frac{1+q}{2+q}\right) m_{\text{wd}}, \quad (6)$$

and using Eqs. (1) and (6), we obtain

$$m_{\text{wd}} \approx \left(\frac{2+q}{1+q}\right) \frac{m_{\text{ej}}}{2h(q)}. \quad (7)$$

As we shall see in Sec. 6, the above equations allow us to infer, from the inferred mass of the ejecta from the fit of the multiwavelength data of GRB 170817A, the parameters of the merging components and of the newborn WD.

### 3. The Prompt $\gamma$ -Ray Emission

GRB 170817 was first detected by the GBM on board the *Fermi* satellite.<sup>2</sup> The gamma-ray emission was confirmed by *INTEGRAL*.<sup>3</sup>

GRB 170817A is as a short burst with a duration ( $T_{90}$ ) of 2.048s, as reported in the NASA/HEASARC database.<sup>a</sup> We performed a Bayesian spectral analysis of the *Fermi*-GBM data by using the Multi-Mission Maximum Likelihood Framework (3ML, see Ref. 41), and the best model is selected by comparing the deviance information criterion (DIC, see Refs. 42, 43). We first fit the data with a single power-law function, and obtained a DIC value of 3138. We then compare this model to the blackbody (Planck) spectrum over the same time interval, and obtained a

<sup>a</sup><https://heasarc.gsfc.nasa.gov/W3Browse/fermi/fermigbrst.html>.



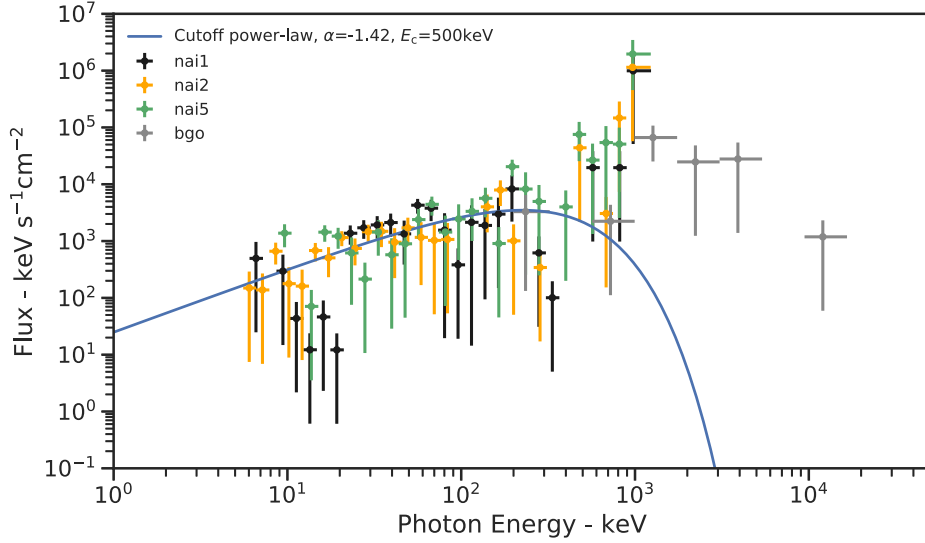


Fig. 1. Spectral fits of  $\nu F_\nu$  spectrum for the entire pulse ( $-0.320$  to  $1.984$  s) of the *Fermi*-GBM observation of GRB 170817A. This time interval is the best fit with a Comptonized function, with a cutoff energy  $E_c = 500 \pm 317$  keV,  $\alpha = -1.42 \pm 0.18$ , and time-averaged flux is  $(1.84 \pm 0.82) \times 10^{-7}$  erg s $^{-1}$  cm $^{-2}$  (see Sec. 3 for details of the data analysis).

DIC value of 3146. We also fit the data with a Comptonized (i.e. a cutoff power-law, hereafter CPL) function, and obtained a DIC value of 3128. The CPL model leads to a DIC improvement of 10 with respect to the power-law model, and of 18 with respect to the blackbody model, which suggests the CPL as the model that best fits the data. We refer to Refs. 44–48 for a detailed Bayesian analysis of the data and the reduction procedure applied to GRBs.

As discussed above, the entire pulse ( $-0.320$  to  $1.984$  s) is best fitted by a CPL with a cutoff energy  $E_c = 500 \pm 317$  keV and power-law index  $\alpha = -1.42 \pm 0.18$  (see Fig. 1). The time-averaged flux is  $(1.84 \pm 0.82) \times 10^{-7}$  erg s $^{-1}$  cm $^{-2}$ . With the measured cosmological redshift of  $z = 0.009783$ , corresponding to a source distance of  $\approx 43$  Mpc, the isotropic energy released in this time interval is estimated to be  $(4.16_{-1.84}^{+3.15}) \times 10^{46}$  erg. The nonthermal energy released at energies above 1 MeV corresponds to only 2.82% of the emission corresponding to  $\approx 1.17 \times 10^{45}$  erg. Therefore, most of the energy is released below MeV energies, which corresponds to  $\approx 4.04 \times 10^{46}$  erg.

We here advance the possibility that the  $\gamma$ -ray prompt emission of GRB 170817A occurs from activity in the merged magnetosphere. We could think of the WD pulsar magnetosphere in an analogous way as the NS pulsar magnetosphere, therefore the presence of the strong magnetic field and rotation produces the presence of a electric field by Faraday (unipolar) induction.<sup>49</sup> Numerical simulations show that the merger forms a transient hot corona with temperatures  $10^8$ – $10^9$  K that cools down rapidly mainly by neutrino emission.<sup>31</sup> Therefore, thermal production of  $e^+e^-$  pairs can occur for short time before it cools below the pair formation energy threshold. The charged particles are accelerated by the electric field to then follow the magnetic field lines generating both curvature and synchrotron photons. Since

the magnetic field lines are curved, photon–photon collisions occur roughly in all directions, so the majority of the photons with energy in excess of  $m_e c^2$  can decay into pairs again and generate a thermal plasma. A minority of photons escape along the rotation axis (see below), leading to the observed nonthermal emission above 1 MeV.

The cross-section of the  $\gamma\gamma \rightarrow e^- e^+$  process is given by

$$\sigma_{\gamma\gamma} = \frac{3\sigma_T}{16}(1 - \bar{\beta}^2) \left[ 2\bar{\beta}(\bar{\beta}^2 - 2) + (3 - \bar{\beta}^4) \ln \left( \frac{1 + \bar{\beta}}{1 - \bar{\beta}} \right) \right], \quad (8)$$

where  $\sigma_T \approx 6.65 \times 10^{-25} \text{ cm}^2$  is the Thomson cross-section, and  $\bar{\beta}$  is the  $e^-$  (or  $e^+$ ) velocity (in units of  $c$ ) in the center of momentum frame

$$\bar{\beta} \equiv \sqrt{1 - \frac{2}{\bar{\epsilon}_{\text{inc}} \bar{\epsilon}_{\text{tgt}} (1 - \cos \theta)}}, \quad (9)$$

being  $\bar{\epsilon}_{\text{inc,tgt}} \equiv \epsilon_{\text{inc,tgt}}/(m_e c^2)$  the normalized energy of the incident and target photons which collide making an angle  $\theta$  measured in laboratory frame.

Photons emitted along the curved magnetic field lines are expected to be absorbed since they will be radiated nearly isotropically. In this case,  $\langle \cos \theta \rangle \sim 0$  and the cross-section becomes maximal at  $\bar{\epsilon}_{\text{inc}} \bar{\epsilon}_{\text{tgt}} \approx 4$ , and  $\sigma_{\gamma\gamma} \approx \sigma_T/4$ . Under these conditions, the  $\gamma\gamma$  optical depth is

$$\tau_{\gamma\gamma} \approx n_{\text{tgt}} \sigma_{\gamma\gamma} r \approx \frac{L_{\text{tgt}} \sigma_{\gamma\gamma}}{4\pi r c \epsilon_{\text{tgt}}} \approx \frac{L_{\text{tgt}} \bar{\epsilon}_{\text{inc}} \sigma_T}{64\pi r m_e c^3}, \quad (10)$$

where  $r$  is the source size and  $n_{\text{tgt}}$  is the density of target photons, which we have estimated as  $n_{\text{tgt}} \approx L_{\text{tgt}}/(4\pi r^2 c \epsilon_{\text{tgt}})$ , where  $L_{\text{tgt}}$  is the luminosity emitted at energies larger than the target photon energy.

For a transient hot corona, most photons are emitted at energies around the peak of the Planck spectrum, which for a temperature of a few  $10^9$  K implies  $\epsilon_{\text{inc}} \sim \epsilon_{\text{tgt}} \sim 3kT \sim 1 \text{ MeV}$ . Assuming a source size  $r \sim R_{\text{wd}} \sim 10^9 \text{ cm}$ , and a target luminosity  $L_{\text{tgt}} \sim 4\pi R_{\text{wd}}^2 \sigma T^4 \sim 10^{51} \text{ erg s}^{-1}$ , the optical depth (10)  $\tau_{\gamma\gamma} \sim 10^{10}$ .

The above conditions imply that most photons interact generating an optically thick pair plasma which explains the dominant blackbody component observed by *Fermi*-GBM. The observed nonthermal component is explained if  $\approx 1\%$  of the photons escape from the system, which can occur near the rotation axis of the WD. There, the interaction angle could approach values as small as  $\cos \theta \sim 1$ , thereby reducing drastically the photon–photon cross-section.

#### 4. Thermal Cooling of the Ejecta as Origin of the Kilonova

The second observed emission associated with GRB 170817A is the optical counterpart at about 0.5 d after the *Fermi*-GBM trigger, i.e. AT 2017gfo.<sup>7,8,50,51</sup> For the modeling of this thermal emission of the expanding ejecta, we must take into account that in a nonhomogeneous distribution of matter, the layers reach transparency at

different times. For simplicity, we consider the ejected matter as a spherically symmetric distribution extending at radii  $r_i \in [R_*, R_{\max}]$ , with corresponding velocities  $v_i \in [v_*, v_{\max}]$ , in self-similar expansion

$$r_i(t) = r_{i,0} \hat{t}^n, \quad v_i(t) = n \frac{r_i(t)}{t} = v_{i,0} \hat{t}^{n-1}, \quad (11)$$

where  $\hat{t} \equiv t/t_*$ , being  $t_* \equiv nR_{*,0}/v_{*,0}$  the characteristic expansion timescale, which is the same for all layers in view of the condition of self-similarity. Here,  $r_{i,0}$  and  $v_{i,0}$  are the initial radius and velocity of the layer (so at times  $t \ll t_*$  close to the beginning of the expansion. The case  $n = 1$  corresponds to a uniform expansion.

The density at the position  $r = r_i$  is given by

$$\rho(r_i) = \frac{(3-m)}{4\pi} \frac{m_{\text{ej}}}{R_{*,0}^3} \left[ \left( \frac{R_{\max}}{R_*} \right)^{3-m} - 1 \right]^{-1} \left( \frac{r_i}{R_*} \right)^{-m} \hat{t}^{-3n}, \quad (12)$$

where  $m_{\text{ej}}$  is the total mass of the ejecta, and  $m$  is a positive constant. The distribution and time evolution given by Eq. (12) ensure that at any time the total mass of the ejecta, i.e. the volume integral of the density, is always equal to  $m_{\text{ej}}$ .

We divide the ejecta into  $N$  shells defined by the  $N + 1$  radii

$$r_{i,0} = R_{*,0} + i \frac{(R_{\max,0} - R_{*,0})}{N}, \quad i = 0, 1, \dots, N, \quad (13)$$

so the width and mass of each shell are, respectively,  $\Delta r = (R_{\max,0} - R_{*,0})/N$ , and

$$m_i = \int_{r_i}^{r_{i+1}} 4\pi r^2 \rho(r) dr \approx \frac{4\pi}{m-3} r_i^2 \rho(r_i) \Delta r, \quad (14)$$

so in view of the decreasing density with distance, the inner layers are more massive than the outer layers. The number of shells to be used must be chosen to satisfy the constraint that the sum of the shells mass gives the total ejecta mass, i.e.

$$\sum_{j=1}^N m_j = m_{\text{ej}}, \quad (15)$$

where we have introduced the discrete index  $j = i + 1$  to differentiate the counting of the shells from the counting of radii given by Eq. (13). In this work, we use  $N = 100$  shells which ensures that Eq. (15) is satisfied with 99% of accuracy.

Under the assumption that the shells do not interact with each other, we can estimate the evolution of the  $i$ th shell from the energy conservation equation

$$\dot{E}_i = -P_i \dot{V}_i - L_{\text{cool},i} + H_{\text{inj},i}, \quad (16)$$

where  $V_i = (4\pi/3)r_i^3$ ,  $E_i$ , and  $P_i$  are the volume, energy, and pressure of the shell, while  $H_{\text{inj},i}$  is the power injected into the shell, and

$$L_{\text{cool},i} \approx \frac{cE_i}{r_i(1 + \tau_{\text{opt},i})}, \quad (17)$$

is the bolometric luminosity radiated by the shell, being  $\tau_{\text{opt},i}$  the optical depth.

Assuming a spatially constant, gray opacity throughout the ejecta, the optical depth of the radiation emitted by the  $i$ th layer is given by

$$\tau_{\text{opt},i} = \int_{\infty}^{r_i} \kappa \rho(r) dr = \int_{R_{\text{max}}}^{r_i} \kappa \rho(r) dr = \tau_{i,0} \hat{t}^{-2n}, \quad (18)$$

$$\tau_{i,0} \equiv \frac{m-3}{m-1} \frac{\kappa m_{\text{ej}}}{4\pi R_{*,0}^2} \frac{\left[ \left( \frac{R_*}{r_i} \right)^{m-1} - \left( \frac{R_*}{R_{\text{max}}} \right)^{m-1} \right]}{\left[ 1 - \left( \frac{R_*}{R_{\text{max}}} \right)^{m-3} \right]}, \quad (19)$$

where we have used Eq. (12), and  $\kappa$  is the opacity.

We adopt a radiation-dominated equation of state for the ejecta and, improving with respect to Ref. 20, accounting for the radiation pressure, i.e.

$$E_i = 3P_i V_i + L_{\text{cool},i}^{\text{abs}} \frac{r_i}{c}. \quad (20)$$

The power injected into the ejecta originates from the newborn central WD.<sup>20</sup> This energy is absorbed and thermalized becoming a heating source for the expanding matter. The power-law decreasing density (12) suggests that the inner the layer the more radiation it should absorb. In order to account for this effect, we weigh the heating source for each shell using the mass fraction, i.e.

$$H_{\text{inj},i} = \frac{m_i}{m_{\text{ej}}} H_{\text{inj}}, \quad (21)$$

where  $m_i$  is the shell's mass, and adopts the following form for the heating source:

$$H_{\text{inj}} = H_0 \left( 1 + \frac{t}{t_c} \right)^{-\delta}, \quad (22)$$

where  $H_0$  and  $\delta$  are model parameters. According to Ref. 20, power from fallback accretion with  $H_0 \sim 10^{45} \text{ erg s}^{-1}$ ,  $\delta \sim 1.3$ , and  $t_c \sim t_*$  (see Table 1), dominates the energy release from the newborn WD at these early-times.

The photospheric radius at a time  $t$  is given by the position of the shell that reaches transparency at that time. Namely, it is given by the position of the shell whose optical depth fulfills  $\tau_{\text{opt},i}[r_i(t)] = 1$ . Using Eq. (18), we obtain

$$R_{\text{ph}} = \frac{R_{\text{max},0} \hat{t}^n}{\left[ 1 + \frac{m-1}{m-3} \frac{4\pi R_{*,0}^2}{\kappa m_{\text{ej}}} \left[ 1 - \left( \frac{R_*}{R_{\text{max}}} \right)^{m-3} \right] \left( \frac{R_{\text{max}}}{R_*} \right)^{m-1} \hat{t}^{2n} \right]^{\frac{1}{m-1}}}. \quad (23)$$

Equation (23) shows that when the entire ejecta is optically thick,  $R_{\text{ph}} = R_{\text{max}}$ . Then, the transparency reaches the inner shells all the way to the instant over which

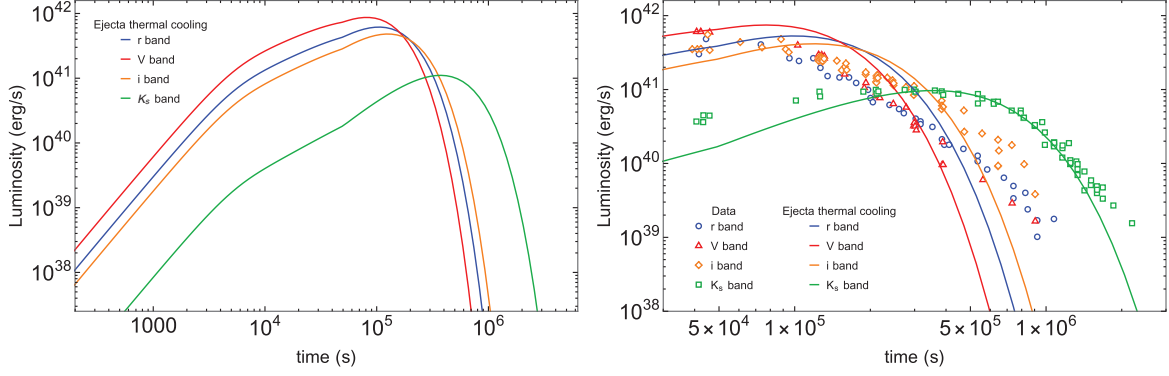


Fig. 2. Left: emission from the expanding, cooling ejecta at early-times in the visible ( $r$  and  $V$ ) and in the infrared ( $i$  and  $K_s$ ) bands, following the theoretical treatment of Sec. 6. Right: zoomed view of the left panel figure at the times relevant for the comparison with the observational data of AT 2017gfo.<sup>7,8,50,51</sup>

$R_{\text{ph}} = R_*$ , reached at  $t = t_{\text{tr},*}$ , when the entire ejecta is transparent. The time  $t_{\text{tr},*}$  is found from the condition  $\tau_{\text{opt},*}[R_*(t_{\text{tr},*})] = 1$ , and is given by

$$\hat{t}_{\text{tr},*} = \left\{ \frac{m-3}{m-1} \frac{\kappa m_{\text{ej}}}{4\pi R_{*,0}^2} \left( \frac{R_*}{R_{\text{max}}} \right)^{m-1} \frac{\left[ \left( \frac{R_{\text{max}}}{R_*} \right)^{m-1} - 1 \right]^{\frac{1}{2n}}}{\left[ 1 - \left( \frac{R_*}{R_{\text{max}}} \right)^{m-3} \right]} \right\}. \quad (24)$$

At  $t < t_{\text{tr},*}$ , the photospheric radius evolves as  $R_{\text{ph}} \propto t^{\frac{n(m-3)}{m-1}}$ , while at later times,  $R_{\text{ph}} \propto t^n$ . For the parameters of our system,  $t_{\text{tr},*} \sim 10^5$  s (see Fig. 2).

The bolometric luminosity is given by the sum of the luminosity of the shells

$$L_{\text{bol}} = \sum_{j=1}^N L_{\text{cool},j}, \quad (25)$$

so the effective temperature of the thermal blackbody radiation,  $T_s$ , can be obtained from the Stefan–Boltzmann law, i.e.

$$T_s = \left( \frac{L_{\text{bol}}}{4\pi R_{\text{ph}}^2 \sigma} \right)^{1/4}, \quad (26)$$

where  $\sigma$  is the Stefan–Boltzmann constant. The power per unit frequency, per unit area, is given by Planck’s spectrum

$$B_\nu(\nu, t) = \frac{2\pi h \nu^3}{c^2} \left[ e^{\frac{h\nu}{k_b T_s(t)}} - 1 \right]^{-1}, \quad (27)$$

where  $\nu$  is the radiation frequency,  $h$  and  $k_b$  are the Planck and Boltzmann constants. Most of the thermal cooling is radiated in the visible, infrared and ultraviolet wavelengths, which we refer to as optical. Therefore, the spectral density (power

Table 1. Numerical values of the theoretical model parameters that determine the thermal cooling of the expanding ejecta which fits the data of AT 2017gf0 shown in Fig. 2.

Parameter	Value
$n$	1.22
$m$	9.00
$m_{\text{ej}} (10^{-3} M_{\odot})$	1.00
$R_{*,0} (10^{11} \text{ cm})$	4.00
$v_{*,0} (10^9 \text{ cm s}^{-1})$	1.00
$\kappa (\text{cm}^2 \text{ g}^{-1})$	0.20
$H_0 (10^{45} \text{ erg s}^{-1})$	8.16
$\delta$	1.30
$t_c/t_*$	1.00

per unit frequency) given by the thermal cooling at a frequency  $\nu$  is

$$J_{\text{cool}}(\nu, t) = 4\pi R_{\text{ph}}^2(t) B_{\nu}(\nu, t), \quad (28)$$

and the luminosity radiated in the frequency range  $[\nu_1, \nu_2]$  can be then obtained as

$$L_{\text{cool}}(\nu_1, \nu_2; t) = \int_{\nu_1}^{\nu_2} J_{\text{cool}}(\nu, t) d\nu. \quad (29)$$

Figure 2 shows the luminosity in the  $r$ ,  $V$ ,  $i$ , and  $K_s$  energy bands obtained from Eq. (29), and compares them with the corresponding observations of AT 2017gf0. For the fit of these data, we have set the parameters, as shown in Table 1.

The value of the parameter  $v_{\text{max},0}$  does not have any appreciable effect in the evolution, so it cannot be constrained from the data. This happens because most of the mass is concentrated in the innermost layers, so they dominate the thermal evolution. For self-consistency of the model, we have set  $v_{\text{max},0} = 2v_{*,0}$ , a value that keeps the outermost shell velocity well below the speed of light at any time in the evolution. As for the initial value of the internal energy of the shells,  $E_i(t_0)$ , we have set them to the initial kinetic energy of each layer,  $E_i = (1/2)m_i v_i(t_0)^2$ .

There is a general agreement of the model with the observations, although it cannot catch any detailed observational feature. There are some extensions to the present model that can increase its accuracy. For instance, we can abandon the assumption of spherical expansion allowing the layers to have a latitude-dependent velocity. Such a detailed treatment goes beyond our present scope that is to show the broad agreement of a WD-WD merger model with the multiwavelength data but not a dedicated model of AT 2017gfo.

## 5. Synchrotron and WD Pulsar Radiation

We have shown above that the expanding matter reaches full transparency at about  $10^5$  s. After this time, the emission originated from the newborn WD as well as the one originated in the ejecta itself, become observable. We here follow the treatment

in Ref. 28 for the explanation of the X-ray afterglow of long GRBs as originating from a newborn spinning NS powering the expanding SN. Here, we simulate the emission generated in the X-rays, in the optical, and in the radio by the synchrotron emission of electrons accelerated in the expanding magnetized ejecta, together with the emission of the newborn spinning WD pulsar.

We show below that synchrotron radiation originating in the merger ejecta dominates the emission up to nearly  $10^8$  s. We find evidence of the newborn WD pulsar emission, owing to magnetic dipole braking, in the X-ray luminosity at approximately  $10^6$  s, when the synchrotron radiation was not fully overwhelming yet, and then at times  $10^8$  s, when the synchrotron luminosity sufficiently decreased for the WD pulsar emission to be fully observed (see Fig. 4 for details).

### 5.1. *Synchrotron emission by the expanding ejecta*

In this model, a fraction of the kinetic energy of the merger ejecta is used to accelerate electrons that, owing to the presence of the magnetized medium provided by the newborn WD, convert their kinetic energy into synchrotron radiation. The electrons are continuously injected from the newborn WD into the ejecta. The magnetic field threading every ejecta layer evolves as

$$B_i(t) = B_{i,0} \left[ \frac{r_{i,0}}{r_i(t)} \right]^\mu = \frac{B_{i,0}}{\hat{t}^{\mu n}}, \quad (30)$$

where  $B_i^{(0)}$  is the magnetic field strength at  $r = r_{i,0}$ , and  $\mu$  gives the spatial dependence of the field at large distance from the newborn WD.

Because the electrons lose their energy very efficiently by synchrotron radiation (see details below), we can simplify our calculation by adopting that the radiation originates from the innermost layer of the ejecta, which we will denote to as  $R_*$ . The evolution of this layer, following Eq. (11), is given by  $R_*(t) = R_{*,0} \hat{t}^n$ ,  $v_*(t) = v_{*,0} \hat{t}^{n-1}$ ,  $t_* = nR_{*,0}/v_{*,0}$ , and the magnetic field at its varying position decreases with time as  $B_*(t) = B_{*,0} \hat{t}^{-n}$ .

The evolution of the distribution of radiating electrons is determined by the kinetic equation accounting for the particle energy losses<sup>52</sup>

$$\frac{\partial N(E, t)}{\partial t} = -\frac{\partial}{\partial E} [\dot{E} N(E, t)] + Q(E, t), \quad (31)$$

where  $Q(E, t)$  is the number of injected electrons per unit time, per unit energy, and  $\dot{E}$  is the electron energy loss rate.

In our case, we assume electrons are subjected to adiabatic losses by expansion and synchrotron radiation losses, i.e.

$$-\dot{E} = \frac{E}{\tau_{\text{exp}}} + \beta B_*(t)^2 E^2, \quad (32)$$

where  $\beta = 2e^4/(3m_e^4c^7)$ ,  $B(t)$  is the magnetic field, and

$$\tau_{\text{exp}} \equiv \frac{R_*}{v_*} = \frac{t}{n} = \frac{t_*}{n} \hat{t}, \quad (33)$$

is the characteristic timescale of expansion.

In order to find the solution to the kinetic equation (31), we follow the treatment of Ref. 53, adapted to our specific physical situation. We consider a distribution of the injected particles following a power-law behavior, i.e.

$$Q(E, t) = Q_0(t)E^{-\gamma}, \quad 0 \leq E \leq E_{\text{max}}, \quad (34)$$

where  $\gamma$  and  $E_{\text{max}}$  are parameters to be determined from the observational data, and  $Q_0(t)$  can be related to the power released by the newborn WD and injected into the ejecta. We assume that the injected power has the form

$$L_{\text{inj}}(t) = L_0 \left(1 + \frac{t}{t_q}\right)^{-k}, \quad (35)$$

where  $L_0$ ,  $t_q$ , and  $k$  are model parameters. We have not chosen arbitrarily the functional form of Eq. (35), actually, both the powers released by magnetic dipole braking and by fallback accretion (see Eq. (22)) obey this sort of time evolution.

Therefore, the function  $Q_0(t)$  can be found from

$$L_{\text{inj}}(t) = \int_0^{E_{\text{max}}} E Q(E, t) dE = \int_0^{E_{\text{max}}} Q_0(t) E^{1-\gamma} dE = Q_0(t) \frac{E_{\text{max}}^{2-\gamma}}{2-\gamma}, \quad (36)$$

which using Eq. (35) leads to

$$Q_0(t) = q_0 \left(1 + \frac{t}{t_q}\right)^{-k}, \quad (37)$$

where  $q_0 \equiv (2-\gamma)L_0/E_{\text{max}}^{2-\gamma}$ .

Having specified the evolution of the ejecta by Eq. (11) and the magnetic field by Eq. (30), as well as the rate of particle injection given by Eqs. (34) and (37), we can now proceed to the integration of the kinetic equation (31).

First, we find the evolution of a generic electron injected at time  $t = t_i$  with energy  $E_i$ . Integration of Eq. (32) leads to the energy evolution

$$E = \frac{E_i (t_i/t)^n}{1 + \mathcal{M} E_i t_i^n \left[ \frac{1}{\hat{t}_i^{n(1+2\mu)-1}} - \frac{1}{\hat{t}^{n(1+2\mu)-1}} \right]}, \quad (38)$$

where we have introduced the constant

$$\mathcal{M} \equiv \frac{\beta B_{*,0}^2 t_*^{1-n}}{n(1+2\mu)-1}, \quad (39)$$

which have units of  $1/(\text{energy} \times \text{time}^n)$ . In the limit  $t/t_* \gg 1$  and  $n = 1$ , Eq. (38) reduces to Eq. (3.3) of Ref. 53, and in the limit  $t_* \rightarrow \infty$ , reduces to the solution presented in Sec. 3 of Ref. 52 for synchrotron losses in a constant magnetic field.



The solution of Eq. (31) is given by

$$N(E, t) = \int_E^\infty Q[E_i, t_i(t, E_i, E)] \frac{\partial t_i}{\partial E} dE_i, \quad (40)$$

where the relation  $t_i(t, E_i, E)$  is obtained from Eq. (38).

We can write  $N(E, t)$  as a piecewise function of time, separating it into different time intervals that allow simplifications and approximations depending upon the physical situation at work, and on the behavior of the energy injection given by Eq. (37). All the observational data of GRB 170817A are contained in the time interval  $t < t_b$  and at electron energies in the range  $E_b < E < E_{\max}$  (see definition of  $t_b$  and  $E_b$  below) where synchrotron losses are dominant. Under these conditions, the solution of Eq. (40) is well approximated by

$$N(E, t) \approx \begin{cases} \frac{q_0}{\beta B_{*,0}^2 (\gamma - 1)} \hat{t}^{2\mu n} E^{-(\gamma+1)}, & t < t_q, \\ \frac{q_0}{\beta B_{*,0}^2 (\gamma - 1)} \left(\frac{t_q}{t_*}\right)^k \hat{t}^{2\mu n - k} E^{-(\gamma+1)}, & t_q < t < t_b, \end{cases} \quad (41)$$

and we have defined

$$E_b = \frac{\hat{t}^{2\mu n - 1}}{\mathcal{M} t_*^n}, \quad t_b = t_* (\mathcal{M} t_*^n E_{\max})^{\frac{1}{2\mu n - 1}}. \quad (42)$$

With the knowledge of  $N(E, t)$ , we can proceed to estimate the synchrotron spectral density (energy per unit time, per unit frequency) from  $J_{\text{syn}}(\nu, t) d\nu = P_{\text{syn}}(\nu, E) N(E, t) dE$ , where  $P_{\text{syn}}(\nu, E)$  is the synchrotron power per unit frequency  $\nu$ , radiated by a single electron of energy  $E$ . Most of the synchrotron radiation is emitted in a narrow range of frequencies around the so-called photon critical frequency,  $\nu_{\text{crit}}$ . Thus, we can assume electrons emit the synchrotron radiation at

$$\nu \approx \nu_{\text{crit}} \approx \alpha B_* E^2, \quad (43)$$

where  $\alpha = 3e/(4\pi m_e^3 c^5)$ . This gives a relation between the electron energy and the radiation frequency, and  $P_{\text{syn}}(\nu, E)$  can be approximated to the bolometric power

$$P_{\text{syn}}(\nu, E) \approx P_{\text{syn}}(\nu) = \beta B_*^2 E^2(\nu) = \frac{\beta}{\alpha} B_* \nu. \quad (44)$$

Within this approximation, the spectral density is

$$J_{\text{syn}}(\nu, t) \approx P_{\text{syn}}(\nu) N(E, t) \frac{dE}{d\nu}. \quad (45)$$

It can be seen from Eq. (41) that in each time and frequency interval we can write

$$N(E, t) = \eta \hat{t}^l E^{-p}, \quad (46)$$

where  $\eta$  and the power-law indexes  $l$  and  $p$  are known constants from Eq. (41). With this, the spectral density (45) becomes

$$J_{\text{syn}}(\nu, t) = \frac{\beta}{2} \alpha^{\frac{p-3}{2}} \eta B_{*,0}^{\frac{p+1}{2}} \hat{t}^{\frac{2l - \mu n(p+1)}{2}} \nu^{\frac{1-p}{2}}. \quad (47)$$

The synchrotron luminosity in the frequencies  $[\nu_1, \nu_2]$  can be then obtained as

$$L_{\text{syn}}(\nu_1, \nu_2; t) = \int_{\nu_1}^{\nu_2} J_{\text{syn}}(\nu, t) d\nu, \quad (48)$$

which in a narrow frequency band from  $\nu_1 = \nu$  to  $\nu_2 = \nu + \Delta\nu$  where  $\Delta\nu/\nu \ll 1$ , can be well approximated as

$$L_{\text{syn}}(\nu, t) \approx \nu J_{\text{syn}}(\nu, t) = \frac{\beta}{2} \alpha^{\frac{p-3}{2}} \eta B_{*,0}^{\frac{p+1}{2}} \hat{t}^{\frac{2l-\mu n(p+1)}{2}} \nu^{\frac{3-p}{2}}, \quad (49)$$

where we have used Eq. (47).

## 5.2. WD evolution and pulsar emission

The central WD emits also pulsar-like radiation. We adopt a dipole + quadrupole magnetic field model.<sup>54</sup> In this model, the total luminosity of spindown is

$$\begin{aligned} L_{\text{sd}} &= L_{\text{dip}} + L_{\text{quad}} \\ &= \frac{2}{3c^3} \Omega^4 B_{\text{dip}}^2 R_{\text{wd}}^6 \sin^2 \chi_1 \left( 1 + \xi^2 \frac{16 R_{\text{wd}}^2 \Omega^2}{45 c^2} \right), \end{aligned} \quad (50)$$

where the parameter  $\xi$  defines the quadrupole to dipole strength ratio as

$$\xi \equiv \sqrt{\cos^2 \chi_2 + 10 \sin^2 \chi_2} \frac{B_{\text{quad}}}{B_{\text{dip}}}, \quad (51)$$

and the modes can be separated:  $\chi_1 = 0$  and any value of  $\chi_2$  for the  $m = 0$  mode,  $(\chi_1, \chi_2) = (90^\circ, 0^\circ)$  for the  $m = 1$  mode, and  $(\chi_1, \chi_2) = (90^\circ, 90^\circ)$  for the  $m = 2$  mode.

The WD evolution is obtained from the energy balance equation

$$-(\dot{W} + \dot{T}) = L_{\text{tot}} = L_{\text{inj}} + L_{\text{sd}}, \quad (52)$$

where  $W$  and  $T$  are, respectively, the gravitational and rotational energies of the newborn WD. We can obtain an analytic, sufficiently accurate solution of Eq. (52) by noticing the following. The power injected in electrons  $L_{\text{inj}}$  is larger than  $L_{\text{sd}}$  and has a shorter timescale with respect to the spindown timescale (see Eq. (35) and Fig. 5), so at  $t < t_q$ , we have  $L_{\text{tot}} \approx L_{\text{inj}}$ . At later times,  $L_{\text{tot}} \approx L_{\text{sd}}$ , so the luminosity should approach the spindown luminosity

$$L_{\text{sd}} = L_{\text{sd},0} \left( 1 + \frac{t}{\tau_{\text{sd}}} \right)^{-s}, \quad (53)$$

where  $s = (n_b + 1)/(n_b - 1)$ , being  $n_b$  the so-called braking index ( $n_b = 3$  for a pure dipole and  $n_b = 5$  for a pure quadrupole), and  $\tau_{\text{sd}}$  is the spindown timescale

$$\tau_{\text{sd}} = \frac{1}{2\mathcal{A}\Omega_0^2}, \quad (54)$$

being  $\mathcal{A} = (2/3)(B_{\text{dip}}^2 R_{\text{wd}}^6)/(c^3 I)$ , and  $\Omega_0$  the initial angular velocity of the WD.

With the above, Eq. (52) is integrated analytically accounting for changes in the WD structure. We describe the WD as an effective Maclaurin spheroid,<sup>55</sup> so the angular velocity,  $\Omega$ , is related to the spheroid eccentricity,  $e$ , by

$$\Omega^2 = 2\pi G\rho g(e), \quad g(e) = \frac{(3 - 2e^2)(1 - e^2)^{1/2} \arcsin(e)}{e^3} - \frac{3(1 - e^2)}{e^2}, \quad (55)$$

where  $\rho = 3m_{\text{wd}}/(4\pi R_{\text{wd}}^3)$  is the density of the sphere with the same volume of the spheroid, being  $m_{\text{wd}}$  and  $R_{\text{wd}}$  the corresponding values of the mass and radius of the WD. The total energy of the spheroid is also a function of the eccentricity as

$$E = T + W = \pi G\rho I_0 \mathcal{F}(e), \quad (56)$$

where  $I_0 = (2/5)m_{\text{wd}}R_{\text{wd}}^2$ , and

$$\mathcal{F}(e) = -2 + \frac{3(1 - e^2)^{2/3}}{e^2} + \frac{(4e^2 - 3)(1 - e^2)^{1/6}}{e^3} \arcsin(e) \approx -\frac{4e^2}{15}, \quad (57)$$

being the last line a series expansion of the function  $\mathcal{F}$  which is accurate enough for low values of the eccentricity and which allows to give an analytic solution for the eccentricity as a function of time.

Then, integrating Eq. (52) and using Eqs. (56) and (57), we obtain

$$e(t) \approx \sqrt{\frac{15\Theta(t)}{4}}, \quad \Omega \approx \sqrt{2\pi G\rho\Theta(t)}, \quad (58)$$

where

$$\Theta(t) = -\mathcal{F}(e_0) + \mathcal{G}(t), \quad (59)$$

$$\mathcal{G}(t) = \frac{L_0 t_q}{\pi G\rho I_0 (k - 1)} \left[ \left(1 + \frac{t}{t_q}\right)^{1-k} - 1 \right] + \frac{L_{\text{sd},0} \tau_{\text{sd}}}{\pi G\rho I_0 (s - 1)} \left[ \left(1 + \frac{t}{\tau_{\text{sd}}}\right)^{1-s} - 1 \right], \quad (60)$$

where  $e_0$  is the initial value of the spheroid eccentricity, and we have used that the function  $g(e)$  in Eq. (55) satisfies  $g(e) = -\mathcal{F}(e)$ , at the order of our approximation. We recall that the moment of inertia changes with the eccentricity as  $I = I_0(1 - e^2)^{-1/3} \approx I_0(1 + e^2/3)$ . The corresponding parameters of the model that explains the afterglow emission at different wavelengths are presented in the next section.

## 6. Model Parameters from the Multiwavelength Data

We proceed to determine the model parameters that best fit the GRB 170817A afterglow. We list in Table 2 the value adopted for each parameter of the present model to fit the multiwavelength data of GRB 170817A shown in Fig. 3. We did not consider here data at MeV energies because it is only present in the prompt emission that we have already discussed in Sec. 3 and is explained by a different mechanism from the synchrotron radiation. There are observations in the 30 MeV–10 GeV energy band by AGILE<sup>67</sup> which give upper limits  $\sim 10^{44}$ – $10^{45}$  erg s<sup>−1</sup> in

Table 2. Numerical values of the theoretical model of synchrotron radiation of Sec. 5 that fit the multiwavelength observational data of GRB 170817A as shown in Fig. 3.

Parameter	Value
$\gamma$	1.13
$k$	2.70
$\mu$	1.50
$L_0$ ( $10^{39}$ erg s $^{-1}$ )	1.80
$B_{*,0}$ ( $10^9$ G)	1.00
$E_{\max}$ ( $10^6 m_e c^2$ )	1.00
$t_q$ ( $10^7$ s)	1.22
$\xi$	0.00
$B_{\text{dip}}$ ( $10^{10}$ G)	1.30
$P$ (s)	12.21

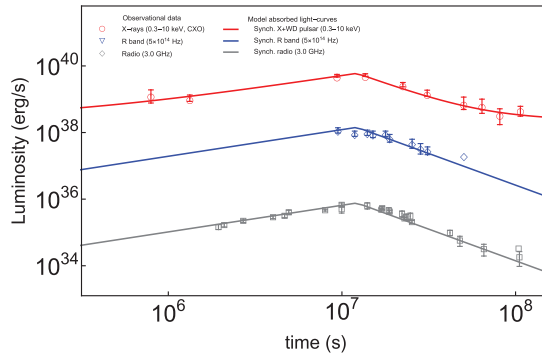


Fig. 3. Comparison of the theoretical (solid curves) light-curves with the observational data (points) of GRB 170817A, in selected energy bands from the radio to the gamma-rays. The radio data at 3 GHz have been taken from Refs. 56–63; the infrared (F606W HST band) data points are retrieved from Refs. 63–64; the X-ray (0.3–10 keV) data from CXO are taken from Ref. 66.

the time interval  $\sim 10^3$ – $10^6$  s. For the parameters of Table 2, no emission is indeed expected at these energies because the maximum synchrotron radiation frequency obtained from Eq. (43) falls below 10 GeV before  $\sim 10^4$  s. The synchrotron luminosity vanishes at these energies at longer times.

Having discussed the gamma-rays, we turn now to the X-rays, optical and radio emission. Figure 3 compares the absorbed luminosity predicted by the model (see Sec. 4), as a function of time, in selected energy bands, with the corresponding observational data of GRB 170817A. We have here included the X-ray data the 0.3–10 keV energy band from the *Chandra* X-ray Observatory (CXO) including the latest observations,<sup>66</sup> the infrared data from the HST at  $\approx 5 \times 10^{14}$  Hz,<sup>63–65</sup> and the radio data at 3 GHz.<sup>56–63,66</sup>

The model shows a satisfactory fit of the data in the X-rays, optical and radio data, both where the luminosity rises, at times  $t \sim 10^6$ – $10^7$  s, and where it fades off, at  $t \gtrsim 10^7$  s. We show a closer view in Fig. 4 of the X-rays, optical, and radio luminosities around the time of the peak luminosity. The synchrotron luminosity

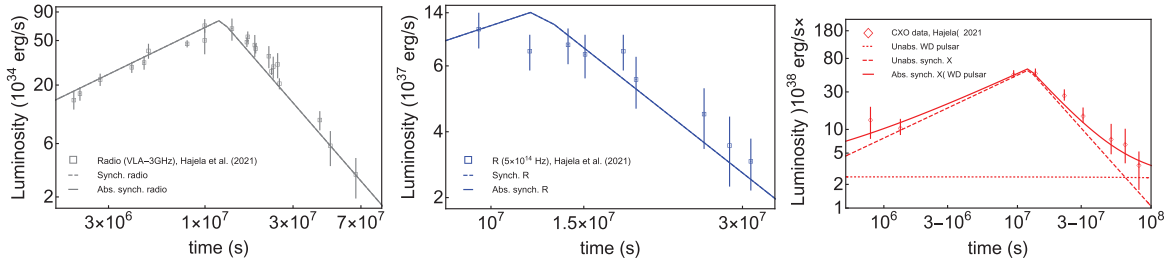


Fig. 4. Zoomed views of the radio (left), optical (center), and X-ray (right) luminosities around transparency. The dashed curves represent the unabsorbed luminosities. The dotted curve in the right panel shows the contribution from the newborn WD pulsar which causes the deviation from the pure synchrotron power-law luminosity at times  $\gtrsim 3 \times 10^7$  s.

rises as a power-law while the energy injection is constant, i.e. up to  $t \approx t_q = 1.2 \times 10^7$  s, while it decreases as a power-law at later times. Probably the most interesting feature that can be seen from these zoomed views appears in the X-ray emission, where we can see in addition to the synchrotron luminosity, evidence of the WD pulsar emission owing to the magnetic dipole braking. The contribution from the pulsar emission is seen first at  $t \sim 10^6$  s when the synchrotron radiation is rising but is still comparable with the pulsar spindown luminosity. Then, the synchrotron luminosity takes over, reaches a peak at approximately  $10^7$  s, and then decreases. While the optical and radio counterparts continue to fade with time as dictated by the synchrotron radiation, the accuracy of the X-ray data of the CXO presented in Ref. 66 allows to identify a clear deviation in the X-rays at a few  $10^7$  s from such a power-law behavior. This is again the signature of the emergence of the WD pulsar emission.

We have used the entity of this deviation to constrain the WD pulsar parameters. Since the pulsar emission depends on the WD radius (see Sec. 5.2), we first estimated the mass of the newborn WD. To accomplish this task, we must apply the considerations of Sec. 2. From the inferred mass of the ejecta,  $m_{\text{ej}} = 10^{-3} M_{\odot}$  (see Table 1), we obtain an upper limit to the binary mass ratio via Eq. (7), by requesting that the newborn object be a stable, sub-Chandrasekhar WD, i.e.  $m_{\text{wd}} \lesssim 1.4 M_{\odot}$ , which leads to  $q \lesssim 0.87$ . According to this maximum mass ratio and the ejecta mass value, Eq. (5) constraints the secondary mass to the range  $m_2 \lesssim 0.85 M_{\odot}$ . With the knowledge of  $q$  and  $m_2$ , Eq. (2) constrains the total binary mass to  $M \lesssim 1.82 M_{\odot}$ . Thus, the primary component must satisfy  $m_1 \lesssim 0.97 M_{\odot}$ .

We assume that the newborn WD is stable, therefore it might have a mass close but not equal to the Chandrasekhar mass, since some mass will be accreted via matter fallback. Hereafter, we shall adopt in our estimates  $m_{\text{wd}} \approx 1.3 M_{\odot}$ , so a radius  $R_{\text{wd}} \approx 3.4 \times 10^8$  cm. With these WD structure parameters, we can proceed to constrain the magnetic field strength and rotation period.

The X-ray emission data show that deviation from the pure synchrotron emission behavior starts at  $\approx 3 \times 10^7$  s, and extends up to when we have data, namely, up to  $\approx 10^8$  s (see Fig. 4). This would suggest to chose this time for the spindown timescale

$\tau_{\text{sd}}$ , but at the moment it is only a lower limit to  $\tau_{\text{sd}}$  because the luminosity did not reach yet the power-law given by the pulsar luminosity.

Hereafter, we assume a pure dipole (i.e.  $\xi = 0$ ) because the fit of the X-ray emission does not require at the moment the quadrupole component (see Fig. 4). By eliminating the rotation angular velocity between the pulsar luminosity (50) and the spindown timescale (54), we can express the magnetic field strength as

$$B_{\text{dip}} = \frac{3^{1/2} c^{3/2} I}{2^{3/2} L_{\text{sd}}^{1/2} R_{\text{wd}}^3 \tau_{\text{sd}}}, \quad (61)$$

where  $I$  is the moment of inertia. We can use Eq. (61) to give an upper limit to  $B_{\text{dip}}$  by setting as values of  $L_{\text{sd}}$  and  $\tau_{\text{sd}}$ , the values of the latest value of the X-ray luminosity data, i.e.  $L_{\text{sd}} = L_X \approx 4.87 \times 10^{38} \text{ erg s}^{-1}$ , and  $\tau_{\text{sd}} \approx 10^8 \text{ s}$ . With this, we obtain an upper value  $B_{\text{dip,max}} \approx 7.46 \times 10^{11} \text{ G}$ . To this upper value of  $B_{\text{dip}}$ , it corresponds an upper value of the initial rotation period which can be obtained by calculating  $P_0 = 2\pi/\Omega_0$  from Eq. (50), i.e.

$$P_0 = 2\pi \left( \frac{2B_{\text{dip}}^2 R_{\text{wd}}^6}{c^3 L_{\text{sd}}} \right)^{1/4}, \quad (62)$$

from which we obtain  $P_{0,\text{max}} \approx 75.25 \text{ s}$ . We can further constrain the rotation period by seeking for values of the magnetic field strength and rotation period in agreement with the model presented in Sec. 3 for the prompt emission. Such a mechanism is expected to release magnetic energy stored in the magnetosphere, i.e.

$$E_B \approx \frac{1}{6} B_{\text{dip}}^2 R_{\text{wd}}^3, \quad (63)$$

so we need a dipole magnetic field strength

$$B_{\text{dip}} = \left( \frac{6E_B}{R_{\text{wd}}^3} \right)^{1/2} \approx \left( \frac{6E_{\text{prompt}}}{R_{\text{wd}}^3} \right)^{1/2}. \quad (64)$$

If we assume that the entire energy of the prompt emission,  $E_{\text{prompt}} \approx 4.16 \times 10^{46} \text{ erg}$  (see Sec. 3) is paid by the magnetosphere energy, we obtain a magnetic field  $B_{\text{dip}} = 9.61 \times 10^{10} \text{ G}$ . If we require the magnetic field energy to cover only the nonthermal component of the prompt, i.e.  $1.17 \times 10^{45} \text{ erg}$  (see Sec. 3), then the dipole magnetic field becomes  $1.30 \times 10^{10} \text{ G}$ . For the above magnetic field values, Eq. (62) gives, respectively,  $P_0 \approx 30 \text{ s}$ , and  $P_0 \approx 12 \text{ s}$ . The WD pulsar luminosity shown in Figs. 3 and 5 corresponds to the latter case.

The energy released (and injected into the ejecta) by the fallback accretion phase is  $E_{\text{fb}} = H_0 t_*/(\delta - 1) \approx 3.34 \times 10^{48} \text{ erg}$ . Energy and angular momentum are transferred to the newborn WD during this phase, and since the rotational to gravitational energy ratio of a uniformly rotating WD is of the order of  $10^{-2}$ ,<sup>32</sup> the newborn WD has gained about a few  $10^{46} \text{ erg}$  of rotational energy during this phase. This might produce at a rotation period decrease of the order of a second, which confirms that the WD must be already fast rotating at birth.

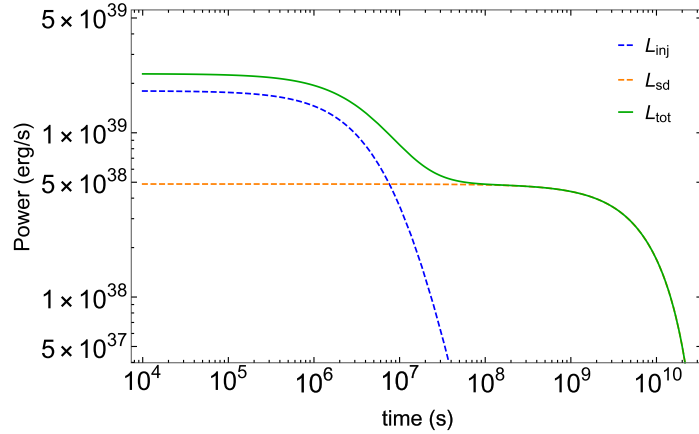


Fig. 5. Power injected into the ejecta by the newborn WD and the pulsar emission as given, respectively, by Eqs. (35) and (50). See the main text for further details.

In Fig. 5, we plot the power injected in energetic electrons from the WD,  $L_{\text{inj}}$ , and the luminosity due to magnetic dipole braking,  $L_{\text{sd}}$ . Both components release an energy of the order of  $10^{46}$  erg. From the inferred rotation period of 12.21 s, the initial eccentricity turns out to be  $e_0 \approx 0.39$ , so the moment of inertia is about 5% bigger than the one of the equivalent spherical configuration. Using the evolution equations (58), we obtain that the moment of inertia, for instance from  $10^4$  s to  $10^8$  s, changes in about 0.03%. This small change in the structure of the WD, and the associated change in the rotational and gravitational energy, are sufficient to pay for the energy released by the ongoing magnetospheric phenomena responsible for the injection of particles into the ejecta and for the pulsar emission; see Sec. 5.2.

## 7. Conclusions

We have here addressed a self-consistent explanation of GRB 170817A, including its associated optical emission AT 2017gfo, based on a WD-WD merger. The most recent data of *Chandra* of the X-ray emission of GRB 170817A at  $\sim 10^8$  s ( $\sim 1000$  d) after the GRB trigger,<sup>21,22</sup> indicate an X-ray re-brightening. This is explained by the emergence of the pulsar-like activity of the newborn WD (see Figs. 3 and 4), as predicted in Refs. 13, 20. We have here inferred that the newborn object is consistent with a massive ( $\sim 1.3 M_{\odot}$ ), fast rotating ( $P \gtrsim 12$  s), highly magnetized ( $B \sim 10^{10}$  G) WD, formed in a  $1.0 + 0.8$  WD-WD merger (see Secs. 2 and 6).

The post-merger emission at different wavelengths is explained as follows. The prompt gamma-ray emission detected by the *Fermi*-GBM, with a luminosity of  $\sim 10^{47}$  ergs $^{-1}$  and observed duration of  $\lesssim 1$  s, can be explained by the transient hot corona produce at the merger. The high temperature produces photons that undergo  $e^-e^+$  pair creation, the pairs are accelerated by the electric field induced by the  $10^{10}$  G magnetic field and the WD rotation, thereby producing photons. The system is highly opaque to these photons (see Sec. 3) to the  $\gamma\gamma$  pair production process. Only a small percentage of photons is expected to be able to escape from

the system along the polar axis, leading to the small amount of nonthermal emission observed above 1 MeV, while the rest is expected to form a nearly thermal plasma.

The ejecta expand with velocities  $\sim 10^9$  cm s $^{-1}$ , and release energy by thermal cooling (see Sec. 4) and synchrotron radiation (see Sec. 5), powered by the newborn WD at the merger (see Sec. 5.2). fallback accretion onto the newborn WD injects energy into the ejecta at early-times, heating up the ejecta. The ejecta is optically thick up to nearly  $10^5$ , so the ejecta cool by diffusion while it expands. The thermal radiation is in agreement with the data of the early optical counterpart AT 2017gfo (see Fig. 2). This explanation is markedly different from the *nuclear kilonova* from decay of r-process synthesized heavy nuclei in an NS-NS merger ejecta.

The signature of the synchrotron radiation is identified from nearly  $10^6$  s, which explains the rising and decreasing luminosities with the same power-law slopes in the X-ray, optical and radio emissions (see Fig. 3 for details).

The X-ray data are essential for identifying the emergence of the newborn WD as a pulsar. We have shown evidence of the pulsar emission around  $10^6$  s and at late-times  $10^8$  s, causing the X-ray luminosity to deviate from the power-law emission of a pure synchrotron emission (see Figs. 3 and 4). These data reveal a rotation period  $\gtrsim 12$  s, and magnetic field of  $\sim 10^{10}$  G. The follow-up of the GRB 170817A X-ray emission in the next months/years to come is crucial to confirm this prediction.

Summarizing, GRB 170817A/AT 2017gfo are explained by a WD-WD merger. The  $10^{-3}M_{\odot}$  expelled in the merger expand and radiates via thermal and synchrotron cooling. The former explains AT 2017gfo and the latter the late-time X-rays, optical and radio emission. In this line, the association of GW170417A with GRB 170817A<sup>1</sup> is not confirmed in our treatment based on the new data in the X-rays, optical, and in the radio up to  $10^8$  s. Therefore, we indicate the necessity to further inquire on the spacetime sequence of the early part of these events.

Indeed, WDs of parameters approaching the present ones have been already identified, e.g. the WD in V1460 Her with  $P \approx 39$  s,<sup>68</sup> and the most recent observation of the WD in LAMOST J024048.51+195226.9 with  $P \approx 25$  s.<sup>69</sup> WDs of similar properties have been proposed as a model of SGRs and AXPs.<sup>70–73</sup> Therefore, the newborn WD pulsar in GRB 170817A could show itself in the near future as an SGR/AXP in the GRB 170817A sky position.

## References

1. B. P. Abbott *et al.*, *Astrophys. J. Lett.* **848** (2017) L12, arXiv:1710.05833 [astro-ph.HE].
2. A. Goldstein, P. Veres, E. Burns, M. S. Briggs, R. Hamburg, D. Kocevski, C. A. Wilson-Hodge, R. D. Preece, S. Poolakkil, O. J. Roberts, C. M. Hui, V. Connaughton, J. Racusin, A. von Kienlin, T. Dal Canton, N. Christensen, T. Littenberg, K. Siellez, L. Blackburn, J. Broida, E. Bissaldi, W. H. Cleveland, M. H. Gibby, M. M. Giles, R. M. Kippen, S. McBreen, J. McEnery, C. A. Meegan, W. S. Paciesas and M. Stanbro, *Astrophys. J. Lett.* **848** (2017) L14, arXiv:1710.05446 [astro-ph.HE].
3. V. Savchenko, C. Ferrigno, E. Kuulkers, A. Bazzano, E. Bozzo, S. Brandt, J. Chenevez, T. J. L. Courvoisier, R. Diehl, A. Domingo, L. Hanlon, E. Jourdain, A. von Kienlin,



- P. Laurent, F. Lebrun, A. Lutovinov, A. Martin-Carrillo, S. Mereghetti, L. Natalucci, J. Rodi, J. P. Roques, R. Sunyaev and P. Ubertini, *Astrophys. J. Lett.* **848** (2017) L15, arXiv:1710.05449 [astro-ph.HE].
4. B. P. Abbott et al., *Astrophys. J. Lett.* **848** (2017) L13, arXiv:1710.05834 [astro-ph.HE].
  5. E. Pian et al., *Nature* **551** (2017) 67, arXiv:1710.05858 [astro-ph.HE].
  6. I. Arcavi, G. Hosseinzadeh, D. A. Howell, C. McCully, D. Poznanski, D. Kasen, J. Barnes, M. Zaltzman, S. Vasylyev, D. Maoz and S. Valenti, *Nature* **551** (2017) 64, arXiv:1710.05843 [astro-ph.HE].
  7. P. S. Cowperthwaite et al., *Astrophys. J. Lett.* **848** (2017) L17, arXiv:1710.05840 [astro-ph.HE].
  8. M. Nicholl et al., *Astrophys. J. Lett.* **848** (2017) L18, arXiv:1710.05456 [astro-ph.HE].
  9. B. Paczynski, *Astrophys. J. Lett.* **308** (1986) L43.
  10. D. Eichler, M. Livio, T. Piran and D. N. Schramm, *Nature* **340** (1989) 126.
  11. R. Narayan, B. Paczynski and T. Piran, *Astrophys. J. Lett.* **395** (1992) L83, arXiv:astro-ph/9204001.
  12. L. Li and Z.-G. Dai, *Astrophys. J.* **918** (2021) 52, arXiv:2106.04788 [astro-ph.HE].
  13. J. A. Rueda, R. Ruffini, Y. Wang, Y. Aimuratov, U. Barres de Almeida, C. L. Bianco, Y. C. Chen, R. V. Lobato, C. Maia, D. Primorac, R. Moradi and J. F. Rodriguez, *J. Cosmol. Astropart. Phys.* **10** (2018) 006, arXiv:1802.10027 [astro-ph.HE].
  14. C. Yue, Q. Hu, F.-W. Zhang, Y.-F. Liang, Z.-P. Jin, Y.-C. Zou, Y.-Z. Fan and D.-M. Wei, *Astrophys. J. Lett.* **853** (2018) L10, arXiv:1710.05942 [astro-ph.HE].
  15. R. T. Wollaeger, C. L. Fryer, E. A. Chase, C. J. Fontes, M. Ristic, A. L. Hungerford, O. Korobkin, R. O’Shaughnessy and A. M. Herring, *Astrophys. J.* **918** (2021) 10, arXiv:2105.11543 [astro-ph.HE].
  16. O. Korobkin, R. T. Wollaeger, C. L. Fryer, A. L. Hungerford, S. Rosswog, C. J. Fontes, M. R. Mumpower, E. A. Chase, W. P. Even, J. Miller, G. W. Misch and J. Lippuner, *Astrophys. J.* **910** (2021) 116, arXiv:2004.00102 [astro-ph.HE].
  17. Y. L. Zhu, K. A. Lund, J. Barnes, T. M. Sprouse, N. Vassh, G. C. McLaughlin, M. R. Mumpower and R. Surman, *Astrophys. J.* **906** (2021) 94, arXiv:2010.03668 [astro-ph.HE].
  18. J. Barnes, Y. L. Zhu, K. A. Lund, T. M. Sprouse, N. Vassh, G. C. McLaughlin, M. R. Mumpower and R. Surman, *Astrophys. J.* **918** (2021) 44, arXiv:2010.11182 [astro-ph.HE].
  19. B. Côté, C. L. Fryer, K. Belczynski, O. Korobkin, M. Chruslińska, N. Vassh, M. R. Mumpower, J. Lippuner, T. M. Sprouse, R. Surman and R. Wollaeger, *Astrophys. J.* **855** (2018) 99, arXiv:1710.05875 [astro-ph.GA].
  20. J. A. Rueda, R. Ruffini, Y. Wang, C. L. Bianco, J. M. Blanco-Iglesias, M. Karlica, P. Lorén-Aguilar, R. Moradi and N. Sahakyan, *J. Cosmol. Astropart. Phys.* **2019** (2019) 044, arXiv:1807.07905 [astro-ph.HE].
  21. E. Troja, B. O’Connor, G. Ryan, L. Piro, R. Ricci, B. Zhang, T. Piran, G. Bruni, S. B. Cenko and H. van Eerten, arXiv e-prints (2021), arXiv:2104.13378 [astro-ph.HE].
  22. E. Troja, H. van Eerten, B. Zhang, G. Ryan, L. Piro, R. Ricci, B. O’Connor, M. H. Wieringa, S. B. Cenko and T. Sakamoto, *Mon. Not. R. Astron. Soc.* **498** (2020) 5643, arXiv:2006.01150 [astro-ph.HE].
  23. M. Livio and P. Mazzali, *Phys. Rep.* **736** (2018) 1, arXiv:1802.03125 [astro-ph.SR].
  24. M. Della Valle and L. Izzo, *Astron. Astrophys. Rev.* **28** (2020) 3, arXiv:2004.06540 [astro-ph.SR].
  25. R. Ruffini, R. Moradi, J. A. Rueda, L. Li, N. Sahakyan, Y. C. Chen, Y. Wang, Y. Aimuratov, L. Becerra, C. L. Bianco, C. Cherubini, S. Filippi, M. Karlica, G. J.

- Mathews, M. Muccino, G. B. Pisani and S. S. Xue, *Mon. Not. R. Astron. Soc.* **504** (2021) 5301, arXiv:2103.09142 [astro-ph.HE].
26. J. A. Rueda, R. Ruffini, M. Karlica, R. Moradi and Y. Wang, *Astrophys. J.* **893** (2020) 148, arXiv:1905.11339 [astro-ph.HE].
  27. Y. Wang, J. A. Rueda, R. Ruffini, L. Becerra, C. Bianco, L. Becerra, L. Li and M. Karlica, *Astrophys. J.* **874** (2019) 39, arXiv:1811.05433 [astro-ph.HE].
  28. R. Ruffini, M. Karlica, N. Sahakyan, J. A. Rueda, Y. Wang, G. J. Mathews, C. L. Bianco and M. Muccino, *Astrophys. J.* **869** (2018) 101, arXiv:1712.05000 [astro-ph.HE].
  29. L. Li, X.-F. Wu, W.-H. Lei, Z.-G. Dai, E.-W. Liang and F. Ryde, *Astrophys. J. Suppl.* **236** (2018) 26, arXiv:1712.09390 [astro-ph.HE].
  30. L. Becerra, K. Boshkayev, J. A. Rueda and R. Ruffini, *Mon. Not. R. Astron. Soc.* **487** (2019) 812, arXiv:1812.10543 [astro-ph.SR].
  31. L. Becerra, J. A. Rueda, P. Lorén-Aguilar and E. García-Berro, *Astrophys. J.* **857** (2018) 134, arXiv:1804.01275 [astro-ph.SR].
  32. K. Boshkayev, J. A. Rueda, R. Ruffini and I. Siutsou, *Astrophys. J.* **762** (2013) 117, arXiv:1204.2070 [astro-ph.SR].
  33. W. Benz, A. G. W. Cameron, W. H. Press and R. L. Bowers, *Astrophys. J.* **348** (1990) 647.
  34. J. Guerrero, E. García-Berro and J. Isern, *Astron. Astrophys.* **413** (2004) 257.
  35. P. Lorén-Aguilar, J. Isern and E. García-Berro, *Astron. Astrophys.* **500** (2009) 1193.
  36. R. Longland, P. Lorén-Aguilar, J. José, E. García-Berro and L. G. Althaus, *Astron. Astrophys.* **542** (2012) A117, arXiv:1205.2538 [astro-ph.SR].
  37. C. Raskin, E. Scannapieco, C. Fryer, G. Rockefeller and F. X. Timmes, *Astrophys. J.* **746** (2012) 62, arXiv:1112.1420 [astro-ph.HE].
  38. C. Zhu, P. Chang, M. H. van Kerkwijk and J. Wadsley, *Astrophys. J.* **767** (2013) 164, arXiv:1210.3616 [astro-ph.SR].
  39. M. Dan, S. Rosswog, M. Brüggen and P. Podsiadlowski, *Mon. Not. R. Astron. Soc.* **438** (2014) 14, arXiv:1308.1667 [astro-ph.HE].
  40. M. Nauenberg, *Astrophys. J.* **175** (1972) 417.
  41. G. Vianello, R. J. Lauer, P. Younk, L. Tibaldo, J. M. Burgess, H. Ayala, P. Harding, M. Hui, N. Omodei and H. Zhou, arXiv e-prints (2015) arXiv:1507.08343 [astro-ph.HE].
  42. D. J. Spiegelhalter, N. G. Best, B. P. Carlin and A. Van Der Linde, *J. R. Stat. Soc. Series B* **64** (2002) 583.
  43. E. Moreno, F. J. Vazquez-Polo and C. P. Robert, arXiv e-prints (2013), arXiv:1310.2905 [stat.ME].
  44. L. Li, *Astrophys. J. Suppl.* **242** (2019) 16, arXiv:1810.03129 [astro-ph.HE].
  45. L. Li, *Astrophys. J. Suppl.* **245** (2019) 7.
  46. L. Li, *Astrophys. J.* **894** (2020) 100, arXiv:1908.09240 [astro-ph.HE].
  47. L. Li, F. Ryde, A. Pe'er, H.-F. Yu and Z. Acuner, *Astrophys. J. Suppl.* **254** (2021) 35, arXiv:2012.03038 [astro-ph.HE].
  48. L. Li and B. Zhang, *Astrophys. J. Suppl.* **253** (2021) 43, arXiv:2101.04325 [astro-ph.HE].
  49. P. Goldreich and W. H. Julian, *Astrophys. J.* **157** (1969) 869.
  50. E. Troja *et al.*, *Nature* **551** (2017) 71, arXiv:1710.05433 [astro-ph.HE].
  51. D. Lazzati, D. López-Cámara, M. Cantiello, B. J. Morsony, R. Perna and J. C. Workman, *Astrophys. J. Lett.* **848** (2017) L6, arXiv:1709.01468 [astro-ph.HE].
  52. N. S. Kardashev, *Sov. Astron.* **6** (1962) 317.
  53. F. Pacini and M. Salvati, *Astrophys. J.* **186** (1973) 249.

54. J. Pétri, *Mon. Not. R. Astron. Soc.* **450** (2015) 714, arXiv:1503.05307 [astro-ph.HE].
55. S. Chandrasekhar, *Ellipsoidal Figures of Equilibrium* (1969).
56. K. D. Alexander, E. Berger, W. Fong, P. K. G. Williams, C. Guidorzi, R. Margutti, B. D. Metzger, J. Annis, P. K. Blanchard, D. Brout, D. A. Brown, H. Y. Chen, R. Chornock, P. S. Cowperthwaite, M. Drout, T. Eftekhari, J. Frieman, D. E. Holz, M. Nicholl, A. Rest, M. Sako, M. Soares-Santos and V. A. Villar, *Astrophys. J. Lett.* **848** (2017) L21, arXiv:1710.05457 [astro-ph.HE].
57. G. Hallinan, A. Corsi, K. P. Mooley, K. Hotokezaka, E. Nakar, M. M. Kasliwal, D. L. Kaplan, D. A. Frail, S. T. Myers, T. Murphy, K. De, D. Dobie, J. R. Allison, K. W. Bannister, V. Bhalerao, P. Chandra, T. E. Clarke, S. Giacintucci, A. Y. Q. Ho, A. Horesh, N. E. Kassim, S. R. Kulkarni, E. Lenc, F. J. Lockman, C. Lynch, D. Nichols, S. Nissanke, N. Palliyaguru, W. M. Peters, T. Piran, J. Rana, E. M. Sadler and L. P. Singer, *Science* **358** (2017) 1579, arXiv:1710.05435 [astro-ph.HE].
58. S. Kim *et al.*, *Astrophys. J. Lett.* **850** (2017) L21, arXiv:1710.05847 [astro-ph.HE].
59. K. P. Mooley, E. Nakar, K. Hotokezaka, G. Hallinan, A. Corsi, D. A. Frail, A. Horesh, T. Murphy, E. Lenc, D. L. Kaplan, K. de, D. Dobie, P. Chandra, A. Deller, O. Gottlieb, M. M. Kasliwal, S. R. Kulkarni, S. T. Myers, S. Nissanke, T. Piran, C. Lynch, V. Bhalerao, S. Bourke, K. W. Bannister and L. P. Singer, *Nature* **554** (2018) 207, arXiv:1711.11573 [astro-ph.HE].
60. K. P. Mooley, D. A. Frail, D. Dobie, E. Lenc, A. Corsi, K. De, A. J. Nayana, S. Makhathini, I. Heywood, T. Murphy, D. L. Kaplan, P. Chandra, O. Smirnov, E. Nakar, G. Hallinan, F. Camilo, R. Fender, S. Goedhart, P. Groot, M. M. Kasliwal, S. R. Kulkarni and P. A. Woudt, *Astrophys. J. Lett.* **868** (2018) L11, arXiv:1810.12927 [astro-ph.HE].
61. K. D. Alexander, R. Margutti, P. K. Blanchard, W. Fong, E. Berger, A. Hajela, T. Eftekhari, R. Chornock, P. S. Cowperthwaite, D. Giannios, C. Guidorzi, A. Kathirgamaraju, A. MacFadyen, B. D. Metzger, M. Nicholl, L. Sironi, V. A. Villar, P. K. G. Williams, X. Xie and J. Zrake, *Astrophys. J. Lett.* **863** (2018) L18, arXiv:1805.02870 [astro-ph.HE].
62. D. Dobie, D. L. Kaplan, T. Murphy, E. Lenc, K. P. Mooley, C. Lynch, A. Corsi, D. Frail, M. Kasliwal and G. Hallinan, *Astrophys. J. Lett.* **858** (2018) L15, arXiv:1803.06853 [astro-ph.HE].
63. L. Piro, E. Troja, B. Zhang, G. Ryan, H. van Eerten, R. Ricci, M. H. Wieringa, A. Tiengo, N. R. Butler, S. B. Cenko, O. D. Fox, H. G. Khandrika, G. Novara, A. Rossi and T. Sakamoto, *Mon. Not. R. Astron. Soc.* **483** (2019) 1912, arXiv:1810.04664 [astro-ph.HE].
64. J. D. Lyman *et al.*, *Nature Astronomy* **2** (2018) 751, arXiv:1801.02669 [astro-ph.HE].
65. G. P. Lamb, J. D. Lyman, A. J. Levan, N. R. Tanvir, T. Kangas, A. S. Fruchter, B. Gompertz, J. Hjorth, I. Mandel, S. R. Oates, D. Steeghs and K. Wiersema, *Astrophys. J. Lett.* **870** (2019) L15, arXiv:1811.11491 [astro-ph.HE].
66. A. Hajela *et al.*, arXiv e-prints (2021), arXiv:2104.02070 [astro-ph.HE].
67. F. Verrecchia *et al.*, *Astrophys. J. Lett.* **850** (2017) L27, arXiv:1710.05460 [astro-ph.HE].
68. I. Pelisoli, T. R. Marsh, R. P. Ashley, P. Hakala, A. Aungwerojwit, K. Burdge, E. Breedt, A. J. Brown, K. Chanthorn, V. S. Dhillon, M. J. Dyer, M. J. Green, P. Kerry, S. P. Littlefair, S. G. Parsons, D. I. Sahman, J. F. Wild and S. Yotthanathong, *Mon. Not. R. Astron. Soc.* **507** (2021) 6132, arXiv:2109.00553 [astro-ph.SR].

69. I. Pelisoli, T. R. Marsh, V. S. Dhillon, E. Breedt, A. J. Brown, M. J. Dyer, M. J. Green, P. Kerry, S. P. Littlefair, S. G. Parsons, D. I. Sahman and J. F. Wild, arXiv e-prints (August 2021), arXiv:2108.11396 [astro-ph.SR].
70. J. G. Coelho, D. L. Cáceres, R. C. R. de Lima, M. Malheiro, J. A. Rueda and R. Ruffini, *Astron. Astrophys.* **599** (2017) A87.
71. J. A. Rueda, K. Boshkayev, L. Izzo, R. Ruffini, P. Lorén-Aguilar, B. Külebi, G. Aznar-Siguán and E. García-Berro, *Astrophys. J. Lett.* **772** (2013) L24, arXiv:1306.5936 [astro-ph.SR].
72. K. Boshkayev, L. Izzo, J. A. Rueda Hernandez and R. Ruffini, *Astron. Astrophys.* **555** (2013) A151, arXiv:1305.5048 [astro-ph.SR].
73. M. Malheiro, J. A. Rueda and R. Ruffini, *PASJ* **64** (2012) 56, arXiv:1102.0653 [astro-ph.SR].